Universidad Autónoma de Madrid

Doctoral Thesis

New approaches to anti-multipactor coatings for space applications

Author
Valentin C. Nistor

Supervisor
Dr. Luis Galan Estella

A thesis submitted in fulfilment of the requirements
for the degree of Doctor of Philosophy
in
Advanced Materials and Nanotechnology

Departamento de Física Aplicada, Facultad de Ciencias

November 2015

"Dedicated to my family"

Acknowledgements

Me gustaría agradecer en primer lugar a Prof. Dr. Luis Galán Estella, el director de esta tesis, por los conocimientos científicos y el apoyo que me ha trasmitido, por la valiosísima ayuda y cariño que he recibido de su parte y su dedicación profesional durante todos estos años, que han hecho posible la realización de esta tesis, así como su gran mérito en la redacción de este manuscrito.

También me gustaría agradecer a la Dra. Isabel Montero por su motivación, disponibilidad y los buenos consejos cuando más lo he necesitado.

Quiero también expresar mis más sinceros agradecimientos a José Antonio por haberme iniciado en las técnicas experimentales durante mi inicio en el doctorado y por su gran apoyo y paciencia.

Finalmente quiero agradecer a todas las personas de mi entorno profesional y personal que, de una forma u otra, han enriquecido mi vida durante la estancia en la Universidad Autónoma.

Contents

Table of Contents

Abbreviations

UAM - Universidad Autónoma de Madrid

ESTEC - European Space Research and Technology Centre

CERN- Organisation européenne pour la recherche nucléaire

SLAC - Stanford Linear Accelerator Center

MULCOPIM -Multipactor, Corona and Passive Intermodulation

LHC - Large Hadron Collider

CSIC - Consejo Superior de Investigaciones Cientificas

ICMM - Instituto de Ciencia de Materiales de Madrid

VSC - Val Space Consortium

EM – Electro Magnetic

ONERA - Le centre français de recherche aérospatiale

SEE - Secondary Electron Emission

SE - Secondary Electron

EDC - Energy Distribution Curve

SEY - Secondary Electron Yield

REELS - Reflection Electron Energy Loss Spectrum

DC - Direct Current

EC - Electron Cloud

RF- Radio Frequency

MEST - Multipactor Electron Simulation Tool

IL - Insertion Loss

UHV - Ultra High Vacuum

PVD - Physical Vapour Deposition

GLAD – Glancing angle deposition

FWHM - Full Width at Half Maximum

INFN - Instituto Nazionale di Fisica Nucleare

PES Photoemission Spectroscopies

XPS - X-Ray Photoemission Spectroscopy

SEM - Scanning Electron Microscopy

FE - SEM Field Emmision Scanning Electron Microscopy

EDX - Energy Dispersive X-Ray spectroscopy

AFM - Atomic Force Microscopy

MP - Multipactor

MPT - Multipactor Threshold

Acronyms

Ep = primary energy

λ = Inelastic mean free path

2D = Two dimensional

3D = Three dimensional

Φ = Work function

BSE = backscattered electron emission, yield and phenomenon.

Alodine = standard coating for space applications

δ = True secondary emission yield, or skin depth

η = Inelastically backscattered electron emission

ε = Elastically backscattered electron emission

E_1 = SEY first cross-over energy (E_1 = lower value of the two possible Ep for SEY = 1)

E_p = Energy of primary or incident electron in the SEE process.

EDX = Energy dispersive X-ray analysis.

XAES = X-ray Auger Spectroscopy

ICMM = Instituto de Ciencia de Materiales de Madrid, part of CSIC.

IL = Insertion loss in dB

IL enhancement factor = IL(sample) / IL(reference)

DC = Direct current, low frequency limit.

MP = Multipactor

MPL = Multipactor power level or threshold

MPL enhancement = 10·Log(MPL(sample)/MPL(reference)) dB

RF = radio frequency SEE = Secondary electron emission, as a phenomenon or process.

SEM = Scanning electron microscopy.

SEY = Secondary electron emission yield (normal incidence), also as a phenomenon or process.

UAM-AP = Applied Physics Department of UAM.

VSC = Val Space Consortium

XPS = X-ray photoemission spectroscopy.

Resumen

Nuevas perspectivas en recubrimientos anti-multipactor para aplicaciones en el espacio

El efecto Multipactor es un fenómeno perjudicial en dispositivos de alta potencia de RF en vacío de gran importancia tecnológica, industrial y económica. Es un viejo problema en la industria espacial, en los aceleradores de partículas de gran energía, en dispositivos toroidales de energía termo-nuclear, en generadores de potencia de RF, y muchas tecnologías electrónicas avanzadas.

El efecto o descarga Multipactor se genera y alimenta por la Emisión de Electrones Secundarios (SEE) en las superficies del dispositivo. Por eso siempre su solución o mitigación pasa por reducir esta SEE de los materiales usados en las partes críticas del dispositivo.

Los laboratorios de los aceleradores SLAC, CERN, KEK,… y ESTEC y VSC de ESA han dedicado un gran esfuerzo a este problema. Nuestro grupo colabora con los grupos en SLAC, CERN y ESA.

El objetivo final y global del trabajo de esta tesis doctoral era el desarrollo y aplicación de recubrimientos anti-multipactor para aplicaciones espaciales de alta potencia de RF, para mitigar o suprimir la descarga multipactor con recubrimientos de baja SEE, estables en el aire y con baja resistencia superficial en la banda Ku (alrededor de 12 GHz).

La búsqueda de materiales con baja SEE entra en conflicto con otras propiedades requeridas estrictamente para su aplicación en el espacio. Estas son principalmente muy buena conductividad eléctrica y gran estabilidad en el aire. Esta última está claramente en conflicto con la baja SEE y la alta conductividad. Este enfoque basado en las propiedades físico-químicas de las superficies se ha agotado sin encontrar una buena solución al Multipactor.

A partir de en algunas observaciones tanto de nuestro laboratorio como de otros y que no habían sido consideradas en toda sus implicaciones, esta tesis doctoral se basa en varias hipótesis de trabajo importantes y novedosas:

i) los diferentes requerimientos que no se pueden cumplir con un solo material se pueden satisfacer por capas de diferentes materiales haciendo uso de las diferentes escalas y penetraciones de las diferentes propiedades requeridas (modelo de capas del recubrimiento).

ii) la rugosidad superficial de gran relación de aspecto es muy eficiente en reducir fuertemente la SEE aparente o eficaz y esta propiedad es de la forma y no del tamaño.

iii) la rugosidad superficial de gran relación de aspecto aumenta la resistencia superficial de RF pero esto es una propiedad de la forma y del tamaño. Reduciendo suficientemente el tamaño puede hacerse compatible (ii) y (iii).

Para la obtención de dicho tipo de rugosidad superficial en el material mejor conductor y de referencia en la industria espacial, Ag electrodepositada, se propuso realizar una amplia y concienzuda investigación en técnicas de micro y nano-estructuración de superficies.

Otros objetivos eran desarrollar los recubrimientos y sus aplicaciones en dispositivos prácticos en estrecha colaboración con la industria espacial para satisfacer toda una serie de requerimientos industriales y económicos para su aplicación.

Desarrollo del trabajo y metodología

Este trabajo de investigación se ha desarrollado en dos grandes proyectos. Cada uno formado por un proyecto del Plan Nacional de I+D+i y otro paralelo de ESA. En ellos han colaborado el grupo de la UAM, el grupo de I. Montero en el ICMM del CSIC, la empresa Tesat Spacecom y ESTEC y VSC de ESA. En esta tesis se presenta el trabajo realizado por el doctorando en la UAM.

El trabajo en el primer gran proyecto y tema principal de esta Tesis, tuvo varias etapas:

Definición de las capas (materiales, tamaños, estructura, ..) del recubrimiento.

Desarrollo de técnicas de preparación y caracterización de los procedimientos y los recubrimientos. Se investigaron más de diez técnicas de micro estructuración de superficies. Para la más prometedora se estudiaron nueve variantes, se prepararon unas cien muestras para estudiar más de cinco propiedades, además se prepararon nueve muestras preindustriales. La investigación fue tecnológica: el objetivo era alcanzar los resultados buscados en menos tiempo. El estudio científico de procesos y mecanismos estaba subordinado al método de la bisección o de ensayo y error.

Definición de la técnica y procedimiento óptimo: grabado químico poroso y posterior mentalización con Au.

Aplicación a cinco dispositivos industriales. Caracterización científica de los resultados.

Caracterización tecnológica e industrial de los dispositivos tratados.

Discusión y valoración de los resultados y propuestas para nuevas investigaciones.

Los excelentes y novedosos resultados de este primer gran proyecto han permitido la realización de los proyectos siguientes.

Estas propuestas dieron lugar al segundo gran proyecto también formado por dos proyectos paralelos realizados por los mismos grupos y centros.

En este segundo gran proyecto se ha logrado mantener la práctica supresión del Multipactor alcanzada en el primero pero ahora con recubrimientos de conductividad óptima, la máxima posible, la de los recubrimientos de Ag lisos estándar de la industria. Para ello se han obtenido rugosidades superficiales especiales de escala 100 nm. En este proyecto se desarrolló una de las técnicas "descubiertas" en el proyecto anterior pero para la que no hubo suficiente recursos ni tiempo: grabado auto-organizado con haces de iones asistido por deposición de máscara-surfactante por sputtering.

Chapter 1

Introduction

1.1 Secondary Electron Emission and Multipactor Effect

Secondary electron emission (SEE) is a phenomenon or process by which specific bounded electrons (with negative energy) of an atom are detached and freed (with positive energy and called secondary electrons) as consequence of the interaction or collision with an incident energetic electron (called primary electron). This atom may be part of a molecule, gas, liquid, or solid. This definition is sometimes generalized to include other energetic particles as the cause, such as ions or atoms. However, in the case of photons as the cause, it is known as photoemission.

Usually and more strictly, SEE refers to emission of electrons into vacuum from a solid surface caused by the impact of incident primary electrons in conditions of absence of any external field.

The study of SEE was part of the vanguard of solid state physics at its infancy in the beginnings of the 20^{th} century. Of course, it was mainly motivated the technological applications of materials of high SEE yield (SEY), such as in electron multipliers. Soon, photoemission became technologically more important and the solid state physics vanguard moved to photoemission. It was much less complex than SEE and much more productive in both fundamental solid state physics and technology. Thus fundamental physics of SEE remained somehow at "ralenti" until very recently, maintained by its applications in Scanning Electron Microscopy (SEM). Only since one decade, SEE theory is able to accurately calculate SEY of some materials. However, there still remains a problem for technology: SEE is extremely sensitive to the surface of the materials and those of technological interest are not sufficiently well characterized.

Recent renewed interest in SEE is instigated by its crucial role in malfunction problems encountered in several advanced technologies. Multipactor effect or multipaction and electron cloud refer to a class of phenomena which interfere in the operation of high power RF devices in space, high energy particle accelerators, tokamak (a class of thermonuclear fusion device), klystrons, multi-stage tubes, and other vacuum devices with intense electromagnetic fields at very high frequency. In these processes, a cloud of free electrons in vacuum grows in avalanche and in resonance the RF field. The energy is supplied by the RF field and the electrons by the SEE from the material surfaces exposed to the electron cloud. This electron discharge can easily be started by low energy (seed) electrons from SEE or photoemission from external sources. After avoiding resonant conditions by proper design of the electromagnetic field, there always remain some critical parts which require material surfaces of very low SEY or anti-multipactor coatings.

This technological research was focused mainly on the development and implementation of innovative materials with advanced characteristics and properties, capable of improving the performance of high RF devices and components of communication satellite system payload designs. This comes as an imperative requirement for a space industry, with an ever increasing demand of handling high power levels. The importance of these materials is also enhanced by the testing procedures on actual physical devices incorporated on a communication satellite. On the other hand, the findings can be stretched to other important fields. The electron cloud build-up behaviour is a constant open-case study not only for the aerospace industry and particle accelerators. Its presence generally affects the reach of optimum power levels, from high RF device signals to TeV proton beams.

Many research groups investigated on physico-chemical properties of materials for application in anti-multipactor coatings, such as those at SLAC, CERN, KEK, and UAM (for ESTEC, ESA). However, it was soon found that there was an impeding and unavoidable problem with that approach: the increase of the SEY upon exposure to the air was higher for those surfaces of lower SEY in clean as-prepared conditions. This is crucial for the space industry since anti-multipactor coatings have to be exposed to the atmospheric air and cannot be *cleaned, conditioned,* or *scrubbed* in situ in space. The solution came from the so-called “SEE suppression effect” of surface roughness of high

aspect ratio. This is mainly a geometrical or morphological effect, a kind of partial black-body effect. In fact, those surfaces are optically dark.

We will just remember a few old milestones:

First reports on the Multipactor effect: Gutton (1924) [1] and Farnsworth (1934) [2]

A first ESA review on Multipactor: Woode and Petit (1989) [3].

Recent reviews on Multipactor: ECSS (2013) [4], Kishek & Lau & Ang & Valfells & Gilgenbach (1998) [5], Parodi (2011) [6], MULCOPIM ESA Workshop (2014) [7], EVEREST ESA project [7a-d].

First thorough review on SEE: Bruining's book (1954) [8].

First reports on SEE: Austin & Starke and Lenard (1902 - 05) [9].

First theories of SEE: Lenard (1925), Baroody (1950), and Dekker & Van Der Ziel (1952) [9], Dekker (1958) [10].

Some first research works on anti-multipactor coatings by SLAC [11, 12] and CERN [13, 14] laboratories:

First anti-multipactor coatings based in the SEE properties of surface roughness: Forman (1977) [15] and Current (1984) [16].

First patent on anti-multipactor coatings based in the SEE properties of surface roughness: Derfler & Perchermeir & Spitzer (Max Planck Gesellschaft, 1984), [17].

1.2 Technological research of UAM-CSIC-ESA-Tesat and Spain National Plan

1.2.1 Background research

The entire research of ESA on anti-multipactor coatings since its beginning in 1985 until recently (2008) was performed by the group of Prof. F. Rueda and L. Galán at the Applied Physics Department of Universidad Autónoma de Madrid (UAM) in the frame of several ESA ESTEC projects [18-22]. Then, their work continued until 2014 but others research groups also collaborated in the anti-multipactor coatings research of ESA [23-25].

New research groups on anti-multipactor coatings incorporated into the technological research supported by ESA:

I. Montero (CSIC) 2008 (ESA AO4025, CCN-02 extension project)

M. Belhaj (ONERA) 2010 (EVEREST project)

B. Gimeno (Universidad de Valencia) 2012 (EVEREST project)

The work initiated in 1985 in the Applied Physics Department of UAM was for characterizing the SEY of *Alodine*® coating (chromate conversion coating, corrosion-protection surface treatment for aluminium) the reference anti-multipactor coating of ESA, to be used in the first Earth observation satellite of the series ERS of ESA. Other standard coatings such as Ag and Au plating, and Cu, were also studied besides the bare aluminium alloy. The two main ESA reference documents on Multipactor effect and prevention [3, 4] contain also the results of that work. Only in 2014, that research was updated for Ag plating by the EVEREST project [24].

That study [18] also showed that the relation between SEY and Multipactor threshold was not clear-cut. The Multipactor power threshold appeared to be a function of the ratio (E1 = first cross-over energy / SEY-max), actually, proportional to square root of this ratio. However, the correlation was poor, a very large dispersion or random error was present. This fact was not attributed to other uncontrolled SEY parameters but to the uncertainty of SEY: it could easily be modified by manipulation or atmospheric air exposure between the SEY and Multipactor tests.

After those initial works, the research on anti-multipactor coatings continued focused on other potential materials such as nitrides, carbides and silicides of light transition metals like Ti, Cr, V, and others [20-21] following the lines of the research in other laboratories such as SLAC and CERN. Those compounds have metallic conductivity and corresponding low SEY, however, they are much more stable in air than the corresponding pure metals. It was found that even the best anti-multipactor coatings experienced a slow deterioration of their SEE properties (essentially, increase of the yield) when exposed to the air for a sufficiently long time, even up to the month scale, called "aging". Time was an important factor since extreme humidity and temperature did not seem to accelerate significantly the process. The requirement of good surface conductivity appeared to be crucial in aging since it implies metallic character and thus leading to surface reactivity in air. On the contrary, *Alodine* was very stable in air;

however countervailing, it had very poor surface conductivity. The formation of surface oxide and hydroxide chemical bonds can only be part of the aging of the SEY of metallic materials. For example, Au does not oxidize in air; however, surface adsorption of oxygen or carbon containing molecules produces an increase of SEY at low primary energies, very important energies for the Multipactor effect. Thus, the stable low SEY of *Alodine* remains somehow unexplained.

As a consequence of research on a broad variety of materials, the group of UAM presented at MULCOPIM 2005 a series of gap-transformer wave guides for 9.5 GHz manufactured in Mg alloy with a multilayer porous coating which showed Multipactor power thresholds 3.2 – 7.4 dB higher than those of the same devices of standard Ag-plated Al alloy. That was the first time surface roughness was used for mitigating Multipactor in high-power RF devices for space applications. The structure of the coating was a 1 – 2 μm thick layer of either Au or Ag on a porous ceramic MgO 5 μm thick protective layer (*Anomag*^{TM}) on the surface of the Mg alloy device. The pore size varied from 200 nm to 5 μm (averages 1.0 – 2.3 μm) and represented 27 % of the surface area. The insertion loss (in dB) increased in a factor of 2.4 respect to the standard Ag-plated Al alloy devices, while for *Alodine* that factor was 3.8.

Those results were really excellent [26] but RF space technology in Mg alloy is still beyond any foresight. Furthermore, the dielectric interlayer (MgO) could give rise to high surface impedance effects [27, 28] if the thickness of the metallic overlayer (Ag or Au) was not sufficient for avoiding the RF field to penetrate down to the complete "sandwich" Ag (porous metal) / MgO (porous dielectric) / Mg (metal).

The use of porous or rough surfaces was an important turning point in anti-multipactor research. Until then, in most laboratories, UAM, SLAC, CERN, KEK… the research was focused on the bulk properties of the surface materials of the anti-multipactor coatings. In UAM, for the case of space applications, there was found an incompatibility or contradiction among main requirements for an anti-multipactor coating:

- low SEY at low primary energies,
- high surface conductivity, and
- long chemical stability under air exposure,

in order to be met by a single material. Best materials for first two criteria form easily oxides and hydroxides in air. Thus, the effect of surface roughness in significantly

reducing effective SEY represented an alternative approach to anti-multipactor coatings since allowed more tolerance respect to the requirement of low intrinsic SEY for the surface material.

Main results of the research were presented at ESA workshops MULCOPIM 2000 (ESA WPP-178), 2005, 2008, 2011, and 2014 [29].

It is interesting to realize nowadays with a developed knowledge that in those early time of ESA project PO 162594 (1996) [20] some anti-multipactor coatings of TiN prepared by sputtering deposition assisted by low-energy Ar ion bombardment were actually "contaminated" with some metal "surfactant" (Fe, Cr, …) from the sample stage which produced a high-aspect-ratio surface roughness in the scale of 50 nm! Those samples had very low SEY at low primary energies and exceptionally high Multipactor thresholds [20, 30]. Ten years before finding out the importance of the process after project ESA AO 4025 CCN-2 [25].

The investigations summarized in this section were also supported by the Spain National Plan [31] whose support was indispensable for carrying out that research. The work of the Department of Applied Physics of the UAM on anti-multipactor coatings has followed the technological interests of the European Community as managed by ESA. This agrees widely with the purposes of the I+D+i National Plan of Spain in the area of Space. In fact, all that research was concurrently and affluently supported by projects of that I+D+i Plan.

1.2.2 Main research of this thesis - ESA AO 4025 CCN-2 project

The conclusions achieved in those previous research projects were expressed in the goals and working hypotheses for a new TRP (Technology Research Programme) project (extension or Contract Change Notice) supported by ESA and Tesat Spacecom for continuing the work in new advanced anti-multipactor coatings: *Porous Inert Metal Coatings for Controlling Secondary Emission*.

- The anti-multipactor surface treatment should be developed for the well-known space technology of Ag-plated Al alloy devices for high-power RF applications.
- Significant SEY reduction will be searched based on the hypothesis of the SEY "suppression" effect of surface roughness of high aspect ratio.

- Inert or noble metal porous (or rough) coatings will be used to achieve both: optimum values, control, reproducibility, homogeneity, and stability in air for the secondary electron emission yield and the electrical conductivity.
- No dielectric layers or templates will be used in order to avoid abnormal surface RF impedance values.
- Ag and Au should be preferred because of their high conductivity.
- Porosity of surface roughness should not modify the RF field inside the waveguide and it should be small compared to machining finish, i.e., well below 10 μm.

The project had three main parts:

- Literature Research and Study for evaluating potential materials and techniques.
- Experimental Study on Small Research Samples of an ample variety of selected materials and techniques.
- Preparation of Selected Coating on Multipactor Samples for testing their RF behaviour and Multipactor threshold.

All goals were achieved. A detailed report of the work performed is given in 12 presentations and 5 technical notes and reports to ESA and Tesat Spacecom [29]. Main results of the research were presented at MULCOPIM 2008, 2011, and 2014 [29].

The research summarized above was also supported by Spain National Plan [31 b), c)].

1.2.3 Extended research for ESA ITI B00011822 project

As a consequence of the achievements and learnings from the previous research, a new project supported by ESA and Tesat Spacecom was undertaken to continue the work in new, advanced anti-multipactor coatings: *Optimization of Surface Roughness of Anti-Multipactor Coatings for Low Insertion Losses and Secondary Emission Suppression for High Power RF Components in Satellite Systems* [23]. This time, it was an ITI type B project (Innovation Triangle Initiative. Demonstration of feasibility and use).

The main objective was to enhance Multipactor threshold, without penalizing insertion loss, to be achieved by: decreasing roughness size and, maintaining roughness shape. This was based on two working hypothesis: significant suppression of secondary electron emission can be obtained by high-aspect roughness shape (already experimentally

demonstrated) and insertion loss decreases with roughness size (only theoretically predicted).

This project was successfully developed. Nanostructuring of noble metal surfaces to special simple smooth high-aspect-ratio profiles was performed by a new ion beams technique: ion beam etching while hard metal masking by sputtering. Strong secondary electron emission suppression is achieved with negligible increase of RF surface resistance. Insertion loss only comparable to the best (flat smooth Ag plating) was obtained [32].

The project and main results of the research were presented at MULCOPIM 2011, and 2014 [7, 23, and 29].

Initial work and some important results of this project are also reported in this thesis.

1.3 Scientific research and technological applications

There is not a simple unidirectional linear sequence in the relation between scientific research and the resulting technological applications which are supposed to produce an increase of industrial productivity and consequent economic development:

Scientific research → Technological applications → Productivity increase → Economic development

In the most fruitful conditions, there is a complex frame of interactions and correlations among the three activities of university/scientific and industry institutions or centres: scientific knowledge, technical knowledge, technological development. These interactions include fluxes of knowledge and trainings in both directions, as well as the development of stocks of knowledge, methods, and techniques. There are also fluxes of trained people, scientists and engineers. See [33 - 36] and references therein.

In other poorer conditions, the relation of the research in the University to the technological development is merely through the introductions of the publications in the specific applied field. Both the definition of the goals and the evaluation of the achievements are performed by authors themselves in the frame of a study of the

specialized literature. Thus, that relation may become weakened because of the pressure for publishing in scientific journals with predominantly academic referees.

On the other hand, in a direct collaboration of the University with the private capital industry there might be some problems arising because of the final goals of the late: private profit. In their milder form, there might be a neglect of scientific achievements and focusing in particular problems of no significant scientific or technological interest.

All these advantages and problems are supposedly optimized in a public research frame as ESA.

However, in ESA research projects, at least in those involving materials science we have known closely, there are often some essential methodology errors. Research on yet unknown properties and procedures is encapsulated in a time schedule with payment milestones based on initial not-well-informed optimistic projections. Thus, research is pushed from scientific approach to a trial-and-error one because of the enhanced focus on the sort range.

Scientific approach:

→ scientific and technological data →

→ determination of relevant parameters and laws by long series of experiments

→ application to solve the problem

optimized success in the long range

increased scientific knowledge and data

Trial and error approach:

scientific and technological data → prediction of relevant parameters and laws

→ trial experiment → add result to data → new prediction → new trial experiment

evaluate results with respect to the goal considering costs, feasibility, …

within a certain tolerance not clearly established

probable satisfactory success in the short range

optimum result probably missed

minimum increase in scientific knowledge and data

The need of financial support to maintain operational the laboratories pushes them to initial optimistic projections and easy acceptance of unrealistic projects.

1.4 Motivation and scope of this work

The technological importance of anti-multipactor coatings for high-power RF devices in space is incessantly increasing.

Our laboratory had performed all the research in collaboration with ESA on SEY studies and anti-multipactor coatings since its beginning until present time.

The ESA reference anti-multipactor coating *Alodine* has as drawback a relatively poor electrical conductivity at RF which is becoming a problem of increasing technological importance.

Previous research of our laboratory had shown that anti-multipactor coatings based in physico-chemical properties of materials had inevitable limitations under the stringent requirements of space applications. It had also shown that new anti-multipactor coatings should be based on the SEE *suppression* effect of surface roughness of high aspect ratio.

This work developed several techniques to efficiently produce such surfaces of conductive metals. Particularly, by chemical etching of Ag and subsequent Au metallization, it was possible to build devices with no multipacting even at the highest available power and stable in air in the long range (scale of year). They had also much lower insertion loss than *Alodine*.

This work has also shown that for decreasing even further insertion loss as required by space industry, it is necessary to decrease the size scale of surface roughness below one micron. This work has developed a technique, ion etching assisted by sputtering mask deposition, which easily produce surface roughness on Ag with optimized size and shape characteristics as well as SEY *suppression* and lowest insertion loss.

This thesis reports on a broad and thorough investigation on materials and techniques for advanced anti-multipactor coatings. It also presents the performance in multipactor power threshold and insertion loss of real RF space industry devices manufactured with selected

anti-multipactor coatings developed in our laboratory. These devices were tested by the laboratories of two leading institutions in Europe: ESA and Tesat Spacecom.

Bibliography chapter 1

[1] C. Gutton, Sur la décharge électrique à fréquence très élevée, Comptes-Rendus Hebdomadaires des Séances de l'Académie des Sciences, vol.178, p.467, 1924.

[2] Farnsworth, P.T., Television by Electron Image Scanning, Journal of the Franklin Institute, Vol.2, p.411, 1934.

[3] Woode and J. Petit: Diagnostic Investigations on the Multipactor Effect, Susceptibility Zone Measurements, and Parameters Affecting a Discharge. ESTEC Working Paper No. 1556, Nov. 1989.

[4] European Cooperation for Space Standardization Space engineering (ECSS) Multipaction design and test. ECSS-E-20-01A Rev.1. 1 March 2013, http://everyspec.com/ESA/download.php?spec=ECSS-E-20-01A_REV-1.047803.pdf

[5] Rami A. Kishek, Y.Y. Lau, L.K. Ang, A. Valfells, and R.M. Gilgenbach, Multipactor Discharge on Metals and Dielectrics: Historical Review and Recent Theories, Physics of Plasmas 5 (5), 2120 (1998).

[6] R. Parodi: Multipacting, INFN, http://arxiv.org/pdf/1112.2176.pdf]

[7] http://mulcopim.webs.upv.es/welcome.html

a) EVEREST. FINAL PRESENTATION DAYS - 2-3-4 February 2015 – ESA/ESTEC. https://indico.esa.int:443/indico/event/75/session/7/material/3/0.pdf

b) P.Mader, C.Feat, M.Humbert, J.C.Lafond, P.Lepeltier, J.Puech, J.Sinigaglia: TAS-F multipactor results in EVEREST project. The 8th European Conference on Antennas and Propagation (EuCAP 2014). https://www.infona.pl/resource/bwmeta1.element.ieee-art-000006902104.

c) A.Al-Mudhafar, J.Puech, C.Miquel-Espanya, D.Raboso, H.Hartnagel, EVEREST consortium: EVEREST Simulation Campaign Results on Multipactor Effect Using CST Particle Studio™, The 8th European Conference on Antennas and Propagation (EuCAP 2014) http://ieeexplore.ieee.org/stamp/stamp.jsp?tp=&arnumber=6902058.

d) J. Puech, C. E. Miquel-Espana, D. Raboso, Everest Consortium: EVEREST preliminary results on high RF power phenomena, The 8th European Conference on Antennas and Propagation (EuCAP 2014) https://www.infona.pl/resource/bwmeta1.element.ieee-art-000006902057.

[8] H. Bruining, Physics and Applications of Secondary Electron Emission, McGraw-Hill, Pergamon, 1954.

[9] See references in Bruining's book [8].

[10] Dekker, A.J., Secondary electron emission, in Solid State Phys. 1958, Academic Press: New York. p. 251-315.

[11] E.L.GARWIN, E.W.HOYT, R.E.KIRBY, T.MOMOSE: Secondary Electron Yield and AES Measurements on Oxides, Carbide and Nitride of Niobium, SLAC - PUB - 3470 (JAP) 1984.

[12] Nyaiesh, Garwin, King, Kirby: Properties of thin anti-multipactor TiN and Cr2O3 coatings for klystron windows, J Vac Sci Technol A 4 (5) 2356, 1986.

[13] C. Scheuerlein: The Influence of an Air Exposure on the Secondary Electron Yield of Copper, Diploma Thesis (10/02/1997), CERN-THESIS-2002-022 (CERN, 1997).

[14] B.Henrist, N.Hilleret, C.Scheuerlein: The Secondary Electron Yield of the Non Evaporable Getter Alloys TiZr and TiZrV, Vacuum Technical Note 98-08, 1998.

[15] R. Forman: Secondary-electron-emission Properties of Conducting Surfaces With Application to Multistage Depressed Collectors For Microwave Amplifiers, NASA technical paper 1097, Nov. 1977.

[16] A. Curren and K. A. Jansen*:* Secondary electron emission characteristics of ion-textured copper and high-purity isotropic graphite surfaces. NASA, Washington, DC, NASA TP-2342, 1984.

[17] H.Derfler, J.Perchermeir, H.Spitze: Coating For A Surface Subject To Exposure To A High-Frequency Field To Prevent Interference Resulting From Secondary Electron Emission, US Patent 4559281.

[18] L. Galán, F. Rueda, et al: Study of secondary emission properties of materials used for high power RF components in space. Final Report ESA ESTEC Contract No. 6577/85/NL/PB, ESA, Noordwijk, Holland. Issues 1987 and 1990.

[19] L. Galán, F. Rueda, et al: Development of a computer model for the multpactor effect. Final Report ESA ESTEC Contract No 6577/85/NL/PB 1990/Rider, ESA, Noordwijk, Holland (1991).

[20] L. Galán, F. Rueda, et al: *Coatings to prevent Multipactor effect in RF high power components for space*. Final Report ESA ESTEC Contract No. P.O. 162594(1996), ESA, Noordwijk, Holland (1998).

[21] L. Galán et al: Multipaction study and coating selection and Analysis and design of a software for the simulation of the multipactor effect, MEST in Surface treatment and coating for the reduction of Multipactor and PIM effects in RF components. Final Report ESA Contract No. 17025/03/NL/EC (AO 4025). ESA, Noordwijk, Holland (2005).

[22] L. Galán, V. C. Nistor, et al: Porous Inert Metal Coatings for Controlling Secondary Electron Emission. Final Report ESA Contract No. 17025/03/NL/EC (AO 4025) CCN-02. ESA, Noordwijk, Holland (2008).

[23] L. Galán, V. C. Nistor, et al: Optimization of Surface Roughness of Anti-Multipactor Coatings for Low Insertion Losses and Secondary Emission Suppression for High Power RF Components in Satellite Systems. Final Report ESA ITI project Proposal B00011822. Prime, Tesat Spacecom. Subcontractors: UAM and CSIC. ESA, Noordwijk, Holland (2014).

[24] L. Galán, V. C. Nistor, et al: Evaluation and validation of electromagnetic software, test facilities and test standard in Europe to predict and test RF breakdown and passive intermodulation. Final Report ESA TRP, ESA-CNES M-AO40/02-01-06-17 (EVEREST project). Prime, CNES. Subcontractors: 17 entities including universities, public research centers, and companies. ESA, Noordwijk, Holland (2014).

[25] L. Galán, V. C. Nistor, et al: RF breakdown in multicarrier operation. Final Report ESA TRP 19918/06/NL/GLC, CCN-02. Prime, Aurorasat. Subcontractors, CSIC, UAM. ESA, Noordwijk, Holland (2010).

[26] L. Galan et al: Method and Structure for Inhibiting Multipactor. United States Patent US007623004B2. Nov. 24, 2009.

[27] D Sievenpiper, L Zhang, R F Jimenez Broas, N G Alexópolous, E Yablonovitch: High-Impedance Electromagnetic Surfaces with a Forbidden Frequency Band. IEEE Transactions on Microwave Theory and Techniques, 47 (1999) 2059-2074.

[28] O. Luukkonen, C. Simovski, G. Granet, G. Goussetis, D. Lioubtchenko, A. V. Räisänen, and S. A. Tretyakov*:* Simple and Accurate Analytical Model of Planar Grids and High-Impedance Surfaces Comprising Metal Strips or Patches. arXiv:0705.3548v3 [physics.class-ph] 2 May 2008. (EEE Transactions on Antennas and Propagation, Vol. 56, No. 6, pp. 1624--1632, June 2008).

[29] Documents available from V. C. Nistor (valentin.nistor@cern.ch) and L. Galán (luis.galan@uam.es)

[30] N.Díaz, S.Castañeda, J.M.Ripalda, I.Montero, L.Galán, S. Feltham, D.Raboso, and F.Rueda: Materials of Low Secondary Electron Emission to Prevent the Multipactor Effect in High-Power RF Devices in Space. 6th Spacecraft Charging Technology Conference, AFRL-VS-TR-20001578, 1 September 2000. ALSO: Workshop on Multipactor, RF and DC Corona and Passive Intermodulation in Space RF Hardware, Noordwijk, ESA WPP-178 (2000) (unpublished), p. 97.

[31] a) AYA2012-39832-C02-02, b) AYA2009-14736-C02-02, c) ESP2006-14282-C02-01/, d) ESP2002-04509-C04-04, e) CICYT, ESP99-1112, f) DGCYT PB94-0201, g) CICYT MAT92-0258, h) CICYT ESP-89-0182.

[32] Luis. A González: Practical Control of Multipactor Threshold and Insertion Losses on RF Satellite Devices and Study of Secondary Electron Emission for Multipactor and Electron Cloud Mitigation, PhD. Thesis in Advanced Materials and Nanotechnology, Departamento de Fisíca Aplicada, Facultad de Ciencia, Universidad Autónoma de Madrid, June 5, 2015.

[33] Manuel Acosta Seró, Daniel Coronado Guerrero. Las relaciones ciencia-tecnología en España. Evidencias a partir de las citas científicas en patentes. Economía industrial, ISSN 0422-2784, Nº 346 (2002).

[34] http://www.minetur.gob.es/Publicaciones/Publicacionesperiodicas/EconomiaIndustrial/RevistaEconomiaIndustrial/346/05%20MANUEL%20ACOSTA.pdf

[35] Daniel Coronado Guerrero, Manuel Acosta Seró, Rosario Marín Muñoz. La contribución de la universidad al desarrollo de tecnología industrial. Diferencias sectoriales, regionales y factores determinantes. XXIX Reunión de Estudios Regionales. Santander, 27 y 28 November 2003.

[36] http://www.aecr.org/web/congresos/2003/textos_acept/A.4/Microsoft%20Word%20-%20I.104.A.pdf

Chapter 2

Basic Principles

2.1 Secondary Electron Emission

2.1.1 SEY: definition and properties

Since 1921 when A. Einstein was awarded a Nobel prize in physics for the discovery of the photoelectric effect, we have reached a better understanding of the interaction between elementary particles and mater, the quantum nature of light and electrons and grasp the concept wave–particle duality with the subsequent dynamics of the emitted subatomic particles, energy transfer momentum, scatter mechanisms, etc. The emission of secondary electrons of materials plays a key role in many fields, from particle accelerators and high power devices in space to plasma fusion reactors. The phenomenon was discovered in 1902 by the German physicists L. Austin and H. Starke [1].

When an electron of sufficient energy (primary electron) impacts on the surface of a material it can produce the emission of more electrons from the material; this physical process is called secondary electron emission (SEE). SEE is a part of a complex processes at atomic level involved in the interaction electron beam - solid surface [2-4]. It can be separated in several steps:

a) penetration of primaries, suffering scattering and energy losses,

b) some primaries are scattered back toward surface and to vacuum again with no energy loss (elastic backscattered electrons) or after some energy loss (inelastic backscattered electrons)

c) generation of internal secondaries during primary electron scattering and energy losses,

d) transport of the internal secondary electrons through the material with further scattering, energy losses, and secondaries generation in a cascade process,

e) final escape of the electrons (secondary and backscattered) over the vacuum barrier, including further scattering, energy losses.

The first three steps are dominated by interactions such as elastic and inelastic dispersion, plasmons and excitons loss of energy, transitions between energy bands, and absorption at an energy level or band. The generation depth of secondaries (Fig. 1) in metals is 0.5 to 10 nm depending on atomic number. In dielectrics, it is much larger, 10 to 30 nm. For backscattered electrons, the bulk escape depth in μm/cm^3 is approximately 2.8*$E_p^{1.54}$ [4].

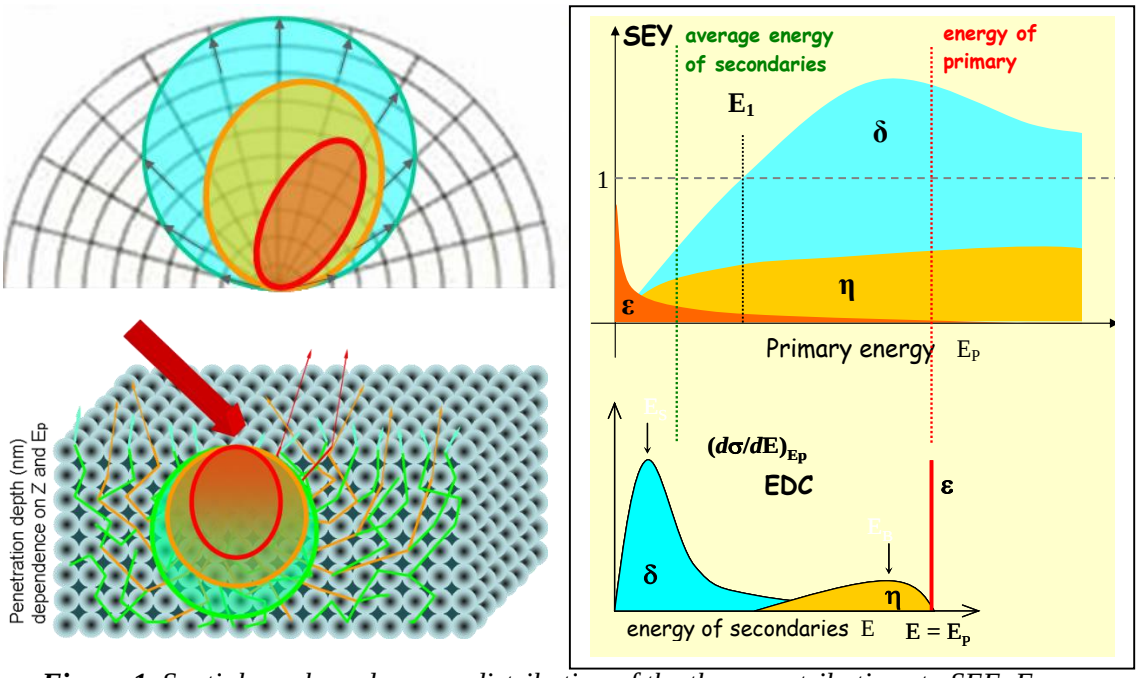

Figure 1. *Spatial, angle and energy distribution of the three contributions to SEE. Energy distribution curve or energy spectrum.* ***p****: primaries,* ***ε****: elastically backscattered primaries,* ***η****: inelastically backscattered primaries, and δ: true secondaries. Total SEE:* $\sigma = \delta + \eta + \varepsilon$.

The secondary electron emission coefficient or yield (SEY) of a material surface, usually symbolized as σ, is the ratio of the number of emitted electrons to the number of incident or primary electrons of defined incident energy and angle, in field-free conditions and under vacuum conditions.

For primary energies above ~ 100 eV, most emitted electrons are true secondary electrons (originally belonging to the material) with low energies, conventionally less of 50 eV, with an emission coefficient δ. For very high primary energies (several keV) δ might become very small compared to σ and above statement does not hold, but this range is not of relevance for Multipactor effect.

Others emitted electrons are known as backscattered, with a coefficient η. They are assumed to be primary electrons backscattered again into vacuum by collisions with the surface material. These emitted electrons can have energies up the impacting or primary energy. Sometimes those electrons emitted elastically with the same energy of the primary or impacting electron are distinguished as elastically backscattered, with coefficient ε. In this case, $\sigma = \delta + \eta + \varepsilon$. If as usual, ε is considered included in η, then $\sigma = \delta + \eta$.

A typical dependence of these coefficients on primary electron energy is shown in Figure 2. At the present time, the limit of SEY as primary energy approaches 0 eV, is being studied [5]. Pure clean metals show $\sigma \to 0$ for primary energy $E_p \to 0$, but for surface contamination and insulators $\sigma \to 1$ for $E_p \to 0$.

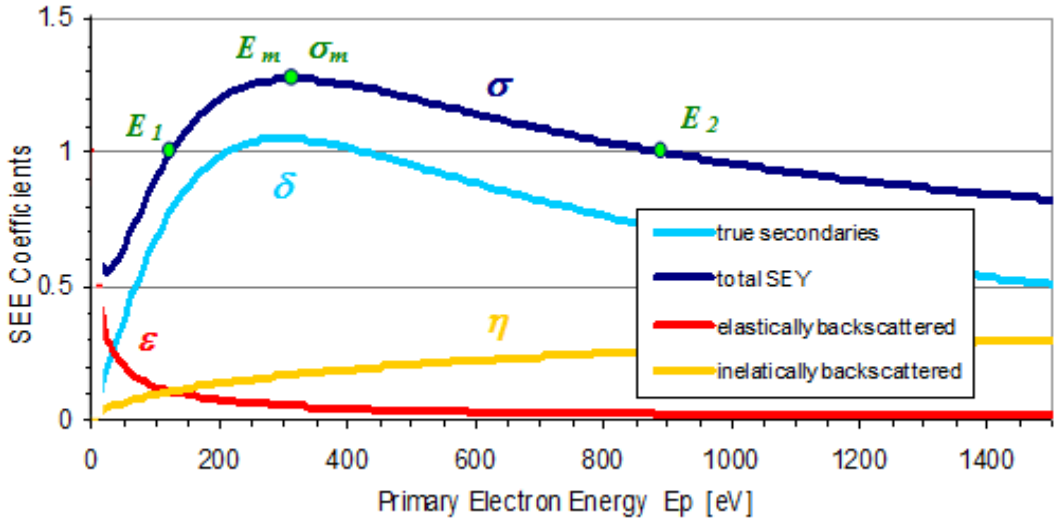

***Figure 2**. Typical dependence of SEY coefficients on primary electron energy.*

The energy limit of 50 eV between true secondaries and backscattered is somehow arbitrary and a convention, only practical or physically meaningful for primary energies greater than about 100 eV. For lower primary energies, the emission energy ranges of true secondaries and inelastically backscattered overlap significantly and their numbers (intensity) eventually become smaller than that of the elastically backscattered electrons. A spectrum showing the energy distribution of the emitted electrons has more detailed information (energy losses, secondary electron generation, conduction band structure, work function) and is known as Energy Distribution Curve (EDC) or Reflection Electron Energy Loss Spectrum (REELS) [2], [6], (see Fig. 3).

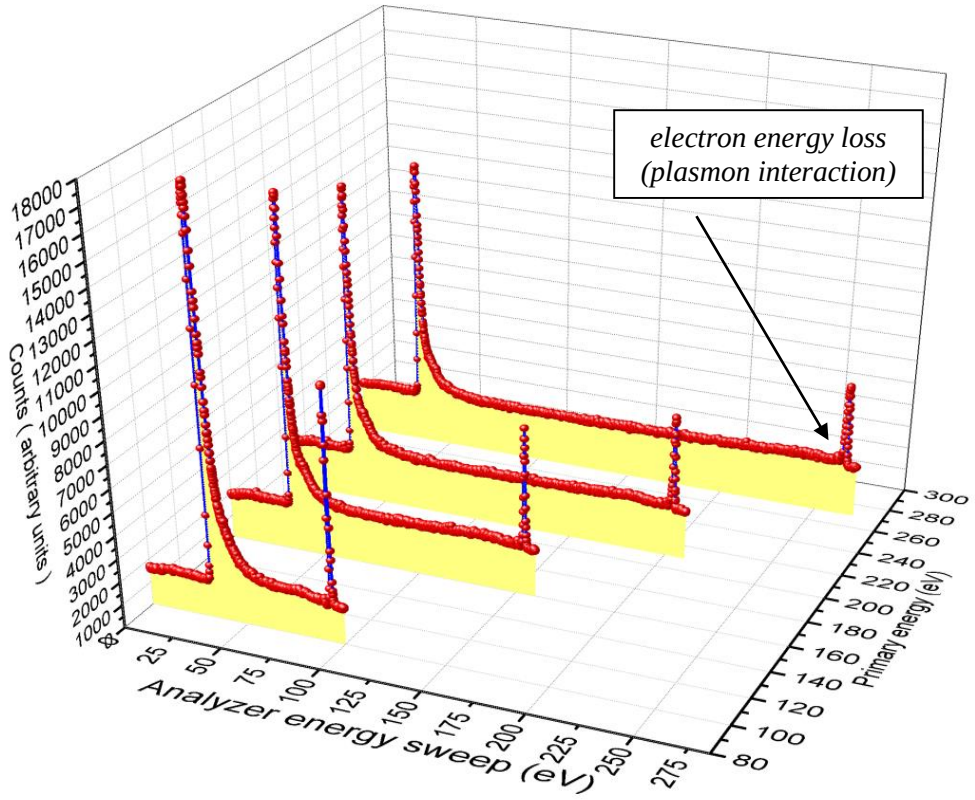

Figure 3. *Electron distribution curve of pure silver, for different primary electron energies*

In principle, a higher potential barrier at the surface should decrease the escape probability for any electron even for those of higher energy.

When measuring SEY, the primary or incident electrons are supplied by the electron beam of an electron gun. The primary electron energy E_p is determined by the potential difference between the sample at V_s and the thermionic cathode of the electron gun (usually a hot metal, W, Ta, etc.), at V_g:

$$E_p = \mathrm{e} * (V_s - V_g)$$

This is just the "nominal" primary energy. There is an uncertainty of about ± 1 eV due to the difference between the work-function values of the sample ϕ_s and the cathode ϕ_g, both being 5 ± 1 eV, since voltage meters measure only potential differences between Fermi levels (see Fig. 4).

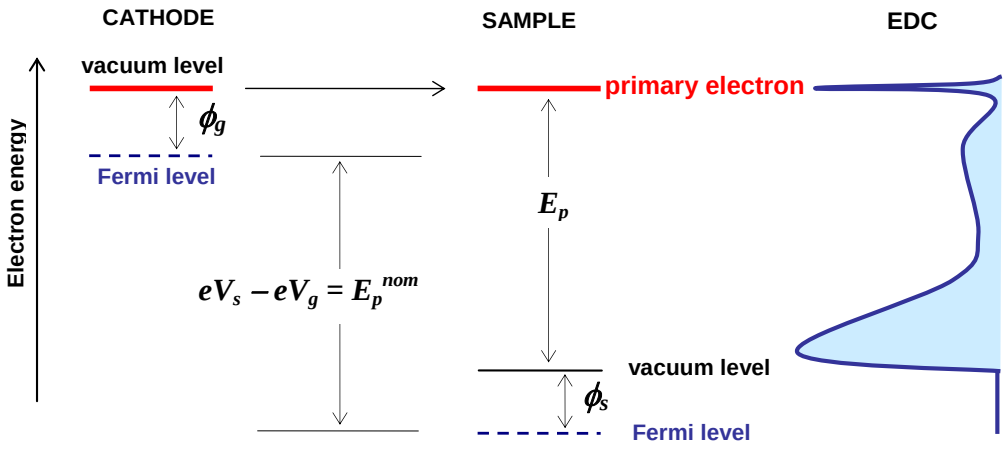

***Figure 4**. Electron energy diagram of primary electrons accelerated by a potential difference $V_s - V_g$ from the cathode to the sample. It also shows the relation with the work functions and the EDC (Energy Distribution Curve) measured with the electron energy analyser.*

True electrons have an emission angle distribution close to the cosine or Lambert's law. Backscattered electrons have a modified emission angle distribution law with higher intensity in the reflection direction (Fig. 5).

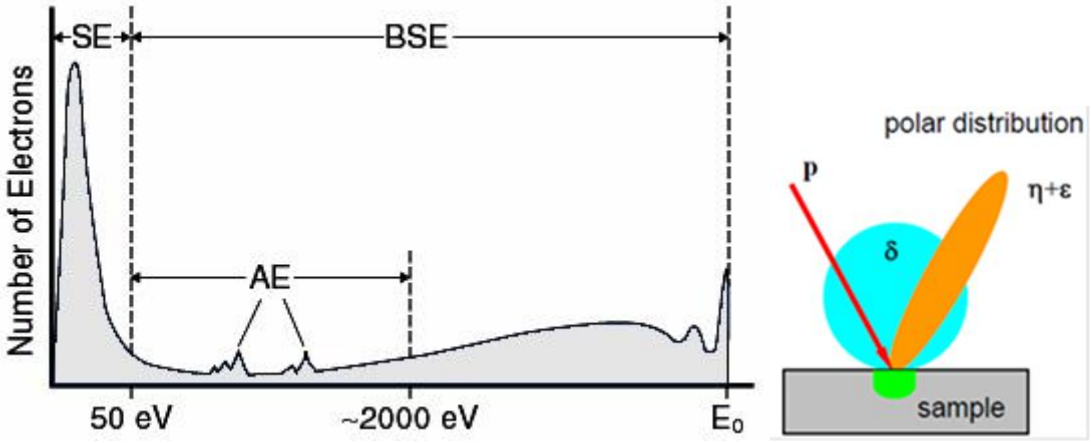

***Figure 5.** Electron Energy Spectrum. Secondary electrons (SE) form a large low-energy peak. Auger electrons (AE) produce relatively small peaks on the backscattered electron (BSE) distribution. Figure after Goldstein et al. 1981. Left side – polar distribution of the coefficients.*

All these properties, σ, δ, η, ε, EDC, and emission angle distributions, depend on the incident primary electron energy and angle. These functions are necessary for a detailed and accurate simulation of the Multipactor effect. However, the dependence $\sigma(E_p)$ of the total secondary emission on the primary energy E_p for normal incidence, usually named SEY, is considered the most important, and the others can be estimated approximately from general empirical laws.

SEY-primary-energy curves are most often so simple that can be characterized by a few parameters: σ_m (> 1, usually) and E_m for the maximum, and the cross-over energies E_1 and E_2 where $\sigma = 1$, i.e., $\sigma(E_1 \le E_p \le E_2) \ge 1$, see Fig. 2.

2.1.2 SEY testing

For the measurement of the emitted current, a weak electrostatic field is usually set in order to avoid both low-energy secondary electrons returning back to the surface and 2nd-generation secondary electrons from surrounding surfaces (e.g., collector or vacuum chamber walls) generated by energetic secondary electrons (backscattered electrons). This is achieved by a small negative bias (-10 to -50 V) to the sample with respect to the surroundings, or by positive bias of the surrounding. Ideally, this field should be spherically symmetrical respect to the emitting spot, i.e., created by a spherical collector or vacuum chamber.

In more complex testing arrangements, spherical grids and collectors (and several electrometers) are used to obtain field free conditions around the sample to be tested, avoiding 2nd-generation secondary electrons from surrounding surfaces, and measuring both primary and secondary electron currents, all together and simultaneously. However, the usual simpler arrangement described here has sufficient accuracy, see Figures 6 and 7.

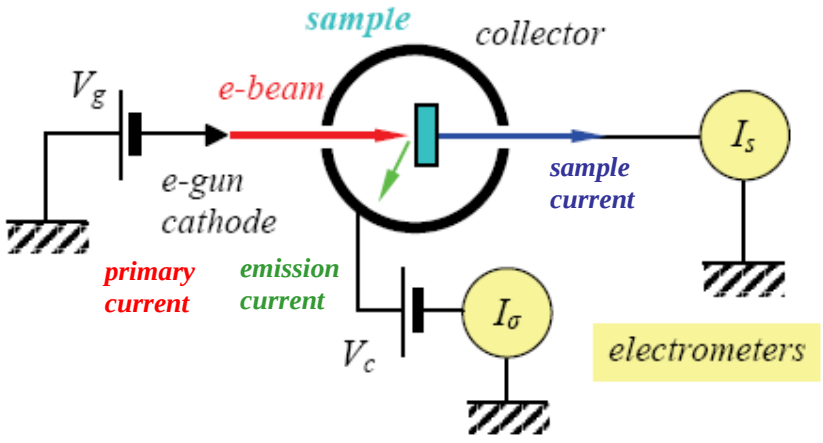

Figure 6. *SEY experimental setup (with collector around the sample)*

An electron gun supplies the primary electrons or electron beam to irradiate the sample. The primary electron energy E_p is determined by the potential difference between the sample at V_s and the cathode of the electron gun (usually a hot cathode), at V_g:

$$E_p = e\,*(V_s - V_g) \qquad \text{(in Fig. 4, } V_s = 0 \text{ and } V_g < 0)$$

This is just the "nominal" primary energy. There is an uncertainty of about ±1 eV due to the difference between the work-function (surface potential barrier) values of the sample ϕ_s and the cathode ϕ_g, both being usually 5 ± 2 eV, since voltage meters measure only potential differences between Fermi levels.

The electron currents coming in and out the sample are: the primary current I_p from the e-gun, the emission current I_σ going to the surroundings (collector or the analysis chamber walls), and the sample current I_s.

If we use a coherent sign convention, $I_p > 0$ for example, then $I_\sigma < 0$ always (as it is measured by the collector electrometer) and $I_s > 0$ when $\sigma > 1$ (as it is measured in the sample electrometer), since $I_p + I_\sigma + I_s = 0$ because of the condition of no charge accumulation for a conductive sample connected to ground at a constant bias.

Therefore, for the SEY = σ, the following expressions might be used:

$$\sigma = \frac{|I_\sigma|}{I_p} = -\frac{I_\sigma}{I_p} \qquad \text{general definition}$$

$$\sigma = \frac{I_\sigma}{I_s + I_\sigma} \qquad \text{with the setup of Fig. 6}$$

$$\sigma = 1 - \frac{I_s}{I_F} \qquad \text{with the setup of Fig. 7, and Faraday cup: } \sigma_F = 0 = 1 - \frac{I_F}{I_p}$$

An optimum experimental arrangement is a spherical collector around the sample, as schematized in Fig. 6. In this case, I_σ is measured in the collector meter positively biased at V_C, the current sample I_s is measured by the sample meter connected to ground and biased negatively and has the sign of $\sigma - 1$.

The secondary electron emission coefficient or yield (SEY) is thus:

$$\sigma = -\frac{I_\sigma}{I_p} = \frac{|I_\sigma|}{I_p} \qquad (I_\sigma < 0), \text{ thus } \sigma = \frac{I_\sigma}{I_p} = \frac{I_\sigma}{I_\sigma + I_s}$$

In Fig. 7, with no collector included in the setup, the I_p is measured with a Faraday cup instead of the sample: $I_F = I_s = -I_p$ for $\sigma_F = 0$, is always negative. When testing a sample, the sample and the collector all together form a Faraday cup.

The condition of sample charge neutrality $I_p + I_\sigma + I_s = 0$ is an approximation, while the 2nd-generation secondary emission from the surroundings falling on the sample is

neglected. This is a very good approximation if the appropriate sample bias is used. The sample is set -20 to -50 V respect to the collector or to the chamber in order to repel those electrons.

When a collector is not available, only the sample current I_s is measured. In this case, the e-gun current I_p is previously measured with a Faraday cup or calibrated by a reference sample with well-known SEY properties (equation):

$$I_p = -\frac{1}{(\sigma_{ref} - 1)} I_s(ref),$$

where σ_{ref} and I_s *(ref)* are respectively the secondary electron emission coefficient and the sample current to ground of a reference sample, usually a Faraday cup.

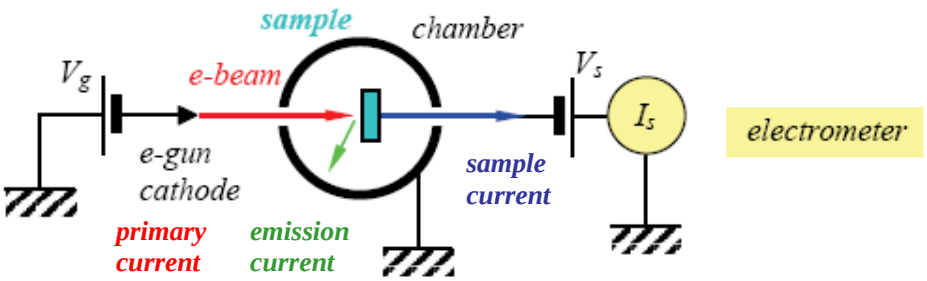

Figure 7. *SEY experimental setup (without collector around the sample). The red, green, and blue arrows correspond to the primary, secondary, and sample electron currents. The electrometers give positive charge currents*

The UHV systems available for all our SEY measurements are shown in Figures 8 a) and b), and the method is based on measuring sample current to ground Is, described above. The incident electron gun current I_p is measured by the Faraday cup (Fig. 8 a)), biased to +50 V, and checked by a clean reference samples (typically SEY of Pt and BSE of graphite). Only SEY of several clean noble metals such as Pt, Au, Ag, or Cu are reliable references. Clean conditions are achieved by low-energy Ar ion bombardment and checked by a maximum first cross over energy E_1. This has previously been established by XPS surface chemical analysis. Checking or calibration with reference samples is important because for very low primary energies the e-gun current detected by the Faraday cup might be different from that incident on the sample. It is also the experimental verification of the overall test accuracy.

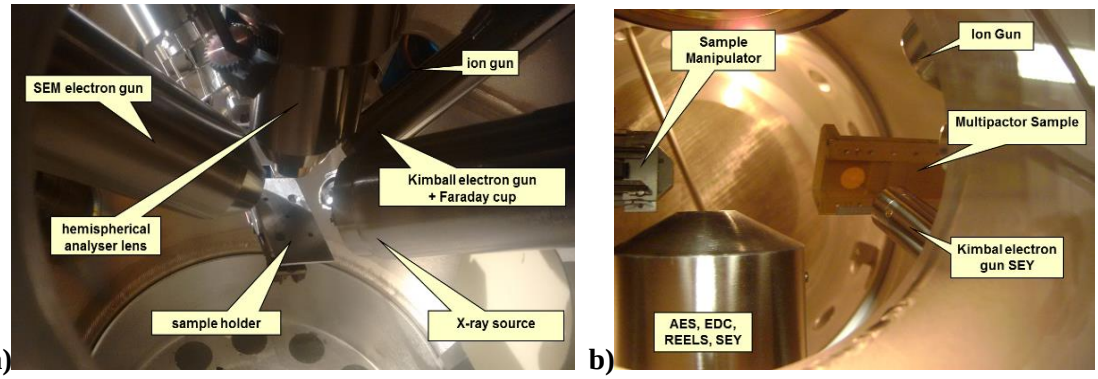

Figure 8. *Description of the UHV systems for SEY measurements; Left a) equipped with a Faraday cup; Right b) without Faraday cup*

A combination of techniques optimized for the particular experimental arrangement is usually the best calibration technique. In our laboratories we used mostly reference samples and faraday cup system for an accurate I_p calibration. We also cross-checked the results with literature studies of pure metals [7], [8] and estimated an error of less than 3%.

The instrumental errors, directly experimentally and statistically measured, are: 0.01×10^{-9}A for the current, and 0.3 eV for the electron energy (voltage).

The calculated instrumental relative error $\Delta\sigma$ / (σ–1) is about 1 %. The measured statistical dispersion of a σ value is about 0.03 (from many SEY tests at a point separated by in time by more than 6 h to avoid surface conditioning).

The e-gun should be able to supply a stable beam current for all required energies with controlled low dose. These low values are necessary to avoid surface "conditioning" or structural alterations by the electron beam [9]. This effect, also known as "scrubbing" [10] tends to modify SEY by surface processes. Also the total dose or fluency should be small (below 10^{-7}C/mm^2), for metallic or conductive samples.

In general, for any surface analysis technique, and more important in relation to surface conditioning, ultra-high vacuum is recommended in the analysis chamber.

Minimization of electron dose becomes even more crucial in dielectric or non-conductive samples. Then, primary charge is trapped on the surface and a surface charge potential grows affecting to the real energy of primary electrons thus producing SEY-energy values very different from the uncharged sample one. This effect can be avoided by using a pulsed e-beam with low-dose pulses. The induced image charge on the sample substratum or stage can still be measured with a fast oscilloscope. A Kelvin probe detecting the corresponding surface potential can also measure the charge trapped on the

surface on a non-conductive sample in the pulsed method. Some dielectric samples may also be charged by tribo-electrification before irradiation. The surface potential must be in this case measured and removed before SEY measurements.

Apart from the instrumental errors (e.g. in the measurements of e-gun energy and sample currents, noise induced in cables and electric contacts) the main problems in the accuracy of SEY measurements are the accuracy of the e-gun primary current impacting on the sample. This last one becomes crucial for very low primary energies.

Main difficulties in secondary electron emission yield measurements are:

- Low current (10^{-9} A), low energy (20 – 2000 eV) monochromatic regulated electron gun with a beam well focused on the sample even at low energies. Pulsed operation is necessary for dielectric samples or avoiding surface "conditioning".
- Secondary electron collector of complete solid angle, defining a field-free volume or at least with spherically symmetric electrostatic extracting field. This field is necessary for detecting secondaries of very low energy and to avoid second-generation secondaries from the collector (produced by energetic backscattered emission from the sample) impinging on the sample. Energy scanning by the electron gun cathode voltage and sample at constant bias for a low constant field around the sample.
- Precision measurement of current on the sample and the collector. The primary current is measured by the collector and the sample connected together.
- The collector can be avoided if the currents on the sample and on a good Faraday cup (capturing all the primary electrons) are precisely measured.
- At least one grid over the collector is necessary for discriminating secondary energy, i.e., for measuring backscattered emission (energy > 50 eV).

All this difficulties worsen for low primary energies of great importance for Multipactor and e-cloud effects. It is then a problem to determine the real primary current impinging on the sample. Most of the difficulties are solved using a calibration sample of well-known SEY; and thus obtaining the effective primary current. This could be polycrystalline Pt or Au cleaned in situ by ion etching and heat treatments.

2.1.3 Experimental evidences of secondary emission yield decrease with surface roughness

The interest to implement porous surfaces to inhibit the Multipactor effect started when insulating structured materials like Anomag coated with a thin layer of Au showed an

abnormal low SEY. The suppression was attributed to the superficial morphology of high aspect ratio of the multilayer. However, the improvement in multipactor threshold required the surface material to be have a good electrical conductor in a thickness of at least twice the skin depth.

As mentioned before, experimental data on this effect were rather scarce at that time. However, it was experimentally known since the very beginning of the research on Secondary Electron Emission [11]; it was very well known that the maximum SEY of soot was about 0.5. Thus, it was empirically applied in several technological laboratories such as NASA [12] and Culham Laboratory, AEA Fusion [13]. A brief account of studies before 1970 can be found in [14].

In the early 1970's, it was demonstrated that surfaces with low secondary electron yield (less than 1) can be prepared by evaporating metal films in a relatively high residual gas pressure (0.7 mb), [14,15, and references therein]. They used noble metals as Cu, Ag, Au, and Pt and obtained maximum SEY values in the range 0.5 - 1.0, see Fig. 9.

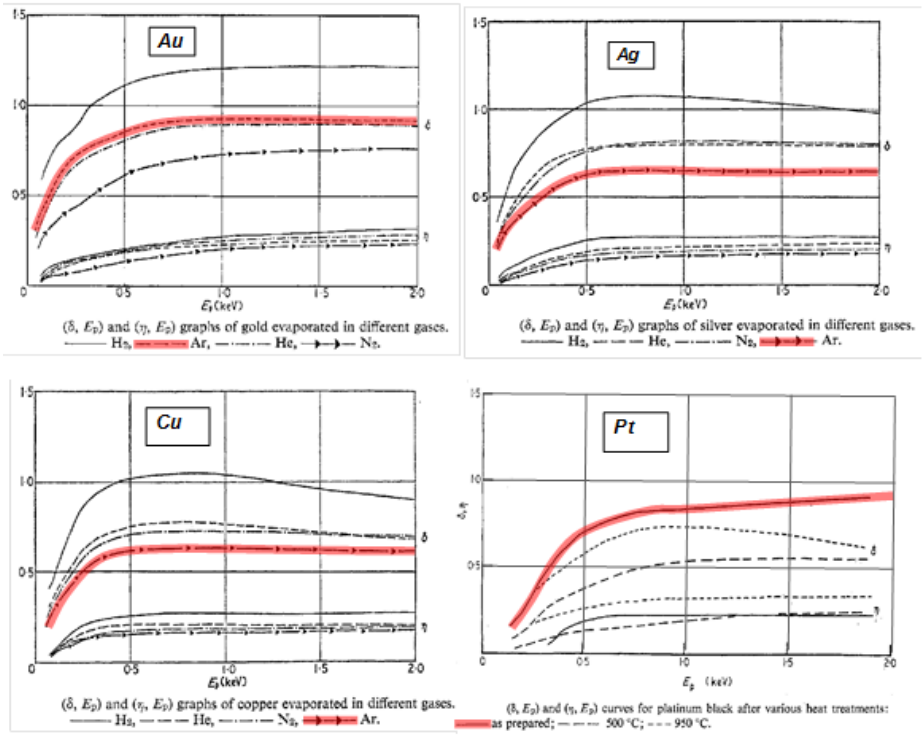

Figure 9. *SEY curves of noble metals evaporated in 0.5 Torr Ar, and other gases [14, 15].*

These coatings were done by physical thermal evaporation. See Fig.10 for some experimental examples of the surface morphology obtained: separate grains (possibly columnar structures) of 100 - 300 nm size.

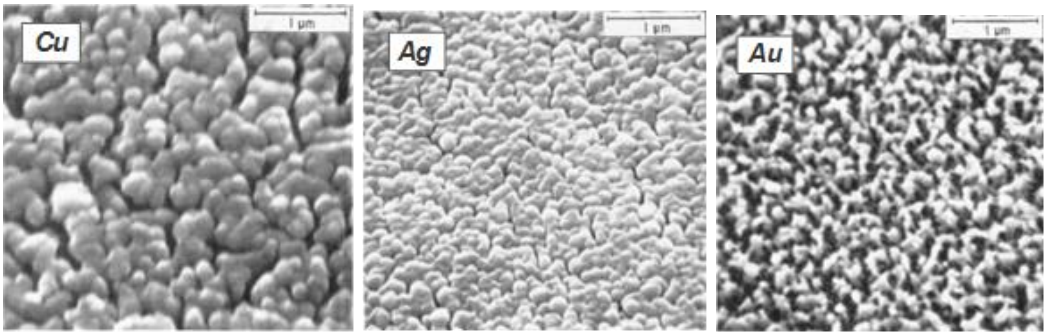

Figure 10. *SEM micrographs of noble metals evaporated in 0.5 Torr He. Evaporation rate: 0.9 μg/cm²/s, [14].*

In this range of the surface roughness size, it exhibits a strong interaction with light through the surface plasmon absorption and the normal colour of the material can be strongly modified becoming usually darker, even completely black [16]. Thus, these coatings are often referred to as black metals.

During a long research, 1973 - 98, deeply textured surfaces were obtained at NASA by simultaneous ion etching of a "soft" metal substrate and sputtering deposition of a "hard" metal mask by one unique ion gun [12, 17, and references therein]. More details on the technique are given in the chapter dedicated to nano-structured surfaces by masked preferential ion sputtering. Black metal films were also obtained. Important reductions of SEY were achieved for Cu and Ti using Ta and Mo for masking. Interpretation of reported SEY data is not clear because the technique of measuring SEY was not always completely accurate. Figure 1 shows additional reliable data indicating a very strong effect of secondary emission suppression by surface roughness.

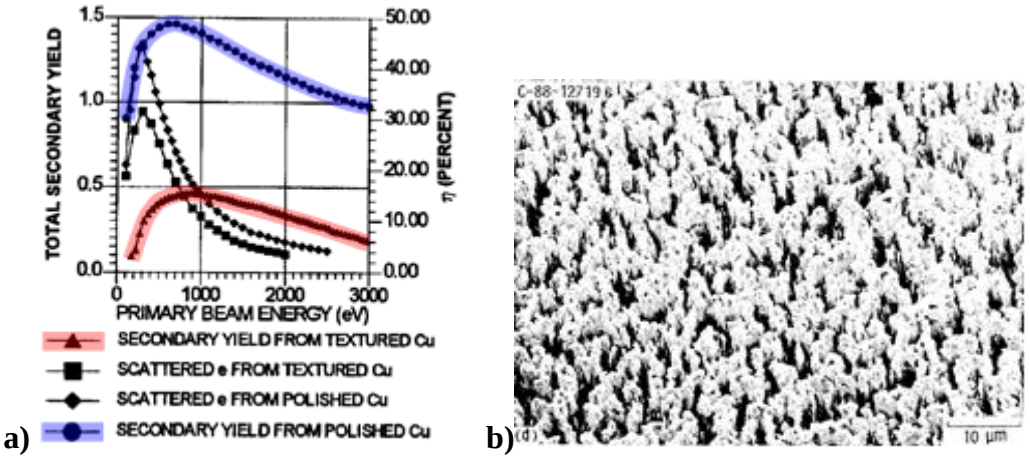

Figure 1. *a) SEY of the polished Cu sample and b) an SEM of Mo-Masked Ion-Textured Cu surface*

Above are presented two more examples: a) SEY of polished Cu (blue) and of ion textured Cu (red), from ref. [17], and b) SEM of an ion-textured Cu surface from [12].

Very similar results were incidentally obtained by Cu sputtering ion etching, in a glow discharge of a DC diode, at CERN [18], see Figure . The effect was attributed to the angular dependence of the sputter yield and to surface impurities.

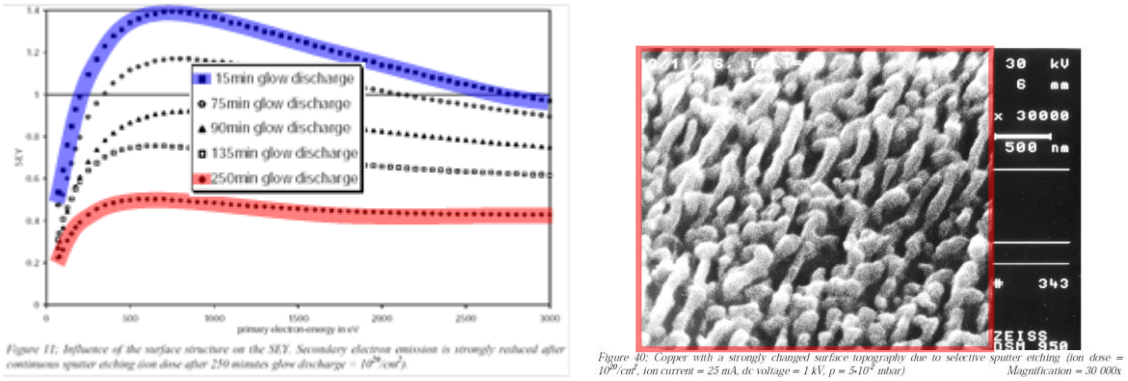

***Figure 12**. SEY evolution with increasing ion dose and SEM of a modified Cu surface after etching*

Also at CERN, Cu surfaces with similar surface morphology and SEY were obtained by a different approach: in-situ baking at 350ºC for 5 min in air, followed by a 6 h vacuum bake-out [19], see Figure. The creation of dendritic structures on a small Cu sample produces a surface with an SEY lower than unity.

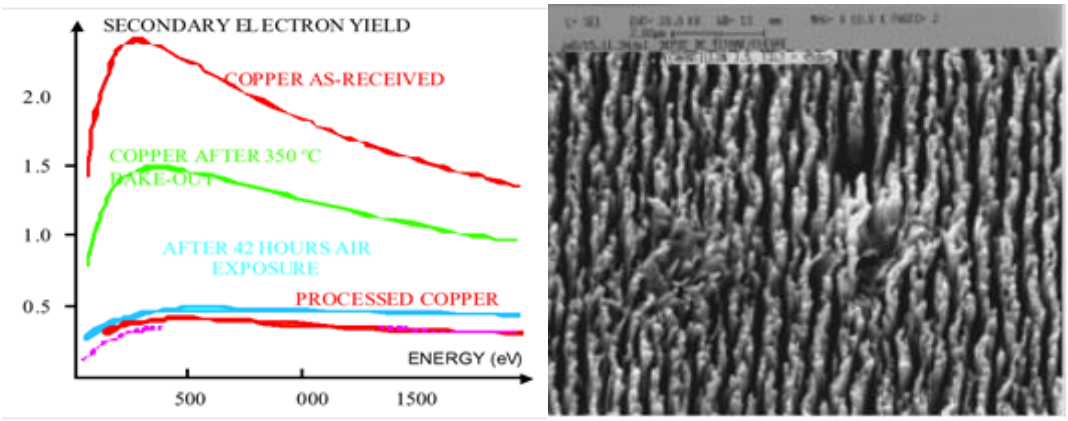

***Figure 13.** SEY and SEM analysis of textured Cu surface by thermal treatment at CERN [19].*

In 2003, it was reported strong suppression of secondary electron emission from diamond surfaces with dense whisker formation [20], see Fig. 14. These whiskers were formed by plasma etching of a diamond thin film with columnar growth obtained by chemical vapour deposition (CVD). The etching plasma was obtained by a RF discharge in $3*10^{-2}$ mb in air.

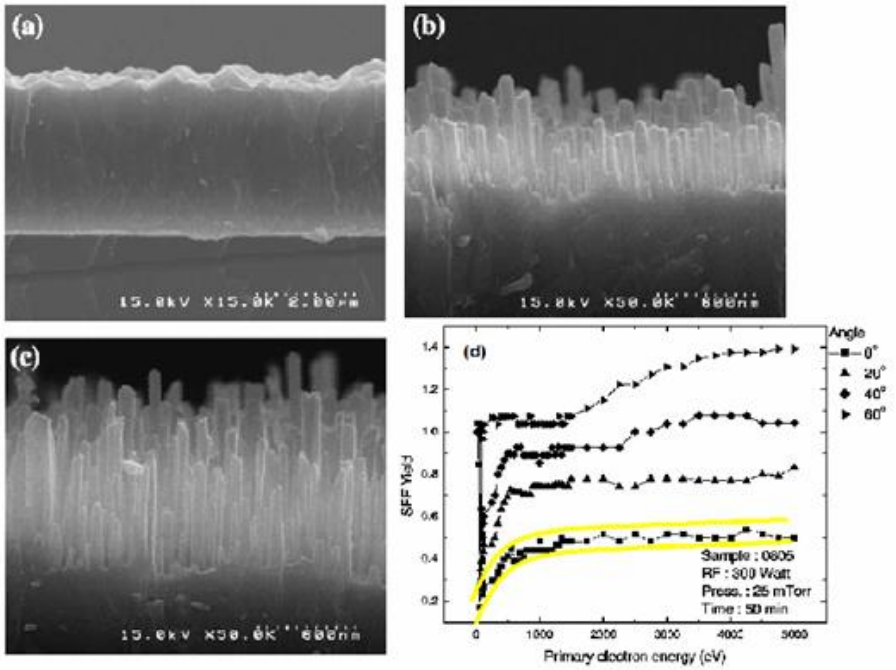

Figure 14. *SEM and SEY analysis of textured diamond surface obtained by CVD and air-plasma etching [20]*

This last case reviewed, as corresponding to a coating of insulating material: diamond, has no interest for application in wave guides. Because of the small scale, 100 nm, the electrical surface conductivity cannot be improved by a metal over layer of the required thickness, two orders of magnitude larger. We bring it here only as demonstration of secondary emission suppression by rough surfaces of large aspect ratio. With this same aim, we describe now some recent experiments at SLAC, Stanford University, for implementing computational results on grooved surfaces [21] in a large scale of mm. Figs. 15 and 16 show the tested surfaces and their SEY results [22, 23].

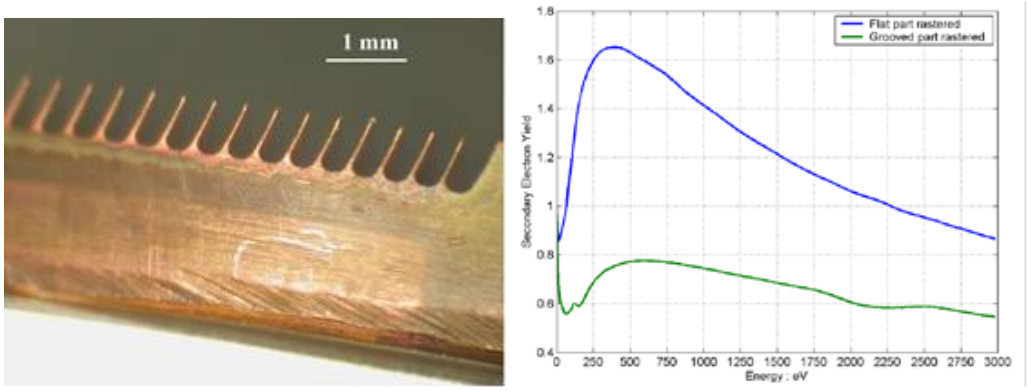

Figure 15. *Photo and measured SEY of a grooved Cu surface, the grooved surface and adjacent flat surface were tested for SEY, SLAC [22]*

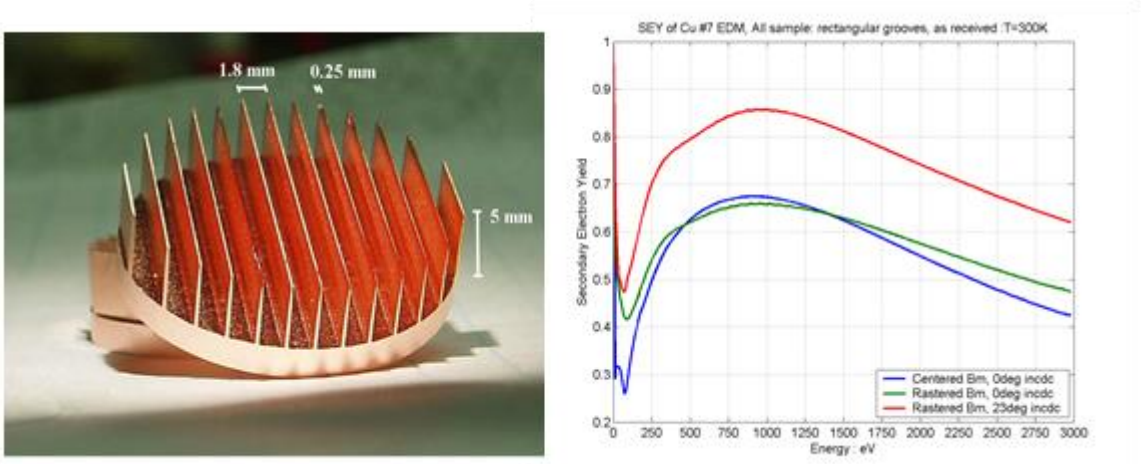

Figure 16. *Photo and measured SEY of a grooved Cu surface, for normal and 23º incidence angle, SLAC [23]*

In summary, a suppression effect of secondary electron emission by rough surfaces of high aspect ratio has been observed for roughness size from 100 nm to 10 mm scales.

2.1.4 Explanation of SEY suppression by surface roughness

There is yet no real theory of the suppression of secondary electron emission by surface roughness. There are several plausible explanations supported by some numerical simulations.

This effect was experimentally known since many decades ago. It was already mentioned and naively explained in Bruining's publication in 1954 [11]. In the early 1990's, some effort was done to explain it using numerical simulations [24-28], however, some defects of the theoretical model for the secondary emission process impeded the "observation" of the effect until they were corrected in 1995 [29]. Since then, other more accurate models for the secondary emission process have allowed to confirm the effect and to study its relation with surface roughness [21, 30]. We should mention a model [31] that includes the essential aspects of secondary electron emission model as ours (MEST software tool [32]) but in a more complicated manner, however, maybe unnecessarily.

These numerical studies have clearly shown the direct relation between secondary emission suppression and surface roughness of high aspect ratio; see Fig. 17.

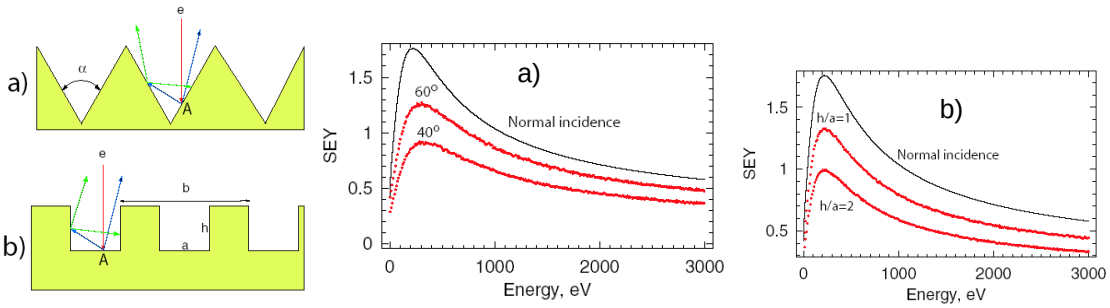

Figure 17. *Numerical simulation of effective SEY of rough surfaces [21], showing SEY-suppression dependence on aspect ratio: a) [2tan (α/2)]$^{-1}$ = 0.87, 1.37, and b) h/a = 1. 2.*

It seems that it has no relation with the size of the roughness (thus, size is a parameter that can be optimized by another requirement, such as RF performance; there might be a low limit though, see below). However, there are some properties of secondary emission that are not well represented in the theoretical models since they are not able to reproduce the modified shape of the experimental SEY-energy curves of rough surfaces, see Fig. 18.

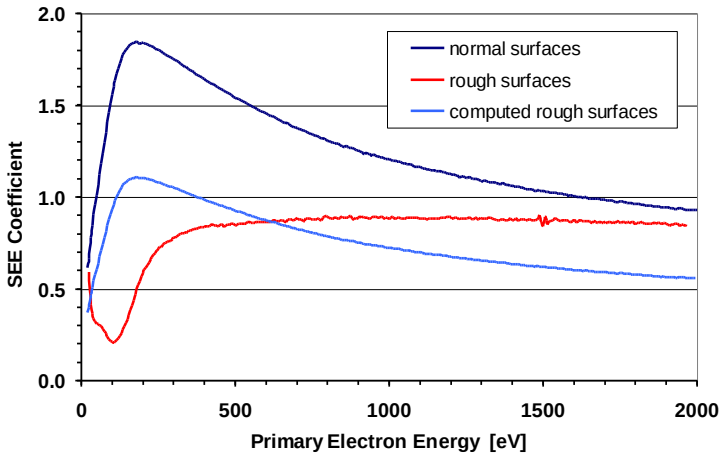

Figure 18. *Typical shape of SEY vs. primary energy curves for rough surfaces compared to those of normal "flat" surfaces and those computed by numerical simulations for rough surfaces, see text. Schematic diagram without experimental data value.*

From the results of simulations some explanations can be put forward in order to understand this effect:

- surface roughness produces more surface area per unit cross section and larger contribution of low incident angles, both contributing to increase SEY,

- but, for increasing aspect ratio, emitted electrons have increasing probability of impinging on protruding parts of the surface,
- these secondary primaries will produce 2nd generation of secondaries with a certain probability of impinging on protruding parts of the surface,
- as the average energy of secondaries decrease on every generation, an absorption effect of secondaries can be produced since SEY < 1 for low primary energies for all materials, see Fig. 19,
- for this to happen the probability of a secondary electron to impinge again on the surface should be large, i,e, high-aspect-ratio roughness is necessary,
- it is also clear that a large value of the first cross-over energy E_1 favours the effect.

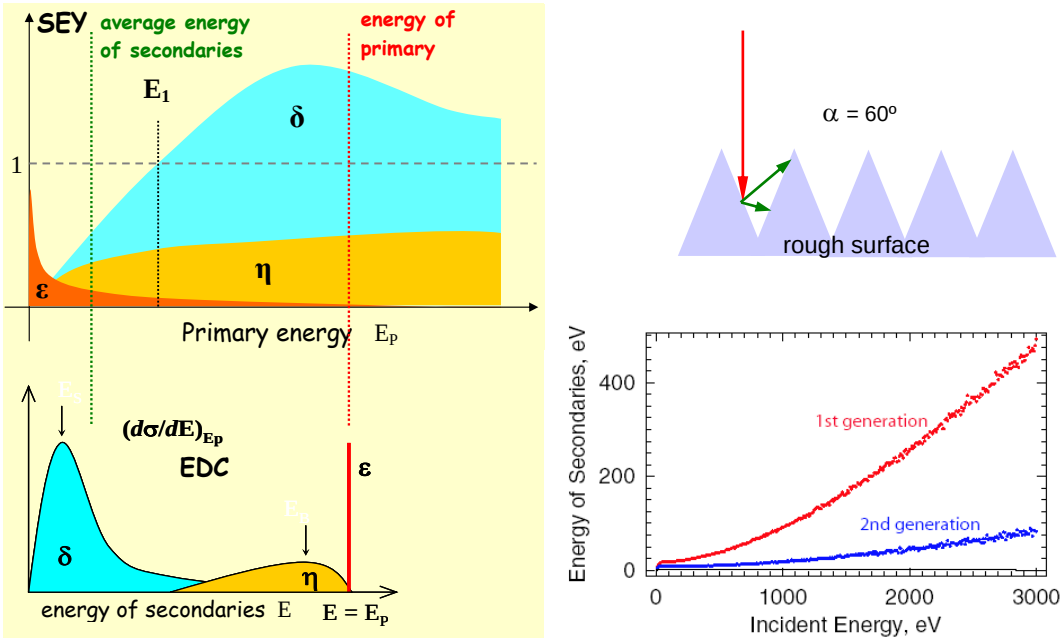

Figure 19. *Mechanism of secondary electron suppression by rough surfaces. Part of the secondaries are incident again on the surface producing 2nd generation of secondaries. On each generation of secondaries, the average energy decreases strongly [12]. Until, for energy < E_1 they are partly absorbed or "suppressed".*

In all simulations of secondary emission from rough surfaces, it is assumed that secondaries are emitted from the point of the surface where the primary electron impacts. This means that roughness size is assumed large compared with the size of the region where secondaries are produced. Since the region where secondaries are produced is

actually something like a hemisphere with radius 1 - 5 nm, roughness size should be greater than 50 nm for the SEY suppression effect to work.

More recent theoretical and experimental studies that confirm the SEY suppression effect of rough 3D surfaces with high aspect ratio are described in [33] and [34].

The explanation of SEY suppression by surface roughness gives additional importance to one of the main SEY properties of a potential anti-multipactor coating based on the surface roughness effect: a large value for the first cross-over energy E_1. Thus, a relatively high value for the maximum SEY, σ_m, could be tolerable if the corresponding energy, E_m, is also high. In this respect, it is of interest to consider some physical properties of more inert metals shown in Table I.

Table I. Some physical properties of clean inert metals of interest for anti-multipactor coatings

PROPERTY	**Ag**	**Au**	**Pd**	**Pt**	**Rh**	**Ir**	**Ru**	**Os**	**Re**
SEY $\mathbf{E_1}$ [eV]	150	150	125	150					100
SEY $\boldsymbol{\sigma_m}$	1.5	1.6	1.4	1.8					1.2
SEY $\mathbf{E_m}$ [eV]	650	700	550	750					700
Resistivity [μΩ·cm]	**1.6**	**2.4**	**9.9**	**10.4**	**4.7**	**5.1**	**7.3**	**9.2**	**18.7**
Melting [ºC]	962	1064	1552	1772	1965	2410	2310	3045	3180
Vapour pressure at 2000 ºC [Torr]			20	2×10^{-3}	5×10^{-3}	2×10^{-5}	6×10^{-5}	4×10^{-8}	

Their SEY properties are very similar: E_1 = ~ 150 eV, σ_m = 1.5 - 1.8, E_1 = ~ 700 eV (large experimental errors are presumed). The melting point and the vapour pressure are of interest for the deposition techniques, both indicating increasing difficulty in that order. Finally, the resistivity appears as decisive criterion: only Ag, Au, Rh, and Ir are nominated. Therefore, present research directed towards Ag and Au was well aimed.

2.2 Multipactor Effect

2.2.1 Multipactor Effect in Parallel Plate geometry

Multipactor is a well-known, long discussed and complex phenomenon that particle scientists and satellite engineers have being trying to mitigate for years. It is an electron resonance phenomenon that occurs when high RF fields accelerate electrons in a vacuum and causes them to collide with the vicinity walls, which depending on their energies, release one or more electrons into the vacuum. It is based on the formation of an electron cloud and one of the main concerns in the last three decades of the ESA was the risk of discharge on board spacecraft. When the impact energies, number of electrons released and timing of the impacts is such that a sustained multiplication of the number of electrons occurs, the phenomenon will grow exponentially and may lead to operational problems. In space systems, multipaction will cause loss/distortion of the RF signal (increase of noise figure or bit-error-rate) and can damage RF components or subsystems due to excess RF power being reflected back or dissipated by them.

In accelerators, multipaction will produce electron clouds preventing the undisturbed buildup of accelerator energy levels. Multipaction will also cause an increase of local pressure which could lead to a really destructive corona breakdown.

The existence of multipaction is dependent on the following four conditions being met:

- the mean free path of the electrons should be (much) greater than the spacing between the opposing surfaces, which is normally only the case in good vacuum and without any further obstruction in the way (no other dielectric).
- the average number of electrons released is greater than one which is dependent on the secondary electron yield of the surface, which in turn is dependent on the field strength (RF power) between the surfaces.-the time taken by the electron to travel from the surface from which it was released to the surface it impacts with, is to be an integer multiple of one half of the RF period (resonance).
- the availability of free electrons to start of the release of secondary electrons.

In space, free electrons are released from the surfaces by high energy particles, while during on-ground testing they are provided by a radioactive source (strontium 90) or an electron gun).

Secondary electron emission plays an essential role in Multipactor breakdown being the main trigger and sustaining mechanism of the discharge, as shown in the Figure 20 of the computed Multipactor regions for infinite parallel geometry and three representative surfaces.

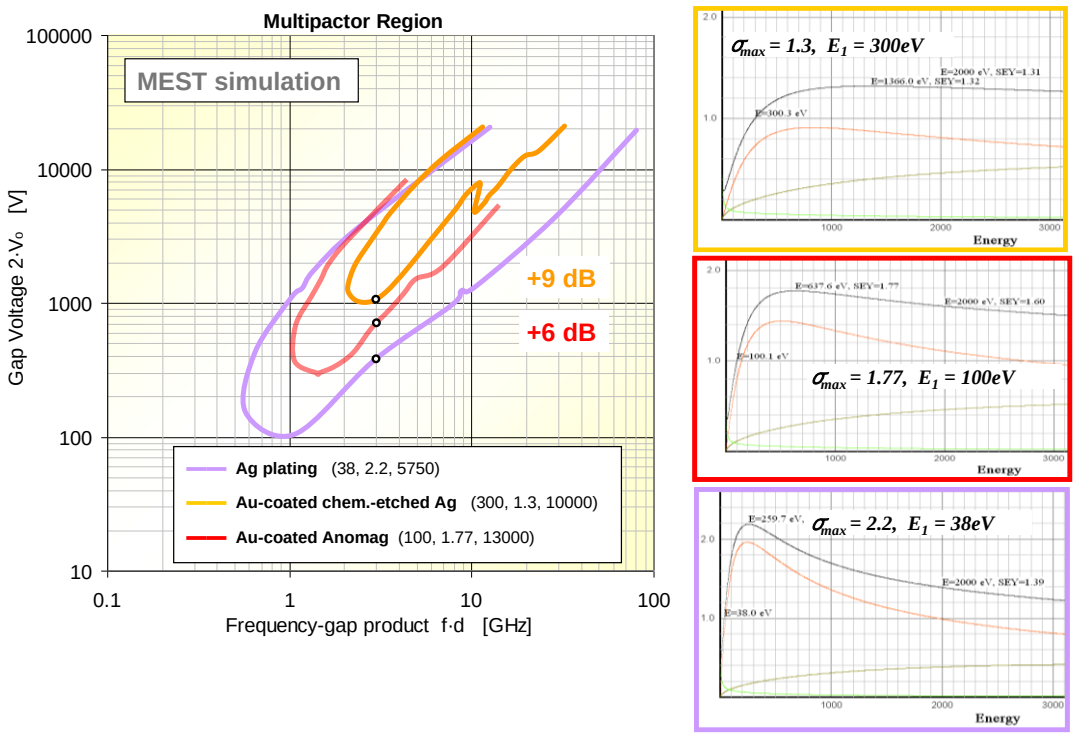

Figure 20. *Multipactor region simulation (MEST) for three types of surfaces of different SEY showing the improvement in the Multipactor threshold with respect to the bear silver surfaces*

The improvement of Multipactor power threshold (over that of standard Ag-plated samples) was computed for the gap distance d = 0.14 mm and frequency f = 12 GHz, appropriate for the multipactor samples (gap transformer) of the ESA AO 4025 CCN-2 project.

On the other hand, the secondary electron emission is a surface process and, as such, is often not well characterized. It depends on the type of material but also on the surface finish: surface contaminants and surface morphology. It is strongly influenced by interactions with environment: exposure to the air, humidity, air contaminants, temperature, etc. In space, it may also be influenced by irradiation with electrons, ions or photons. The uncertainty on the secondary electron emission properties is one of the reasons for the use of safety margins in Multipactor engineering analysis (see ECSS normative document [35]).

Multipactor is the resonant growth of an electron cloud or free electron space charge in RF components by secondary electron emission from exposed surfaces (Fig. 21). When electrons accelerated by the RF field impacts on a surface, secondary electrons are emitted from the surface. Main definitions and properties of secondary electron emission (SEE and SEY) are given in the previous section 2.1.

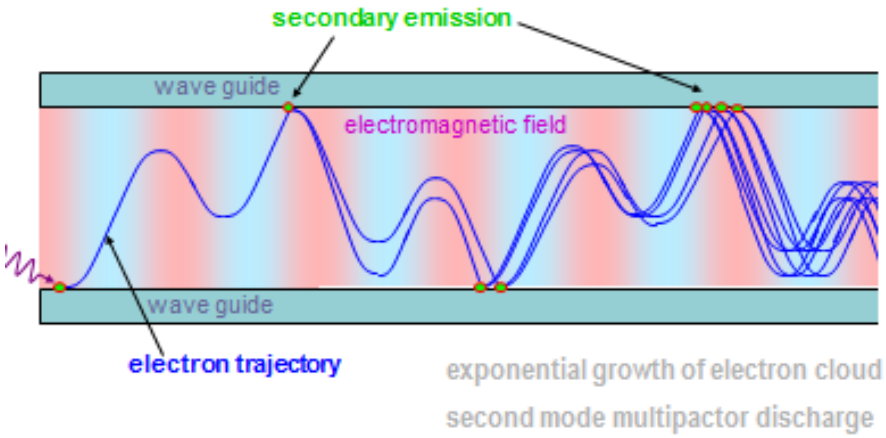

Figure 21. *Electron multiplication in parallel plate geometry of a waveguide*

In Multipactor [36-46], the electron space-charge avalanche is self-maintained by secondary electron emission from the surfaces of the RF component exposed to electron impact. SEE is the electron multiplication mechanism and the RF field supplies the energy for accelerating the electrons. This phenomenon occurs wherever some resonance conditions involving the RF electromagnetic field and the secondary electron emission properties of surface material are met.

The main conditions for the initial exponential growth of the Multipactor discharge are:

a. For the surfaces, $\sigma > 1$ for some range of Ep: $E_1 < E_p < E_2$, attainable by the accelerated electrons;

b. There is a sufficient phase range of the RF field where secondary electrons from a surface are not accelerated back to the surface from which they are emitted, but they are accelerated towards another surface;

c. The RF field phase and amplitude is such that a sufficient amount of these electrons impact on this other surface with a primary energy E_p: $E_1 < E_p < E_2$, i.e., such that $\sigma > 1$, and with a field phase such that the initial conditions of the secondary emission in the previous originating surface are reproduced again in the secondary emission from

this new surface. These initial conditions of a secondary emission event are: incident energy and angle of impacting electron and RF field phase and amplitude respect to the surface normal. In this principal resonant condition, the distance between the surfaces is an important parameter, as can be expected. These are the strong conditions of Hatch and Williams's theory (Fig. 22) of multipaction in parallel plate geometry [40, 41, 44 and 45].

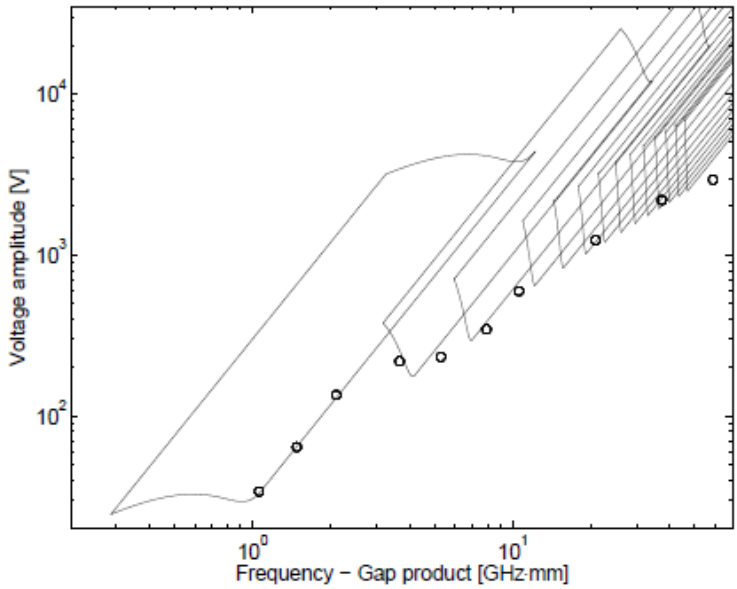

Figure 22. *Hatch and Williams charts for an aluminium surface, together with experimental data by Woode and Petit [36, 46].*

These conditions plus some other simplifying assumptions, like a constant relating emission and impacting energies, lead to a closed zone of Multipactor resonant conditions in gap-voltage vs. frequency-gap product space ($f \times d$, V_0) for each mode (odd integer number of half RF periods for the time between emission and impact for each resonant electron, necessary by resonant condition (c) above). The overlapping of these resonant modes produces a typical Multipactor susceptibility region in ($f \times d$, V_0) space for most material SEE properties (Fig. 23).

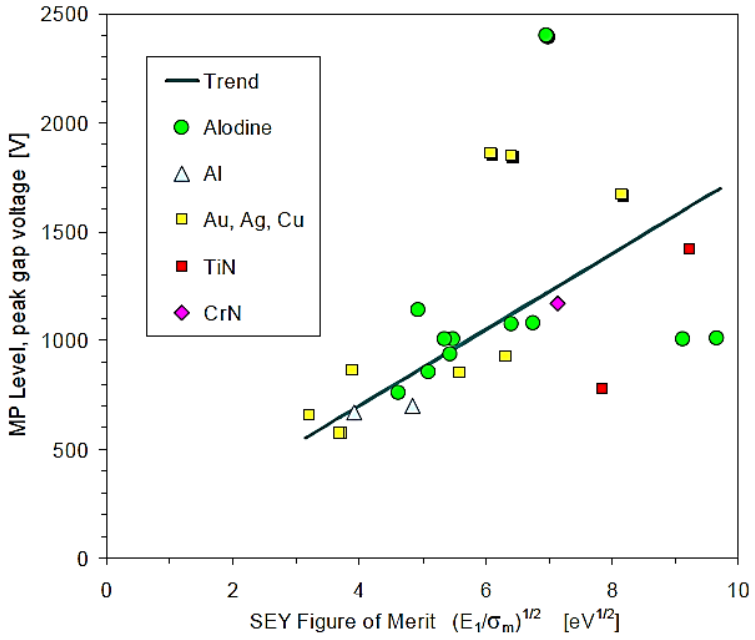

Figure 23. *Results of the experimental study by UAM-ESTEC, 1989 [2, 13, 14]. Multipactor level for f•d = 10.3 GHz•mm. Data dots high-lighted by shadows (MPL > 1500 V) correspond to samples conditioned in situ by RF Ar plasma.*

In *Chapter 8* we mention more recent and improved experimental results on the Multipactor tests for the passive RF devices treated by chemical etching and magnetron sputtering. The growth of the free electron population (cloud) eventually saturates because of the modification of the resonant conditions by the free electron space charge itself, i.e. by the electrical repulsion between electrons (Coulomb interaction) or the induced change in the RF component impedance.

The actual Multipactor susceptibility region has not so clear-cut boundaries because of several simplifying assumptions of Hatch and Williams's theory. One of those reasons is that hybrid modes [43, 44 and 46] are actually produced where resonant condition (c) above, is established between non-consecutive impact-emission SEE events: for example, SEE event (1) → secondary electron → SEE event (2) → secondary electron → SEE event (3), where initial conditions of (1) and (3) are equal but different from (2), and electron trajectories belong to different resonant modes. Also, in the electron cloud there are many electrons which are not in resonant conditions but whose eventual secondary electron lineage can get into resonant conditions.

The SEY for low primary or impacting energies has most influence on Multipactor susceptibility, being the E_1 parameter the most influential one, as shown by experiments

and theories. MEST Multipactor simulation program [49, 50] is designed for testing the influence of different SEE properties or parameters on the Multipactor discharge (Fig. 24).

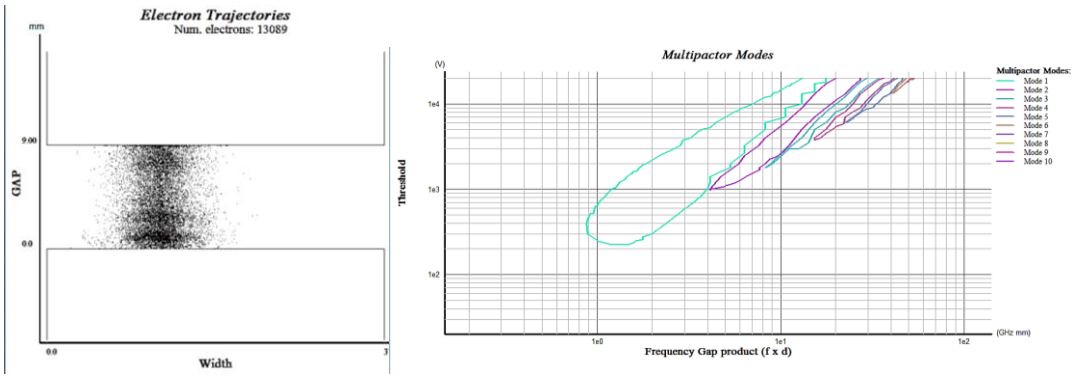

Figure 24. *MEST simulation of an electron cloud and the Multipactor modes [49, 51]*

If vacuum inside the device is poor, free electrons might impact on residual gas molecules and produce the emission of some of their electrons. These gas molecules might be desorbed from the surfaces by the Multipactor electron discharge itself. The electron trajectories are thus truncated or twisted, and the free electron population increased. Also, free gas ions are produced and might form a plasma. At higher pressures, a Corona discharge can occur [49] and lead to the destruction of the device.

2.2.2 Insertion Loss of a RF waveguide

In a waveguide with walls of a conductive material, the RF electromagnetic field induces currents in the near surface region of the material (skin effect) which dissipate power (heat, by Joule effect) from the RF field. Thus the RF field amplitude decreases exponentially $e^{-\alpha_c \cdot dl}$ with length *dl*, where α_c is the attenuation constant. Thus the power decreases as $e^{-2 \cdot \alpha_c \cdot dl}$, and the Insertion Loss (loss of power in logarithmic scale):

$$IL = 10 \cdot \Delta[\log(P)] = d(e^{-2 \cdot \alpha_c \cdot dl})/e^{-2 \cdot \alpha_c \cdot dl} = -2 \cdot \alpha_c \cdot \Delta l/\ln(10)$$

From electromagnetic theory of waveguides [51, 52]:

$$\alpha_c = \frac{2R_s}{b\eta\sqrt{1-(f_c/f)^2}} \cdot G\ (\textit{geometry, mode, } f, f_c) \qquad \eta = \sqrt{\frac{\mu}{\epsilon}}$$

For example,

$$G = \left(1+\frac{b}{a}\right)\left(\frac{f_c}{f}\right)^2 + \frac{b}{a}\left[1-\left(\frac{f_c}{f}\right)^2\right]\left[\frac{m^2ab+n^2a^2}{(mb)^2+(na)^2}\right]$$

for TE modes (m,n) in a rectangular waveguide of size $a \times b$ at frequency f .

The cut-off frequency f_c is:

$$2\pi \cdot f_c \quad = \quad \omega_c = c\sqrt{\left(\frac{n\pi}{a}\right)^2 + \left(\frac{m\pi}{b}\right)^2}, \qquad \text{where } c = (\varepsilon\,\mu)^{-½}$$

For vacuum or air inside the waveguide: $\varepsilon = \varepsilon_o$, $\mu = \mu_o$

The RF surface resistance (for a non-magnetic material) is $R_s = \rho/\delta$ where ρ is the dc resistivity and δ is the RF field penetration or *skin* depth in the material, $\delta = [\rho/(\pi\,\mu_o\,f)]^{1/2}$, see next section.

The R_s is the relevant material parameter for this research in order to control the RF power losses in the waveguides (multipactor samples) due to the anti-multipactor coating. Thus, the concept of surface resistance for high frequencies (RF and micro-waves, and general, RF) is reviewed in the following, as well as the effect of a surface overlayer and of surface roughness, both critical in this research.

A few simulations of the of the electric field distribution for circular and rectangular waveguides are given as examples in in Figs. 25 and 26 below.

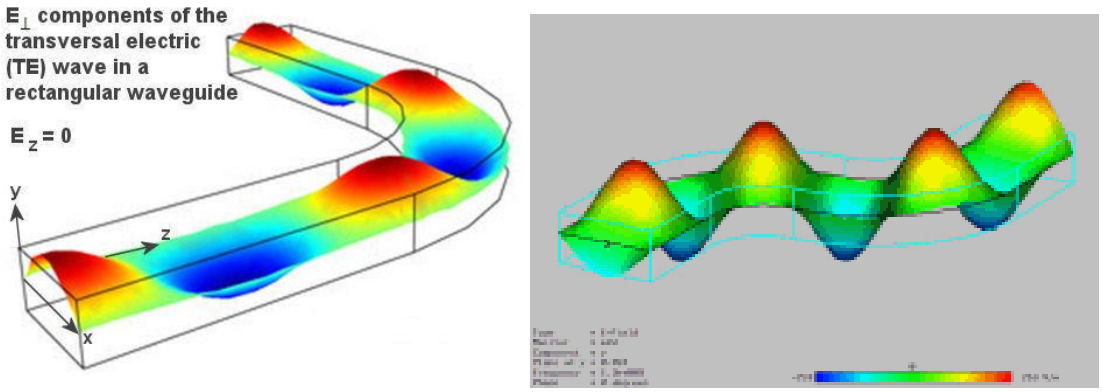

Figure 25. *Transversal component of the electric field in a bended waveguide at 1.3GHz (Prof. Dr.T Weiland – Darmstadt University)*

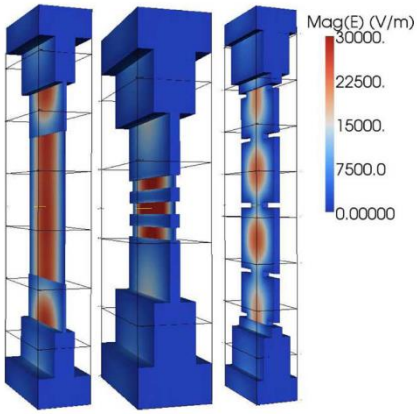

Fig. 11. Sample structure and electric field distribution for the three types of samples. (*from left to right*) Transformer: 0.14-mm gap, low-pass filter: 0.14-mm gap, bandpass filter: 1.31-mm gap. Reference grid lines separated 10 mm are included for dimensional reference. The magnitude of the maximum electric field is represented. Fields have been computed with FEST3D [10].

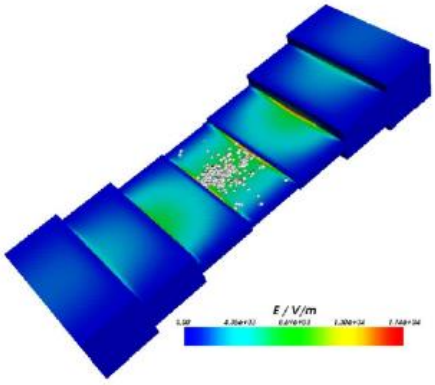

- **Electric Field Density:**
  Critical element: inner gap

Figure 26. *Waveguide Gap Transformer using FEST 3D (C. Vicente et al., IEEE MTT-S Digest, June 2005). White small dots in right figure indicate MP electron cloud.*

A combination of two factors: geometric design and an optimized coating type applied in the critical regions of a waveguide (inner gap) can increase significantly the MP threshold and reduce the power losses.

2.2.3 RF Surface resistance

For the electromagnetic waves in a homogeneous non-magnetic ($\mu = \mu_o$, $\boldsymbol{B} = \mu\boldsymbol{H}$) metallic ($\sigma >> \boldsymbol{i}\omega\varepsilon$, $\boldsymbol{J} = \sigma\boldsymbol{E}$) material, the Maxwell equations in complex form are:

$$\nabla\times\boldsymbol{E} = -\boldsymbol{i}\omega\boldsymbol{B} \qquad \nabla\times\boldsymbol{H} = \boldsymbol{J}$$

Then, $\nabla\times\boldsymbol{J} = -\boldsymbol{i}\omega\sigma\boldsymbol{B} = -\boldsymbol{i}\omega\mu\sigma\boldsymbol{H}$ and $\nabla\times(\nabla\times\boldsymbol{J}) = -\boldsymbol{i}\omega\mu\sigma\,\nabla\times\boldsymbol{H} = -\boldsymbol{i}\omega\mu\sigma\,\boldsymbol{J}$

Let *z* be the propagation direction, and *x* and *y* the directions of $\boldsymbol{E} = \boldsymbol{E}_x\,\boldsymbol{u}_x$ and $\boldsymbol{H} = \boldsymbol{H}_y\,\boldsymbol{u}_y$, respectively (transversal wave), then $\boldsymbol{J} = \boldsymbol{J}_x(z)\,\boldsymbol{u}_x$ is only function of *z*, and therefore,

$$\nabla\times\boldsymbol{J} = \partial_z\boldsymbol{u}_z\times\boldsymbol{J}_x\,\boldsymbol{u}_x = \partial_z\boldsymbol{J}_x\,\boldsymbol{u}_y \quad , \quad \nabla\times(\nabla\times\boldsymbol{J}) = \partial_z\boldsymbol{u}_z\times\partial_z\boldsymbol{J}_x\,\boldsymbol{u}_y = -\partial_z^2\boldsymbol{J}_x\,\boldsymbol{u}_x = -\partial_z^2\boldsymbol{J} \quad \text{and}$$

$$\partial_z^2\boldsymbol{J} = \boldsymbol{i}\omega\mu\sigma\,\boldsymbol{J} = \boldsymbol{K}\,\boldsymbol{J}$$

Since the wave cannot increase while propagating and loosing energy (Joule effect, $\boldsymbol{J} = \sigma\boldsymbol{E}$), only the exponentially decreasing solution is possible

$\boldsymbol{J} = \boldsymbol{J}_o\exp(-\boldsymbol{K}\,z) = \boldsymbol{J}_o\exp(-(1+\boldsymbol{i})\,z/\delta)$ where $\boldsymbol{K}^2 = \boldsymbol{i}\omega\mu\sigma$, $\boldsymbol{K} = (1+\boldsymbol{i})(\tfrac{1}{2}\omega\mu\sigma)^{1/2} = (1+\boldsymbol{i})/\delta$

defining the **skin depth** $\underline{\delta = (\tfrac{1}{2}\,\omega\,\mu\,\sigma)^{-1/2} = (\pi\,\mu_o\,\sigma\,f)^{-1/2}.}$

The real current in the conductor is $J_x = J_o\exp(-z/\delta)\cos(\omega\,t - z/\delta)$, i.e., an exponentially attenuated wave with wave length $\lambda = 2\pi\delta$. The wave is practically absorbed in $5\times\delta$ or in $\tfrac{3}{4}\times\lambda$ (Fig. 27).

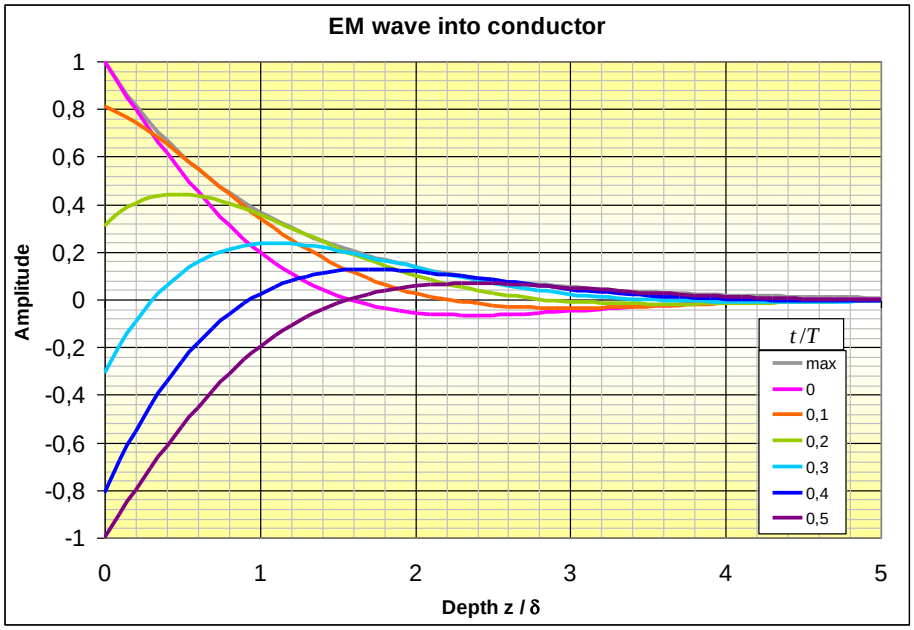

Figure 27. *Propagation of an electromagnetic wave in a conductor*

The wave length in vacuum or in air is $\lambda_o = c / f = (\varepsilon_o \mu_o f^2)^{-1/2}$ and

$$\lambda_o / \lambda = [(\pi \mu_o \sigma f)/(\varepsilon_o \mu_o f^2)]^{1/2} = [(\pi \sigma)/(\varepsilon_o f)]^{1/2} >> 1,$$

since for metallic materials $\sigma >> \varepsilon_o f$.

As an example, for a frequency of 10 GHz :

f = 10 GHz ε_o = 8.854 × 10^{-12} F/m λ_o = 2.998 cm	σ [S/m]	λ_o / λ
Ag	6.30×10^7	4.73×10^4
C (graphite)	3×10^5	3.3×10^3

For a wave incident on conductor with an angle θ_o , the "refraction" angle θ in the conductor is $\sin(\theta) = \lambda / h = (\lambda / \lambda_o) \sin(\theta_o)$ because $\sin(\theta_o) = \lambda_o / h$; therefore, $\lim(\theta)_{\theta o \to 90^o} = (\lambda / \lambda_o) = = 0.001 – 0.02^o$, for Ag and graphite, respectively, i.e., the direction of the wave in the conductor is always practically normal to the surface.

Thus, in above description, the surface of the conductor is normal to the z axis; let us say, the plane $z = 0$.

The power dissipated per surface area $dxdy$ is $dP = dxdy \cdot \int_o^\infty |\boldsymbol{J}\cdot\boldsymbol{E}|\, dz$

$$\int_o^\infty |\boldsymbol{J}\cdot\boldsymbol{E}|\, dz = (1/\sigma)\cdot\int_o^\infty |\boldsymbol{J}^2|\, dz = (1/\sigma)\cdot|\boldsymbol{J}_o^2|\cdot\int_o^\infty \exp(-2\cdot z/\delta)\, dz = \tfrac{1}{2}\,(\delta/\sigma)\cdot|\boldsymbol{J}_o^2| = R_s\cdot|\boldsymbol{H}_o^2|$$

For the last step $\boldsymbol{J}_{xo} = (1/\delta)\cdot(1+\boldsymbol{i})\cdot\boldsymbol{H}_{yo}$ and $R_s = (\delta\,\sigma)^{-1} = \rho/\delta$, which are reviewed next.

In applying the theorem of Stokes for a rectangle $S = dy\times(z\to\infty)$

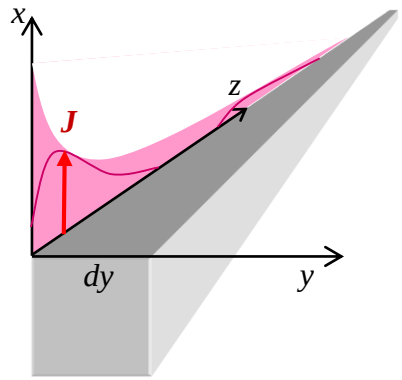

$$\oint_{C(S)} \vec{H}\cdot d\vec{l} = \int_S \vec{\nabla}\times\vec{H}\cdot d\vec{S} = \int_S \vec{J}\cdot d\vec{S} = dy\cdot\int_0^\infty J\cdot dz = dy\cdot J_{xo}\cdot\int_0^\infty e^{-(1+\bar{i})z/\delta}\cdot dz = dy\cdot\frac{\delta}{1+\bar{i}}\cdot J_{xo} = dy\cdot H_{yo}$$

$\boldsymbol{H}\cdot d\boldsymbol{l}$ takes equal and opposite values in both long (infinite) sides of the rectangle and $\boldsymbol{H} = 0$ for $z\to\infty$.

By definition, the surface impedance is $\boldsymbol{Z} = \boldsymbol{E}_{xo}/\boldsymbol{H}_{yo} = R_s + X_s\,\boldsymbol{i}$, therefore

$$\boldsymbol{Z} = (1/\sigma)\cdot\boldsymbol{J}_o/[\delta\cdot(1+\boldsymbol{i})^{-1}\boldsymbol{J}_o] = (\rho/\delta)(1+\boldsymbol{i})$$

and the surface resistance :

$$R_s = \rho/\delta = (\pi\,\mu_o\,\sigma f)^{1/2}/\sigma = (\pi\,\mu_o f/\sigma)^{1/2}$$

- ***Surface Resistance of a Layered Near Surface Region***

For a near surface region formed by parallel layers of homogeneous conductors, the continuity of $\boldsymbol{E}_x$ at the interfaces is the only condition needed to connect the solutions to Maxwell equations in each conductor.

For the first layer at the surface $\boldsymbol{J} = \boldsymbol{J}_o\exp(-(1+\boldsymbol{i})\,z/\delta_o)$ and multiplying by σ_o

$\boldsymbol{E} = \boldsymbol{E}_o\exp(-(1+\boldsymbol{i})\,z/\delta_o)$ $\quad z\in[0,\,d_o]$, and for the other layers also

$\boldsymbol{E} = \boldsymbol{E}_1 \exp(-(1+\boldsymbol{i})(z-d_o)/\delta_1)$ $\quad z \in [d_o, d_o+d_1]$ $\quad \boldsymbol{E}_1 = \boldsymbol{E}_o \exp(-(1+\boldsymbol{i})\, d_o/\delta_o)$ (continuity of $\boldsymbol{E}$) and so on.

Since the power dissipated in the conductor walls of the waveguide is the cause of the attenuation of the transmitted wave and of the insertion loss, let us calculate the dissipated power per unit surface area. In the case above of an homogeneous conductor

$$dP/dA = \int_o^\infty |\boldsymbol{J}\cdot\boldsymbol{E}|\, dz = \tfrac{1}{2}\,(\delta/\sigma)\cdot|\boldsymbol{J}_o^2| = R_s\cdot|\boldsymbol{H}_o^2| = \tfrac{1}{2}\,\delta\,\sigma\,|\boldsymbol{E}_o^2| = \tfrac{1}{2}\,|\boldsymbol{E}_o^2|/R_s$$

Using this last equation for calculating R_s in the layered conductor

$$\int_o^\infty |\boldsymbol{J}\cdot\boldsymbol{E}|\, dz = \int_o^\infty \sigma\cdot|\boldsymbol{E}^2|\, dz =$$

$$= \sigma_o\cdot|\boldsymbol{E}_o^2|\cdot\int_o^{d_o} \exp(-2\cdot z/\delta_o)\, dz + \sigma_1\cdot|\boldsymbol{E}_1^2|\cdot\int_{d_o}^{d_o+d_1} \exp(-2\cdot(z-d_o)/\delta_1)\, dz + \ldots =$$

$$= \sigma_o\cdot|\boldsymbol{E}_o^2|\cdot\int_o^{d_o} \exp(-2\cdot z/\delta_o)\, dz + \sigma_1\cdot|\boldsymbol{E}_1^2|\cdot\int_o^{d_1} \exp(-2\cdot z/\delta_1)\, dz + \ldots =$$

$$= \tfrac{1}{2}\,(\delta_o\,\sigma_o)\cdot|\boldsymbol{E}_o^2|\,(1-\exp(-2\cdot d_o/\delta_o)) + \tfrac{1}{2}\,(\delta_1\,\sigma_1)\cdot|\boldsymbol{E}_1^2|\,(1-\exp(-2\cdot d_1/\delta_o)) + \ldots$$

In the case of one surface layer, $d_1 \to \infty$, and

$$\int_o^\infty |\boldsymbol{J}\cdot\boldsymbol{E}|\, dz = \tfrac{1}{2}\,(\delta_o\,\sigma_o)\cdot|\boldsymbol{E}_o^2|\,(1-\exp(-2\cdot d_o/\delta_o)) + \tfrac{1}{2}\,(\delta_1\,\sigma_1)\cdot|\boldsymbol{E}_1^2| =$$

$$= \tfrac{1}{2}\,(\delta_o\,\sigma_o)\cdot|\boldsymbol{E}_o^2|\,(1-\exp(-2\cdot d_o/\delta_o)) + \tfrac{1}{2}\,(\delta_1\,\sigma_1)\cdot|\boldsymbol{E}_o^2|\cdot\exp(-2\cdot d_o/\delta_o) =$$

$$= \tfrac{1}{2}\,|\boldsymbol{E}_o^2|[(\delta_o\,\sigma_o)\cdot(1-\exp(-2\cdot d_o/\delta_o)) + (\delta_1\,\sigma_1)\cdot\exp(-2\cdot d_o/\delta_o)]$$

Thus, for the effective R_s

$$R_s^{-1} = (\delta_o\,\sigma_o)\cdot(1-\exp(-2\cdot d_o/\delta_o)) + (\delta_1\,\sigma_1)\cdot\exp(-2\cdot d_o/\delta_o)$$

Since $(\delta_1\,\sigma_1) = (\delta_o\,\sigma_o)\cdot(\sigma_1/\sigma_o)^{1/2}$, then

$$R_s^{-1} = (\delta_o\,\sigma_o)\cdot[1-\exp(-2\cdot d_o/\delta_o) + (\sigma_1/\sigma_o)^{1/2}\cdot\exp(-2\cdot d_o/\delta_o)]$$

$$= (\delta_1\,\sigma_1)\cdot[(\sigma_o/\sigma_1)^{1/2}\cdot(1-\exp(-2\cdot d_o/\delta_o)) + \exp(-2\cdot d_o/\delta_o)]$$

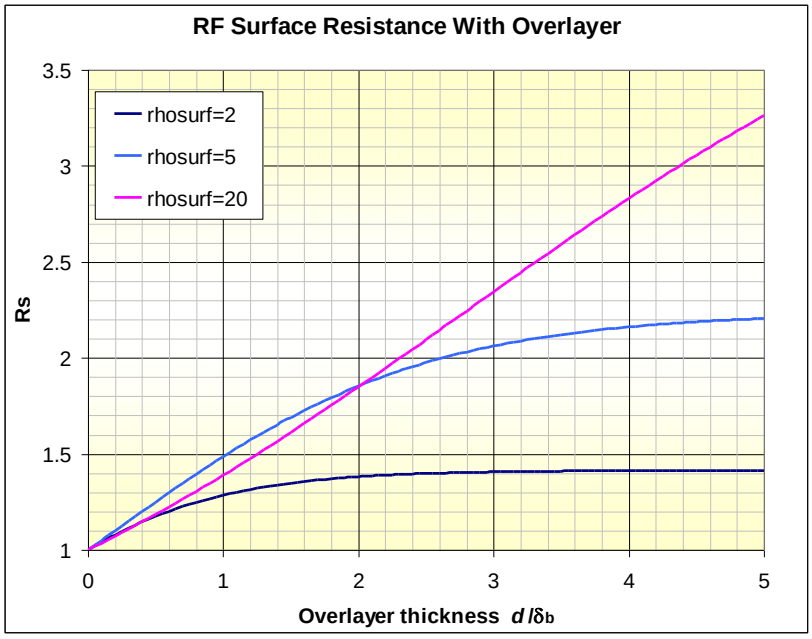

Figure 28. *Surface resistance of a material as a function of the overlayer thickness*

Fig. 28 describes the RF surface resistance dependency on an overlayer of thickness d, in conditions of the surface resistivity 2×, 5×, and 20× that of the bulk (δ_b is the skin depth of the bulk). For example for $\rho(Au)/\rho(Ag) = 1.5$, $\rho(Ni)/\rho(Ag) = 4.4$, $\rho(Pt)/\rho(Ag) = 6.7$, *and* $\rho(Ti)/\rho(Ag) = 26$. For $f = 12$ *GHz* and *Ag*, $\delta = 560$ *nm*.

2.2.4 A Layered Model for RF surface resistance calculation

The effect of surface roughness on insertion loss of RF devices with rough metallic walls has been studied theoretically as well as experimentally since many decades ago. A brief and good review and as well as new results of interest for this project can be found in the work of Filipovic *et al* [53] and references therein. They study the effect for 3D regular arrays of simple geometrical indentations or grooves by a finite element method using the commercial software High Frequency Structure Simulator (HFSS). They solve the electromagnetic field inside the conductor (modelled like a dielectric) down to several skin depths sufficient to simulate the remaining deep bulk as perfect conductor. They validated their computation results by comparing with more exact theoretical calculations [54].

More recently, another excellent review with special emphasis on random surface roughness is found in the work of Tsang *et al* [55] and references therein. This paper

reviews the analytical theory, numerical simulations and experimental results. Analytic second-order small perturbation, numerical transfer matrix, method of moments, and numerical finite element methods were used to study the electromagnetic wave propagation in a rough surface environment. They study 2D and 3D cases, and describe the rough surface characterization and the extraction of roughness parameters from profile measurements. Their work has some mathematical difficulty but is of great interest as treating realistic surfaces and deserves further study if this subject is to be pursued.

The literature on this subject is too ample and specialized to be reviewed in detail. The references mentioned above [53-56] are a good starting point for further study. Nevertheless, we list some other references [56-63] for one or another point of interest.

However, we should mention that one problem of great interest for our project: the effect of a thin surface coating of another material, does not seem to have been treated in the literature. In this technical note, we propose a simple and practical approach to handle a class of uncomplicated cases: 2D, transverse, and limited slope roughness profiles. Easy and precise solutions to these cases might allow attaining general qualitative or approximate conclusions applicable to real problems encountered in our research.

It depends on both the shape and the size of the roughness relative to the skin depth and complex calculations should be used for its accurate determination. However, with some small deficit of precision, a simple approximated formula may be used in most cases:

$$\frac{R_s}{R_{s,o}} = 1 + \frac{\Delta R_s}{R_{s,o}} \frac{2}{\pi} \arctan\left(\kappa \left(\frac{\Delta}{\delta} \right)^2 \right)$$

where, $R_{s,o}$ corresponds to the smooth flat surface, $(\Delta R_s / R_{s,o})$ is a shape constant defining the asymptotic value, Δ is the rms roughness parameter, and κ is another shape constant defining the behaviour at low roughness. For equilateral triangular transverse grooves: $(\Delta R_s / R_{s,o}) = 1$, $\kappa = 1.4$, and the model case most used. For triangular transverse grooves of aspect ratio height to period r: $(\Delta R_s / R_{s,o}) = (1+4 \cdot r^2)^{1/2} - 1$. Δ depends both on shape and size of the roughness, and it is the only way the formula depends on size apart from shape. For the triangular grooves of period p above: $\Delta = r \cdot p/(2\sqrt{3})$.

NOTE: In the following, a model is developed based in generalizing the equation

$$\frac{1}{R}=\frac{\delta}{\rho}=\int_0^\infty \frac{1}{\rho}e^{-\frac{z}{\delta}}dz$$

for inhomogeneous materials where ρ and δ are functions of *z*. However, this equation cannot be generalized in this way. In the other hand, the equation

$$\frac{1}{R}=\frac{\delta}{\rho}=2\int_0^\infty \frac{1}{\rho}e^{-2\frac{z}{\delta}}dz$$

is of general validity, for homogeneous and inhomogeneous materials, see Section of Surface Resistance of a Layered Near Surface Region, above. This last equation has the same mathematical form; the only difference is different scales when applying to the physical problem. However, the model developed below is calibrated against known results for a few cases. In this calibration, scales are adjusted for obtaining the reference results. Therefore, the model developed below has also a physical support once definition and scales are adjusted properly.

In a waveguide, the power attenuation measured in dB is proportional to the attenuation constant. For conductive metallic surfaces the attenuation constant is proportional the RF surface resistance *R* and so does insertion loss *IL* in dB:

$$\alpha_c=\frac{R}{Z\cdot W} \qquad\qquad IL=\frac{R}{Z}G$$

where $Z\cdot W$ and Z/G have units of resistance×length and resistance, respectively, and depend on the geometry and the frequency.

In a homogeneous non-magnetic conductive material, *R* and the skin depth δ at microwave frequencies are:

$$R=\frac{\rho}{\delta} \qquad\qquad \delta=\sqrt{\frac{\rho}{\pi\mu_o f}}$$

where σ and $\rho = 1/\sigma$ are respectively the dc conductivity and resistivity of the material, and *f* is the frequency. In such a material:

$$\frac{1}{R} = \frac{\delta}{\rho} = \frac{1}{\rho}\int_0^\infty e^{-\frac{z}{\delta}} dz = \int_0^\infty \frac{1}{\rho} e^{-\frac{z}{\delta}} dz$$

is a mathematic identity.

In our model, we generalize this in two ways:

i) In a material inhomogeneous in depth, both ρ and δ can be considered a local material property, functions $\rho(z)$ and $\delta(z)$ of the depth *z* from the surface.

ii) In a material with a rough surface, the tangent magnetic field and the current have contour intensity surfaces which tend to the real geometrical surface of the conductor for $f \to \infty$. In a layered model defined by these contour intensity surfaces, the effective resistivity of a layer is increased by the increased effective length of the layer due to roughness and decreased by increased effective thickness also due to roughness, see Fig.2.2.14. These effects are supposed to be included in effective resistivity factor *A* which will depend on the field inside the conductor, and thus on $\rho(z)$, surface geometry, and *f*.

$$\frac{1}{R} = \int_0^\infty \frac{1}{\rho \cdot A} e^{-\frac{z}{\delta}} dz$$

The utility of this approach will rely on the possibility of finding a simple analytical expression for *A*. The simplest case for this approach is a transversally grooved surface (transversal to current flow). From theoretical considerations confirmed by experimental results, *A* should tend to the ratio of the rough surface area to the flat surface area both for $f \to \infty$ or $z \to 0$, and should tend to 1 for $z \to \infty$. Thus, we assume expression:

$$A = \sqrt{1 + 4 \cdot r_o^2 \left(\frac{h}{h_o}\right)^2}$$

where r_o is a geometrical shape parameter (= h_o/p for symmetrical triangular grooves, as in *Figs.31 - 33*) and (h/h_o) is the relative effective height of the rough current layer. (h/h_o) = 1 for $f = \infty$ or $z = 0$, and = 0 for $z = \infty$. Now, all the dependence on the field inside the

conductor is in the analytical expression of (h/h_o). For simpler cases, such as triangular grooves, we may reasonably expect that this should have an exponential decrease with $Z \equiv (z/\delta)$, and this decrease should be modulated somehow by the roughness size normalized to the skin depth $X \equiv (h_o/\delta)$, and thus assume:

$$\left(\frac{h}{h_o}\right) = \exp\left(-\frac{z}{\delta}\Phi\left(\frac{h_o}{\delta}\right)\right) = \exp(-Z \cdot \Phi(X))$$

where the function Φ is difficult to establish on simple reasoning. On assumptions above, the RF surface resistance of a rough homogeneous conductor will be a function of $X = (h_o/\delta)$:

$$\frac{1}{R} = \int_0^\infty \frac{1}{\rho \cdot A} e^{-\frac{z}{\delta}} dz = \left(\frac{\delta}{\rho}\right) \int_0^\infty \frac{1}{A(Z,X)} e^{-Z} dZ = \frac{1}{R_o} \int_0^\infty \frac{1}{A(Z,X)} e^{-Z} dZ$$

where R_o is the RF surface resistance of the conductor with flat surface. The relative RF surface resistance:

$$\frac{R}{R_o} = F(X)$$

has been theoretically calculated with different complex mathematical techniques aided by numerical computation using sophisticated software tools, *see Sec.2.2.1 and 2.2.2* above and [53]. These theoretical results have found some experimental support when data were available.

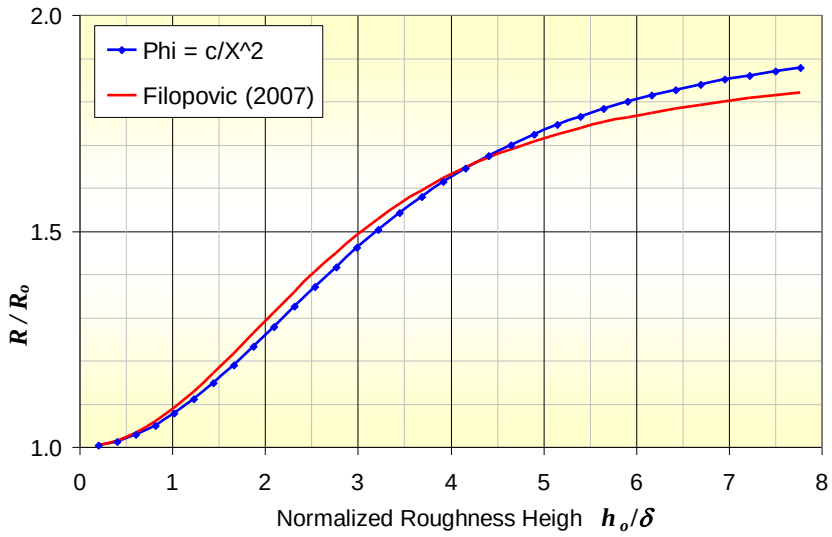

Fig. 29. *Relative RF surface resistance versus roughness size for equilateral triangular transverse grooves. Fitting theoretical results of Filipovic [53] with the simplest trial function* $\Phi(X) = c/X^2$*, see text.*

Relying on those theoretical calculations, our approach is to solve the integral equation for A (*Z*, *X*):

$$\frac{1}{F(X)} = \int_0^\infty \frac{1}{A(Z,X)} e^{-Z} dZ$$

This is kind of a Laplace transform equation. However, in our case, it is more practical to solve it by a trial and error approach assisted by nonlinear least squares fitting. It is easy to see that a simple function as $\Phi(X) = c/X^2$, with only one fitting parameter, allows already qualitative good results, *Fig.29.*

We have found another simple Φ(X) function with three adjustable parameters which allows fitting published theoretical results within their expected error. When these parameters are determined by fitting some reliable theoretical result, the model is calibrated. If then the model explains satisfactorily other different theoretical computations, the model is correspondingly validated. In *Figs 30 and 3*1 we present calibration with theoretical results of Filipovic *et al* [53] and Matsushima *et al* [56], respectively. *Fig. 32* shows that those theoretical results are not completely mutually consistent. On the other hand, *Fig.31 and 32* validate the model since they show that it properly explains the influence of different aspect ratios. Unless indicated, our model is calibrated with Filipovic's data [53].

Fig.33 also qualitatively validates the model as showing current layers very similar to those calculated by Matsushima *et al* [56]. The profiles of the current layers are drawn as triangular for our model, even though their shape is not determined, but only their relative effective length $A(Z, X)$. They should nevertheless tend to the conductor surface as $Z \rightarrow 0$ or $X \rightarrow \infty$.

Our layered model is prepared for easily taking into account the effect of a coating of another material. The value of ρ, and consequently of δ, can be switched to a new value for all the current layers with $z \le d_s$ (d_s = thickness of the surface coating). If $k^2 = \rho/\rho_b$ is the ratio of surface coating to bulk or substrate resistivities, then $\delta/\delta_b = k$, and the RF surface resistance is calculated by:

$$\frac{1}{R} = \left(\frac{\delta}{\rho}\right)\int_0^{Z_s/k} \frac{1}{A(Z', X/k)} e^{-Z'} dZ' + \left(\frac{\delta_b}{\rho_b}\right)\int_{Z_s}^{\infty} \frac{1}{A(Z, X)} e^{-Z} dZ$$

where $Z_s = d_s/\delta_b$, and the physics requires that $\rho_b \cdot A(z/\delta_b, h_o/\delta_b)\cdot\exp(z/\delta_b) = \rho_b \cdot A(Z, X)\cdot\exp(Z)$ in the bulk, becomes $\rho\, A(z/\delta, h_o/\delta)\cdot\exp(z/\delta) = \rho\, A(Z', X/k)\cdot\exp(Z')$ in the surface coating.

And the relative RF surface resistance is now calculated by:

$$\frac{1}{F(X)} = \frac{R_o}{R} = \frac{1}{k}\int_0^{Z_s/k} \frac{1}{A(Z', X/k)} e^{-Z'} dZ' + \int_{Z_s}^{\infty} \frac{1}{A(Z, X)} e^{-Z} dZ$$

Unfortunately, there seems to be no theoretical or experimental data available for testing or validating this ability of our layered model: calculating the effect of a surface layer of different material on the RF resistance of a rough surface.

This is important for this research since an anti-Multipactor coating will require, besides surface roughness, stable low-SEY materials in the surface, which are much less conductive than silver.

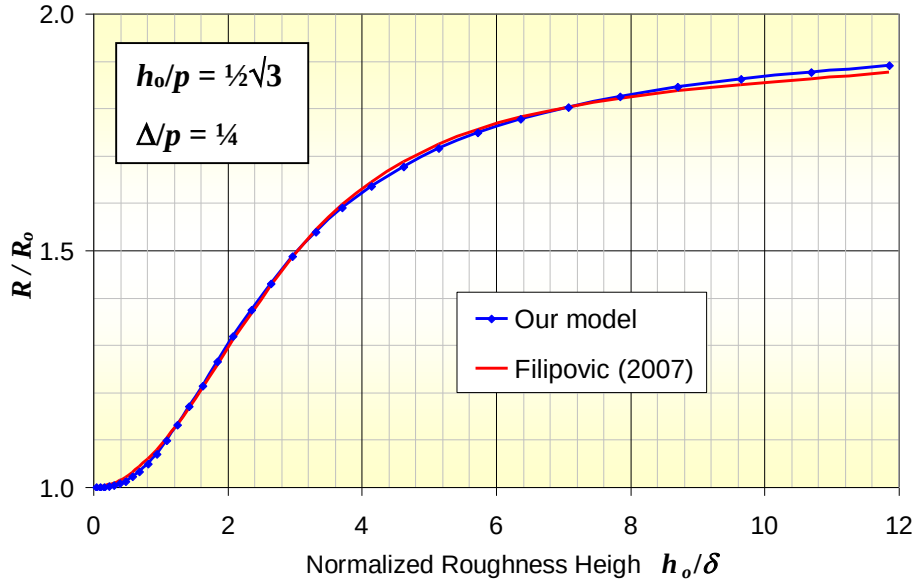

Figure 30. *Relative change of RF surface resistance versus roughness size for equilateral triangular transverse grooves. Calibration plot of the layered model against theoretical results of Filipovic [53]. Δ = rms roughness.*

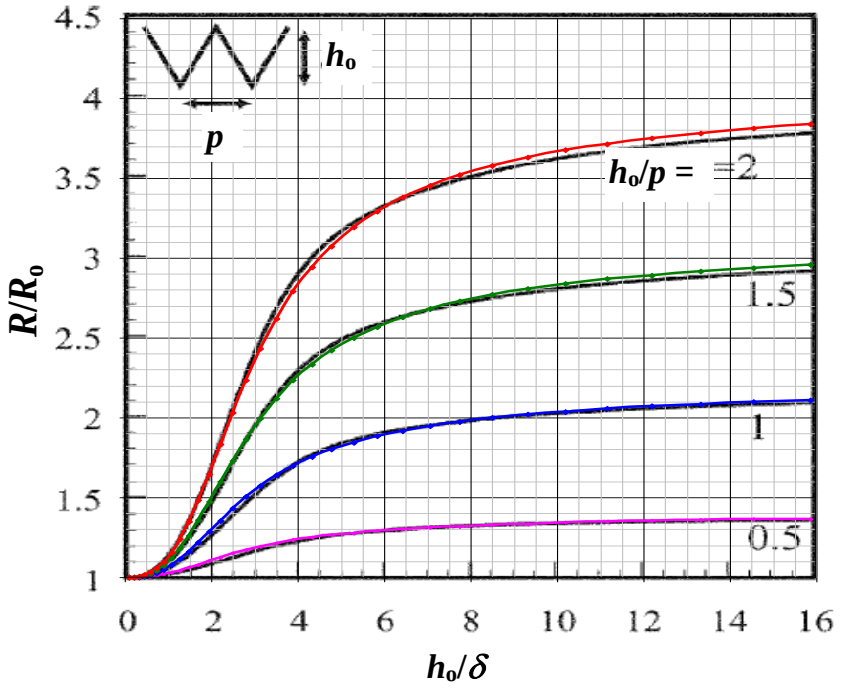

Figure 31 *Relative RF surface resistance versus normalized roughness size for triangular transverse grooves of different aspect ratios. Calibration plot of our layered model (colour lines) against theoretical results of Matsushima [56] black lines.*

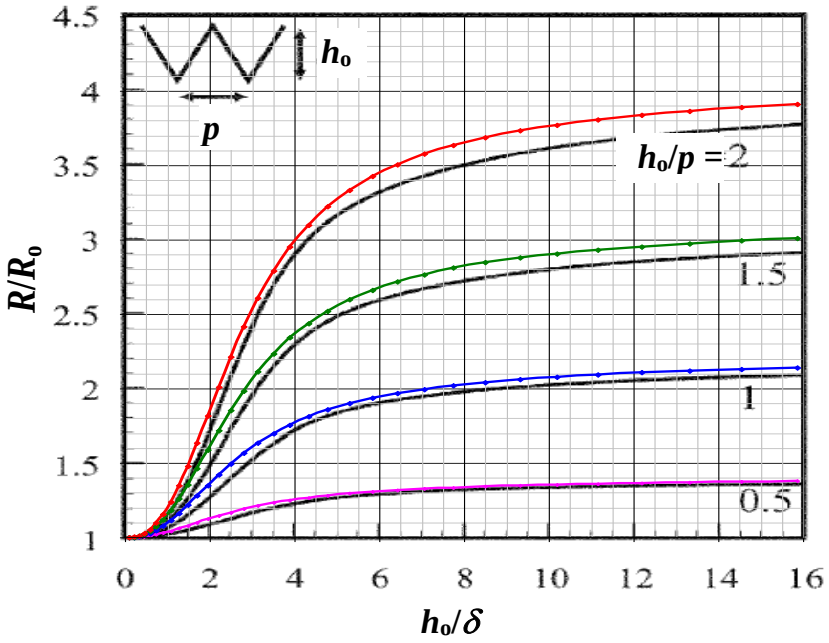

Figure 32. *Relative RF surface resistance versus normalized roughness size for triangular transverse grooves of different aspect ratios. Theoretical results of Matsushima [56], black lines; and layered model, coloured lines, calibrated with Filipovic's data [53].*

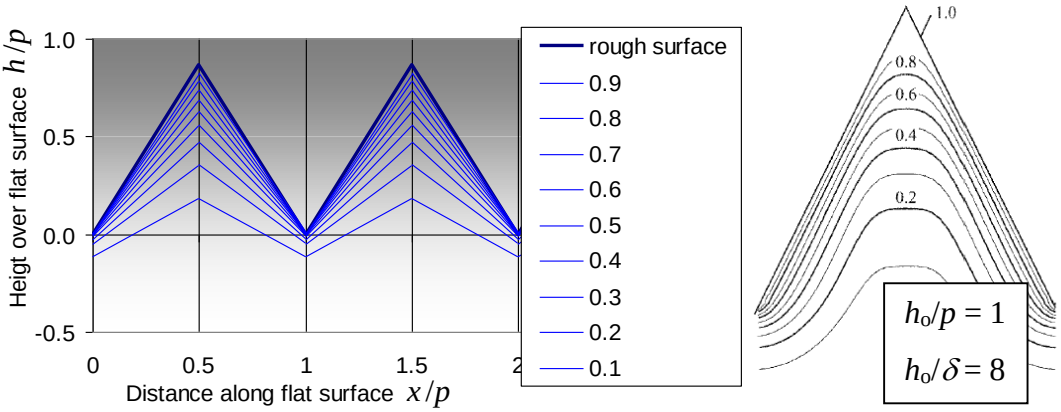

Figure 33*. Intensity contours inside the conductor. Left: relative current intensity in our model for equilateral triangular transverse grooves. Right: theoretical results of Matsushima [56] for the tangent magnetic field intensity.*

Bibliography chapter 2

[1] L. Austin and H. Starke. Ueber die Reflexion der Kathodenstrahlen und eine damit verbundene neue Erscheinung secundärer Emission. Annalen der Physik, 314(10):271–292, 1902.

[2] a) H. Bruining. Physics and Applications of Secondary Electron Emission: Pergamon Science Series: Electronics and Waves-a Series of Monographs. Pergamon, January 1962).

b) H. Bruining and J. H. De Boer. Secondary electron emission: Part I Secondary electron emission of metals. Physica, 5(1):17–30, 1938.

[3] Ludwig Reimer. Scanning Electron Microscopy. Physics of Image Formation and Microanalysis, Volume 45 1998, ISBN: 978-3-642-08372-3 (Print) 978-3-540-38967-5.

[4] A. J. Dekker, Secondary Electron Emission, in Solid State Physics (F. Seitz and D. Turnbull, Academic Press, 1958), Vol. 6, pp. 251-315.

[5] R. Cimino, L. A. Gonzalez, R. Larciprete, A. Di Gaspare, G. Iadarola, and G. Rumolo. Detailed investigation of the low energy secondary electron yield of technical Cu and its relevance for the LHC. Phys. Rev. ST Accel. Beams 18, 051002 – Published 18 May 2015.

[6] Egerton, Ray. Electron Energy-Loss Spectroscopy in the Electron Microscope (2011).

[7] S. Clerc, John R. Dennison, R. Hoffmann, J. Abbott. On The Computation of Secondary Electron Emission Models, IEEE Trans. on Plasma Sci., 34(5) October 2006, 2219-2225. DOI: 10.1109/TPS.2006.883379.

[8] Seiler, H., Secondary electron emission in scanning electron microscope, J. Appl. Phys.,54,1,R1-R18, 1983.

[9] Baglin, V., Bojko, J., Scheuerlein, C., Gröbner, O., Taborelli, M., Henrist, B., & Hilleret, N. (2000). The secondary electron yield of technical materials and its variation with surface treatments (No. LHC-Project-Report-433).

[10] R. Cimino, I. R. Collins, M. A. Furman, M. Pivi, F. Ruggiero, G. Rumolo, and F. Zimmermann. Can Low-Energy Electrons Affect High-Energy Physics Accelerators?. Phys. Rev. Lett. 93, 014801 – Published 29 June 2004.

[11] H. Bruining, "Physics and applications of secondary electron emission", Pergamon, 1954.

[12] A. N. Curren et al: NASA Technical Paper 2967, NTIS, Springfield, Virginia, USA (1990).

[13] A. Woode and B. Lloyd, (1993).

[14] S.Thomas and E.B.Pattinson: "The controlled preparation of low SEE surfaces by evaporation of metal films under high residual gas pressures", J. Phys. D: Appl. Phys., 3 (1970) 1469-1474-2.

[15] B. Wright and E. B. Pattinson: "Secondary electron emission from platinum-black-coated surfaces", J. Phys. D: Appl. Phys., 7 (1974) 1560-1565.

[16] P. Taneja, P. Ayyub, and R. Chandra: "Size dependence of the optical spectrum in nanocrystalline silver", Phys.Rev. B, 65 (2002) 245412-1-6.

[17] J. A. Dayton, Jr.: "A Review of the Suppression of Secondary Electron Emission from the Electrodes of Multistage Collectors", IEEE 18th Int. Symp. on Discharges and Electrical Insulation in Vacuum, Eindhoven, 1998.

[18] Scheuerlein C. et al, CERN-Thesis-2002-022, 10/02/1997.

[19] V. Baglin, J. Bojko, O. Gröbner, B. Henrist, N. Hilleret, C. Scheuerlein, and M. Taborelli: "The secondary electron yield of technical materials and its variation with surface treatments". Proceedings of EPAC2000, Vienna, Austria, 2000. LHC Proj. Rep. 433, LHC, CERN, Geneva, Switzerland.

[20] S. W. Lee, Y. J. Baik, C. J. Kang, and D. Jeon, "Suppression of secondary electrons from diamond by whisker formation", Appl. Surf. Sci., 215 (2003) 265–268

[21] G. Stupakov and M. Pivi, "Suppression of the effective secondary emission yield for a grooved metal surface", LCC-0145, SLAC-TN-04-045, Stanford, California, USA, Jun. 2004.

[22] M. Pivi, T. Raubenheimer, R. Kirby, F. LePimpec: "Electron simulations, experimental R&D work at SLAC and update on code benchmarking", International Linear Collider at Stanford Linear Accelerator Centre, Jun. 2005.

[23] M. Pivi: "Overview of Electron Cloud Studies and R&D for the International Linear Collider", ILC-American Workshop, International Linear Collider at Stanford Linear Accelerator Center, 13-15 Oct. 2004.

[24] J. Kawata et al: Jpn. J. Appl. Phys. 31 (1992) 1453.

[25] J. Kawata et al: J. Phys. Soc. Jpn. 63 (1994) 795.

[26] J. Kawata et al: J. Phys. Soc. Jpn. 63 (1994) 3907.

[27] K. Ohya et al: Jpn. J. Appl. Phys. 33 (1994) 1153.

[28] K. Nishimura et al: Jpn. J. Appl. Phys. 33 (1994) 4727.

[29] J. Kawata, K. Ohya, and K. Nishimura: "Simulation of secondary electron emission from rough surfaces". J. Nucl. Mater. 220–222 (1995) 997-1000.

[30] A. A. Krasnov: Vacuum, 73 (2004) 195.

[31] M. A. Furman and M. T. F. Pivi: Phys. Rev. S.T. Accel. Beams, **5** (2002) 124404

[32] J. de Lara, F. Pérez, M. Alfonseca, L. Galán, I. Montero, E. Román, and D. Raboso: "Multipactor prediction for on-board spacecraft rf equipment with the MEST software tool", IEEE Transactions on Plasma Science, 342 (2006) 476 - 484.

[33] M. Ye et al., Suppression of secondary electron yield by micro-porous array structure, J. Appl. Phys. 113, 074904 (2013).

[34] Meng Cao, Na Zhang, Tian-Cun Hu, Fang Wang and Wan-Zhao Cui, Secondary electron emission from rough metal surfaces: a multi-generation model, 2015, Journal of Physics D: Applied Physics, Volume 48, Number 5.

[35] European Cooperation for Space Standardization (ECSS), Space engineering multipactor design and test, ECSS-E-20-01A, rev 1 edition, March 2013.

[36] A. Woode & J. Petit, Diagnostic Investigations into the Multipactor Effect, Susceptibility Zone Measurements and Parameters Affecting A Discharge, ESTEC Working Paper 1556, November 1989.

[37] Abstract Book, Workshop on Multipaction and Passive Intermodulation Products Problems in Spacecraft Antennas, ESTEC, December 1990.

[38] Final Presentations & Working Meeting: Multipactor & PIM in Space RF Hardware, ESTEC, January 1993.

[39] A. J. Marrison, R. May, J.D. Sanders, A. D. Dyne, A. D. Rawlins, J. Petit, A study of Multipaction in Multicarrier RF Components, Report no AEA/ TYKB/31761/01/RP/05 Issue 1, January 1997.

[40] A. J. Hatch and H.B. Williams, J. Appl. Phys. 25, 417 (1954).

[41] A. J. Hatch and H.B. Williams, Phys. Rev. 112, 681 (1958).

[42] R. Woo, Multipacting Discharges between Coaxial Electrodes, J. Appl. Phys. 39, 1528----1533 , (1968).

[43] R. A. Kishek , Y. Y. Lau , L. K. Ang , A. Valfells and R. M. Gilgenbach "Multipactor discharge on metals and dielectrics: Historical review and recent theories", Phys. Plasmas, vol. 5, no. 5, pp.2120 -2126 1998.

[44] Hatch, A. J., Williams, H. B. 1954. "The Secondary Electron Resonance of Low-Pressure High-Frequency Gas Breakdown". Journal of Applied Physics, Vol 25, Num 4, April 1954.

[45] Vaugham, J. R. M. "Multipactor". IEEE Transactions on Electron Devices, Vol 35(7), pp.: 1172-1180, July 1988.

[46] Richard Udiljak, Multipactor in Low Pressure Gas and in Nonuniform RF Field Structures, Chalmers University.

[47] L. Galán, C. Morant, F. Rueda, J. M. Sanz, and J. Barbero. "Study of secondary emission properties of materials used for high power RF components in space". Final Repot, ESA-ESTEC Contract 6577/85/NL/PB, ESA (1987).

[48] L. Galán, P. Prieto, C. Morant, L. Soriano, and F. Rueda. "Study of secondary emission properties of materials used for high power RF components in space".

[49] F. Pérez, J. de Lara, L. Conde, M. Alfonseca, L. Galán, D. Raboso, "CEST and MEST: Tools for the simulation of radio frequency electric discharges in waveguides, Simulation Modelling Practice and Theory" , Volume 16, Issue 9, October 2008, Pages 1438-1452, ISSN 1569-190X, http://dx.doi.org/10.1016/j.simpat.2008.08.002.

[50] J. de Lara, F. Pérez, M. Alfonseca, L.Galán, I. Montero, E. Román, D. Raboso, Multipactor Prediction for On-Board Spacecraft RF Equipment with the MEST Software Tool. IEEE Transactions on Plasma Science, 34, Issue 2 (2006) 476 – 484.

[51] R. Collin, Field Theory of Guided Waves, 2nd edition. New York: IEEE Press, 1991.

[52] Book edited by Ahmed Kishk, "Electromagnetic Waves Propagation in Complex Matter", ISBN 978-953-307-445-0, July 5, 2011 under CC BY-NC-SA 3.0 license.

[53] M V Lukic, D S Filipovic: Modeling of 3-d surface roughness effects with application to μ-coaxial lines; IEEE transactions on microwave theory and techniques, 518-525 (2007).

[54] C. L. Holloway and E. F. Kuester, "Power loss associated with conducting and superconducting rough interfaces," IEEE Trans. Microw. Theory Tech., vol. 48, no. 10, pp. 1601–1610, Oct. 2000. [55] L Tsang, H Braunisch, R Ding, and X Gu: Random Rough Surface Effects on Wave Propagation in Interconnects, IEEE Transactions on Advanced Packaging, 33 (2010) 839-656.

[56] A. Matsushima and K. Nakata: Power loss and local surface impedance associated with conducting rough interfaces," Elect. Commun. Jpn., vol. 89, no. 1, pt. 2, pp. 1–10, Jan. 2006.

[57] E. Hammerstad and O. Jensen: Accurate models for microstrip computer-aided design. IEEE MTT-S Int. Microw. Symp. Dig., Washington, DC, May 1980, pp. 407–409.

[58] Quan Chen, Hoi Wai Choi, and Ngai Wong: Robust Simulation Methodology for Surface-Roughness Loss in Interconnect and Package Modelings. IEEE TRANSACTIONS ON COMPUTER-AIDED DESIGN OF INTEGRATED CIRCUITS AND SYSTEMS, VOL. 28, NO. 11, NOVEMBER 2009.

[59] Q. Chen and N. Wong: Efficient numerical modeling of random rough surface effects in interconnect resistance extraction. Int. J. Circ. Theor. Appl. 2009; 37:751–763

[60] M. Koledintseva, A. Koul, F. Zhou, J. Drewniak, S. Hinaga: Surface Impedance Approach to Calculate Loss in Rough Conductor Coated with Dielectric Layer. 978-1-4244-6307-7/10 ©2010 IEEE.

[61] Y. Shlepnev, C. Nwachukwu: Roughness Characterization for Interconnect Analysis. Simberian Inc., 8/18/2011.

[62] J.-F. Liu, F. L. Krawczyk, S. S. Kurennoy, D. L. Schrage, A. H. Shapiro, T. Tajima, R. L. Wood. RF SURFACE RESISTANCE OF COPPER-ON-BERYLLIUM AT CRYOGENIC TEMPERATURES MEASURED BY A 22-GHZ DEMOUNTABLE CAVITY. PAC2003, Portland, Oregon, May 12-16, 2003. LA-UR-03-3153.

[63] V. C. Nistor, L. Aguilera, I. Montero, D. Raboso, L A. González, L Soriano , L. Galán, U. Wochner, and D.Wolk., Strategies for Anti-Multipactor Coatings of Suppressed Secondary Emission and Low Insertion Losses for High Power RF Components in Satellite Systems. MULCOPIM 2011.

Chapter 3

Magnetron sputtering of structured copper

3.1 Background research on Structured Zone Model (SZM)

Black metals were firstly called when materials like Cu, Ag, Au, or Pt were deposited in the form of fine grains, at submicrometer scale, with the property of a new strong absorption of light, which modified strongly their normal colour, shifting often to a darker shade, even black [1]. For the high surface curvature of nanometric grains, light (a transversal wave) can interact strongly with the intense surface plasmons of metals (a longitudinal wave of the free electrons of the conducting band) [2], [3]. The science and technology of this phenomenon is called plasmonics. It is possible to generate in transmission or reflection all shades of colours using submicron structures in metals such as Cu, Ag, Au, etc. [4].

The growth by physical techniques of thin films, composed of separated vertical columns can often generate horizontal grain bunches with interesting properties. This kind of multiple submicron ´´blackbody´´ structures (cavities among columns) on the near surface of these materials are also found responsible for the alterations in the normal behaviour of not only with photons, but also in electron-matter interaction processes. Pioneers like Pattinson et al in the 1970s [1], were the first in reporting a suppression (strong reduction) of the secondary electron emission as a roughness effect. They implemented a flash thermal evaporation technique of deposition. This effect was also achieved over time employing other physical coating methods.

Sputtering deposition is a versatile physical vapour deposition (PVD) technique, widely implemented in the fabrication of structured thin films that offers the possibility of growing almost any type of metals and oxides on virtually any substrate. The coating mechanism is based on ejecting material by ion impact from an atom source called target onto a substrate, under ionized gas environment. The energetic bombardment of the

surface layers by ions or neutral particles produces an energy transfer and if the energy transferred to a lattice atom is greater than the binding energy, then clusters or individual atoms are released into vacuum. Under low pressure inert gas, plasma is generated and sustained by a high potential difference between anode and cathode (target). To maintain a good vacuum and clean residual gas, continuous pumping and flow of gas are used (differential pumping). A magnetic field can was used to confine secondary electrons on helical paths close to the target and increase thus the gas ionization efficiency. Many types of magnetron sources are available, from DC to RF, single/double anode, with pulsed/continuous operation, balanced/unbalanced, making PVD a versatile coating technique. Depending on the nature of each application and the materials involved, the overall conditions (pressure, substrate temperature, magnetron power, gas flow, deposition rate...) of the process should carefully be analyzed. In our case, the aim was focused on creating porous metal coatings of high aspect-ratio in relatively high inert gas pressure and low substrate temperature. Rich literature information on the growth mechanisms is available [5], [6], pointing at the 3D Volmer-Weber as the most frequent one for an early stage of island formation of metals on metals, which in specific conditions eventually lead to surface structures of diverse aspect-ratios, which is the goal of this study.

A structure zone empirical model (SZM) dominated by competition polycrystalline/amorphous growths was developed along the years [7], [8], and [9].

J.A. Thornton initiated this research in 1974. A more recent review on this subject can be found in [10].

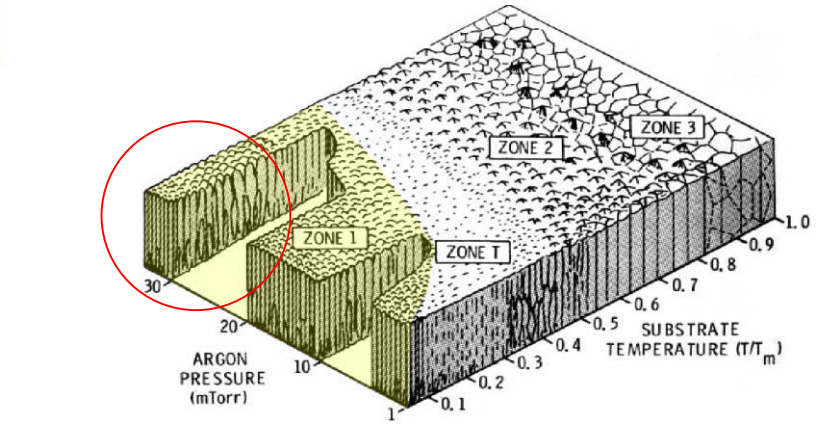

Figure 3.1. Thornton's zone diagram of growth structures: temperature - gas pressure diagram, *[7]. Zone of interest is Zone 1: porous or separate columnar growth. This type of growth is also strongly favoured by high growth rates.*

The low energy incoming atoms are confined close to the arriving spot, unable of bulk diffusion (needs high activation energy) or to desorb or coalesce on the surface, forming thus separated initial nuclei by surface diffusion which needs lower activation energy. This occurrence is an important consequence of atomic shadowing, acting in synchrony with the low adatom mobilities that characterize low T/T_m deposition. Its formation can be enhanced by the surface irregularities, favouring the columnar or fibred structures defined by voided open boundaries (oriented usually toward the atom source). In summary, the bunches or clusters of columnar grains (Fig. 3.1) are formed in conditions of only some surface diffusion (no bulk diffusion) and important influence of shadowing effects as well as substrate induced structure [10].

In our research, this model was a useful tool for predicting the nature of near surface morphology of copper thin films. However, the surface aspect ratio is not fully explained by the SZM. Zone 1, comprised the range of 1 to 30 mTorr (1.3×10^{-3} and 4×10^{-2} mbar) of sputtering gas pressure and $0.1 < T/T_m < 0.3$ (for Cu, $T_m = 1357.7$ K) was of particular interest, based on the premises that the grain spacing could act like a trap for secondary electrons. The temperature range of the substrates was set from a maximum of +407ºC (T/T_m = 0.3 at the Zone1 – ZoneT border) to close to negative values (-20 ºC corresponding to $T/T_m = 0.18$). It is also known that small changes in sputtering conditions can generate different types of grain sizes and interspacing, influencing the optical and electronic properties of the material (Fig.3.2).

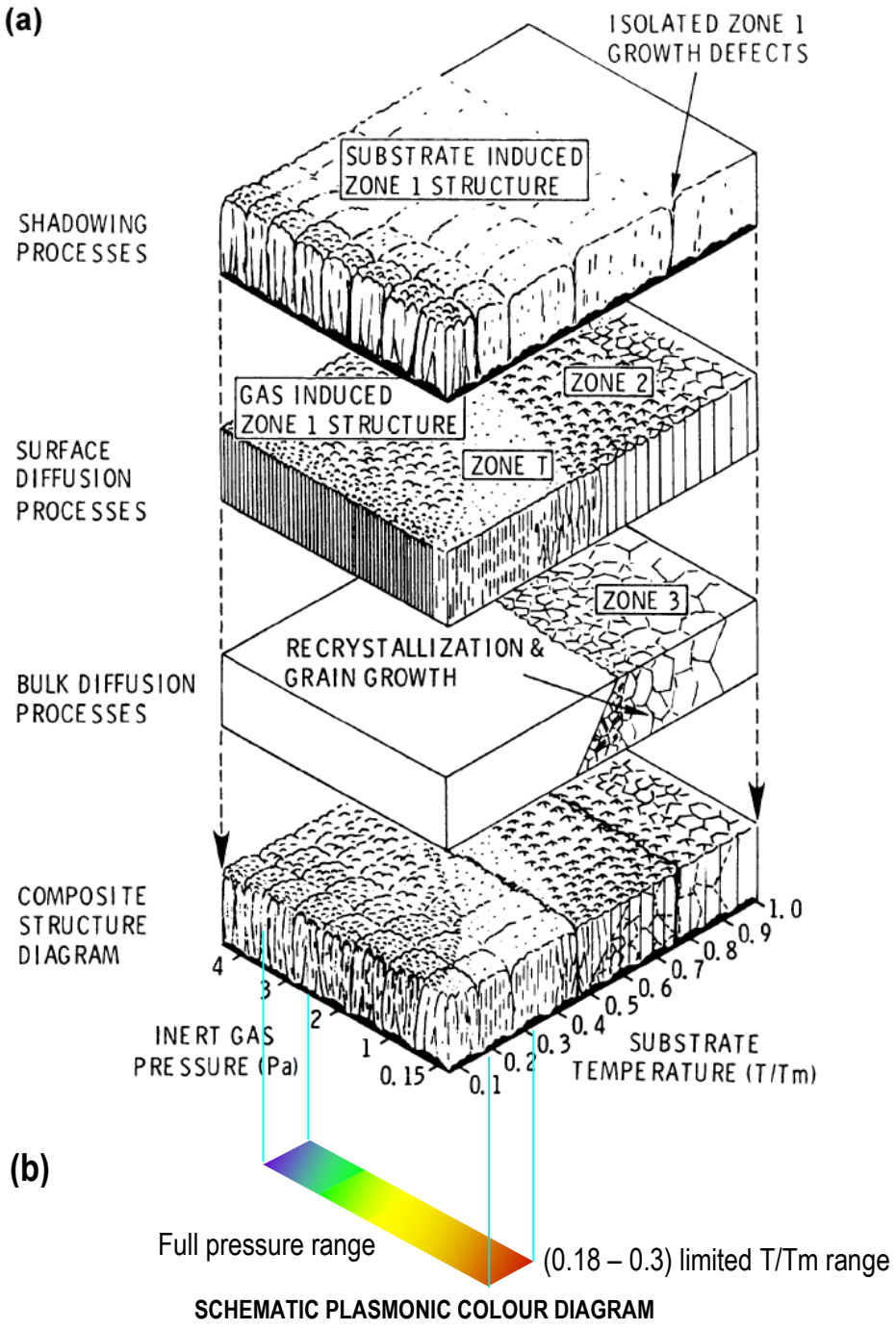

Figure 9-2 (a) Schematic representation of sputtered-film structures showing the superposition of shadowing, surface-diffusion, and bulk-diffusion processes that establish structural zones. (Reprinted with permission from Ref. 6, © 1977 Annual Reviews Inc.) (b) SZM for thick

Figure 3.2 (b) *Schematic representation of plasmonic colours resulting for 1 micron thick Cu films deposited by magnetron sputtering (our work).*

3.2. Experimental technique and setup

Figures 3.3 and 3.4 show the working principle and a picture of the experimental system for magnetron deposition of structured Cu films. The system generated a high power DC plasma confined magnetically over the Cu target thus producing by sputtering an intense Cu particle beam over the 25 cm diam. sample stage, holding several substrates of different sizes. The sample stage could be heated up to 400ºC by three halogen lamp heaters or cooled down up to – 20ºC by a stainless steel "cold finger" attached to copper sample holder, refrigerated by water or liquid nitrogen. A shutter allowed initiating deposition when conditions for a "black" deposition were achieved.

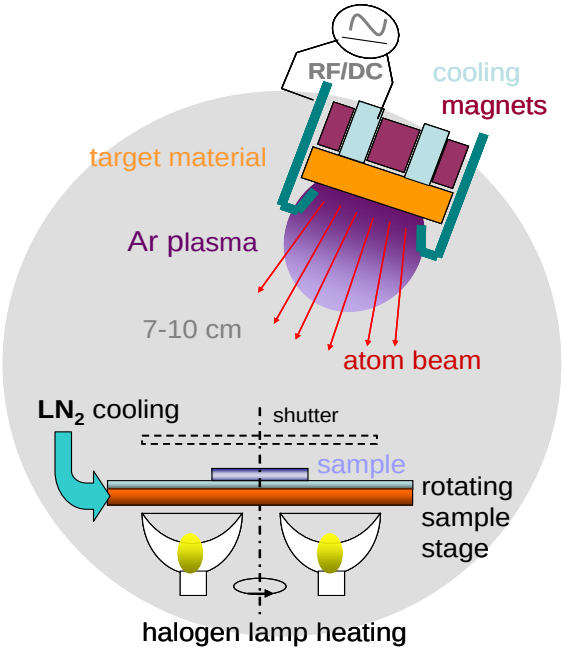

Figure 3.3. *Schematics of the copper magnetron sputtering system*

A total of 18 copper magnetron sputtering depositions (batches) from a target disc were performed using Ar as ionizing gas on different types of substrates. At room temperature some samples experienced adhesion problems and peeling-off effects, especially on Si wafer. For this reason, an approximately 1 micron thick first layer of normal smooth copper with good adherence was deposited before growing the structured columnar layer. Many combinations of growth rate (given by the magnetron power, gas pressure and substrate temperatures) were tested in order to obtain different levels of columnar packaging growth. The spacing between magnetron anode and cathode was varied from 0.25 to 0.75 mm, as well as the distance to the sample holder, from 7 to 10 cm, at an angle of arriving atoms set constantly at the "magic angle" 54.73° (Fig. 3.4). These geometric

changes allowed the mapping of the SZM in conditions of a stable plasma. The power applied to the plasma discharge ranged from 80 to 170 Watts, providing coatings with thicknesses between 0.8 μm and 2.7 μm, for different gas pressures.

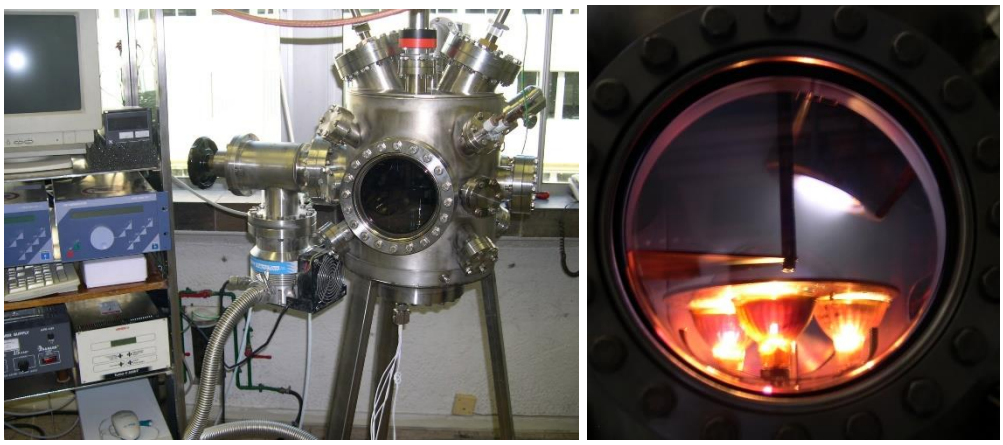

Figure 3.4. *Preparation chamber and geometrical setup*

The sputtering process can be improved by optimizing the pumping system in order to reach base pressures below 10E-7 mbar, improving thus the amount of initial residual gas, as well as the effects of film growths at lower than -20° C of substrate temperature.

3.3. Surface characterization

3.3.1 Optical analysis

The presence of sub-micron grains in an opaque metal film, with sizes smaller than the wavelength of incident light, leads to a wide variety of unexpected optical properties such as strongly enhanced transmission of light through the surface and wavelength filtering. These intriguing effects are now known to be due to the interaction of the light with electronic resonances at the surface of the metal film, and they can be controlled by adjusting the size and geometry of the grown structures [11]. This knowledge is opening up exciting new opportunities in applications ranging from sub wavelength optics and optoelectronics to chemical sensing and biophysics.

The samples in the picture of Fig.3.5 show the range of colours obtained by this technique. Although the brightness may differ from one type of substrate to another (glass, Si, Ag,

Cu, Al) the tone of colour is maintained for the samples coated under the same conditions. We observed that these colours are very stable in air; they are not modified even after years.

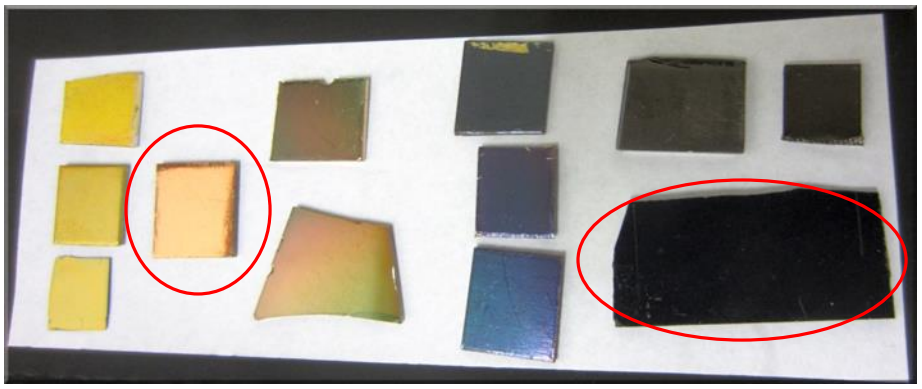

***Figure 3.5**. Visual aspect of several Cu coatings by magnetron sputtering, ranging from typical red for smooth films to dark tones for structured surfaces*

Figure 3.6 shows the typical reflectance spectra of different industrial metals with a non-structured technological surface [12]. Note that for copper, above 600 nm wavelength, the reflectance is over 80%, much higher than the experimental results we obtained and depicted in Fig. 3.7.

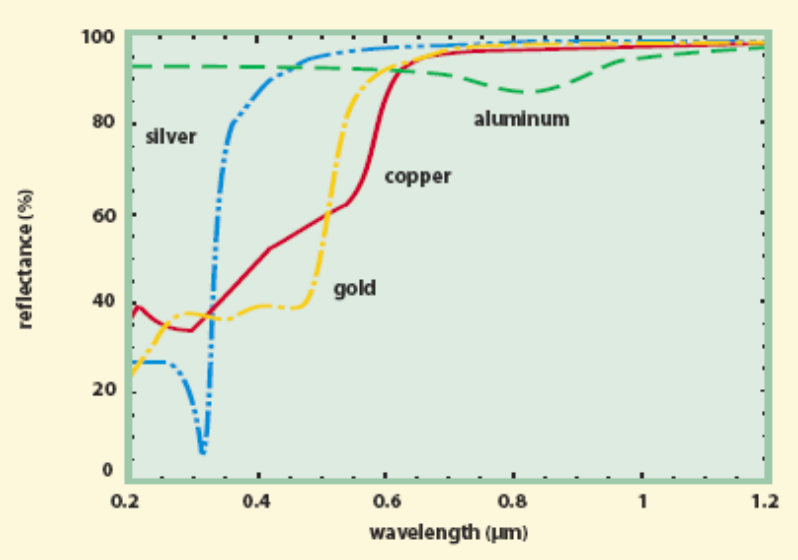

***Figure 3.6.** Typical reflectance of common non-structured metals with smooth surfaces [12]*

.

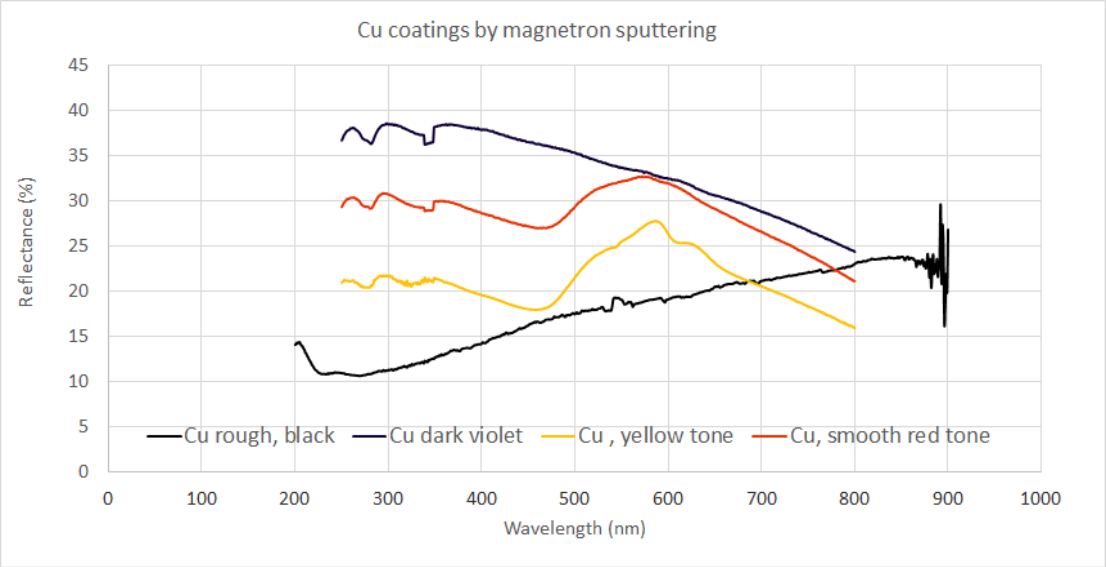

Figure 3.7. *Spectra showing the reflectance dependency of wavelength for thin Cu films grown by magnetron DC sputtering on Ag substrates*

The four analysed Cu films showed a reflectance lower than 40% in the UV and visible region with violet Cu having the highest reflectance, while the black copper had the lowest. The surface roughness of the films influences the reflectance spectra, and thus higher surface roughness gives rise to lower reflectance [13]. It was observed that the nature of the substrate influenced somewhat on the tone of colour and the brightness (for a given deposition batch). Therefore, the substrate influence a little on the morphology of the grown film; since no light is supposed to reach the substrate. This could be an explanation for a higher reflectance of the violet sample.

The yellow and red tone colour films have distinct characteristics in 480–700 nm range whereas the dark tone films do not exhibit such a peak in this wavelength range.

3.3.2. Scanning electron microscopy (SEM) analysis

Representative images of the surface morphology and the coating profile are presented in Fig.3.8 and Fig 3.9. Rough “black” Cu coatings were formed by columnar grains which grew uniformly, loosely packed or forming tight bunches loosely packed. The columnar layer thickness was about 1 μm.

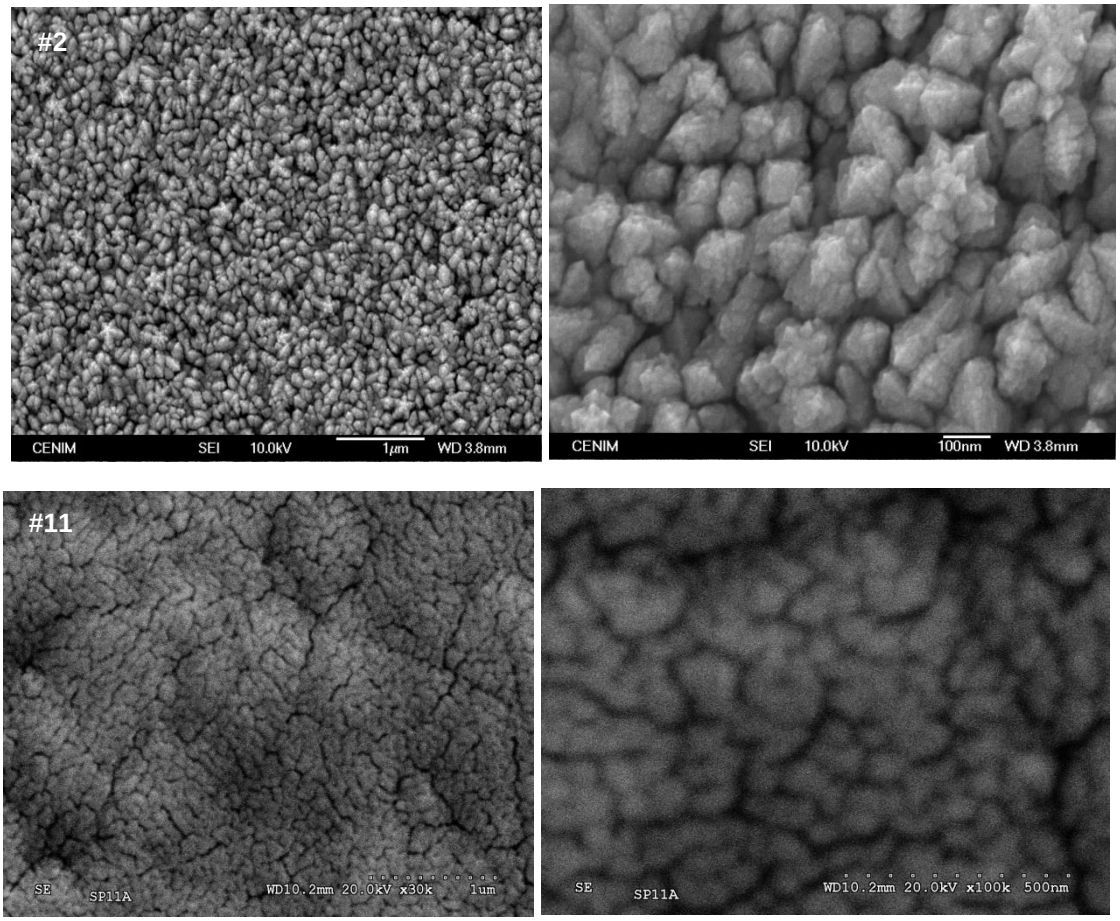

Figure 3.8. SEM images of the surface morphology of rough "black" Cu (magnetron sputtering). *Two representative samples with low SEY are presented showing the two types of growth of the columnar grains: uniform loose packing and tight bunching.*

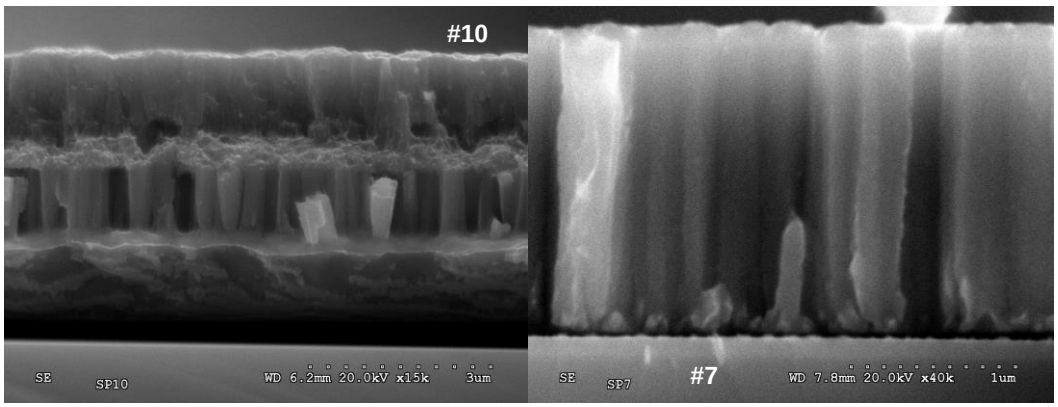

Figure 3.9 SEM images of the coating profile of rough "black" Cu (magnetron sputtering). *Two representative samples over single crystal Si were cleaved and their profile examined. They show a single layer columnar coating (right) and another of several layers: normal smooth over columnar growth*

Those SEM images show that the roughness of "black" Cu samples was of very small size. Examining all the SEM images obtained, the range of the lateral columnar grain size

was found to be 50 - 350 nm with an average size of 150 nm. The proportion of the (projected) surface area of the deep voids or gaps among the grains or bunches of grains (dark black area in SEM images) is supposed to be an important parameter of the SEY suppression properties of these coatings.

3.3.3 X-ray photon spectroscopy (XPS) analysis

The secondary emission yield of a material is highly sensitive to its surface properties. Factors such as the oxidation state, the degree of contamination and the surface morphology can generate a different response for the same type of bulk material. In order to determine which one is the dominant, an X-ray photoelectron spectroscopy (XPS) analysis of magnetron sputtering deposited copper coatings was performed. XPS, being a spectroscopy of emitted electrons, has an analysis depth somehow comparable to that of SEY. A XPS comparison among a structured black Cu and a smooth red Cu, both deposited by magnetron sputtering and exposed to the air for similar time, and a Goodfellow polycrystalline pure Cu foil cleaned one in vacuum by Ar^+ ion bombardment is shown in the above Figs. 3.10 b) , 3.11 and 3.12 . Fitting the XPS Cu $2p_{3/2,1/2}$ core level and XAES Cu $L_3V_{4,5}V_{4,5}$ valence band spectra with reference XPS and XAES spectra of pure clean CuO, Cu_2O, and Cu metal, should allow to estimate the amount of these chemical Cu states in the surface of the samples.

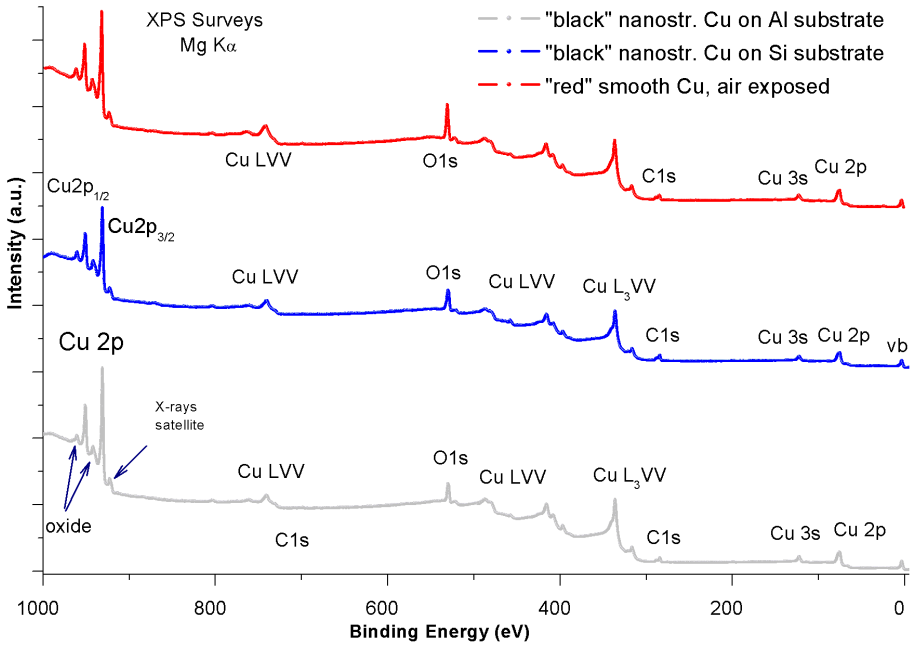

Figure 3.10 *a) XPS general spectra for flat and structured Cu surfaces, on 2 types of substrate*

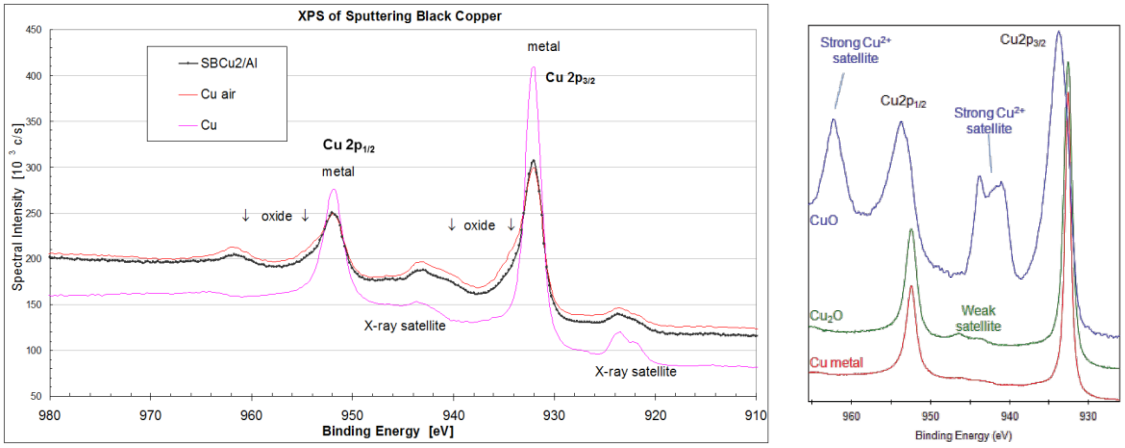

Figure 3.10b). *Comparison between experimental data (left) and literature reported data (right) of Cu 2p region, XPS Mgkα source*

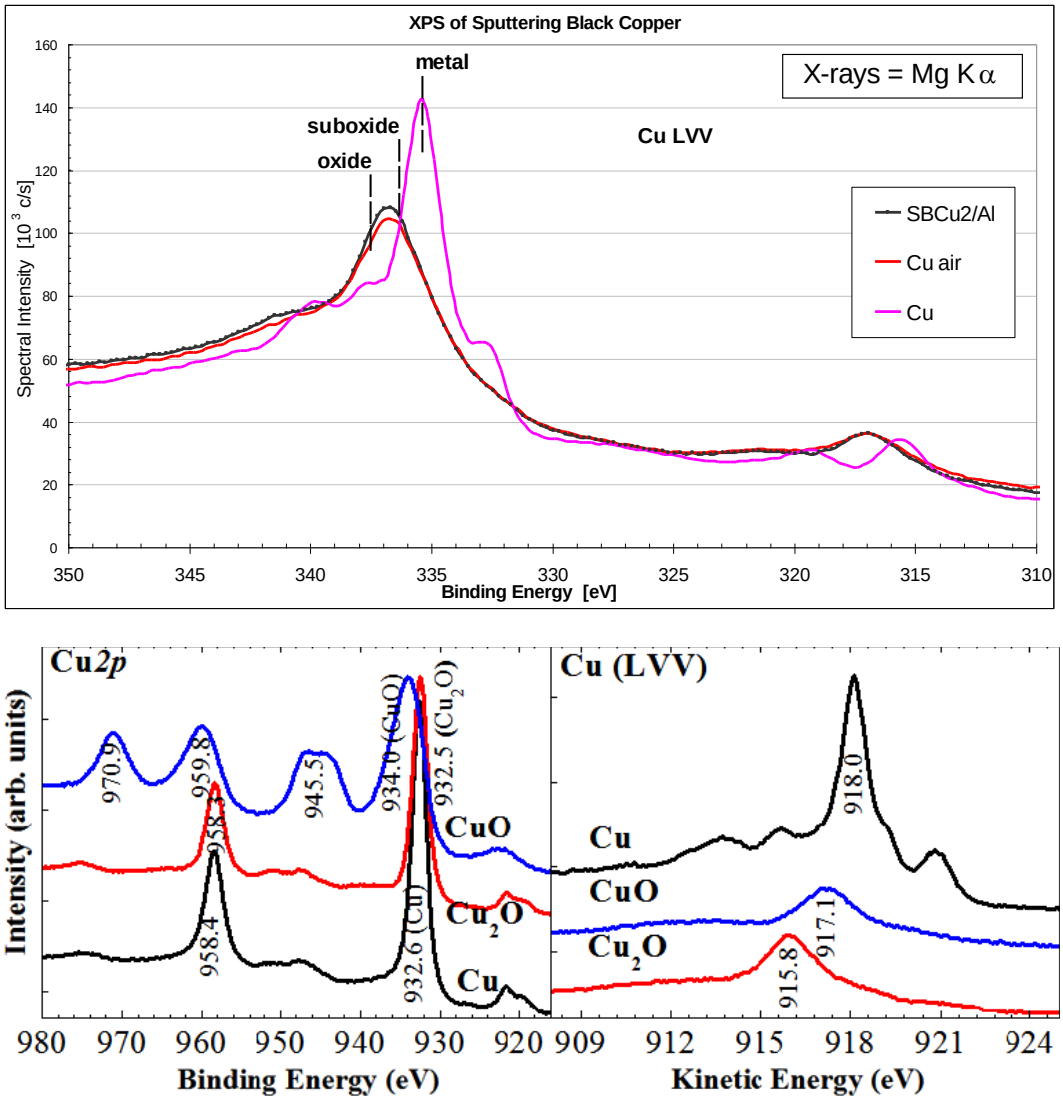

Figure 3.11. *Comparison with literature results on the Auger lines of experimental rough Cu (upper graph) and Cu oxide growth in oxygen pressure [14]*

However, without any detailed quantitative analysis, it is possible to observe that the oxidation states of both the rough and the smooth Cu samples deposited by magnetron sputtering were very similar and cannot explain their differences in SEE properties.

It is also obvious that both oxides are present since XPS Cu 2p spectra clearly show that the amount of Cu^{2+} is less than the sum of Cu^{1+} plus Cu^{0}, with a rough approximation of about 1/3 of it; while from the XAES Cu LVV it is also possible to infer that the amount of Cu^{0} is much less than the sum of Cu^{1+} plus Cu^{2+}, less than 1/10 of this. The "waving" of the Co^{0} spectrum looks in opposite phase to those of the oxidized samples! Thus, the thickness of the surface oxidized layer is at least twice the photoelectron mean free paths, about 4 nm. With more detailed analysis, it can be seen that the peak of the (Cu^{1+} + Cu^{2+})

structure in the XAES spectra is closer to the Cu^{1+} reference peak, indicating less amount of Cu^{2+}, let us say about 33 % of total oxidized layer.

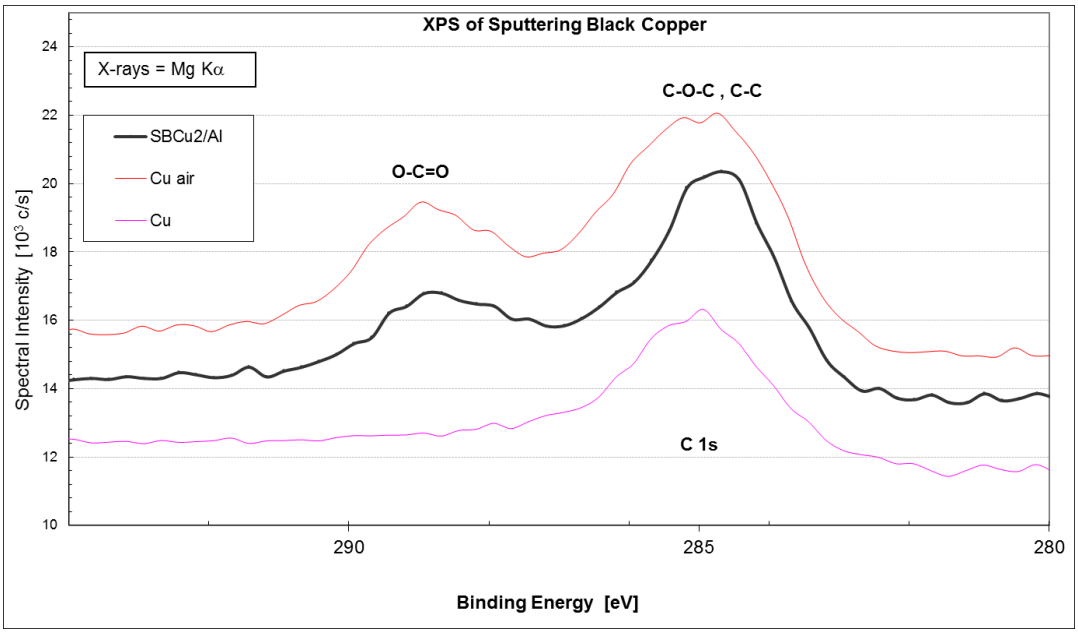

Figure 3.12. *The XPS C1s region of 3 types of Cu surfaces: structured (middle), smooth reference (up), both exposed to air and with lower intensity, the Ar^+ cleaned Cu*

All the samples were prepared in a vacuum poorer than UHV and exposed to air afterwards for a short time (minutes) before the XPS and SEY measurements in a different UHV system. As a consequence, the Cu samples adsorbed oxygen and carbon containing molecules on the surface. Fig.3.12. shows the carbon contamination state for the same above mentioned samples. Both magnetron Cu coated samples present the typical hydrocarbons components C-C, C-H, C-O, and C=O absorbed on the surface upon air exposure. The C-C graphitic carbons appear at 284.6 eV binding energy, while the C=O carbons generate a peak at 288.9 eV, in good agreement with the literature studies [14]. The higher-than-usual relative C=O component intensity indicates a possible contamination during magnetron sputtering deposition [15].

The same type of Cu coating on different substrates (Si, Ag, Al, Cu) placed on the same sample holder, were also measured by XPS. As expected, similar degree of contamination was found.

As a general conclusion, the "suppression" of SEY of the high-aspect-ratio structured samples deposited by magnetron cannot be attributed to the chemical nature of the surface of those samples.

3.3.4 Electron dispersive X-ray spectroscopy (EDX) measurements

The measurements were performed with an ESED detector INCAx-sight from Oxford Instruments with a resolution of 3 nm at 25kV and accelerating beam voltage of 0.3-30 kV. Compared with the XPS technique, the EDX offers information related to the chemical composition from a deeper bulk region of the sample, since the energy of excitation beam source and the electron escape volume are higher. The signal intensity depends mainly on the accelerating voltage and material density.

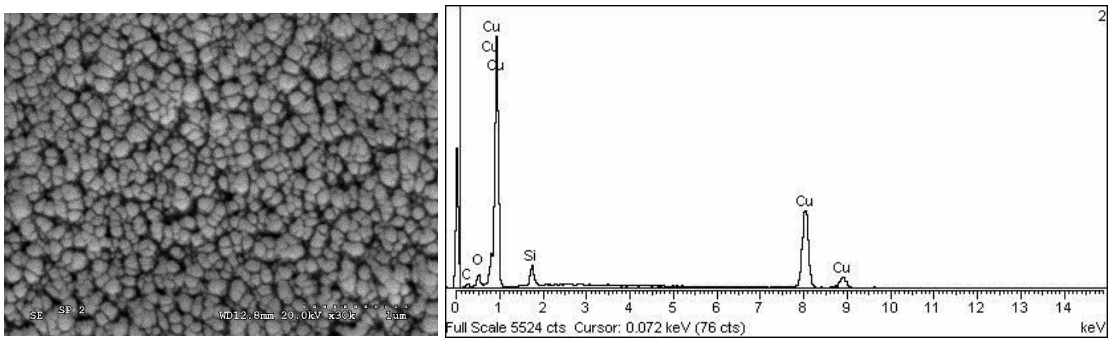

Figure 3.13. *EDX analysed area and element composition peaks for a 1.5 µm layer of magnetron sputtered Cu on Si wafer*

The results from an EDX spectrum of a rough thin film copper grown by magnetron sputtering on Si wafer show as expected (Fig.3.13), the presence of Cu, Si, O and C with no additional contaminants. The examined area of 3×3 µm was homogeneous. It was estimated that the penetration depth in the bulk (above 2 µm) was higher in this case than the thickness of the Cu layer, justifying thus the presence of the signal coming from the substrate material.

These results are in a good agreement and complement the XPS measurements.

In all the EDX measurements of different batches of Cu coating, the only detected elements were copper and the corresponding substrate.

3.3.5 Secondary electron yield (SEY) measurements

As described above, around 50 samples were prepared by sputtering magnetron with a variety of conditions resulting in a large variety of colours, surface morphologies, and SEY properties or parameters. However, an approximate or diffuse classification may be done. A class or group of samples, named *dark*, with dark black, grey, violet, or green hues, prepared according to zone 1 of SZM diagram in the extreme of high pressures

(p/Pa = 3 – 9 Pa, $T/T_m \sim 2$), with columnar grains loosely packed (with deep voids among them or strong high aspect ratio roughness), showed low SEY with some dispersion: σ_m = 1.25 ±0.10, E_1 = 165 ±20 eV. A second group of samples, named red, prepared according to zone T of SZM diagram (p/Pa ≈ 0.13 Pa, $T/T_m \approx 0.3$), with a smooth surface and normal Cu colour, showed typical high SEY of normal Cu exposed to the air, σ_m = 2.0 ±0.20, E_1 = 27 ±3 eV. Relative SEY dispersion for multipactor applications is $\Delta\sigma_m$ / (σ_m – 1). In a third group would be all the samples with an ample range of intermediate properties. This is reflected in the SEY summary of Fig. 3.14, best dark sample: green data, dark samples: red data, red samples: blue data; and other samples: between last two classes of data.

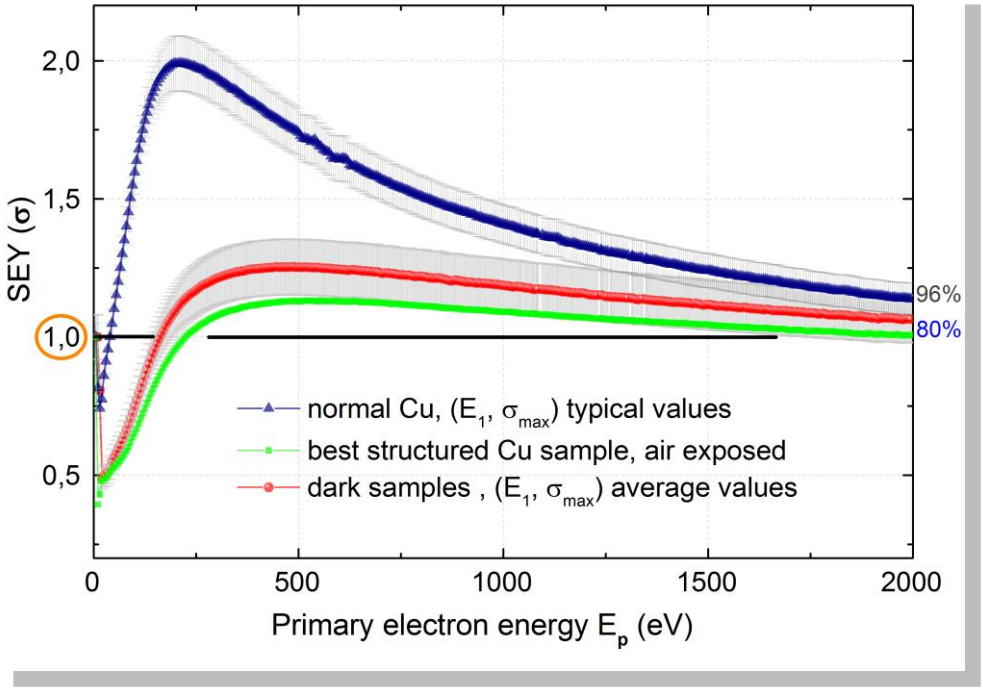

Figure 3.14. *Statistics of the average SEY coefficients for the Cu structured coatings; comparison with smooth reference sample after air exposure*

Table 1 summarizes the evolution of the σ_{max} coefficient, the E_1 - first cross-over energy, the E_m – energy for which the SEY is at a maximum value and the $\sigma_{2000} = \sigma(2000\text{eV})$ for several representative copper coatings.

Sample / colour tone / substrate	***Growth zone in SZM***	***E_1 (eV)***	***σ_m***	***E_m (eV)***	***σ_{2000}***
sp2 black , on Cu	Zone 1	195	**1.25**	600	1.09
sp11 violet, on Ag	Zone 1	212	**1.17**	580	1.04
sp11 violet, on Si	Zone 1	215	**1.13**	520	1.01
sp11 violet, on Cu	Zone 1	163	**1.24**	475	1.04
sp12 dark, on Cu	Zone 1	127	**1.33**	395	1.02
sp12 dark, on Ag	Zone 1	134	**1.29**	395	1.01
sp14 green, on Cu	Zone 1	129	**1.32**	358	1.04
sp13 dark red, on Cu	Zone 1	112	**1.36**	315	1.00
sp13 dark red on Ag	Zone 1	115	**1.34**	330	1.01
sp8 yellow, on Cu	Zone 1/Zone T	73	**1,67**	340	1,32
sp8 yellow, on Ag	Zone 1/Zone T	73	**1,63**	345	1,31
sp10 light red, on Cu	Zone 1/Zone T	46	**1.65**	240	1.15
sp9 light red, on Cu	Zone T	60	**1.75**	270	1.20
sp4 red, on Ag	Zone T	30	**1,99**	205	1,14
sp3 red, on Ag	Zone T	21	**2,42**	165	1,17

Table 1. Results of the SEY measurements on Cu samples of different colour tones

There seems to be a relative correlation between the maximum SEY values and the plasmonic colour diagram (see Fig.3.2.b) and Table1.). The lowest coefficients were obtained for the coatings grown under the Zone1 of the SZM conditions, with a dark appearance, while the ones located on the transition Zone1 – Zone T already exhibit a σ_{max} above 1.4. In particle accelerators and high power devices for space applications, the SEY > 1.3 is at the critical acceptance limit and known to be a threshold value for e-cloud formation and multipacting.

3.3.6 X-ray diffraction (XRD) analysis

Figure 3.15 shows the XRD pattern of the magnetron sputtered copper deposited under the conditions of Zone 1 of SZM. The pattern reveals that the coating is entirely polycrystalline.

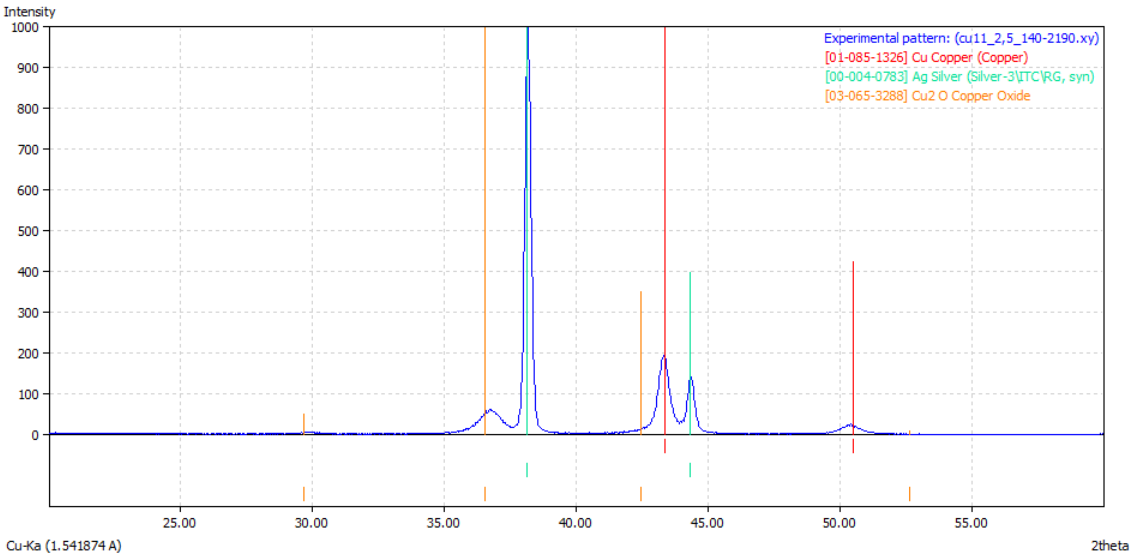

***Figure 3.15**. X-ray diffraction pattern of structured dark copper*

The peak detected at 2θ = 36.7° corresponds to the (111) plane of cubic- structured Cu_2O and another peak at 43.3° corresponding to the (111) plane of metallic copper. In addition, a minor peak at 2θ = 50.4° is observed and corresponds also to the (200) plane of metallic copper. The signal coming from the Ag substrate below the coating is also detected, since the penetration depth of the Cu- Kα (8.04keV) incident X-Rays was above 2.5μm.

Bibliography chapter 3

[1] S Thomas and E B Pattinson, Journal of Physics D: Applied Physics, Volume 3, Number 10. May 1970. The controlled preparation of low SEE surfaces by evaporation of metal films under high residual gas pressures.

[2] Shawn J. Tan, Lei Zhang, Di Zhu, Xiao Ming Goh, Ying Min Wang, Karthik Kumar, Cheng-Wei Qiu, and Joel K. W. Yang, NANO LETTERS, 2014, 14, 4023−4029. Plasmonic Color Palettes for Photorealistic Printing with Aluminum Nanostructures.

[3] Ting Xu1, 2, Yi-Kuei Wu1, Xiangang Luo2, L. Jay Guo1, Plasmonic nanoresonators for high-resolution colour filtering and spectral imaging Nature Communications. Volume: 1, Article number: 59. DOI: doi: 10.1038/ncomms1058, Published 24 August 2010.

[4] George H. Chan, Jing Zhao, Erin M. Hicks, George C. Schatz, and Richard P. Van Duyne, NANO LETTERS, 2007, Vol.7, No. 7, 1947-1952. Plasmonic Properties of Copper Nanoparticles Fabricated by Nanosphere Lithography.

[5] H. Brune, Surface Science Reports, (1998) 121-229- Elsevier. Growth and Properties of Ultrathin Epitaxial Layers.

[6] D. A. King, D. P. Woodruff 1997. Microscopic view of epitaxial metal growth: nucleation and aggregation.

[7] J.A.Thornton, J. Vac. Sci. Technol., 11 (1974) 666; J. Vac. Sci. Technol. A, 4 (1986) 3059.

[8] P.B.Barna and M. Adamik, Thin Solid Films, 317 (1998) 27. Fundamental structure forming phenomena of polycrystalline films and the structure zone models.

[9] I.Petrov, P. B.Barna, L.Hultman, and J.E.Greene: "Microstructural evolution during film growth", J. Vac. Sci. Technol. A, 21 (2003) S117-S128.

[10] Milton Ohring, (Second Edition) 2002, Academic Press. ISBN 0-12-524975-6.
Materials Science of Thin Films. Deposition and Structure. Chapter 9. Film Structure. 9.2 STRUCTURAL MORPHOLOGY OF DEPOSITED FILMS AND COATINGS. 9.2.1 STRUCTURE-ZONE MODELS FOR EVAPORATED AND SPUTTERED COATINGS.

[11] Hemant Kumar Raut, V. Anand Ganesh, A. Sreekumaran Nairand Seeram Ramakrishna, *Energy Environ. Sci.*, 2011, 4, 3779-3804, DOI**:** 10.1039/C1EE01297E, Anti-reflective coatings: A critical, in-depth review.

[12] Edward D. Palik, ed. (1998). Academic Press. Handbook of Optical Constants of Solids III.

[13] A. H. Jayatissa, K Guo and A. C. Jayasuriya. Applied Surface Science 255(23), 2009, 9474–9479. Fabrication of cuprous and cupric oxide thin films by heat treatment.

[14] Dahlang Tahir, Sven Tougaard, J. Phys.: Condens. Matter 24 (2012) 175002 (8pp), doi:10.1088/0953-8984/24/17/175002. Electronic and optical properties of Cu, CuO and Cu_2O studied by electron spectroscopy.

[15] I. Luciu, R. Bartali and N. Laidani J. Phys. D: Appl. Phys. 45 (2012) 345302 (9pp) doi:10.1088/0022-3727/45/34/345302. Influence of hydrogen addition to an Ar plasma on the structural properties of TiO2−*x* thin films deposited by RF sputtering.

[16] Chun-Lung Chu et al, Physica B 404 (2009) 4831–4834. Physical properties of copper oxide thin films prepared by dc reactive magnetron sputtering under different oxygen partial pressures

Chapter 4

Flash thermal direct evaporation (black metals)

Background

The abnormally low SEY of noble metals Cu, Ag, Au, Pt, when deposited as porous or granular thin films by "flash" evaporation in inert gas residual pressure is well known since several decades [1], [2] . These coatings show very dark colour hues and were usually referred to as black metals.

Vacuum thermal evaporation using resistive heating is a good option for metal coating. We used this technique to grow nanostructured silver on metallic substrates. The key parameters were high evaporation rate in (relatively) high-pressure inert atmosphere. However, with the available setup the darkest colour obtained was matt dark grey.

4.1 Technique description and experimental setup

The experimental arrangement and working principle are depicted in Fig. 1. Pure Ag (99.99% from Godfellows) was evaporated from a basket crucible of ∅ = 0.5 mm tungsten wire, by a rapid surge of electrical power (10-15 Amps × 12-8 V × 1-5 min) in a 0.7 mb (500 mTorr) of Ar residual pressure, over a substrate situated at approximately 7 cm distance (normal) to the atom source and at room temperature. The base pressure in the chamber was 2 - 3×10^{-8} mbar and several Ar gas purges were performed before reaching the optimum starting evaporation conditions (2 – 9×10^{-2} mb Ar). The rates of growth varied from 0.15 to 1.5 μg/cm^2/s and the conditions correspond to an extended Zone 1 of Thornton's SZM model [3], [4] where Ag, melting at 961.78 °C, is rapidly evaporated onto a relative cold substrate in form of packed grain bunches in conditions

of low atom mobility. The substrates were not deliberately heated and their temperature was only estimated. Then, the samples were outgassed in UHV at 300ºC for 1 h. It should be noticed that the pressure was far away of the range considered in the SZM model. Experiments showed that in low evaporation rate, low vapour pressure, and high substrate temperature conditions, the growth tendency changes towards a smooth surface. In exchange, a high rate of growth limits the grain coalescence.

Since the melting temperature of W is much higher than Ag, there is no risk of contamination.

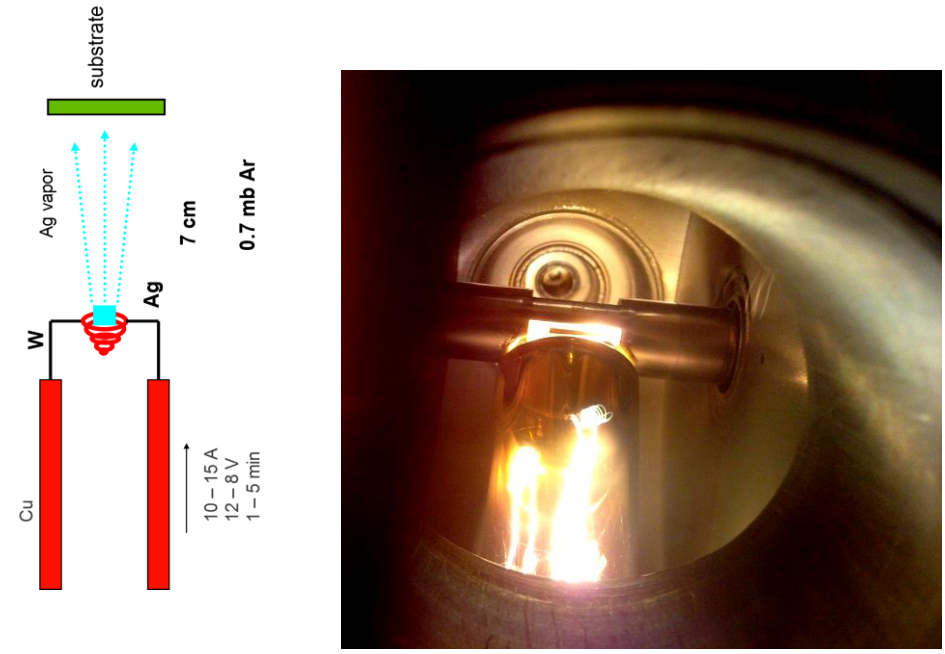

Figure 1. *Experimental arrangement - evaporation in relatively high pressure and at high rate.*

This technique is relatively simple to apply and only few parameters need adjustment to obtain the structured surface finish. Those experiments for evaluating the application potential of the technique were done with small samples and could be carried out *in situ* in the preparation chamber of the surface analysis system.

The conditions used for four representative samples are described below:

Sample #1: 30 min evaporation time, on Ag-plated aluminium (Tesat), visual appearance bright silver white, (Ar pressure close to 2×10^{-2} mb)

Sample #2: 3 minutes evaporation time, on pure Cu foil, light matt grey,

Sample #3: 1 minute evaporation time, over pure Cu foil, dark matt grey,

Sample #4: 5 minutes, on Ag-plated aluminium (Tesat), dark matt grey.

For the last 3 samples we used higher gas pressure and higher deposition rate.

4.2 Surface analysis

4.2.1 SEM/AFM analysis and SEY results

SEM images of the surface morphology for each of the 4 samples are presented in Figs. 2-5. Similar to the rough "black" Cu deposited by magnetron sputtering, columnar grains grew either uniformly and loosely packed, or forming tight bunches loosely packed.
In Fig.3 and 4, AFM images show less resolution and smoothed depth profiles due to very high aspect ratio of the surface roughness.

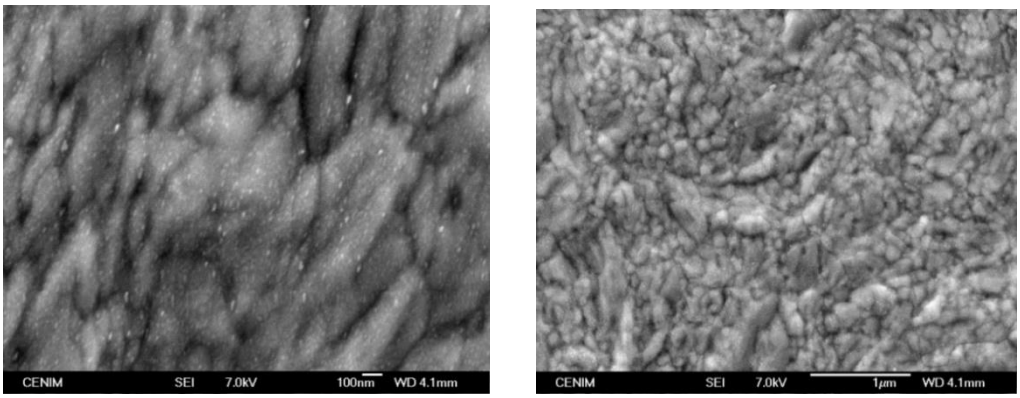

Figure.2 *SEM images of Ag by evaporation in relatively high pressure and at high rate, for sample #1, 30 min, over Ag, normal silver appearance. Grain size 30 nm, bunch size 150 nm.*

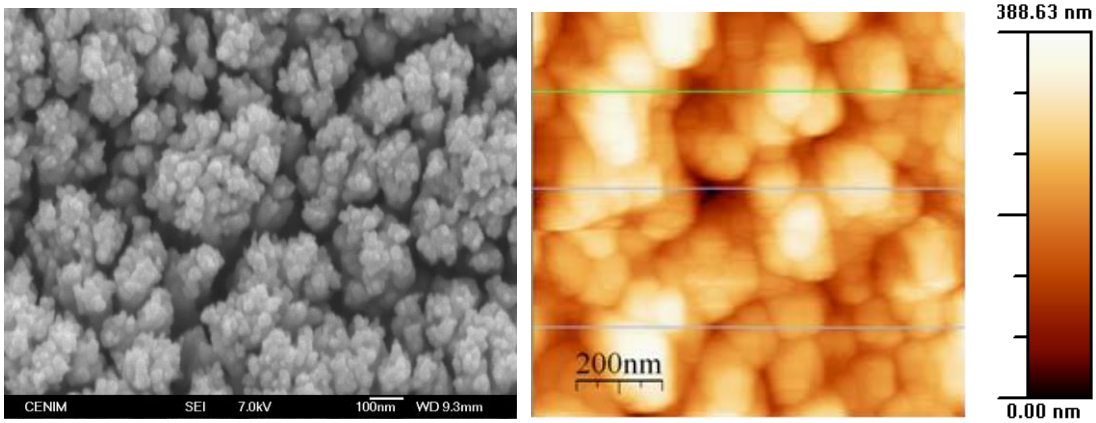

Figure.3 *SEM/AFM images of rough Ag by thermal evaporation in relatively high pressure and at high rate, sample #2, 3 min, on Cu, light matt grey. Grain size 30 nm, bunch size 350 nm.*

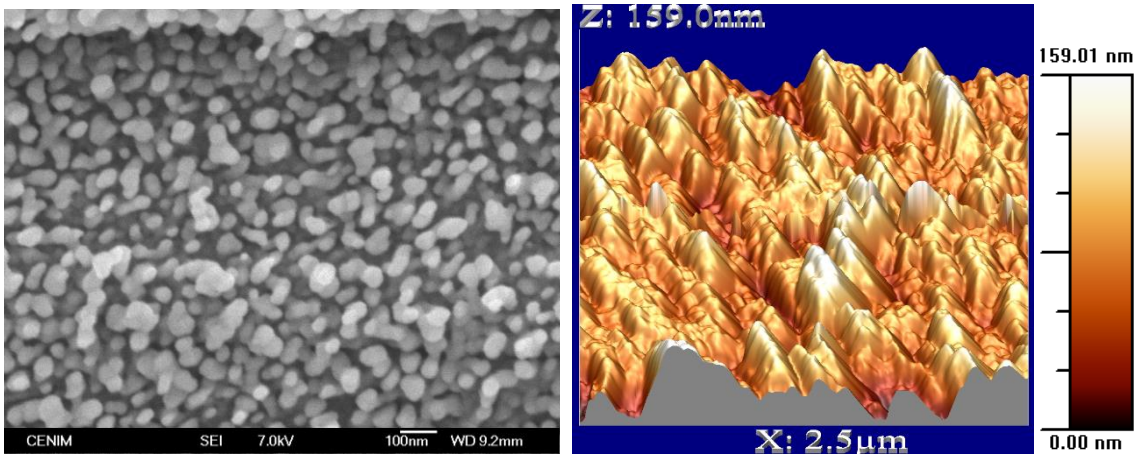

Figure.4 *SEM/AFM images of rough Ag #3 deposited by evaporation in relatively high pressure and at high rate, on right-3D profile from AFM image, sample #3, 1 min, over Cu, dark matt grey. Grain size 50 nm, bunch size 50 nm.*

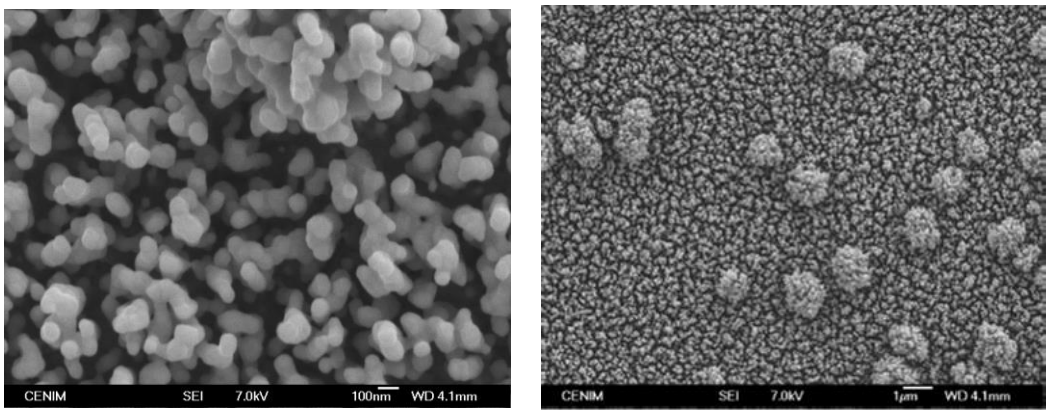

Figure.5 *SEM images of rough Ag #4 by evaporation in relatively high pressure and at high rate, sample #4, 5 min, over Ag, dark matt grey. Grain size 70 nm, bunch size 70 nm.*

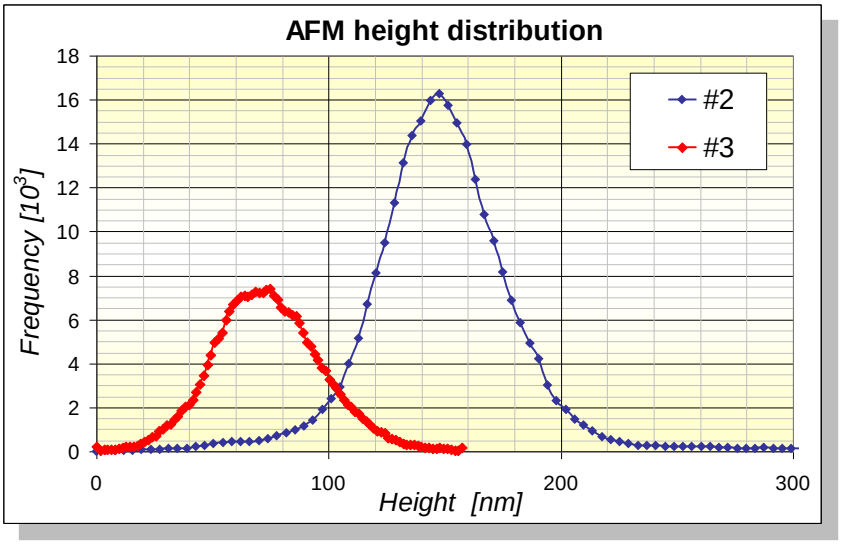

Figure 6. *Height distribution of grown structures, from AFM data for samples #2 and #3*

The silver coating follows the machining defects of the sample at microscopic level.

SEY analysis

The results of SEY measurements are presented in Fig.7 and Table I. They show that SEY suppression was due to surface roughness of high aspect ratio. They show also some relation with pore/hole area (darker area in the SEM images).

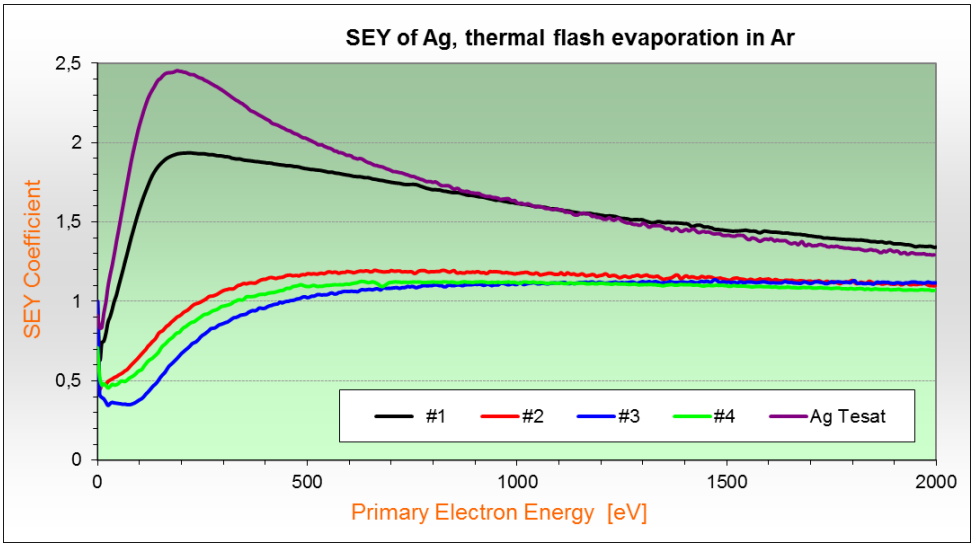

Figure 7. *SEY of the four rough Ag coatings in situ, grown by flash evaporation compared to a reference sample exposed to air (Tesat)*

Sample	substrate	Pressure [mb]	Coating time [min]	E_1 (eV)	σ_m	E_m (eV)	σ_{2000}
#1 - white	Ag	< 0.5	30	45	1.94	215	1.34
#2 - mate grey	Cu	> 0.5	3	255	1.21	820	1.15
#3 – dark grey	Cu	> 0.5	1	430	1.14	1470	1.14
#4 - mate grey	Ag	> 0.5	5	331	1.13	770	1.07

Table I. *SEY of rough Ag surfaces deposited by flash evaporation in relatively high pressure and at high rate for the representative samples*

There is an interesting observation on SEY of rough surfaces of high aspect ratio which is quite general but it is clear in these experimental data. The SEY curve shows a wide minimum at low primary energies but higher than 15 eV. This does not appear in clean metals or in metals exposed to the atmospheric air. This minimum is not an artefact of the

SEY measuring apparatus since this energy region is measured without problems in those smooth flat surfaces. The SEY suppression effect of surface roughness increases with decreasing primary energy until this energy is smaller than a certain energy (about 50 eV for these samples) and then it decreases with decreasing energy.

4.2.2 X-ray photon spectroscopy (XPS) measurements and results

A pure industrial silver reference sample (manufacturer Goodfellows) was bombarded by Ar^+ ions with energies of 2.5 KeV, under vacuum conditions, and compared with a silver coated sample, by thermal flash evaporation exposed to air (sample #4). The results are depicted in Fig. 8. No additional contaminants were found on the surface, apart from the usual C-H, C-O carbon species and oxygen. Furthermore, a closer look at the position and symmetry of the Ag 3d double peak, 5/2 and 3/2 for the coated sample showed the presence of superficial AgO and Ag_2O oxides. The peaks are shifted by approximately 0.5 eV with respect to the metal silver bindings of the clean sample, towards higher binding energies, also reported in literature studies [5].

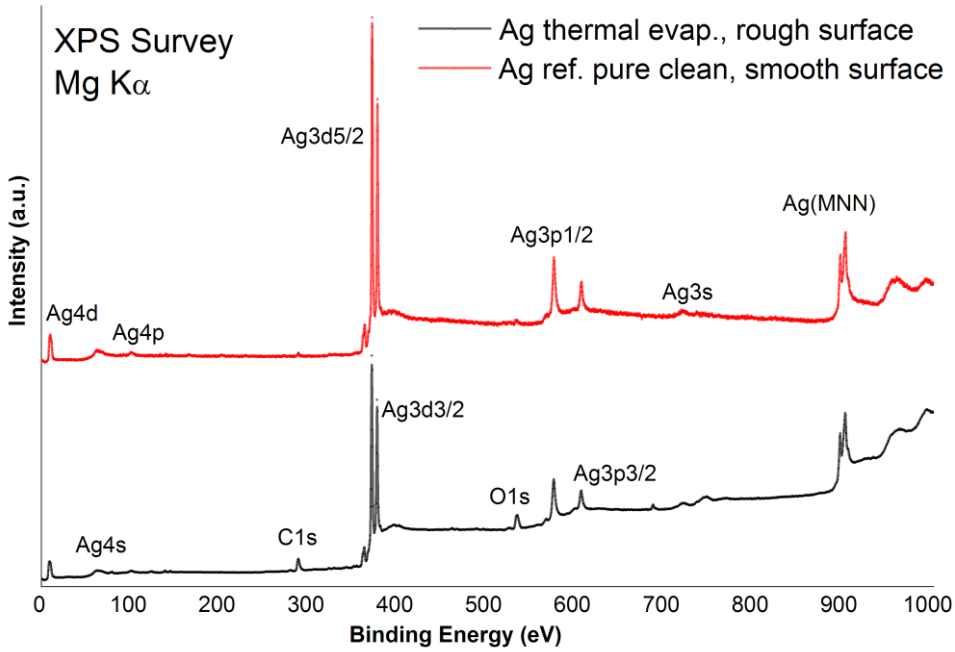

Figure 8. *XPS general spectra comparing an ion etched Ag surface and Ag coating by flash thermal evaporation*

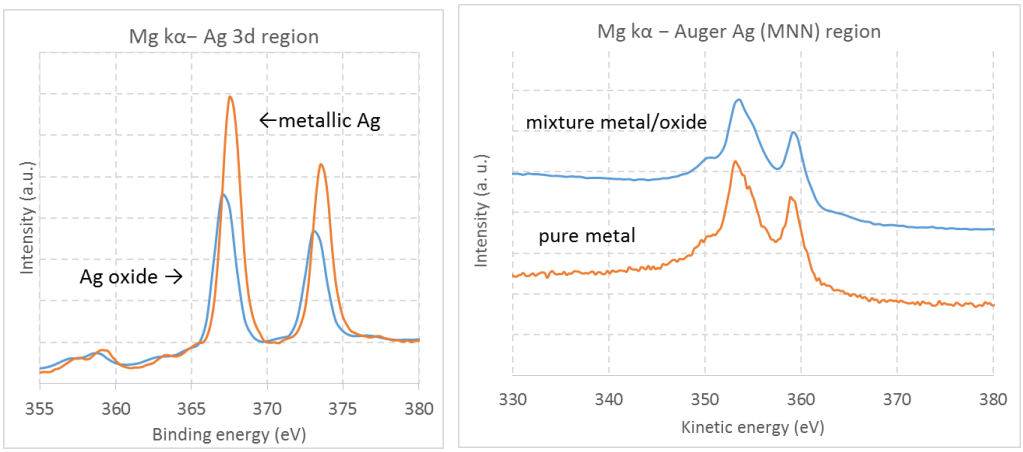

Figure 9. *XPS spectra of Ag 3d region (left) and Auger (MNN)-right, regions for ion etched Ag surface and Ag coating by flash thermal evaporation*

The Auger Ag (MNN) region of clean Ag is dominated by metal bonds while for the thermal evaporated silver, the peak at 353.6 eV indicates the presence of a mixture of AgO and Ag_2O oxides. However the shape of the silver Auger line indicates that Ag_2O component is dominant.

4.2.3. Aging effects and recovery of the surface properties

The effect of air exposure on SEY of rough silver is shown in Figs.10 and 11. The SEY coefficient increased mainly at low primary energies and the figure of merit $FoM = (E_1/\sigma_m)^{1/2}$ decreased from 20 to 5 in 4 months in the case of the sample #3. The initial σ_m is similar for both samples and the aging effects were measured after 2 months for sample #4 and after 4 months for sample #3.

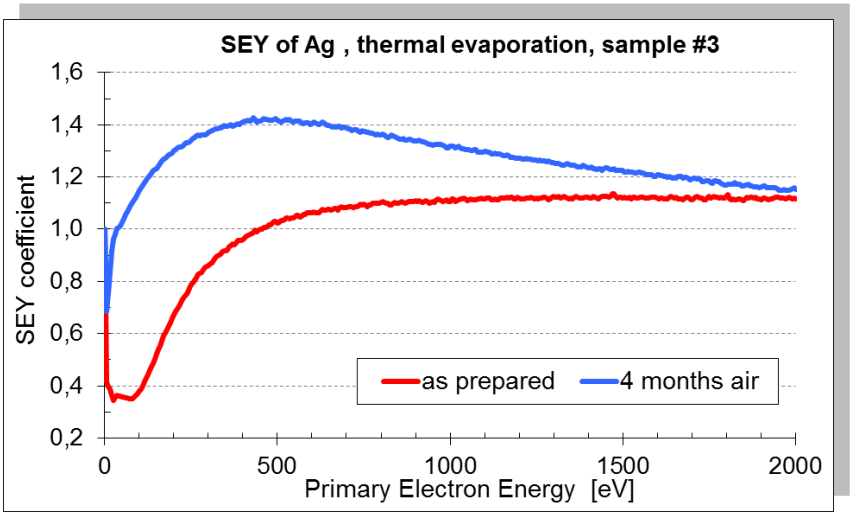

Figure 10. *Effect of air exposure on SEY of rough Ag #3 flash evaporated.*

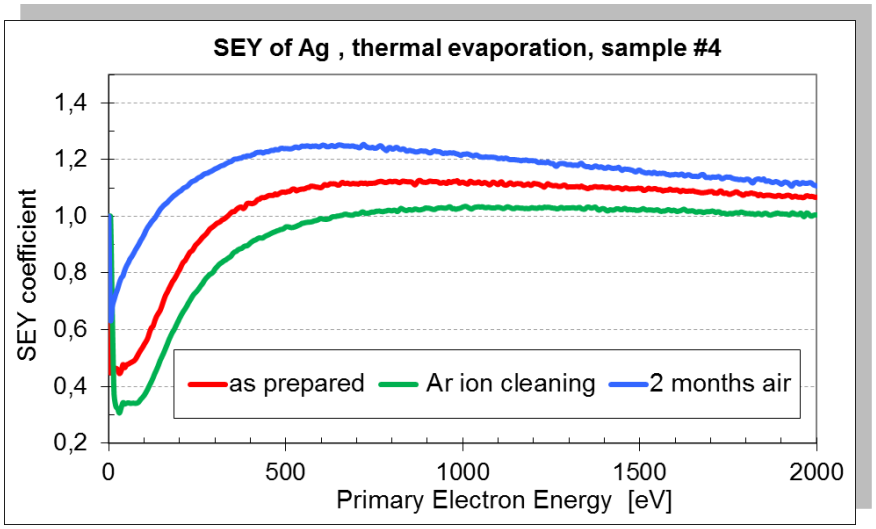

Figure 11. *Effect of air exposure on SEY of rough Ag #4 flash evaporated. The lowest value corresponds to Ar ion cleaning under vacuum.*

For sample Ag#4, a cleaning with Ar ions with energy of 2500eV was also performed in order to remove the contamination and the oxide layer and then measured again. The maximum SEY decreased close to 1, even lower than the initial value.

4.3 Conclusions

Flash evaporation of Ag over Ag plating substrates is a simple and low-cost technique to produce nanostructured Ag surfaces of high aspect ratio which deserve further research for anti-multipactor coatings applications.

Questions to be studied are: aging and passivating overlayers, RF surface resistance, and adherence to the substrate.

This research was not pursued further for wave guides because, at that point in time, the importance of the size scale and RF surface resistance was not yet a pressing requirement from the industrial community. And also because other techniques, the chemical etching and magnetron sputtering, showed better potential advantages.

Bibliography chapter 4

[1] S.Thomas and E.B.Pattinson, "The controlled preparation of low SEE surfaces by evaporation of metal films under high residual gas pressures", J. Phys. D: Appl. Phys., 3 (1970) 1469-1474-2

[2] B. Wright and E. B. Pattinson: "Secondary electron emission from platinum-black-coated surfaces", J. Phys. D: Appl. Phys., 7 (1974) 1560-1565.

[3] P.B.Barna and M. Adamik, Thin Solid Films, 317 (1998) 27. Fundamental structure forming phenomena of polycrystalline films and the structure zone models.

[4] J.A.Thornton, J. Vac. Sci. Technol., 11 (1974) 666; J. Vac. Sci. Technol. A, 4 (1986) 3059.

[5] A.M. Ferraria, A.P. Carapeto, A.M. Botelho do Rego, Vacuum, 86 (2012) 1988-1991.

Chapter 5

Nano-structured surfaces by masked preferential ion sputtering

5.1 Background research

The production of deeply textured surfaces by this ion bombardment technique is based on the fast etching by ion bombardment of a substrate of low cohesive energy (high sputtering yield) or "soft" while a metal of high cohesive energy (low sputtering yield) or "hard", is simultaneously deposited on the surface by sputtering using the same ion beam, under vacuum conditions.

Samples of gold and silver with a deeply structured surface were prepared using the original technique of A. N. Curren (NASA) [1] designed for a similar purpose. This technique requires a wide-diameter high-intensity ion beam under UHV conditions and a special geometric setup.

In the reference experiment [1], Cu and Mo were used respectively. The essential arrangements and working concept for this technique are depicted in Fig.1.

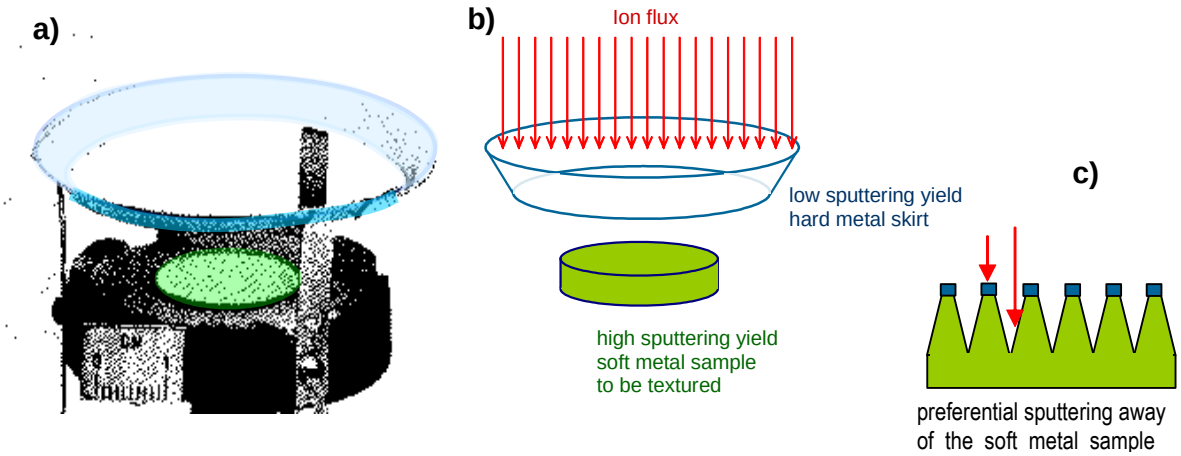

Figure 2. *Essential experimental arrangement and working concept of mask sputtering for deep texturing of metal surfaces*

In the step a) the sample holder with a Cu sample and Mo conical skirt (masking source or target); in b) an intense Ar ion flux sputters out (evaporates) both Mo from the skirt and Cu from the sample; and, c) Mo falls on the Cu surface forming small clusters protecting it from sputtering, and preferential Ar ion sputtering away of unprotected Cu atoms etches deeply the sample surface.

This technique offered a new perspective on the structuring process of the two most important, in our case, conductive metals Au and Ag. The dynamics of growth is not a subject of study as much as the results itself. Even so, many trials were done to achieve a suitable balance between the aspect ratio and the surface resistance.

This technique has recently been *rediscovered* and thoroughly investigated in several of its variants or modes as Ion Etch Masking, Masking Sputtering, Surfactant Sputtering, or Dual Ion Beam Sputtering [2-4].

However, in most of those works, the *mask*, *surfactant*, or *seed* was the soft metal.

5.2 Evaluation of material type

The effective treated area depends mainly on the ion beam size, the geometry of the mask source (total exposed surface and the angle of incidence) and its distance to the sample. Since the ion bombardment is performed simultaneously on two different materials, another important condition to achieve a structured coating is the ratio of their sputtering yields.

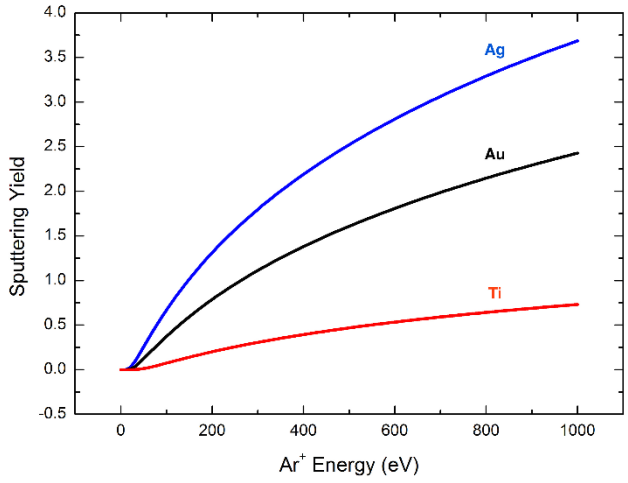

Figure 2**. Relative* **sputtering yield dependency on Ar^+ ion energy [5, 6]*

Since Ag and Au were preferred to Cu for our applications, it was necessary to find out if this technique will work with those metals. Also, the nature of the gas (He, Ne, Ar, or Xe) can be optimized. For this, we considered two criteria: i) the ratio of the sputtering yield of Ag (Au) to that of the mask metal M using ions of noble gas X, $Y_X(Ag)/Y_X(M) \geq Y_{Ar}(Cu)/Y_X(Mo)$ to ensure conditions for preferential sputtering, and ii) to have into account the relative sputtering rate, given by $Y_X(Ag)/Y_{Ar}(Cu)$, in the combined criterion $[Y_X(Ag)/Y_{Ar}(Cu)][Y_X(Ag)/Y_X(M)]$ to ensure that texturing will be sufficiently fast. The ion energy can also be taken into account; it was 1 keV for the reference: Cu, Mo, Ar, [1]. The sputtering yields [5, 6] and the values of both criteria are given in the Appendix below. From the study of these data, several conclusions are obtained:

- Sputtering yields increase with ion energy strongly and compensate a slight decrease of preferential effect, therefore always is better to use the higher ion energy compatible with a high ion flux for the particular ion gun used.
- It is always better to use ions of higher mass: Xe better than Ar. For Ag and Au both, preferential effect and sputtering rate, increase with ion mass; and for Cu and lighter metals, and the preferential effect decrease slightly with ion mass but is compensated by the much higher sputtering rate.
- For masking metal the preferences are for: C, Sc, Si, Ti, Zr, Y, Ta, W, La, Ce, Ca, Re, and Mo, in decreasing order. If we keep to common less-oxidized metals: Ti, Zr, Ta, and W.
- Using Ti as masking metal, Xe as ion, and ≥ 1 keV ion energy, the conditions are much better than those of reference experiment [1]. With Ar and 1 keV, we are still in better conditions. See Table I for some relative values of criteria (i) and (ii).

Table I. Relative mask sputtering yields ratios for preferential sputtering of substrate

	Reference	Case of Cu	Case of Ag	Case of Au	Case of Au	Case of Au
Base metal	Cu	Cu	Ag	Au	Au	Au
Masking metal	Mo	Ti	Ti	Ti	Ti	Ti
Sputtering ion	Ar	Xe	Xe	Xe	Xe	Ar
Energy [keV]	1	1	1	1	2	1
Yield Ratio I*	1	1.36	2.36	2.44	2.17	1.77
Yield Ratio II**	1	1.47	4.42	4.72	6.32	2.08

(*) $Y_X(B)/Y_X(M)$, (**) $[Y_X(B)/Y_{Ar}(Cu)][Y_X(B)/Y_X(M)]$. See Appendix

The suitable chosen combination of materials in our experiments was Ti and Mo as hard metals and Ag and Au as soft metal substrates, sputtered in Ar^+ environment.

5.3 Preparation technique and experimental setups

The original setup was modified to fulfil basic requirements of sample processed area, the degree of structuring, homogeneity and impurity content of metals used as protective `seeds`. The type of ion gun used was Commonwelth Scientific Co. Kaufmann-type mod.2a, with 3 cm beam size and with correlated sized mask targets. In addition, the geometry of the cone was also optimized in order to generate minimum quantities of hard metal that could limit the resistive properties of the final coating, since a larger surface generates more deposited atoms.

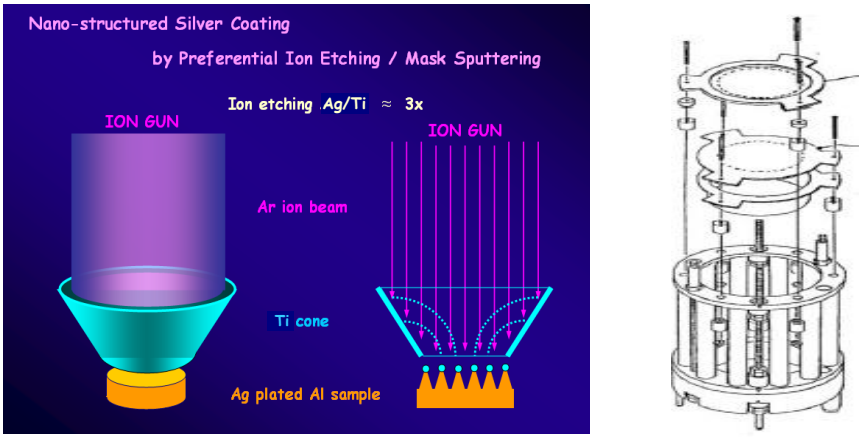

Figure 3. *The working principle of ion etching assisted by mask sputtering for small sized samples and the schematic of the disassembled ion gun*

The first experimental setup for samples with dimensions below 100 mm^2 was used to structure a Au-plated aluminium sample of 5 µm initial Au thickness from Tesat Spacecom. The sample was set in this case on the base of a truncated cone, made of pure Ti foil (25 µm thick, from Goodfellow). This sample-Ti-cone assembly was set in the centre of the 3 cm ion beam of the ion gun as depicted in Fig.3.

The Ar^+ ion beam sputtered Ti over the Au surface and simultaneously sputtered away Au from the unmasked exposed substrate. The working conditions of the process were the following: a base pressure of 10^{-9} mbar, a constant energy of impinging ions of 650

eV, the ion current of 15 mA with incidence angle of 10º to surface normal, the total sputtering time of 30 minutes and an Ar^+ pressure of 10^{-4} mbar. A general view of the UHV system is depicted in Fig. 4.

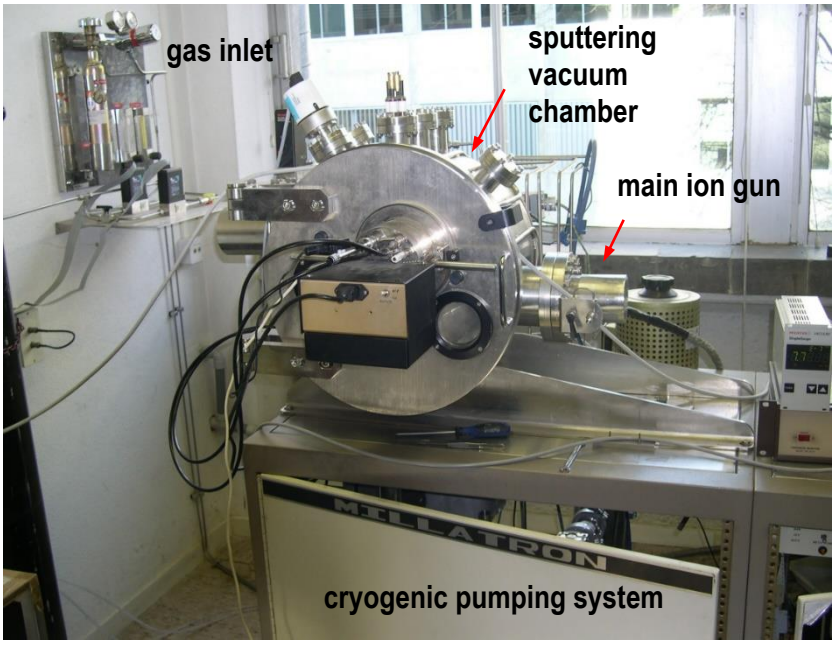

Figure 4. *Double ion beam sputtering system, Millatron, Commonwealth Scientific Corporation used for mask ion etching of gold, small sample sizes*

The double ion beam sputtering apparatus was a Kaufmann-type low-energy high-intensity ion source (maximum performance at 20 mA × 1 kV), assisted by a cryogenic pumping system.

The limitations in sample size and geometry set by this system led to the use of an improved system. In Fig. 5, the same ion gun of 3 cm beam size was set up on a different UHV system, with regulating sample positioning, larger rotating sample stage for wave guide housing and normal beam to sample incidence angle.

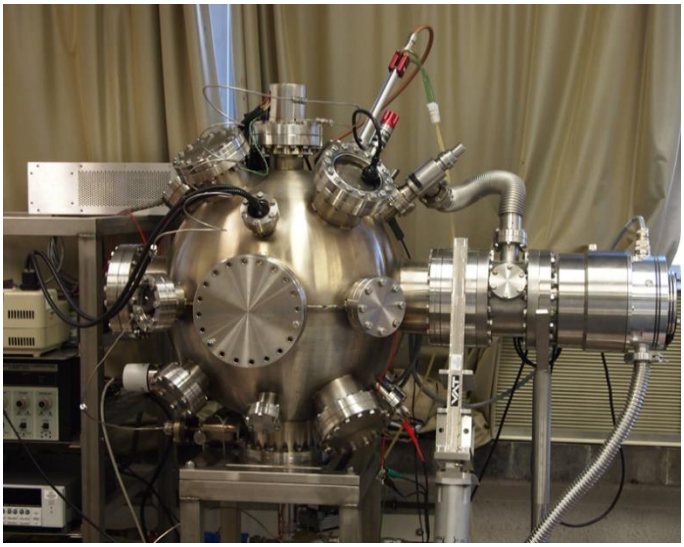

Figure 5. *Custom UHV system used for the coatings of large samples (wave guides)*

The Kaufman-type ion gun design consists in cylindrical magnets surrounding a 0.5 mm diameter filament in the centre and a carbon accelerating grid on top. A current density profile dependency with the distance from the centre was measured at two incident energies 900 eV and 200 eV respectively (see Fig.6).

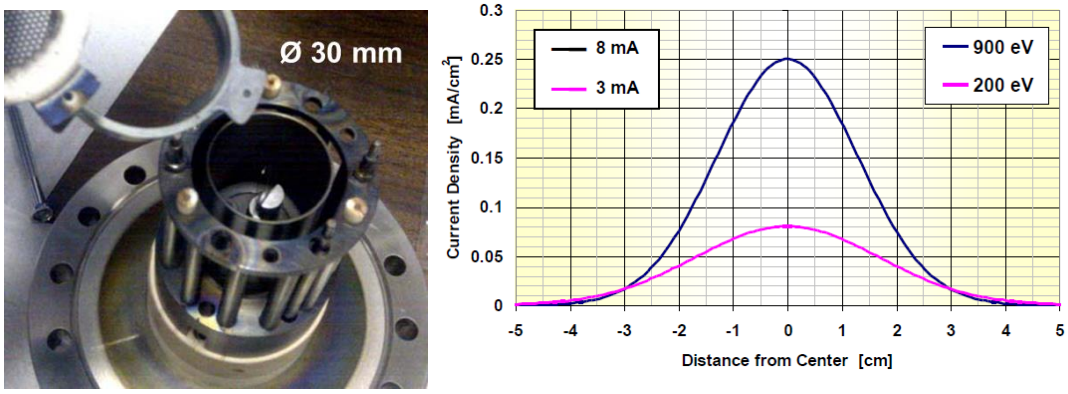

Figure 6. *Picture of the Kaufmann ion gun mounted on a 6" CF flange, disassembled for maintenance. On the right side are the current profiles for the ion energies used. The total current densities are over the whole ion beam.*

With this new setup it was possible to process samples up to 20x50 mm. The current density dispersion of the beam led to necessary adjustments of the geometry setup to achieve uniform and homogeneous coatings. The conditions used for the treatment of the final Multipactor sample were: an ion current density of 1.5 μA/mm^2, the ion energy set at 900 eV and total dose of about 900 μC/mm^2.

5.4 Description of samples

The research on this etching technique was initiated as a solution for a potential viable coating applied to large multipactor samples. The initial tests started with one Au small sample mentioned above, with good results, but since the most common base material for space application is Ag, they continued with standard Ag plated (40 μm thick) probe samples, as received from Tesat. A total of 14 samples with dimensions of (20x50x1) mm and one filter were treated, in a variety of conditions. Representative pictures of Ag and Au surfaces are shown in Fig.7. The optimization of the process required: several coating runs with Mo (4 samples) and Ti truncated cones of different sizes, a check of the beam profile and its symmetry, a sweep in energy from 200 to maximum 900eV for the effect on sputtering rate of the two metals, a check of the sample stage rotating speed and other geometrical adjustments to achieve reasonable surface homogeneity. The changings were reflected in the surface morphology and in the SEY.

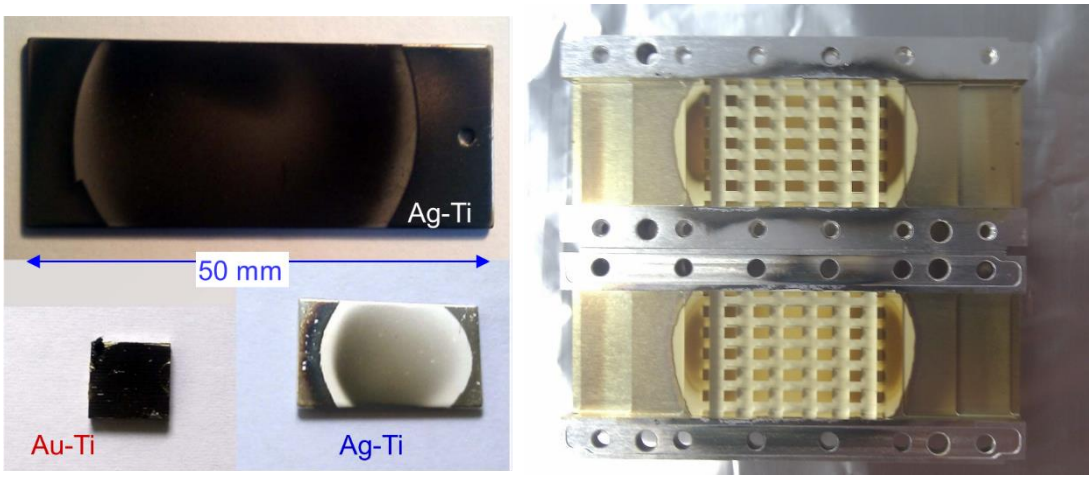

Figure 7. *Representative treated small samples (left) and a treated multipactor sample (right)*

A total of 10 multipactor samples, low pass harmonic filter wave guides, were received from Tesat, six with 40 μm Ag plating and the other four with 10 μm Ag plating. Eight filters were used in the application of the sputtering technique. When the essential questions on evolution of surface roughness and its relation to SEY during surface treatment were known, the experiments with the actual RF devices (filters from Tesat) were initiated. Only the first filter (see Fig. 7, right side) was treated with this setup, for the others the Ti source was replaced with a magnetron target. Experience showed that

processing conditions can vary appreciably when they are adapted to the larger multipactor samples, especially from the surface uniformity of the coating point of view.

5.5 Surface morphology (SEM) of Au-Ti, Ag-Ti and Ag-Mo

The surface resulted structured in the range of hundreds of nanometers, with a very high aspect ratio, as shown in Fig.8. The structure was very uniform and shows only one submicroscopic scale of roughness, that follows the microscopical defects of the surface finishing. The irregular individual structures reach up to 500 nm lateral size and the pattern is formed by walls of about 80 nm thick.

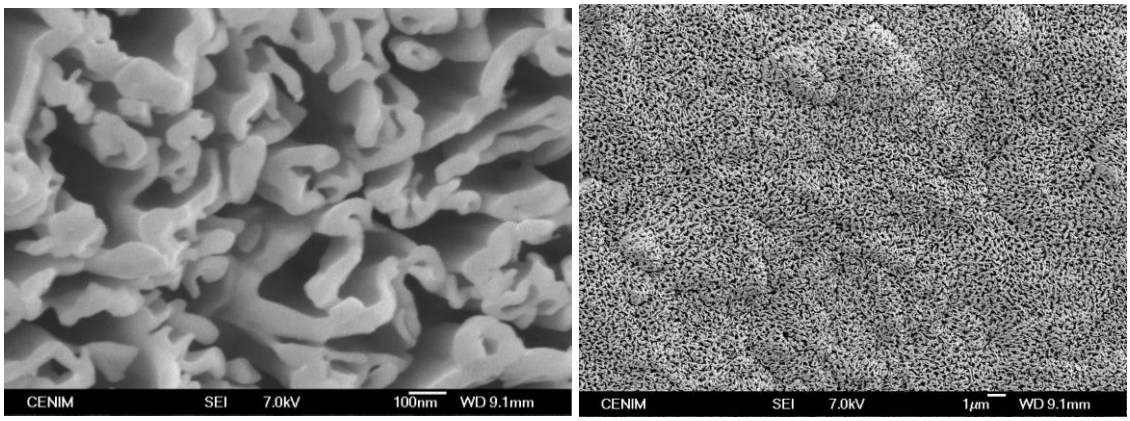

Figure 8. *SEM images of Au structured by Ti (cone) mask sputtering. Morphology of fine roughness, 100 - 200 nm, high aspect ratio, only one size scale.*

The sputtering of Ti over the Au substrate produces grains of irregular shapes randomly distributed over the Au surface. The preferential sputtering of the unmasked Au is insured by the sputtering yield ratio of about 3.5 of Au respect to Ti, in these experimental conditions. The visual appearance of the sample was black colour (Fig. 7).

In the Fig. 9 we show an example of surface morphology achieved by structuring Ag, this time using a Mo cone in 3.4×10^{-3} mb of Ar^+, with ions of 1000 eV energy and a dose of 0.25 mA/cm^2. The sample shows a non-uniform roughness formed by elongated grains with high height/width aspect ratio. These grains seem to be the result of lateral coalescence of conical grains that bunch together in clusters of sizes 1 – 2 μm, forming a second order coarser roughness, also of high aspect ratio.

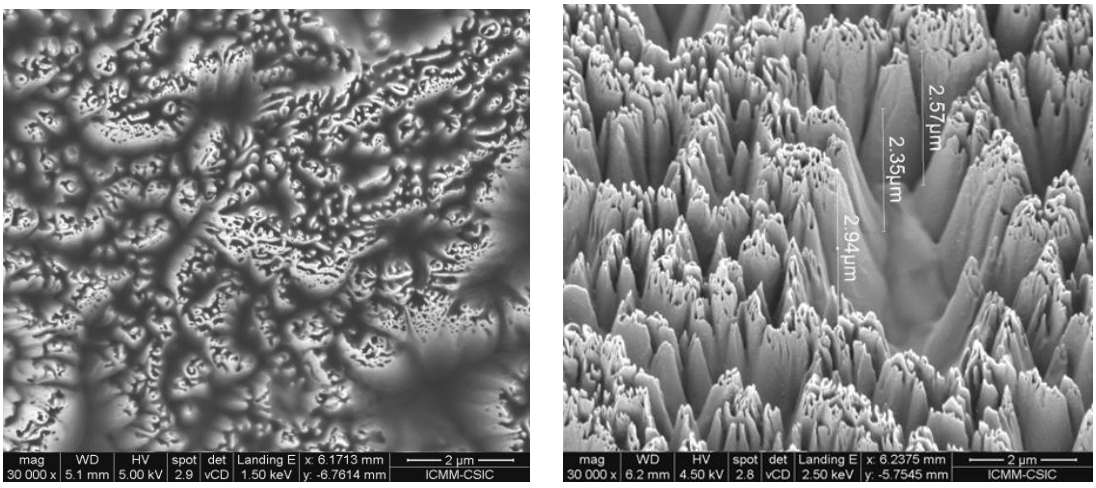

Figure 9. *SEM images of Ag structured by Mo (cone) mask sputtering. Two roughness scales in the range of several microns. Normal view (left) and 45° sample tilt (right).*

This sample showed also large inhomogeneity in the surface density of those clusters, producing macroscopic different shades or variations in tone of darkness.

The change of the seed atoms from Mo to Ti offered a better control on the surface homogeneity, probably related to its lower sputtering yield. A unique, uniform scale of roughness in the range of several hundreds of nanometres was produced (see Fig. 10-left).

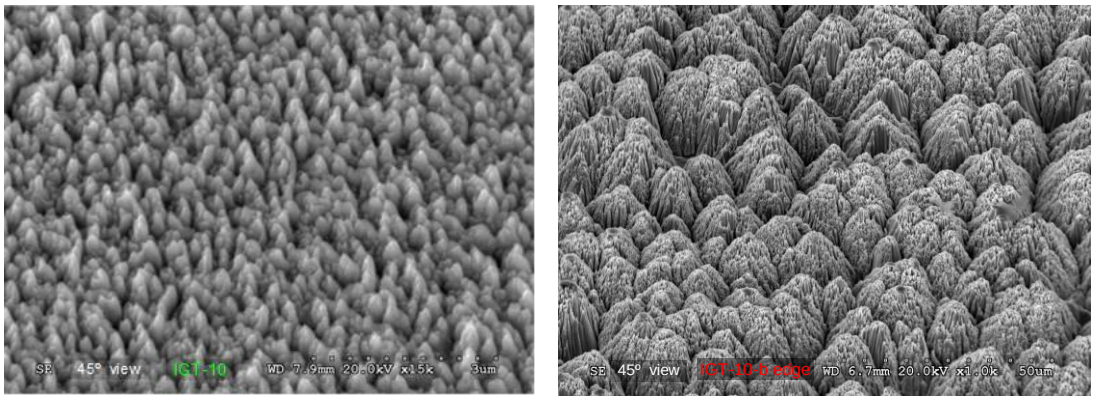

Figure 10. *SEM images of two Ag samples (IGT-10 and IGHT10-b), structured by Ti (cone) mask sputtering. One uniform scale of roughness 300nm (left) and two scales of 200 nm and 8 µm (right). Samples tilted 45°.*

However, a longer exposure to the impinging ions under the same coating conditions created and additional effect. The initial surface morphology appears to be separated conical grains or protuberances which, with further treatment, laterally coalesce into elongated shapes (1D coalescence), and with even continued treatment, cluster into large grains, i.e., second order coarser surface roughness (Fig.10-right).

5.6 SEY measurements and results

For all configurations, after the coating was performed, the samples were exposed to air and measured in a different UHV system. The results of the SEY measurements are presented Figs.11-13. The best results were obtained with Au-Ti and Ag-Ti setups.

In Fig. 11 the Au treated sample shows a σ_m close to 1 and it is compared to a reference sample. It should be pointed out that after nearly one year of exposure to air the SEY properties were quite good: E_1 = 139 eV, σ_m = 1.33, E_m = 680 eV, and σ_{2000} = 1.21. This shows that gold withstands exposure to the air better than silver. This also indicates that the Ti present in the surface has not affected negatively to the stability of the surface.

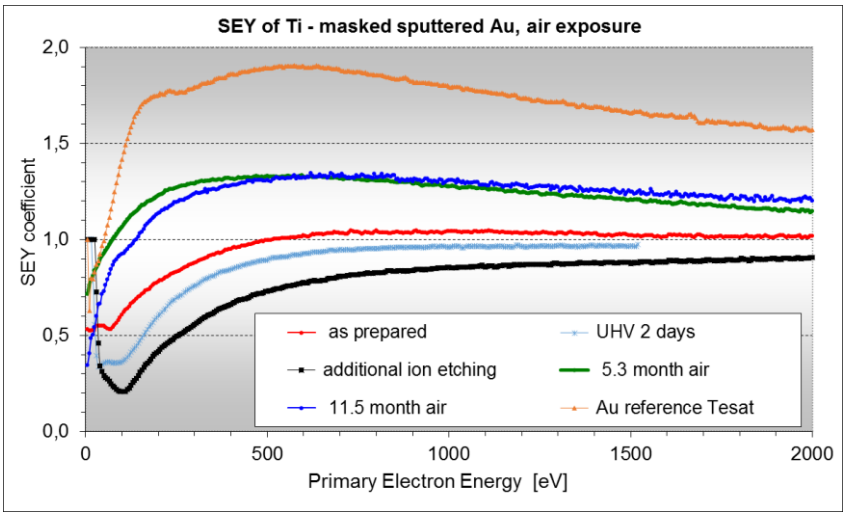

Figure.11. *SEY of Au structured by mask sputtering (Ti cone), evolution with air exposure (as prepared, after air exposure, additional ion etching, in situ extremely low dose ion cleaning).*

Once the first SEY and SEM analysis were performed, an additional Ar ion sputtering of sample was performed in the SEY analysis chamber with parameters: ion energy = 2500 eV, ion current = 9.5 μA, incidence angle 60º, and sputtering time = 2 h, lowering the maximum SEY below unity.

The two representative Ag-Ti samples were also measured and the results are depicted in Figs. 12 and 13. The differences in thesurface topography (Fig. 10) are reflected in the SEY properties. Both samples had similar air exposure time.

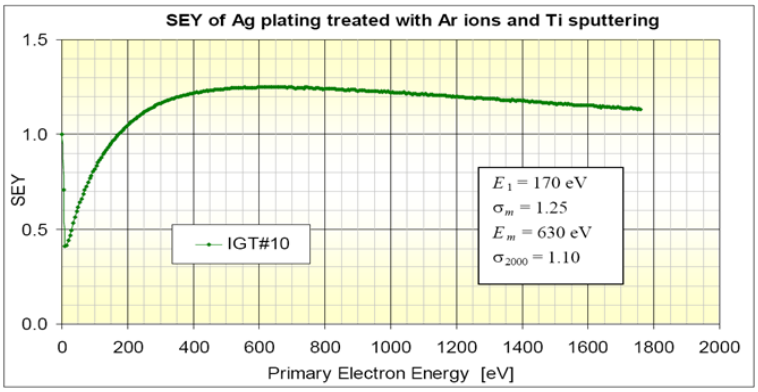

Figure 12. *SEY of Ag structured by mask sputtering (Ti) cone, single nanometric scale of roughness*

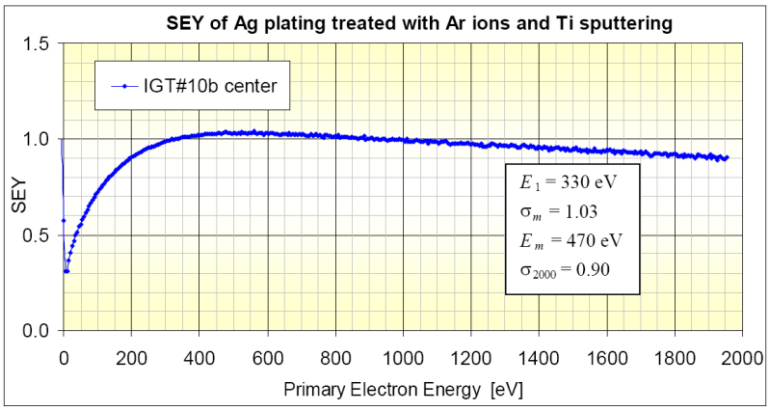

Figure 13. *SEY of Ag structured by mask sputtering (Ti) cone, for two scales of roughness*

Further experiments appeared to confirm that maximum SEY values below 1.10 are only achievable with this type of second-order high-aspect-ratio surface roughness. However, this type of roughness would imply large sizes and consequently large RF surface resistances.

5.7 Quantitative XPS and EDX analysis

5.7.1 Surface composition analysis of gold-titanium

Since preparation of the sample involves Ti deposition (mask) by sputtering, the amount of Ti remaining in the sample is of interest. Quantitative XPS analysis yielded an average surface relative composition Ti:Au of 10±1 % atomic (i.e., one Ti per 10 Au atoms); in

this case, surface is considered as a near surface region defined by the XPS photoelectron mean free paths, i.e., about 2 nm.

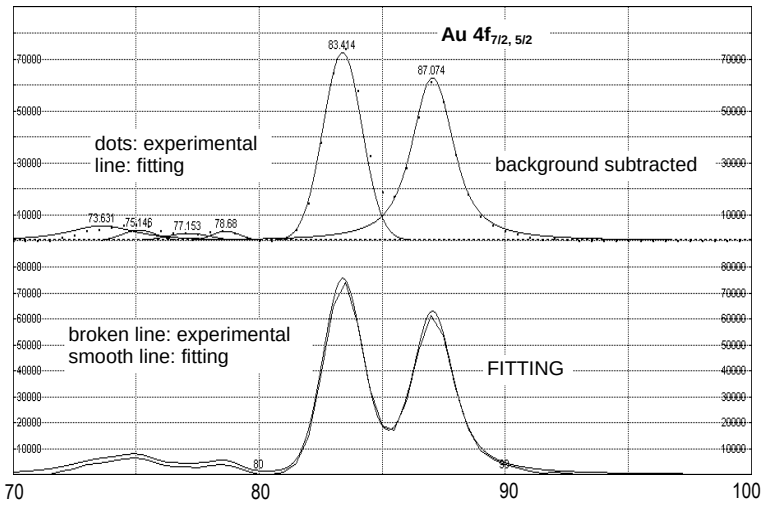

Figure 14 a). *XPS spectrum of Au 4f region for the Au-Ti sample*

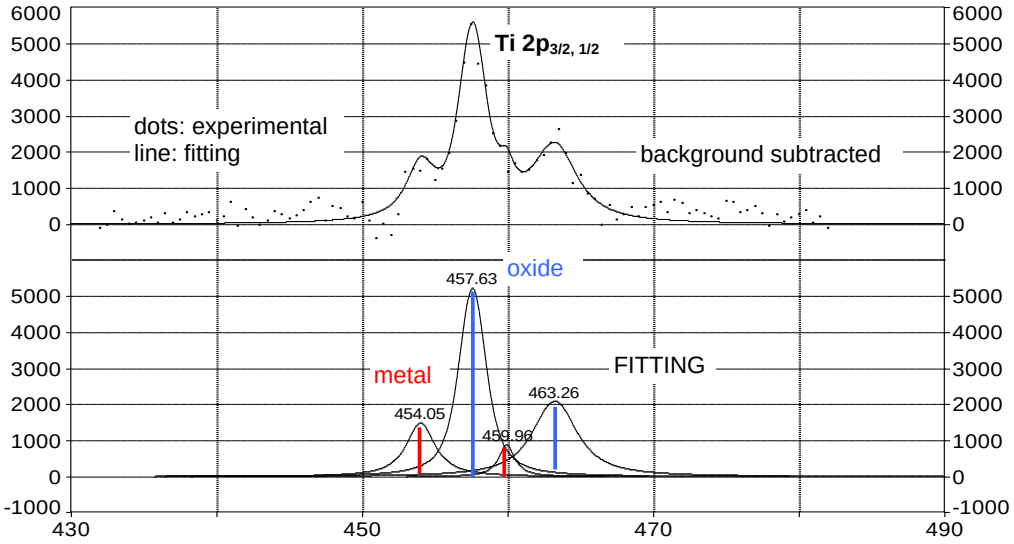

Figure 14 b). *XPS spectrum of Ti 2p region for the Au-Ti sample*

For quantification, main core level lines Au 4f and Ti 2p were used, see Fig.14. a) and b). The XPS sensitivity factor used were: S(Ti2p$_{3/2}$) = 7.35, S(Au4f$_{7/2}$)=8.40, S(Ti2p$_{1/2}$) = 3.81, S(Au4f$_{5/2}$) = 6.57. The results of the relative concentrations soft/hard metal were: ***N(Ti2p$_{3/2}$)/N(Au4f$_{7/2}$) = 0.12, N(Ti2p$_{1/2}$)/N(Au4f$_{5/2}$) = 0.11***. This does not necessarily confirm the presence of any Au-Ti alloy with that composition. In the bulk, there was pure Au, while somewhere close to the surface there we detected metallic Ti, some Ti oxide (TiO_2), and some adsorbed molecules containing C and/or O. The amount of Ti is very small since in spite of it being closer to the surface, XPS detected much more Au.

5.7.2 Surface composition analysis of silver-titanium

Samples IGT10 and IGT10b, described in Figure. 10, had different type of roughness and SEY. They are supposedly under and over treated, respectively, with respect to a supposedly optimum treatment. They were analyzed by two techniques with different surface sensibility: a) EDX, associated to SEM, with an analysis depth about 1 μm, and b) XPS with an analysis depth about 2 nm (Fig. 15).

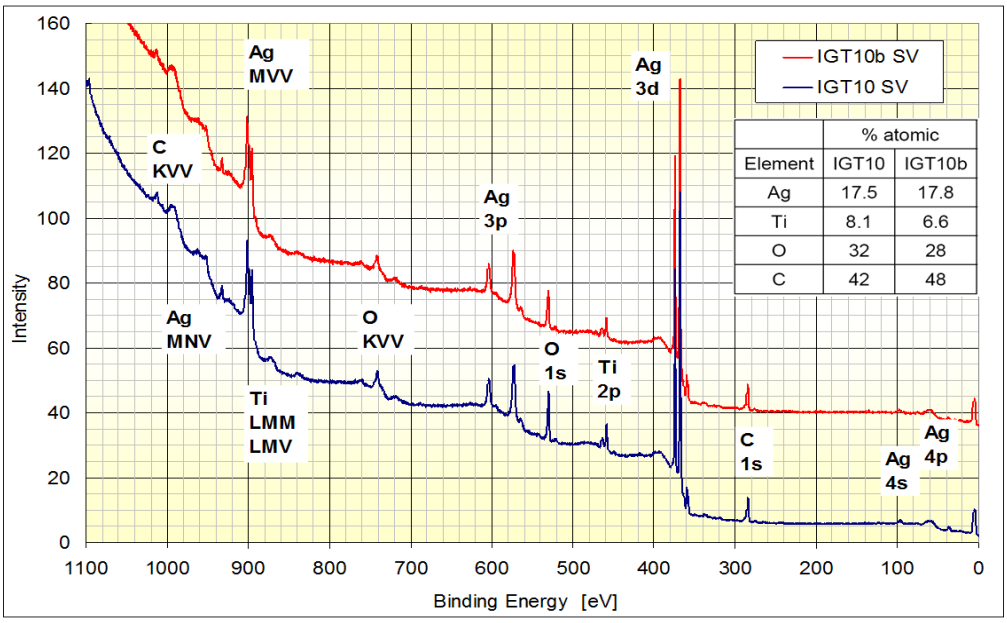

Figure 15. *XPS general spectra of the two representative Ag-Ti samples (IGT10 and IGT10b)*

Moreover, XPS is sensitive to chemical state (able to distinguish Ti metal and oxide) as well as amenable to practical models for non-destructive quantitative analysis in depth, thus further increasing depth resolution. Tables II.1 – II.2 show the quantification results of these analyses.

Table II.1. Apparent surface composition from EDX and XPS

	% atomic			
	IGT10		IGT10b	
Element	EDX	XPS	EDX	XPS
Ag	90.3	17.5	82.7	17.8
Ti	0.67	8.1	1.06	6.6
O	9.05	32	16.2	28
C		42		48

Table II.2. Composition depth profile extracted from the XPS analysis

XPS	Thickness	
Layer	IGT10	IGT10b
C-50%O	1.4	1.5
TiO_2	1.3	1.2
Ag	bulk	bulk

Elements with XPS apparent composition higher than with EDX are in the surface layer respect to the EDX analysis depth of about 1 μm. Values are in agreement with the different analysis depths. Assuming that the oxygen and carbon surface contamination was acquired when the sample surface of Ti over Ag was exposed to the air, Table II.2 results from quantitative XPS analysis with a 3-layer model [7, 8]. XPS chemical shift showed that Ti is completely oxidized. It also showed that only about 20 % of the C is bonded to O; the remaining oxygen in the contamination over layer was probably bonded to H. Hydrogen cannot be detected using either XPS or EDX techniques.

These results were obtained assuming a model of flat layers; they should be very carefully understood since the surface was strongly structured. Very briefly and schematically, for atoms A_1, A_2, and A_3 in the surface, intermediate layer, and bulk, respectively

$$I_1 = K \cdot S_1 . N_1 . (1 - \exp(- d_1/\lambda_1))$$

$$I_2 = K \cdot S_2 . N_2 . \exp(- d_1/\lambda_2) \cdot (1 - \exp(- d_2/\lambda_2))$$

$$I_3 = K \cdot S_3 . N_3 . \exp(- d_1/\lambda_3) \cdot \exp(- d_2/\lambda_3)$$

where I is the XPS intensity, S is the XPS sensitivity factor, N is the atomic density, λ is the inelastic mean free path of the photoelectrons, and d the thickness of the layer.

The EDX measurements showed that in a depth of about 1 μm, the less structured sample IGT-10 has apparently also less concentration of Ti at the surface.

5.8 Conclusions

The main potential advantages of this nanotechnology technique are:

- It is capable of producing surface roughness of sizes from the micrometer to the 10 nanometer scale.
- Aspect ratio of surface roughness can be very high and controlled by the conditions of the preparation process.
- The surface density of the surface structures can be very high.
- The characteristics of the surface roughness, size, aspect ratio, density, can be very homogeneous or uniform in spite of being random or chaotic and not regular or symmetrical; these last characteristics useless for our purpose.
- The resulting "contamination" of Ti (or Mo) can be negligible, below 10 % atomic in a surface layer of less than 5 nm.
- It is capable of easily treat relatively large surface areas compared to other nanotechnology techniques having more detailed control on the surface structures produced.
- The adherence of the rough coating is perfect since it has not been deposited on but excavated in the substrate.

It was an important disadvantage that our particular case (a "soft" heavy substrate and a "hard" light mask, seed or impurity) had scientifically not been studied; our research had to move into new experimental specialized areas. And there was no sufficient time to perform the necessary experiments to clarify the influence of the different parameters or conditions of the process on the resulting surface roughness. Instead of exploring a range of values for each parameter, approximate optimization was obtained by a "trial and error method", by "jumping" in a few trials to hopefully sufficiently close to the optimum values.

In a simple approach or raw approximate explanation of the technique, the deposited Ti or Mo would form random islands which would protect the Ag or Au substrate from being eroded (sputtered) by the ion beam. However, the mechanical effects of sputtering deposition and ion etching alone would not produce nucleation and growth of Ti islands. It is known that in those conditions, there are several other physical mechanisms apart

from sputtering which produce mass flow leading to varied surface morphologies depending on process parameters. We propose as main forces:

- ion mixing or alloying (Ti sputtering deposition and Ar ion bombarding would mechanically produce Ti-Ag alloy),
- ion enhanced diffusion (will activate thermodynamical or chemical forces),
- phase separation or spinodal decomposition (thermodynamics of Ti-Ag produces spinodal decomposition, fast phase separation, formation of Ti islands),
- preferential ion etching (Ti phase separation leaves Ag unprotected under preferential ion etching), and
- selective deposition and shadowing effects (growth of Ti islands and consequent protuberances produces selective deposition and shadowing effects because of oblique Ti deposition).

These would explain the nucleation and growth of islands of the hard metal and consequent protuberances (1st order surface roughness) but there should be some yet-unidentified mechanism for explaining the clustering of protuberances in *cabbage-like* structures without coalescing (2nd order surface roughness).

Bibliography chapter 5

[1] A. N. Curren et al: NASA Technical Paper 2967, NTIS, Springfield, Virginia, USA (1990).

[2] Maxim A. Makeev, Rodolfo Cuerno, and Albert-László Barabási. Morphology of ion sputtered surfaces. Nuclear Instruments and Methods in Physics Research Section B: Beam Interactions with Materials and Atoms, 197(3–4):185–227, December 2002.

[3] Kun Zhang, Marc Brötzmann, and Hans Hofsäss. Surfactant-driven self-organized surface patterns by ion beam erosion. New Journal of Physics, 13(1):013033, January 2011.

[4] H. Hofsäss, K. Zhang, A. Pape, O. Bobes, and M. Brötzmann. The role of phase separation for self-organized surface pattern formation by ion beam erosion and metal atom co-deposition. Applied Physics A, 111(2):653–664, October 2012].

[5] Seah, Clifford, Green and Gilmore, Surf. Interface Anal. 37 444-458 (2005) and Seah, Nucl. Ins. Meth. B 229 (3-4) 348-358
-cited in NPL Sputtering Yields: http://www.npl.co.uk/nanoanalysis/sputtering_yields.html

[6] Yamamura H. Tawara, Energy Dependence of Ion-Induced Sputtering Yields from Monatomic Solids at Normal Incidence, Atomic Data and Nuclear Data Tables 62, 149-253 (1996)

[7] M.P.Seah, "Quantification in AES and XPS", in "Surface Analysis by Auger and X-ray Photoelectron Spectroscopy", D.Briggs, J.T.Grant (ed.), IM Publication and Surface Spectra, 2003, p.345.

[8] D. Y. Petrovykh, J. M. Sullivan and L. J. Whitman: "Quantification of discrete oxide and sulphur layers on sulphur-passivated InAs by XPS", Surf. Interface Anal. 2005; 37: 989-997

Appendix: Yield Ratios for Masking Preferential Sputtering

For the sputtering yields see ref. [5, 6].

First Criterion: Yield Ratio $Y_X(B)/Y_X(M)$, evaluates preferential sputtering. The value (**1.90**) for B = Cu, M = Mo, X = Ar, and energy = 1 keV is taken as a reference. Values ≥ 1.9 are high-lighted in blue.

Table I — Mask metal M = **Ti** — Gas X = **Ar** — Base metal B

Energy [keV]	**Mg**	**Al**	**Cu**	**Ag**	**Au**
1	3.23	1.71	2.89	4.23	3.37
2	3.05	1.69	2.82	4.10	3.35
5	2.91	1.68	2.79	4.08	3.43

Table II — Mask metal M = **Mo** — Gas X = **Ar** — Base metal B

Energy [keV]	**Mg**	**Al**	**Cu**	**Ag**	**Au**
1	2.12	1.12	**1.90**	2.78	2.21
2	1.97	1.10	1.83	2.66	2.17
5	1.85	1.07	1.77	2.60	2.18

Table III — Mask metal M = **Ta** — Gas X = **Ar** — Base metal B

Energy [keV]	**Mg**	**Al**	**Cu**	**Ag**	**Au**
1	2.68	1.42	**2.41**	3.52	2.80
2	2.45	1.36	2.26	3.29	2.69
5	2.24	1.29	2.15	3.15	2.65

Table IV — Mask metal M = **Ti** — Gas X = **Xe** — Base metal B

Energy [keV]	**Mg**	**Al**	**Cu**	**Ag**	**Au**
1	3.23	1.54	2.59	4.49	4.64
2	2.99	1.57	2.41	4.00	4.13
5	2.81	1.60	2.29	3.69	3.83

Table V — Mask metal M = **Mo** — Gas X = **Xe** — Base metal B

Energy [keV]	**Mg**	**Al**	**Cu**	**Ag**	**Au**
1	2.31	1.10	1.85	3.21	3.31
2	2.19	1.15	1.77	2.93	3.03
5	2.09	1.19	1.70	2.75	2.85

Table VI	Mask metal M = **Ta**		Gas X = **Xe**		
	Base metal B				
Energy [keV]	**Mg**	**Al**	**Cu**	**Ag**	**Au**
1	2.01	0.96	1.61	2.80	2.89
2	1.95	1.03	1.58	2.61	2.70
5	1.89	1.07	1.54	2.47	2.57

Second Criterion: $[Y_X(Ag)/Y_{Ar}(Cu)][Y_X(Ag)/Y_X(M)]$, evaluates preferential sputtering and rate. The values for the cases satisfying both criteria are high-lighted in blue.

Table VII	Mask metal M = **Ti**		Gas X = **Ar**		
	Base metal B				
Energy [keV]	**Mg**	**Al**	**Cu**	**Ag**	**Au**
1	3.60	1.01	2.89	6.18	3.92
2	4.50	1.39	3.85	8.16	5.44
5	5.63	1.87	5.17	11.10	7.83

Table VIII	Mask metal M = **Mo**		Gas X = **Ar**		
	Base metal B				
Energy [keV]	**Mg**	**Al**	**Cu**	**Ag**	**Au**
1	2.37	0.66	**1.90**	4.07	2.58
2	2.91	0.90	2.49	5.28	3.52
5	3.58	1.19	3.29	7.06	4.98

Table IX	Mask metal M = **Ta**		Gas X = **Ar**		
	Base metal B				
Energy [keV]	**Mg**	**Al**	**Cu**	**Ag**	**Au**
1	3.00	0.84	**2.41**	5.14	3.26
2	3.61	1.12	3.09	6.54	4.37
5	4.34	1.44	3.99	8.57	6.04

Table X	Mask metal M = **Ti**		Gas X = **Xe**		
	Base metal B				
Energy [keV]	**Mg**	**Al**	**Cu**	**Ag**	**Au**
1	4.34	0.99	2.79	8.40	8.96
2	6.27	1.74	4.08	11.24	12.00
5	9.38	3.02	6.22	16.14	17.42

Table XI	Mask metal M = **Mo**		Gas X = **Xe**		
	Base metal B				
Energy [keV]	**Mg**	**Al**	**Cu**	**Ag**	**Au**
1	3.10	0.71	2.00	6.00	6.40
2	4.60	1.28	2.99	8.24	8.79
5	6.98	2.25	4.63	12.01	12.96

Table XII	Mask metal M = **Ta**		Gas X = **Xe**		
	Base metal B				
Energy [keV]	**Mg**	**Al**	**Cu**	**Ag**	**Au**
1	2.71	0.62	1.74	5.24	5.58
2	4.09	1.14	2.67	7.34	7.84
5	6.29	2.02	4.17	10.82	11.68

Chapter 6

Glancing angle deposition (GLAD)

6.1. Technique evaluation

The necessity for achieving deeply structured rough coatings arises from an experimentally proven fact, that a low SEY could reduce MP level in satellites components. Following this criteria over the years, we have focused our efforts in investigating the growth mechanisms of several metals that more or less fulfil the typical requirements and properties for space applications: low SEY and RF resistance (i.e., low insertion losses and high RF performance), good adherence, air stability, relatively reproducible and low cost fabrication methods…etc., which turned out to be a generalized difficult task. If a single material is not able to gather all the needed characteristics for an anti multipactor coating, then a multi-layer size-controlled strategy becomes a viable alternative.

In this chapter, a combined method is proposed for the generation of a textured coating, choosing from the variety of available materials copper (practically the highest conductivity metal) as a first structured pattern layer and gold (the highest conductivity inert metal) as a thin protective overlayer on top. Both coatings were performed by thermal evaporation in two different systems and also different conditions (glancing angle and normal incidence of the atom source, respectively) and are described below.

In the literature studies [1], [2] it is reported that:

(a) copper is a low ad atom mobility material and also has a good thermal conductivity so when it is being evaporated onto a substrate, the ad atoms arriving to the substrate tend to cool down losing thermal energy and mobility necessary for surface diffusion to fill the voids.

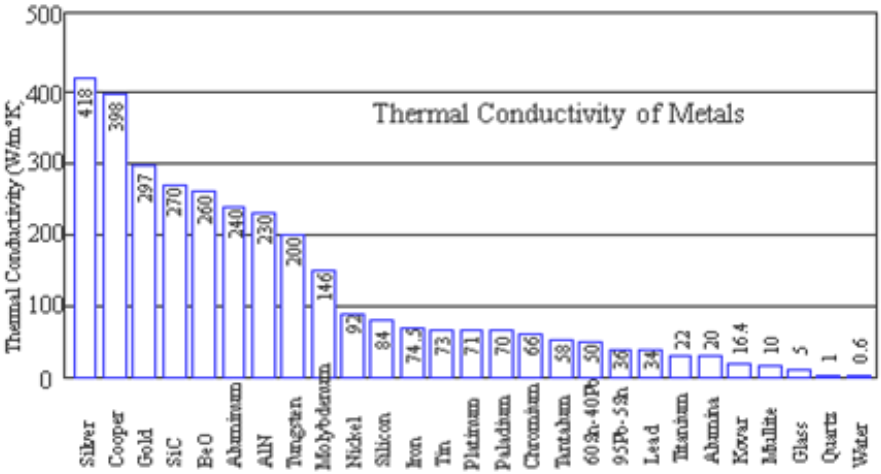

Figure 3. *Thermal conductivity of common metals*

(b) Furthermore, effects of atomic shadowing are produced, creating areas where the vapour flux cannot reach directly.

These factors (a, b) along with other deposition conditions (Ar pressure, coating rate) lead to the formation of columnar microstructures of isolated grains and determine their size and ´´packaging´´ level.

The main benefit of a gold protective overlayer is its inert behaviour and low SEY aging upon air exposure.

6.1.1. General description of GLAD technique

Also known as GLAD (glancing angle deposition) or in some cases STF (sculptured thin films), the recent development of this nanotechnology technique (since 1994 [3]) has produced several books and many hundreds of articles. We will only mention a few [3-6] just sufficient to show the essential features of this technique as a PVD.

Thin films coated by physical vapour deposition, in conditions of the vapour flux arriving at an oblique angle from the substrate normal, and under conditions of limited ad atom mobility to create a columnar microstructure, the resulting structure is columnar and grows at an angle inclined toward the vapour source. There is a fixed relationship between the angle of arriving atoms on the substrate, α, and the inclination angle at which the columnar thin film grows, β. The empirical ‘‘tangent rule’’ $\tan(\beta) = \frac{1}{2}\tan(\alpha)$ is a simple

relationship valid for near normal deposition and gives good results for α smaller than about 50°. For higher angles a more precise called Tate`s rule is implemented [7] .As the porosity of the film is also dependent on the incident flux angle, column growth angle and porosity cannot be chosen independently. If a large columnar angle, more parallel to the substrate is desired, the flux must be deposited at a large oblique angle resulting in a very porous film. Conversely, if a near vertical columnar film is desired, the flux must arrive more perpendicular to the substrate and the resulting film has a tightly packed, dense microstructure.

Generally, the initial substrate surface roughness can be that native or deliberately produced by another technique, and it can be of low aspect ratio. Even in an ideally flat surface, the growth of initial nuclei is random and soon some will make shadow over its nearest neighbours. There is practically no limit for the type of material or the substrate. Either thermal evaporator or sputtering sources are used. However, the atom/molecular beam should be as collimated as possible. Small solid angles or large distances are required. Thus, physical deposition at oblique angle in good vacuum was considered as a good alternative, with lower growth rates compared to other mentioned techniques such as magnetron sputtering or thermal flash evaporation.

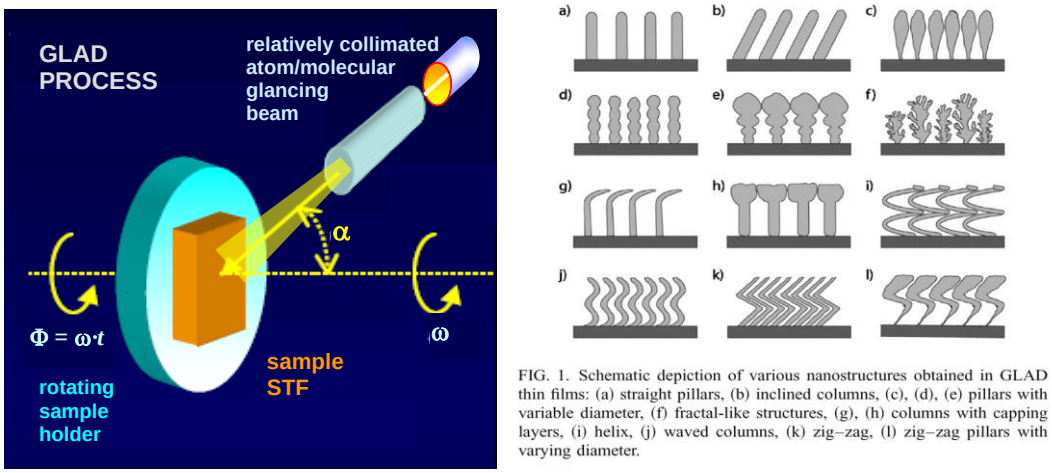

Figure. 2 *Thermal evaporation of Cu in relatively low pressure and at high rate and grazing incident vapour flux , showing vapour flux direction and column growth tendency [5]*

6.1.2 Experimental setup

When fully developed, this technique allows nearly complete three-dimensional control of nano-scale surface texture. Figure 2 shows the working principle and the ideal experimental schematics of the deposition technique for rough copper coatings by GLAD thermal physical evaporation, along with the growth tendencies.

However, in our research, the limited setup available allowed us to perform only depositions with a medium porosity given by angular conditions of $0 < \beta < \alpha \approx 30°$ (see Fig.3). Even in these circumstances, the surface roughness produced deep shadows and only the protruding parts grow forming slanting columns with angle $\beta < \alpha$ and separation (porosity) increasing with α.

This system is equipped with a swinging sample stage. The α angle of the arriving atoms from the crucible is approximately 30° with respect to sample normal. The copper atom source is placed in a rectangular tungsten basket which is heated progressively by an AC power supply up to the evaporation temperature at a practical rate. This sample stages could hold several substrates of different sizes and types. The conditions for a rough deposit were the following: a low pressure inside the chamber, between 3 to 8×10^{-6} Torr, maintained by a turbo and rotatory pump system, substrate temperature fluctuating around 60° and 80 °Celsius during the process, an evaporation rate of 0.2 – 5.6 Å/s in 37 min total exposure time and final thickness of the Cu thin film of about 0.93 μm. The thickness of this coating was measured by a quartz balance during deposition and also estimated from the SEM images at about 20° β tilted angle. This was possible due to the shadowed, uncoated areas created by the machining of the substrate.

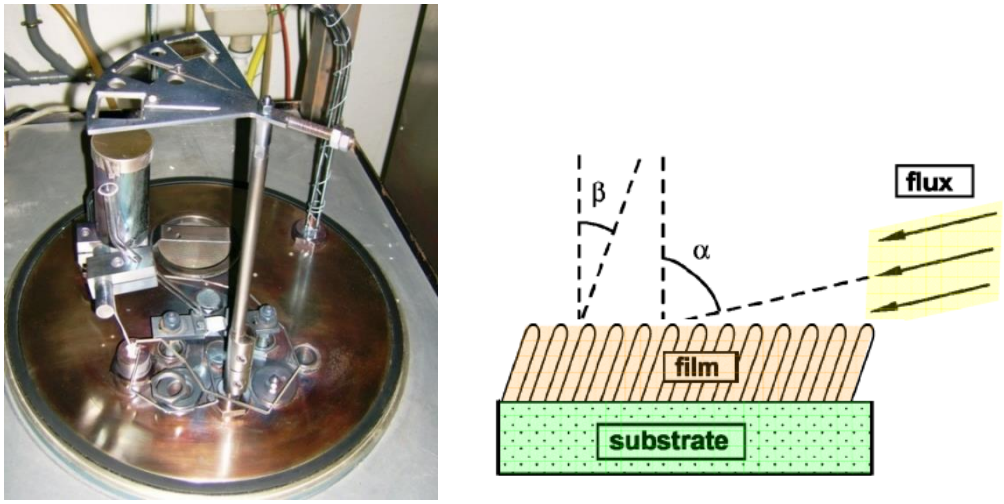

Figure 3. *Picture of the experimental setup and the angle schematics of the arriving atom flux*

Four types of substrates were used, varying deposition parameters and slightly the deposition angle in order to obtain rough coatings of low SEY. Substrates of Ag-plated aluminium from Tesat, microscope glass slides, Al, and single crystal Si with sizes around 1×20×20 mm and 1x10x15 mm were used in every sample holder. We also chose to examine closer the Cu on Al and Ag substrates for their fairly good adherence.

6.2. Experimental results

6.2.1 SEY measurements and SEM analysis

The main results of SEY measurements on rough Cu coatings are presented in Fig. 4 and Table I. The measurements were not performed in situ and the samples had to be exposed to air but only for a few minutes. The first cross-over energy E_1 of rough copper was 238 eV with a σ_{max} of 1.19, much lower than a normal smooth copper sample. However, long exposure of the sample to air, wrapped in aluminium foil increased, as expected, the SEY to almost 2.2 in just 4 months period of time, due to oxidation and water absorption. A mild ion etching (Ar^+ ion energy of 2500 eV) under vacuum restored the sample almost to the same state as recently coated.

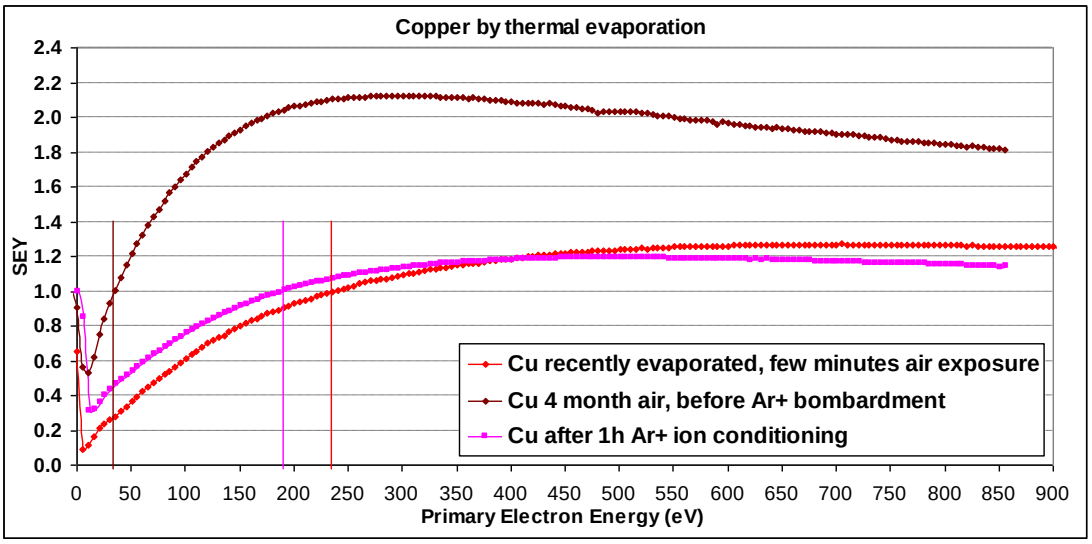

Figure 4. *SEY of rough copper coatings on Al, deposited by GLAD thermal evaporation*

A summary of the main SEY parameters is shown. There is a considerable difference between clean and aged Cu in the secondary emission behaviour.

sample	E_1 (eV)	σ_m	E_m (eV)
Cu recently coated	**238**	**1.27**	**740**
Cu aged in air (4 months)	**34**	**2.13**	**285**
Cu cleaned by Ar^+ ions	**192**	**1.19**	**463**

Table I. *SEY parameters comparison for Cu coating at glazing angle*

Representative images of the surface morphology and the coating profile are presented in Fig. 5. Rough Cu coatings were formed by columnar grains which grew uniformly loosely packed or forming tight bunches loosely packed. The columnar layer thickness was about 1 μm. The grains show a vertical growth with an approximately 20° inclination with respect to surface normal. The parallel dark areas are regions of the Al substrate that were not coated due to shadowing effects created by the "staircase" mechanical machining. The approximate thickness of this coating was also corroborated with the quartz balance monitoring during the process.

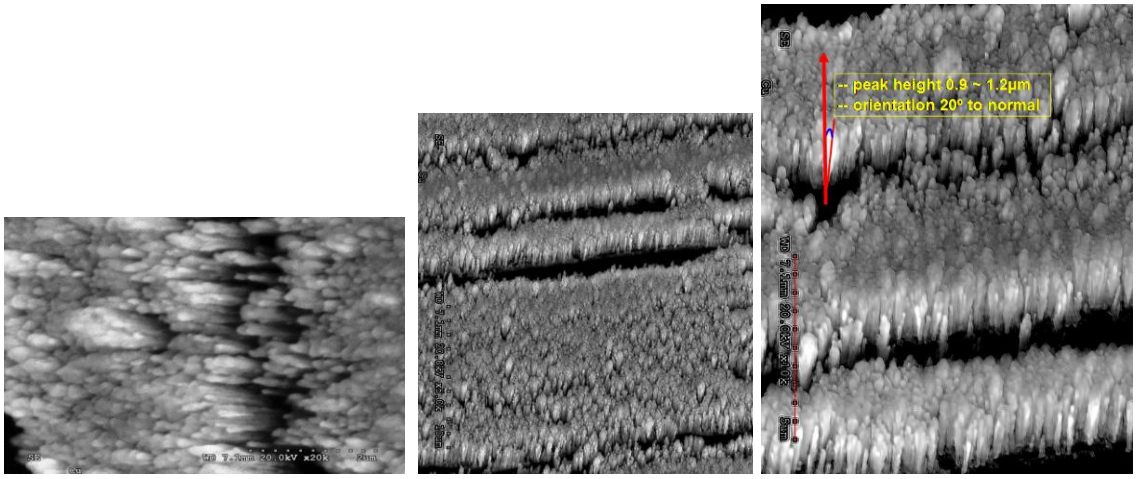

Figure 5. *SEM images of the surface morphology of rough Cu thermal evaporated on aluminium substrate*

The growth of the columnar grains observed at nanometric scale was uniform, with tight bunching and also with the gaps created by the poor machined surface finishing of the Al substrate, as a result of a possible shadowing effect during the coating.

6.2.2 Surface characterization by XPS and EDX

A surface chemical analysis by X-ray Photon Spectroscopy of aged nanostructured Cu reveals the presence of significant amount of carbon and oxygen, which would justify the precarious state of the sample and its high SEY (even though the relative composition was not accurately quantified). The results are shown in Fig.6.

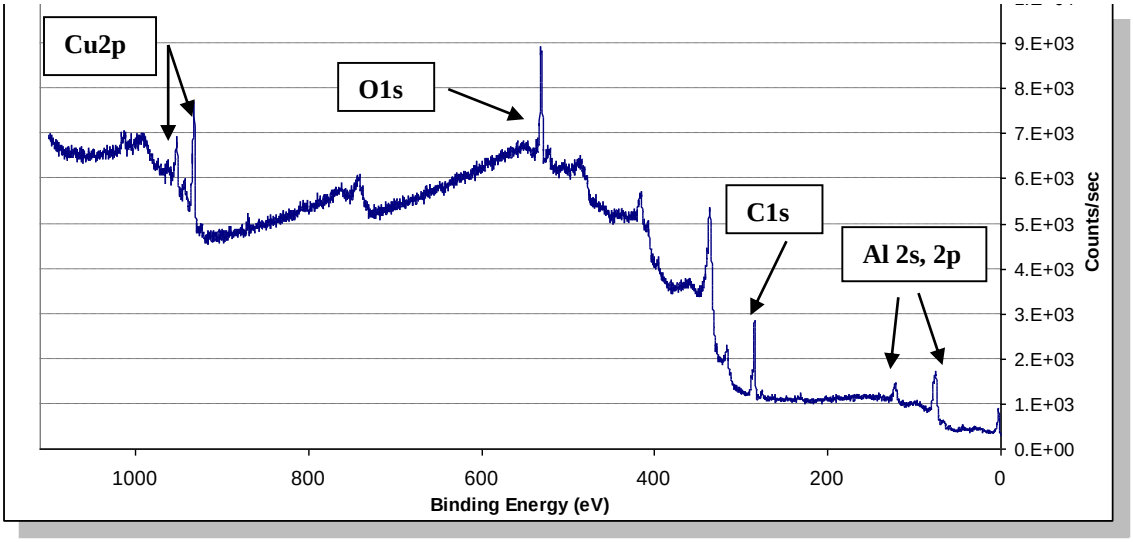

Figure 6. *General overview of the chemical state showing constituent elements of the Cu rough coating on aluminium substrate*

Not surprisingly, the signal coming from Al 2s and 2p levels is also present. We think that is due to the terraces, grooves, and generally structure defects left by the poor mechanical surface finish of the substrate. No other contaminants were detected.

An EDX analysis was also performed on a large area at a deeper sample depth, with the following results shown in Fig. 7 below.

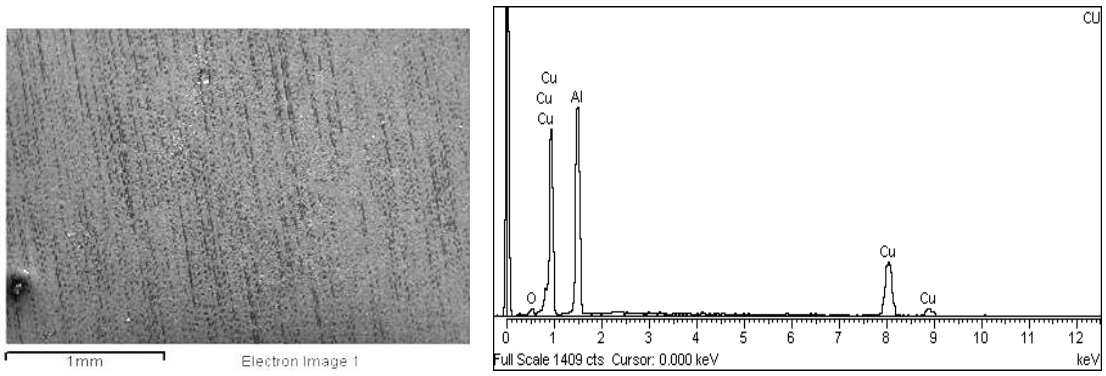

Figure 7*. SEM image (left) of EDX, (1x1 mm) region of interest and resulting elements*

Signal from the same elements as in the XPS measurement were detected. The bulk was not contaminated by other elements during deposition. The black areas of the SEM image are the Al substrate left uncovered by the Cu coating, clearly < <50 %, possibly < 10 %, considering the measured area.

Element	Atomic%
O K	**6.61**
Al K	**59.47**
Cu K	**33.92**
Total	**100%**

Table II*. Relative composition of elements from EDX measurements*

The atomic percentage of each element in the observed region is represented in the above Table II. In this case, the apparent Al atomic concentration, about 60 %, is a result of both the gaps and structure discontinuities, at most 10 %, and also the analysis depth beyond the Cu layer thickness.

6.2.3 Surface treatment for SEY recovery and stability

After achieving a rough sub-micron surface of copper with good conductive properties and relatively high aspect ratio, we turned to the limitations of this coating. It is a highly reactive material and although the initial SEY value was rather low, it is known that it tends to increase in short time when exposed to air, which in this case was also confirmed by the actual measurements ($\boldsymbol{\sigma}_{max}$ went up from 1.2 to 2.1 in months).

A protective, conductive and more inert material such as gold was considered appropriate in preventing the aging effects.

Between the two coatings of Cu and Au, all the samples prepared by GLAD technique were exposed to air and were stored in aluminium foil for 4 months.

The increase in the SEY parameters and the deterioration of the samples is caused by water molecules attachment and oxidizing processes. In order to re-establish the original chemical state and improve surface properties, an intermediate step of cleaning the samples by ion bombardment was performed. For one ´´aged´´ Cu on Ag substrate (from the same coating as the Cu/Al sample described above), a mild ion sputtering (surface cleaning) in the analysis chamber was applied to recover the surface state and the initial SEY. The ion etching was performed with 2500 eV Ar^+ ions and total fluencies of 50 μA $\times$ 60 s / 1 cm^2 , at a constant pressure of 4×10^{-7} mbar. After this step, the Au coating was performed and the SEY of the sample was measured in situ.

Nano-structured gold on copper coating, by thermal evaporation

This is basically a variation of the same technique involved in the research, able to produce in a controllable manner a conformal thin gold layer over the existing pattern of Cu, which maintains the existing roughness below. In this way, a protective coverage over the columnar grains was created without closing the gaps or filling the voids between the grains. This was done by insuring a low deposition rate and relatively high Ar gas pressure so that the Au ad atoms were apparently able to organize around the existing structures. A schematic of the experimental setup and the surface morphology from the SEM analysis are described in Figs.8 and 9.

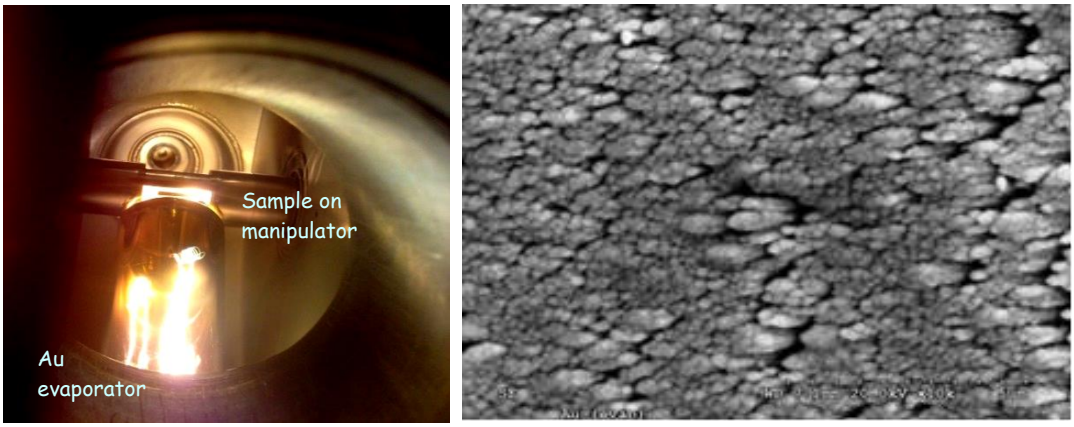

***Figure 8**. The setup for thermal evaporation and the morphology (SEM) of the Au/Cu surface*

Gold was evaporated from a basket crucible of W wire (diameter ∅ = 0.38 mm) by a gradually increasing surge of electrical power (4-6 Amp × 14-18 V × 15 min) in a 0.9 mb Ar residual pressure, over a substrate placed at 5 cm distance (normal incidence), with a starting base pressure of 2E-8 mbar and room temperature. The total deposition time was approximately 15 minutes and after cooling, the sample was moved to the analysis chamber for the SEY measurements.

SEM analysis

The surface does not present visible large scale structural defects (as in the case of Cu on Al substrates), it appears to be much more regular because the first substrate was a homogeneous 40 μm Ag plated substrate from Tesat Spacecom. A closer look at the Au layer in the SEM picture of Fig.9 seem to indicate wider grains and higher packaging level compared to the initial Cu columnar structures.

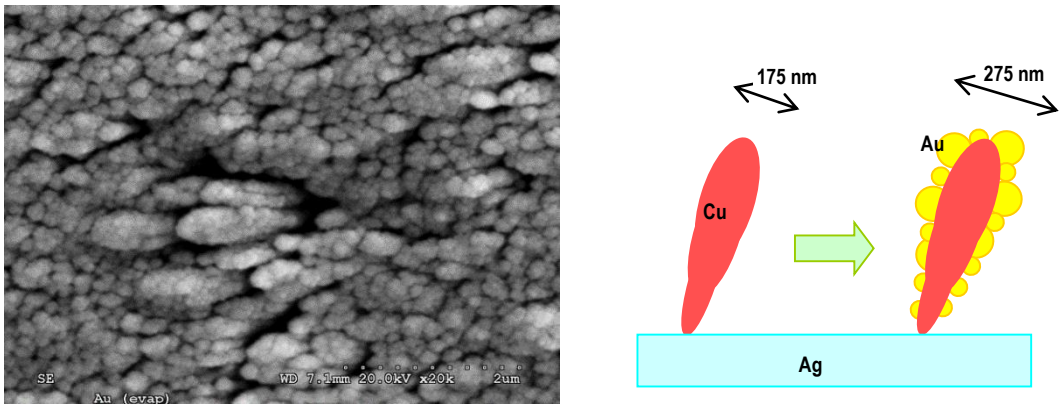

***Figure 9.** SEM images of the rough GLAD Cu under layer and thin Au over layer keeping the same aspect ratio and average grain size as initial bear GLAD Cu coating. Grain size average 150 nm, bunch size 400 nm.*

SEY analysis

The effect of Au coating on the GLAD structured Cu was an increase in E_1: 200 → 250 eV, in σ_m: 1.2 → 1.6, and in E_m: 740 → 1010 eV. This effect of thin Au coating on SEY of rough surfaces of different materials has often been observed in this research. And it could be explained by a *structural SEY suppression factor* preserving the same relation of the material intrinsic SEY curves (flat smooth surfaces). This roughness factor would be smaller (more suppression) for lower energies but could not modify the relation "larger than", because it would be little dependent on the material.

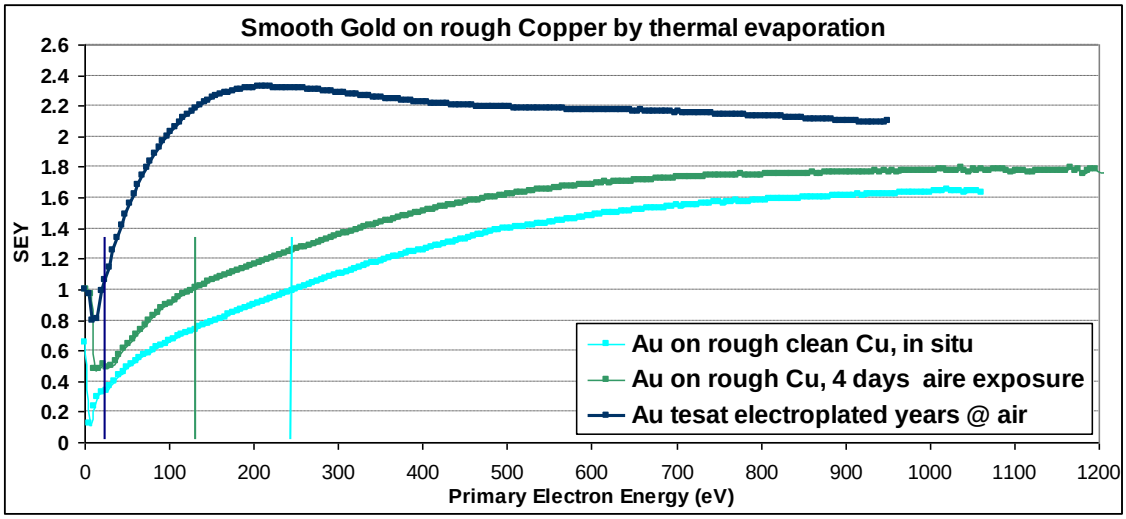

Figure 10. *SEY of the Au/Cu sample, right after Au coating (light blue), and after 4 days at air (green).One sample of normal untreated Au from Tesat is also shown for comparison.*

sample	E_1 (eV)	σ_m	E_m (eV)
Au on Cu, recently coated	**254**	**1.61**	**1010**
Au on Cu aged in air (4 days)	**20**	**1.78**	**1031**
Au by Tesat, air exposed (years)	**129**	**2.32**	**205**

Table III. *SEY parameters comparison for Au/Cu sample*

XPS and EDX analysis

The use of XPS and EDS as complementary chemical analysis techniques showed again its convenience. XPS most sensitive to surface components showed that the Au overlayer was thicker than 3 photoelectron mean free paths, i.e., more than 8 nm, apart from the

common surface contamination with C and O contamination molecules, of about 2 nm. The Ag is also not detected by XPS.

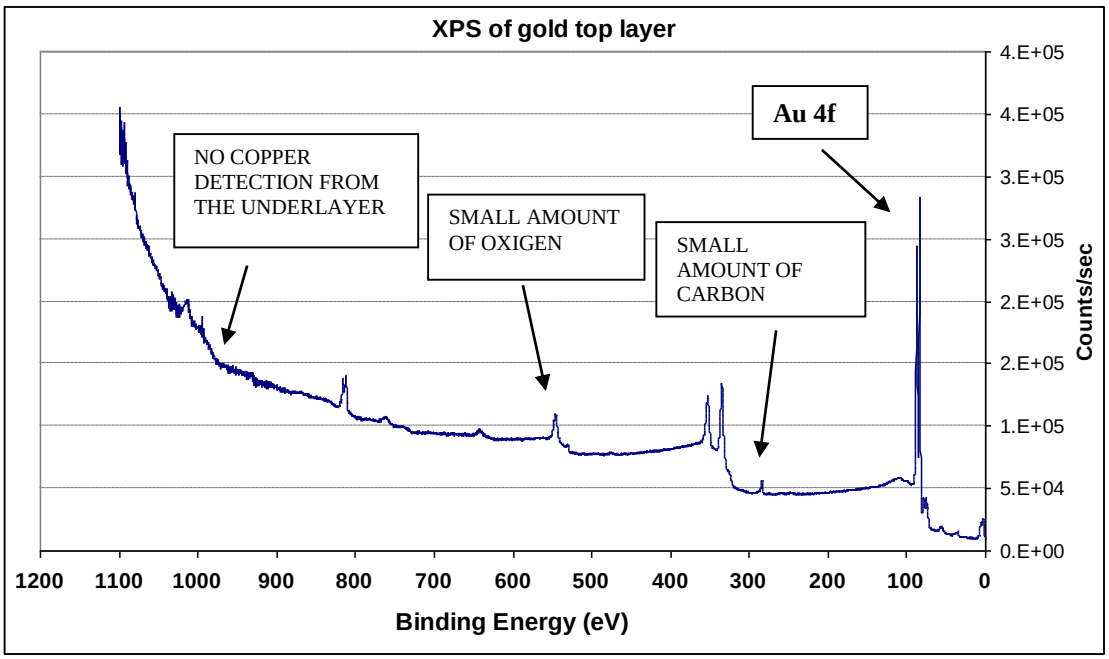

Figure 11. *XPS survey of the gold coated Cu sample by GLAD evaporation technique*

On the other hand, EDX with a probing depth of about 1 μm, showed that the Au overlayer was much thinner than that and the Cu from the GLAD film and Ag from the substrate were clearly detected. However, now, the intensity of the substrate, [Ag]/([Ag]+[Cu]) = 35 %, was certainly closer to the real plain area, see Fig.12 and Table IV. That is because, in this case, the EDX analysis depth barely penetrated into the Ag substrate.

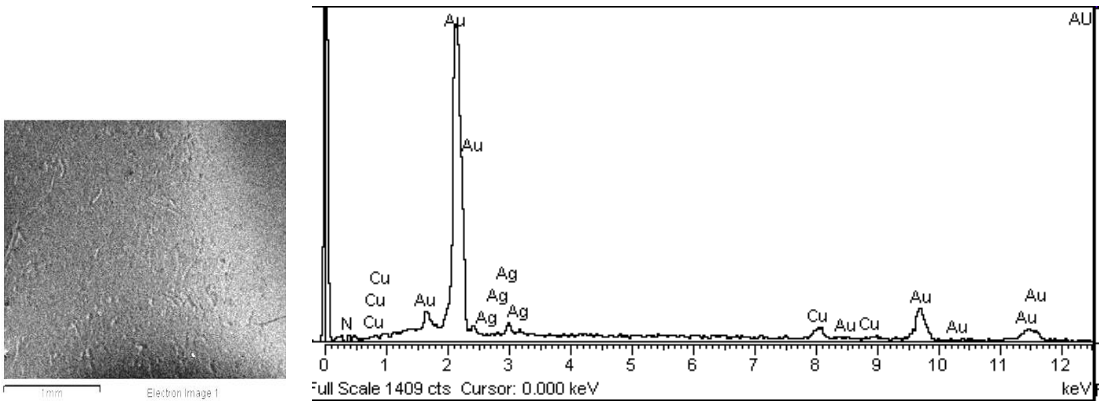

Figure 12. *EDX analysis on 1 mm^{2}region of the gold coated Cu sample by GLAD evaporation*

Element	***AppConc.***	***Intensity***	***Weight%***	***Atomic%***
N K	*0.54*	*0.1981*	*6.50*	*45.3*
Cu K	*2.76*	*1.1292*	*5.87*	*9.0*
Ag L	*1.39*	*0.6330*	*5.26*	*4.8*
Au M	*32.50*	*0.9468*	*82.37*	*40.9*
Totals			*100.00*	*100%*

Table IV. *Constituent elements from the EDX analysis*

The large amount of N was inferred from a poor signal in the EDX spectrum, and thus, probably is an error.

The benefits of using this deposition technique are its versatility in coating a wide range of conductive materials and the possibility to have a geometric control over the size and shape of the grown nano structures. However, limitations in the instrumental setup and the processed samples size discarded this technique as a viable alternative to coat large waveguides samples.

Bibliography chapter 6

[1] Donald M. Mattox, Handbook of Physical Vapor Deposition (PVD) Processing.

[2] E.A. Brandes, G.B. Brook; Smithells. Metals Reference Book, 7th edition, Butterworth-Heinemann, 1992.

[3] K.Robbie, J.C.Sit, and M.J.Brett: "Advanced techniques for glancing angle deposition", J. Vac. Sci. Technol. B, 16 (1998) 1115-1122.

[4] A.C. van Popta, J.M. Sit and M.J. Brett, Hybrid structures, , Proc. SPIE, 2004, 5464: 198-208.

[5] K.Robbie, G.Beydaghyan, T.Brown, C.Dean, J.Adams, and C.Buzea: "Ultrahigh vacuum glancing angle deposition system for thin films with controlled three-dimensional nanoscale structure", Rev. Sci. Instrum., 75 (2004) 1089-1097.

[6] E.Schubert, T.Höche, F.Frost, and B.Rauschenbach: "Nanostructure fabrication by glancing angle ion beam assisted deposition of silicon", Applied Physics A –Materials Science & Processing, 81 (2005) 481–486.

[7] R. N. Tait, T. Samy, and M. J. Brett, Thin Solid Films 226, 196 (1993).

Chapter 7

Wet chemical etching of Ag, Ag-Cu alloy and Au

Wet chemical etching of materials is a well-known technique, widely implemented in micro technological applications, such as semiconductors used for the fabrication of integrated circuits on structured silicon wafers [1-3]. Until the early 1980 s, this simple, efficient method was the dominant for pattern transfer through a mask to underlying insulator, semiconductor or metal layers [4], [5].

The basic principle of a wet chemical etching process is the oxidation of a metal by oxidizing agents followed by formation of metal – ligand complexes to remove the oxidized metal from the surface. The etching rates depend upon the chemical reactivity of metals and the solubility of the ligand complexes [6].

Copper (Cu), silver (Ag), and gold (Au) have drawn attention for a variety of applications because they share unique and similar properties such as high electrical conductivity, corrosion resistance, and reflectivity. These features are consequences of the behavior of valence electrons which originate from the similar electronic structures of group 11 elements: Cu, Ag, and Au [7]. Specifically, electrical resistivity of these materials is lower than that of other metals and the interactions of light with the electron clouds causes surface plasmon resonance (SPR) of these nanostructures to occur at visible frequencies [8].

Because the order of chemical reactivity decreases from Cu > Ag > Au, some etchants can dissolve Cu but not Ag and Au, or Cu and Ag but not Au [9].

Although the electrical resistivity of Au (2.2 μΩ-cm) [7] is higher than that of Cu, the chemical inertness and lower self-diffusion coefficient which translates into improved electro migration resistance relative to other metals suggests that Au can be considered a potential anti multipactor material.

In our study, the etching of silver and gold surfaces was of particular interest due to their high conductivities and stability to air exposure. The main advantage offered by this

technique is its ability to process large samples in chemical baths, which at industrial level could mean a viable economic alternative for technological materials. Several potential etching formulas with strong surface corrosion effect were tried under different conditions.

7.1 Sample definition

7.1.1 Small size research samples

The first trials and the development of the etching process were performed on small research samples (about 12×10×1 mm) and then, the selected process was optimized for Ag plated multipactor samples (RF waveguides) because the dynamics of the etching depended on size and did not work entirely in the same way at large scale.

Samples were originally of Ag plating, Au plating, and Ag-Cu alloy.

The samples of Ag and Au plating were industrial standard coatings deposited electrolytically on aluminium 6061 alloy bulk pieces. The Ag or Au plating is deposited over a first 10 μm thick Ni-P plating for improved adherence over the Al alloy bulk. Ni-P alloy is used for avoiding magnetic properties of Ni.

The Ag-20%Cu samples were cut out of a 50 μm thick foil of the alloy (Goodfellow).

The research samples of 5 μm thick Au plating were cut out of 50×20×1 mm plates manufactured and provided by Tesat Spacecom.

The research samples of Ag plating were quite similar and also provided by the same aerospace company. The thickness of the Ag plating was either 10-12, 16-20, or 38-42 μm.

7.1.2 Multipactor samples

The multipactor samples were actual RF waveguides (Ku-band, WR75 for 11.8 GHz) specially designed and manufactured also by Tesat Spacecom for multipactor and RF performance tests after surface treatment. Their external size was about (40×20×110 mm). They were manufactured of Ag plated Al alloy in three main structures: (i) a waveguide with reduced height gap and transformers on both ends, (ii) a corrugated low pass filter, and (iii) a ridged low pass filter (half of the inner volume). The gap

transformers were of three types as shown in Fig 1. The final geometry of the multipactor tested samples processed by this technique is also shown in Fig.2

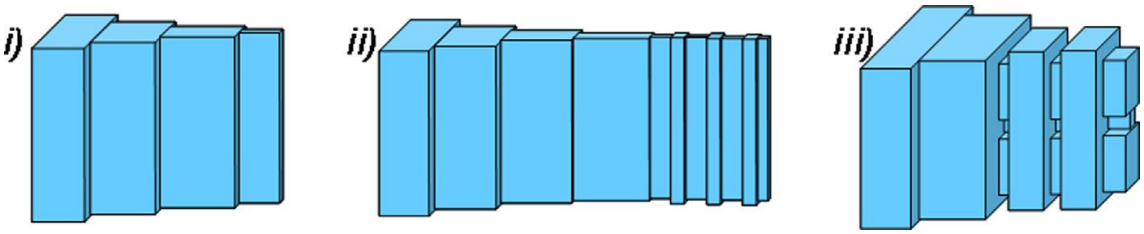

Figure 1. *Schematic diagram for the geometric half - structure of the multipactor samples, (i) reduced height gap transformer, of three types, (ii) corrugated low pass filter, and (iii) ridged low pass filter. Not to scale*

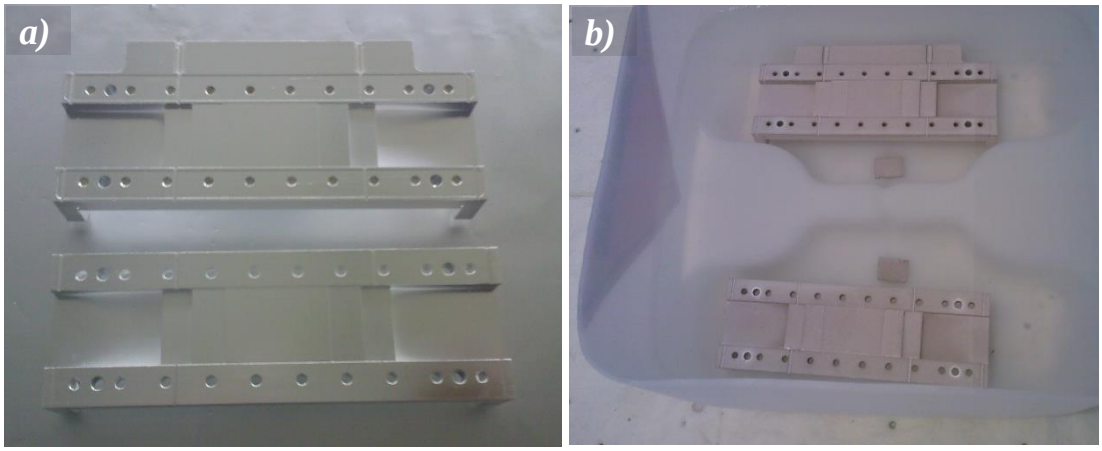

Figure 2. *Photos of the multipactor sample at various stages of chemical etching procedure. a) as received from Tesat, b) after chemical treatment, during second rinsing in deionised water, together with witness samples*

As mentioned before, the selection of metals to be processed by this method was based on the resistivity properties, with priority given to noble metals with a low oxidation potential and thus less chemically reactive, ruling out in this case possible experiments with copper surfaces.

The temperature of the solution is known to play an important part, enhancing in most cases the etching rate. The outcome of an exothermal reaction with metal bulk pieces can also be affected by the heat transfer rate, so each etching process should be adapted for individual geometries and material type.

7.2 Chemical etching of gold

7.2.1 Preparation procedure

Several techniques for chemical attack of Au were tried on Au plating with unsatisfactory results. Wet chemical etching of gold requires a strong oxidizer for separation of the unpaired valence electron, as well as a complex agent which suppresses the reassembly of oxidized Au atoms back into the crystal.

A brief summary of experimental oxidizing agents is described below:

- Diluted "piranha" solution (H_2SO_4 + H_2O_2) at room temperature for 30-50 min provided a set of samples with maximum SEY values ranging 1.8 – 2.1.
- Three other candidates $KI+I_2+H_2O$ (approximate 1μm/min etch rate), $NH_4OH+H_2O_2+CH_3OH$, and HNO_3+HF+H_2O showed similar results, with an insignificant improvement in the E_1 parameter for the last solution.
- A known mixture able to dissolve especially noble metals called "aqua regia" ($HCl+HNO_3$) with 2-4 min etching time produced encouraging results, decreasing the maxim SEY to values of 1.3 –1.4 and high E_1 of 215 eV (see Fig.4 below); but it was still considered not sufficiently low. As a mention, silver is not attacked by aqua regia due to the formation of a silver chloride passivation film.
- Exposure to Hg vapor in low vacuum or in air, producing an increase in SEY.

After each chemical treatment, the samples were rinsed in deionized water with ultrasounds, dried in N_2 flow and put under vacuum for SEY measurements in the least amount of time possible.

7.2.2 SEY results and SEM analysis

The 5 μm thick Au plating small samples treated by aqua regia showed the best SEY behaviour, yet not satisfactory enough to extend the research to a next level of large wave guide filters. Nevertheless the SEM pictures (Fig. 4 a) and b)) show some degree of structuring of the surface after the etching by HCl and HNO_3 mixture, in a mass ratio of 3 to 1. Also, the exposure time to these two acid mixtures was relatively brief in order to avoid further erosion of the Au layer. Longer exposure resulted in peeling off or complete removal of the top layer, making thus the material impracticable.

Shortly after the chemical treatments the samples were submitted first to SEY measurements under vacuum. Figure 3 describes representative negative results of gold plated samples etched in different conditions and types of solutions that are also compared to a reference sample.

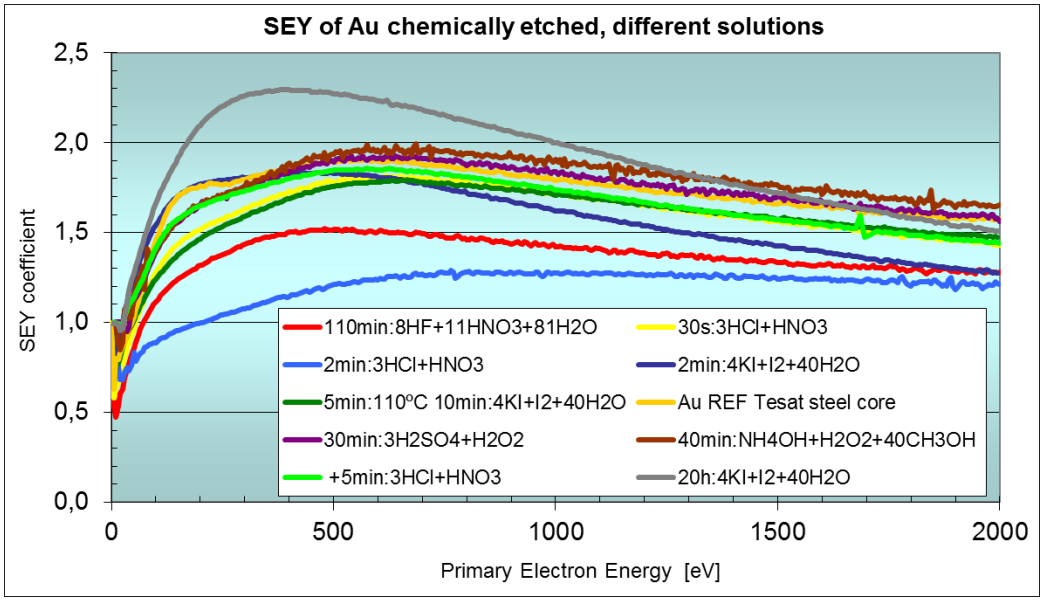

Figure 3. *SEY of gold surfaces chemically etched according to the indicated solution composition and exposure time*

The secondary yield dependency of primary beam for these samples was measured for energies from 0 – 2000 eV. The dispersion in the σ_{max} is quite large and ranges from a minimum of 1.3 (HCl / HNO_3 - 2 minutes) to a 2.4 in the case of KI/I_2, even higher than the non-treated reference sample.

For comparison reasons, the reference sample and the one treated with aqua regia were analyzed by SEM to reveal their surface morphology.

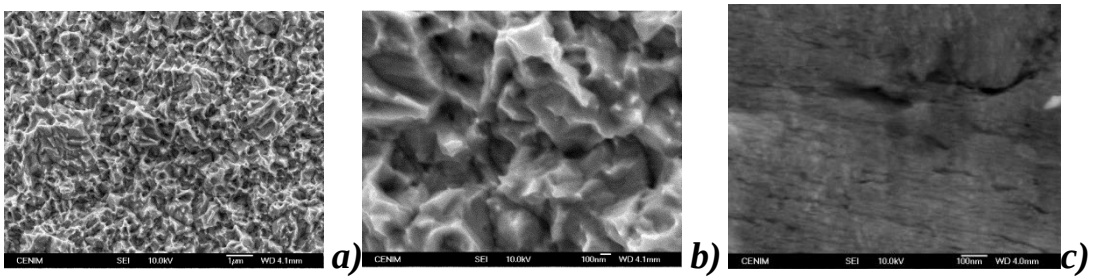

Figure 4. SEM images of a gold surface chemically etched *by a) 3HCl + HNO_3 for 30 s, and b) compared to a reference sample before the treatment, c)*

At 100 nm scale of pictures of Fig 4b) and 4c), the differences of texture for etched and smooth Au surfaces are noticeable. The roughness created by the sharp edges induces only a small decrease in the secondary emission compared with the as received reference

sample. The surface shown does not appear to be of aspect ratio high enough. Considering the nature of the results obtained, further research on Au chemical etching was stopped and reevaluated for different material types.

7.3 Etching of Ag and Ag-Cu alloy

Most of these etching techniques were also applied to small Ag plating samples, with thicknesses 10 – 40 µm, with disappointing results. Except for one particular solution of acids, HF and HNO_3, which was able to produce a rough surface at a controllable etching rate and low SEY values. More than 40 small research samples were treated with different etching solutions, more than 30 of them were etched with a HNO_3+HF+H_2O solution, and about 15 of these with the optimized procedure.

7.3.1 Etching procedure for the small research samples

The optimized composition was 6 volume % of concentrated HF acid and 25 volume % of concentrated HNO_3 acid in distilled water. Note that concentrated acids are not 100 % and that percentage compositions are given as weight %.

Concentrated HF acid (48 wt %)

Concentrated HNO_3 acid (65 wt %)

Distilled water. Details of the chemical products are described in Annex1.

Using molecular weight and density data above, the bath composition would be:

Weight per cent		Molality		Molar per cent		
wt % HF =	3,01	m HF =	0,020	x HF =	3,19	%
wt % HNO3 =	20,45	m HNO3 =	0,042	x HNO3 =	6,87	%

Clean with acetone, methanol, and finally distilled water all instruments to be used, such as beakers, test tubes, holding clips, etc. (note: acetone is not a proper cleaning agent for plastic items).

1) Place a Ag sample in a glass beaker with 100 ml acetone to be cleaned for about 10 min using ultrasounds, then dry it off in nitrogen flow.

2) Prepare 100 ml of HF-HNO_3 solution:

Measure in a plastic calibrated beaker 50 ml of distilled water.

Measure in a plastic container 6 ml of HF (48%) acid.

Measure in a plastic container 25 ml of HNO_3 (65%) acid.

Generally, a large amount of heat is released when strong acids are mixed with water so we added first the acids to the container of water, not the reverse.

Complete this container with additional distilled water until 100 ml of solution.

Allow the solution to cool down to room temperature (the mixing is exothermic).

3) Add 15 ml of HF-HNO_3 solution in a plastic beaker of 25 ml for etching.

4) Place the clean silver sample leaning up against the walls as vertical as possible.

5) Allow 4 min for acid attack in case of 10 μm Ag plating and 5 min for 20 μm Ag samples. For a 40 μm Ag sample, allow only 1 min for acid attack and then take the sample with plastic tweezers and agitate (stirring) it inside the solution for another 1 min.

6) Take the sample out of the acid solution with plastic tweezers and immerse it in distilled water, 100 ml in a glass beaker, under ultrasounds for 10 min.

7) Dry the sample by heating it up to 60°C in air for 10 min, and then allow to cool down to room temperature.

The entire process should be carried out under the corresponding safety conditions: in a soft clean room with laminar flow, using specialized protection equipment (gloves, vapour filtering mask, adequate clothing, goggles… etc).

The procedure described above is essentially the same as for the large multipactor samples, excepting the corresponding larger volumes. The restrains were not so critical for the small research samples in these conditions. The reproducibility was tested with 40 research samples and 10 multipactor samples. Ag plating thickness of 10, 20, and 40 μm were tested; 40 μm was necessary to avoid over etching in sharp corners.

Prior to the chemical etching, surface contamination was removed by successive treatments in ultrasonic baths of acetone, methanol and deionised water, respectively, at room temperature during a total of ten minutes, and then dried out by nitrogen flow.

Once the optimized solution was obtained, two samples of each Ag thickness, nominally 10, 20, or 40 μm, were etched following the procedure above. It was observed that thin Ag coatings (10 μm) sometimes resulted in etching solution reaching the underlying Ni layer thus producing some peeling off and less stable SEY. On the other hand, 40 μm Ag samples were more difficult to etch properly and a special procedure variant (stirring) had to be devised. Consequently, subsequent samples were of 20 μm Ag thickness.

As mentioned before, the size of the roughness was analysed by SEM and the suitable aspect ratio was detected by its "suppression" effect in SEY. This last criterion was much more restrictive that the first one. After sample preparation they were placed in vacuum for surface analysis, with a minimum duration of exposure to air.

7.3.2 Etching procedure for the large multipactor samples

A mixture of 500 cm^3 deionised water (18 MΩ), 60 cm^3 of HF 48 weight % PA-ACS-ISO (M=20.01), then 250 cm^3 of HNO_3 65 weight % PRS (M=63.01), and then 190 cm^3 of water to complete a total volume of 1000 cm^3 is prepared in a high-density polyethylene or similar acid resistant container. Since this is an exothermal reaction, an increase of about 10 ºC above room temperature is detected, along with fumes release at the surface. Then, the solution is poured in a bath, a 2000 cm^3 acid resistant vessel with suitable dimensions for the solution to cover the lying waveguide half shell by 3 cm. Best results are obtained if the solution is allowed to cool down to 28ºC. Once this occurs, one half-shell and its corresponding witness samples are totally immersed at the same time, with the surface to be treated (inner surface of the waveguide) facing upwards. Then, corrosion starts with visible changes in colour shade and brightness of the silver surface during the optimum etching time of about 2 min, 30 sec. The process is also accompanied by the formation of very small gas bubbles over the surface. The most probable reactions, which take place in a cold and diluted mixture, at the unsaturated molar ratio of H_2O: HNO_3: HF = 31.2: 1: 79.1 are:

$$3Ag + 4HNO_3 \longrightarrow 3AgNO_3 + 2H_2O + NO$$
$$4\,AgNO_3 + 2\,H_2O \longrightarrow 4\,Ag + 4\,HNO_3 + O_2$$
$$AgNO_3 + HF \longrightarrow AgF + HNO_3$$
$$4HNO_3 \Leftrightarrow 2H_2O + 4NO_2 + O_2$$

It is known that in acid attack of Ag and other metals, the formation of very small gas bubbles over the surface that eventually coalesce into larger ones may play the roll of a template for the local etching of pores if some dynamical conditions are met [15].

The process is stopped before the surface exceeds the desired level of structuring, by taking the samples out of the bath and rinsing in abundant deionised water, using ultrasound. This step is important and necessary for washing out rest of etchant and small particles from the etching reaction. Field emission from these loosely attached particles

will trigger multipaction, a well-known problem in other technologies [10]. As a final step, the samples are dried with nitrogen flow and stored in UHV conditions. The entire procedure and conditions are repeated for the second half-shell of the waveguide and its corresponding witness samples.

7.3.3 SEM analysis of the small research samples

The samples characterized by SEM (see Figs.5, 6 and 7), presented high aspect ratio surface morphology in the range of microns which performs as a multi-Faraday cage for the incoming electrons, resulting in an overall electron suppression effect. A sponge-like pattern of points and edges was generated by the chemical etch. With other etching formulas, an ample variety of morphologies was found, see Fig.8. In SEM images of Figs. 5-7, it can observed that the sponge-like structure is the main and efficient cause of SEY *suppression*. Macroscopically, the samples lost their brightness and acquired darker tone of colour, due to the enhanced absorption of the electromagnetic radiation by the curved surfaces.

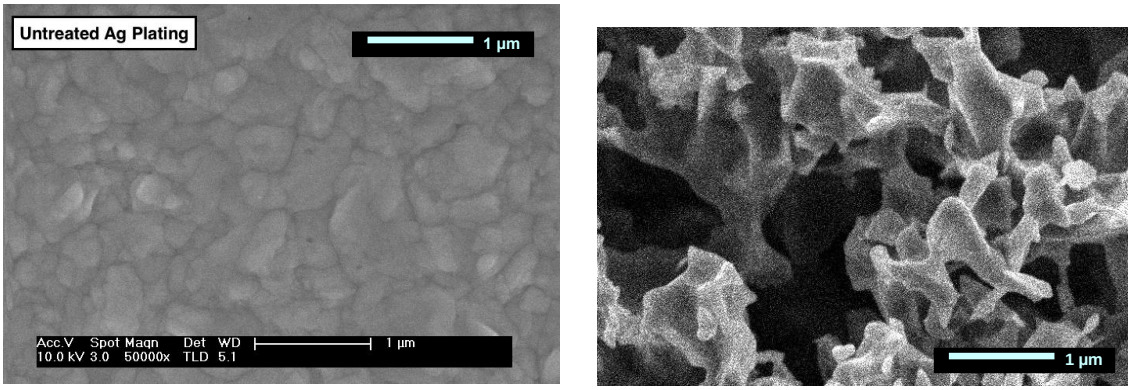

Figure. 5 *SEM images of Ag plating as received (reference sample) and after chemical treatment in HF-HNO_3 acid mixture, at same scale of 1µm*

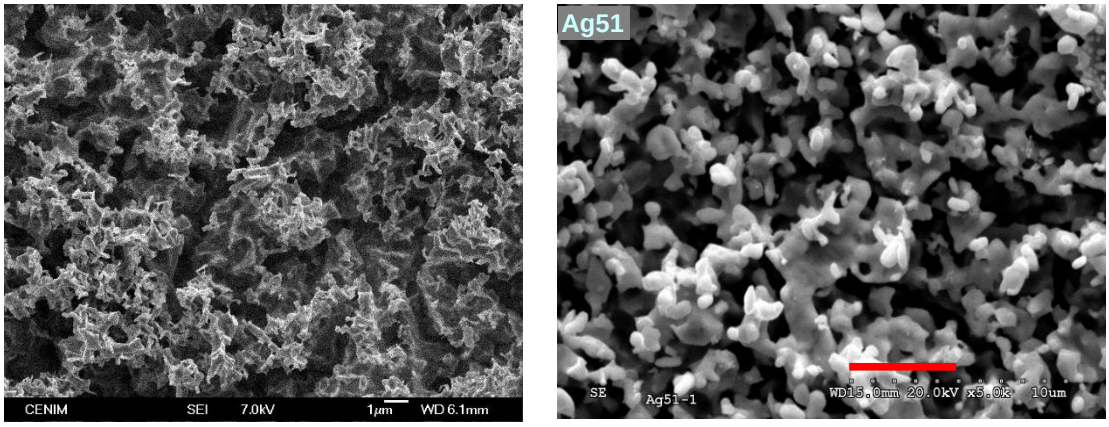

Figure 6. SEM images of Ag plating roughened by the optimized chemical etching
Left: SEY: E_1 = --, σm = 0.89, E_m = 950 eV.
Right; E_1 = --, σ_m = 0.91, E_m = 765 eV. The red scale segment represents 5 μm

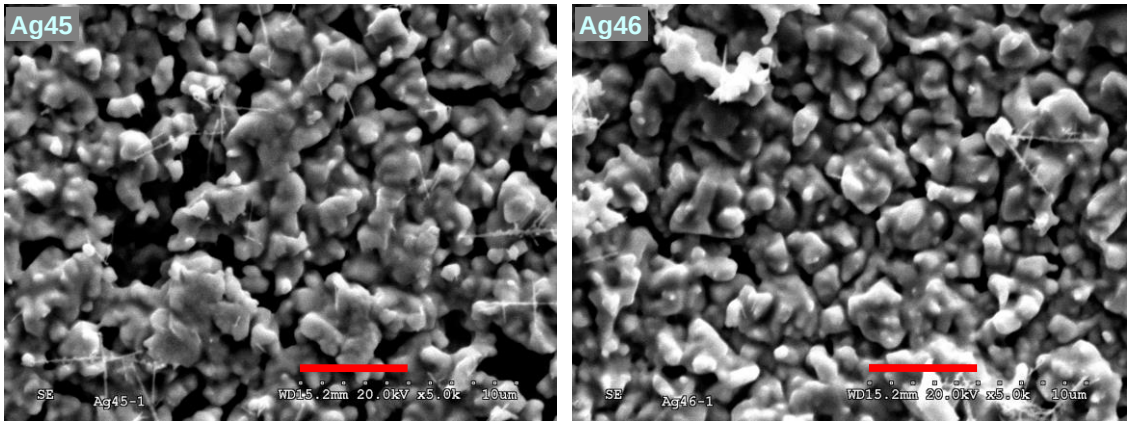

Figure 7. *SEM images of Ag plating roughened by the optimized chemical etching*
Left: SEY: E_1 = 487 eV, σ_m = 1.06, Em = 1025 eV.
Right: SEY: E_1 = 196 eV, σ_m = 1.24, E_m = 705 eV. The red scale segment represents 5 μm.

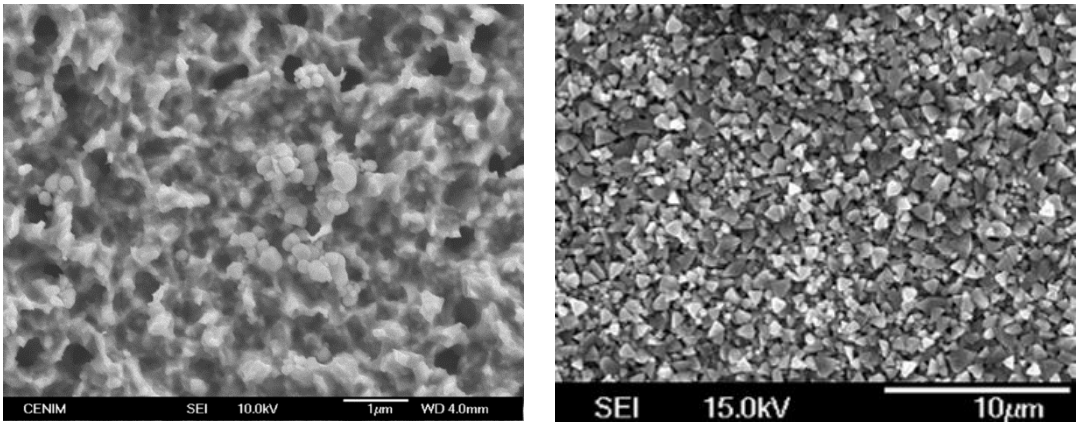

Figure 8. *SEM images of Ag plating roughened by other chemical etching formulas*
Left: NH4OH+H2O2+5CH3OH for 4 min, SEY: E1 = 120 eV, σm = 1.30, E_m = 670 eV. Right: 4KI+I2+40H2O for 30s. , SEY: E1 = 57 eV, σm = 2.1, E_m = 590 eV.

For a first experience, a Ag-20%Cu alloy was used with the same etching solution formula used for Tesat Ag-plated aluminium samples. The sample was cut out of a 50 μm thick

foil of the alloy (Goodfellow) and etched in 6 vol.% HF + 25 vol.% HNO3 in water for 5 min. No different behaviour from pure silver was perceptible. The alloy has also the same appearance of pure silver.

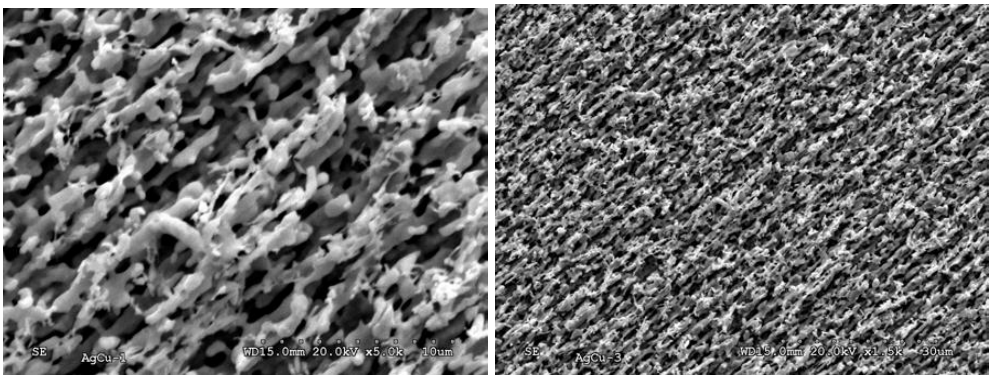

Figure 9. *SEM images of a Ag-20%Cu surface roughened by chemical etching 6 HF + 25 HNO_3 for 5 min.*
SEY: E_1 = 282 eV, σ_m = 1.11, E_m = 575 eV, σ2000 = 1.01

The surface morphology is similar to the pure silver samples (after etching) but with a strong directional texture, probably due to grain microstructure of the original alloy foil.

The analysis of the relation between surface morphology and SEE properties should be done with an appropriate image software tool or rather, with AFM (atomic force microscopy). However, it is easy to appreciate that deeper roughness is associated to better secondary emission properties. This supports the working hypothesis of this research.

Another important observation can be made. There is relative wide variety in the surface morphology resulting from applying supposedly the same surface treatment to identical surfaces. The chemical attack seems to be sensitive to minute differences in the processing conditions, including those of the initial surface. It might be discerned a possible influence of the initial Ag layer thickness.

Roughness sizes bellow 10 μm were necessary for the geometrical precision, required by the microwave wavelength of the multipactor samples.

7.3.4 SEY analysis of the small research samples

The study of the reproducibility and efficiency of this treatment required a statistical analysis. A summary of SEY results for samples treated with the optimized etching solution, are presented in and Fig.10 and also in Table 1.

The dispersion of these experimental results was studied assuming a normal distribution.

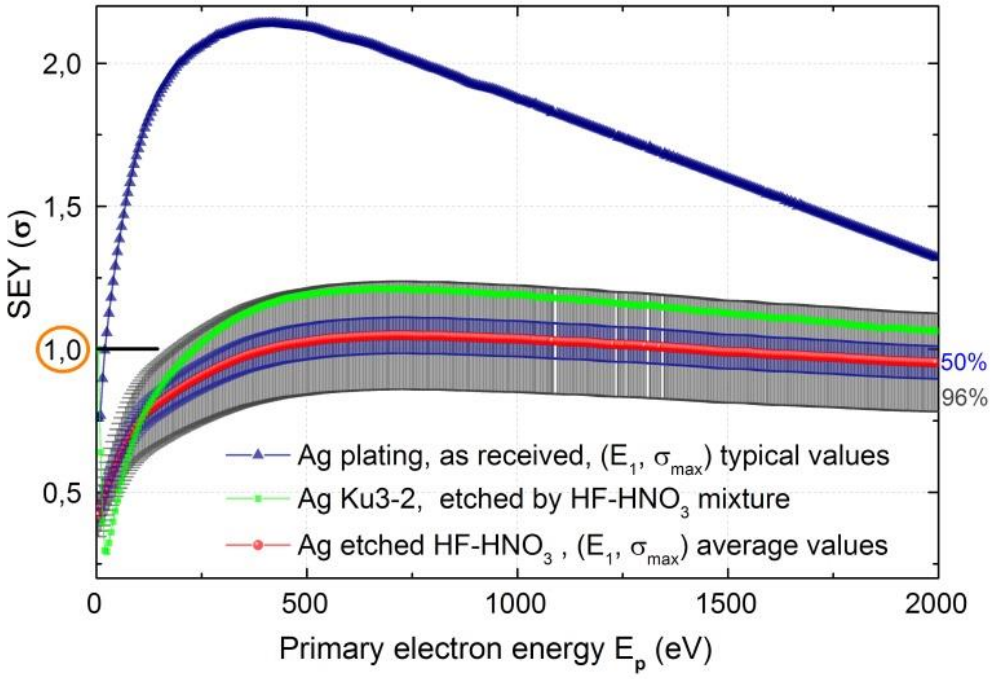

Figure. 10. *Comparison between high SEY coefficient of the "as received", smooth plated silver and the average values of wet chemically etched research samples.*

The mean or average value was computed for each primary energy as well as its typical deviation. Thus, the SEY limits for 50 and 96 % of the samples could be predicted. These estimations are also shown in Fig.10. Since only the upper SEY limits are of interest for the application (anti-multipactor) the prediction is that 75 % of the cases will have SEY $\leq$ 1.1 and $E_1 \geq$ 300 eV. However, a careful observation of the experimental data shows that the distribution does not seem to be normal. In fact, 70 % of the samples fall well inside of the predicted 50 % dispersion limits. Thus, in fact, the prediction is that 85 % of the cases will have SEY < 1.1 and E_1 > 300 eV. On the other hand, about 30 % of the cases show large dispersions (but only 15 % positive), larger than predicted by a normal distribution. Therefore, the conclusion of the reproducibility study seemed to be that there were some uncontrolled accidental factors that produced a few cases altering the average of the reproducible good SEY values of most of the samples.

Sample		SEY properties			
Name	Thickness (μm)	E_1 (eV)	σ_m	E_m (eV)	σ_{2000}
Ag38	10 – 12	353	**1.08**	840	0.99
Ag39	16 – 20	800	**1.00**	800	0.93
Ag40	10 – 12	551	**1.02**	670	0.93
Ag41	16 – 20	755	**1.01**	765	0.94
Ag42	38 - 42	327	**1.08**	730	0.98
Ag43	38 - 42	353	**1.08**	720	0.98
Ag44	16 – 20	418	**1.55**	535	1.18
Ag45	16 – 20	487	**1.62**	600	1.30
Ag46	16 – 20	196	**1.24**	705	1.06
Ag47	16 – 20	390	**1.09**	990	1.02
Ag48	16 – 20		**0.85**	650	0.68
Ag49	16 – 20	204	**1.17**	620	1.00
Ag50	16 – 20	400	**1.04**	670	0.93
Ag51	16 – 20		**0.91**	765	0.87
average		**410**	**1.05**	**740**	**0.95**
50 %		> 300	± 0.06	± 20	± 0.07
96 %		> 200	± 0.19	± 28	± 0.19

Table. 1 *Statistics on the SEY properties of several small samples of similar size, treated with the optimized etching solution in the same conditions*

The defects in the surface preparation could be either in the Ag plating of the aluminium substrates or in the chemical etching of their surface. Observations of the etching process pointed to the first.

7.3.5 Surface analysis by XPS and EDX

The surface analysis of the etched samples was crucial in determining the chemical composition, since this particular method can produce undesired possible residual contaminants or silver halides/ nitrates formation after the etching.

The surface composition and contamination of the silver plating was analysed by EDX and XPS at two depth scales, 1 μm and 5 nm, respectively, at two stages or states: as received and after chemical etching.

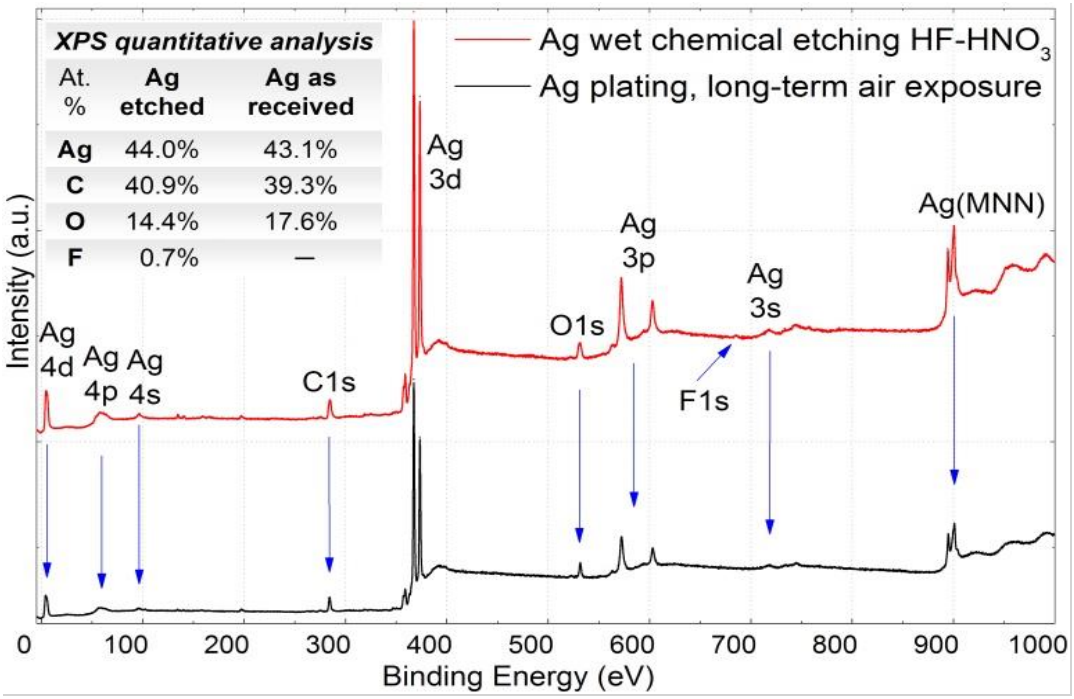

Figure 11. *XPS analysis comparing the chemical composition of a silver reference surface and same sample after the wet chemical etching treatment*

From the XPS intensities of the Ag 3d, C 1s, O 1s, and F1s core levels and the corresponding XPS atomic sensitivity factors [11], the near surface composition was calculated and illustrated in Fig.11. This is the approximate average composition in a depth of the order of about three photoelectron escape depths, i.e., 8 nm. It is only approximate because the depth distribution of those elements affects that resulting average composition. In addition, no Ag oxide or salt could be detected in the Auger MNN transition (it is not detectable in the 3d core level) [12]; this sets a limit to the amount of surface oxide, below 10%. Thus, it can be concluded that the surface of the silver plating was very similar for both states: a carbonaceous surface overlayer typical of the exposure to air and a silver bulk. The only minor modifications due to the chemical etching process were a small increase (20%) of the contamination carbonaceous layer, a smaller (19%) oxygen composition of this overlayer, and a very small F contamination. The thickness of the carbonaceous surface layer could be estimated from quantitative XPS, if the C atomic density in the overlayer is determined. The relevant equation [13], [14] of quantitative XPS is:

$$\frac{I_C}{I_{Ag}} = \frac{S_C}{S_{Ag}} \frac{N_C}{N_{Ag}} \frac{1-\exp(-d/\lambda)}{\exp(-d/\lambda)}$$

where I is the XPS intensity, S is the XPS sensitivity factor, N is the atomic density, λ is the inelastic mean free path of the photoelectron (≈ 2.9 nm, for C 1s and Ag 3d photoelectrons in the overlayer), and d the thickness of the overlayer. For computing d, we needed a model compound of well-known specific values for the necessary data, mainly N_C. Assuming a $C_5O_2H_8$ initial composition as the closest model, the calculated thickness would be in the range of 2 – 3 nm for both states / stages.

Other EDX measurements, using an Oxford Instruments analyser (model INCAx - sight), were also performed to determine bulk composition. No other impurities were detected.

We estimated that an approximate layer of 8 μm in depth of silver was totally removed during the etching process, justifying thus the need for a thick initial plating.

These surface analyses showed that the surface of Ag chemically etched was chemically very similar to that of the untreated as-received Ag plating and that all the SEY reduction is due to the surface roughness of high aspect ratio of the treated surface.

7.3.6 Aging effects

Several samples of the standardization study, were analysed over time in order to monitor the ageing of the SEY, up to five months. The results are summarized in Table 2, with measurements performed after 1 month and 5 months, for the specified samples. The results can also be corroborate with the initial reported values described in Table 1. These measurements confirm a preliminary conjecture: the initial effect of air is a decrease in SEY mainly for low primary energies. Short term ageing in air is shown in logarithmic graphs of Fig. 12.

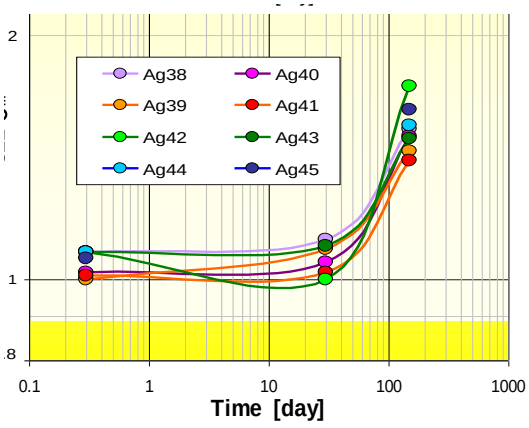

Figure 42. *Logarithmic evolution of σ_{max} coefficient on short term air exposure*

Sample		SEY properties							
		After 1 month air exposure				After 5 month air exposure			
Name	thickness µm	E_1 eV	σ_m	E_m eV	σ_{2000}	E_1 eV	σ_m	E_m eV	σ_{2000}
Ag38	10 – 12	483	1.12	955	1.04	74	1.53	485	1.15
Ag40	10 – 12	556	1.05	1140	0.99	87	1.50	510	1.16
Ag39	16 – 20	434	1.09	905	1.05	81	1.44	510	1.15
Ag41	16 – 20	716	1.02	1080	0.95	87	1.40	580	1.18
Ag42	38 – 42	908	1.00	1035	0.95	78	1.73	525	1.32
Ag43	38 – 42	503	1.10	1020	1.05	91	1.49	535	1.12
Ag44	16 – 20	--	--	--	--	89	1.55	535	1.18
Ag45	16 – 20	--	--	--	--	93	1.62	600	1.30
Average		**600**	**1.06**	**1023**	**1.01**	**85**	**1.53**	**535**	**1.20**

Table. 2 *Statistics on the SEY aging properties of several small samples exposed to air*

There is no physical basis to make a long term prediction of the evolution of SEY with exposure to the air. We can relay only in the generalization of the experimental results to estimate the rate at which a certain surface deteriorates.

7.4 Conclusions

A simple and efficient method of chemical treatment was used to structure silver surfaces in range of microns. This method has its limitations in terms of material type and its original state. Sponge-like structures increase the surface area and modify thus the electrical properties of treated silver. A HF/HNO_3 over-etching of under 10-µm-Ag samples easily reaches close to the Ni-Ag interface and results in easy peeling of Ag coating, so higher initial thicknesses were required. Values of maximum SEY of 1.05±0.05 were reproducible. A diluted solution allows better control of the etching process.

The mechanisms of Ag surface roughening by HF+HNO3 chemical etching was not definitely clarified, however, some suggestion may be made:

- the reaction of the HF+HNO_3 aqueous solution with Ag produces $AgNO_3$, AgF, and O2 and NO gases; and sub-microscopic gas bubbles are formed (AgNO3 is moderately soluble in HNO_3+H_2O, AgF is very soluble in $AgNO_3$+HNO_3 aqueous solution),
- gas bubbles act as etching template by controlling reactant access to the Ag surface and thus are critical for pore formation, if they are not sufficiently stagnant pores are not etched but smooth fast erosion results [15].

Roughness sizes bellow 10 μm were necessary for the geometrical precision, required by the microwave wavelength. The observed aging in SEY properties was a drawback and suggested further research on improving the stability upon air exposure.

Bibliography chapter 7

[1] C. Benoit-Moez, S., Bastide, C. Lévy-Clément, Silicon Nanowires. Condition of Synthesis and Size Selection, 23rd European Photovoltaic Solar Energy Conference and Exhibition, Sept. 2008, Valencia, Spain, pp. 641–644.

[2] M. Steinert, J. Acker, M. Krause, S. Oswald, K. Wetzig. Reactive species generated during wet chemical etching of silicon in HF/HNO3 mixtures, J. Phys. Chem. B110 (2006) 11377–11382.

[3] Kurt W. Kolasinski, Silicon nanostructures from electroless electrochemical etching, Current Opinion in Solid State and Materials Science, Volume 9, Issues1–2, February–April 2005, pp. 73–83, ISSN 1359-0286.

[4] Ranade R. M., Ang S. S., Brown W. D., J. Electrochem. Soc., 140, 3676 (1993).

[5] Williams K. R., Gupta K., Wasilik M., Microelectromech. Sys, 12, 761 (2003).

[6] Xia Y., Kim E., Mrksich M., Whitesides G. M., Chem. Mater., 8, 601.

[7] Trigg G. L., Immergut E. H., Encyclopedia of Applied Physics, Vol. 18, VCH, NY, 1997.

[8] Jain P. K., Huang X., El-Sayed I. H., El-Sayed M. A., Plasmonics, 2, 107 (2007).

[9] Xia Y., Kim E., Mrksich M., Whitesides G. M., Chem. Mater., 8, 601 (1996).

[10] H. Padamsee, J Knobloch, "The Nature of Field Emission From Microparticles and the Ensuing Voltage Breakdown", SRF 981021-14, RF ’98 conf. (1998).

[11] C. D. Wagner, D. Briggs, M.P. Seah, "Practical Surface Analysis", Vol. 1., 2nd Edition, published by J. Wiley and Sons in 1990, ISBN 0-471-92081-9.

[12] A. M. Ferraria, A. P. Carapeto, A. M. Botelho do Rego: "X-ray photoelectron spectroscopy: silver salts revisited", Vacuum 86 12 (2012) 1988-1991.

[13] M.P.Seah, "Quantification in AES and XPS", in "Surface Analysis by Auger and X-ray Photoelectron Spectroscopy", D.Briggs, J.T.Grant (ed.), IM Publication and Surface Spectra, 2003, p.345.

[14] D. Y. Petrovykh, J. M. Sullivan and L. J. Whitman: "Quantification of discrete oxide and sulfur layers on sulfur-passivated InAs by XPS”, Surf. Interface Anal. 2005; 37: 989-997.

[15] A. D. Pauric, S. A. Baig, A. N. Pantaleo, Y. Wang, and P. Kruse: "Sponge-Like Porous Metal Surfaces from Anodization in Very Concentrated Acids" Journal of The Electrochemical Society, 160 (1) C12-C18 (2013).

Annex 1

Products specifications:

Fluorhydric acid HF 48% PA-ACS-ISO (M=20,01) from Panreac S.A. manufacturer.

-quantity: 1L plastic container

-code: 131028.1211

-purity: 48% (M=20.01)

-density: 1.16

Nitric acid HNO3 65% PRS (M=63.01) from Panreac S.A. manufacturer.

Product specifications

-quantity: 1L glass container

-code: 143255.1611

-purity: 65% (M=63.01)

-density: 1.395

Distilled water: 18.2 Mohm.cm

Chapter 8

Multipactor (MP) and Insertion Losses (IL) tests on treated low band pass filters waveguides

8.1 Introduction

In the first ESA research project (AO4025-CCN2), the result of the preliminary research on different materials and techniques described in chapters above, was that silver chemically etched was the surface material with better potential for applying in multipactor samples to be tested for RF performance and Multipactor breakdown.

In this chapter, the final tests on the multipactor samples with that final coatings, based on **chemical etching**, are reported firstly, Sec.8.1 – 8.5. The process how the successful surface treatment defined (selected) was refined for coating the multipactor waveguide samples, is also described in an approximate chronological order. This is described with some detail since it is the culmination of the previous research work, the application to real devices of interest in space technology.

That research (ESA AO4025-CCN2) achieved excellent results in the practical suppression of multipactor discharge but, in spite of insertion loss being improved respect to the reference *Alodine* anti-multipactor coating, it was however still high for the new requirements of space industry. Thus, in the second ESA research project (ITI), the research was focused in improving insertion loss while maintaining high multipactor threshold levels. This was attained roughening the Ag plating by ion etching assisted by mask sputtering deposition, the **sputtering** based technique, as described in chapters above. *Sec.8.6 – 8.8* reports on the final Insertion Loss and Multipactor tests of multipactor samples treated by the *sputtering technique*.

Chemically etched silver surfaces

First, the chemical treatment developed for small research or witness samples had to be adapted and optimized for the larger waveguide multipactor samples. This was not trivial as it is shown in chapter above. Pieces of Ag-plated aluminium more or less similar to real waveguides (called bricks) were supplied by Tesat for this task.

A Ag-plated aluminium multipactor sample with the surface treated by the optimized procedure for chemical etching was tested in ESTEC together with an untreated sample for reference. A poor multipactor level of 1100 W compared to 700 W of the reference sample, was the result. This led to test a new surface coating: gold-coated chemically etched silver.

This bad behaviour of the chemically etched silver surface, in spite of its low SEY, could be due to either field emission by sharp points of the surface or to a fine powder left by the chemical treatment which was not cleaned out in that first multipactor sample.

Gold-coated chemically-etched silver surfaces

As a consequence of that bad result, continuing research on coatings led to try a thick coating of gold (2 μm) on chemically etched silver obtaining a significant improvement of the SEY. Thus, this treatment was applied to the first multipactor sample (with a chemically etched silver surface) and then it was tested again in ESTEC. This sample showed no multipactor discharge when tested up to 5300 W. This is practical suppression of Multipactor and an excellent accomplishment of the project main goal.

Later, another four Ag-plated aluminium multipactor samples were treated with a refined procedure and sent to ESTEC for testing.

Finally, all the five multipactor samples were tested at Tesat with good general results which showed the extraordinary potential of this surface treatment for suppressing the multipactor effect.

Gold-coated mask-sputtering-ion-etched silver

Since the insertion loss enhancement due to the micron-scale surface roughness of the Au-coated chemically-etched Ag plating was still high for some new advanced RF devices (harmonic low-pass corrugated filters) of interest in space industry, the new technique based on sputtering was developed for ion etching the surface roughness of appropriate size and shape. Eight harmonic low pass filters as multipactor samples were treated for optimizing that technique described in chapters above. Finally, practical suppression of multipacting and roughness enhancement of insertion loss was achieved which is reported in *Sec.8.6 – 8.8.*

8.2 The initial MP sample treated by chemical etching

8.2.1 Introduction

Initially, only one multipactor sample was tested for multipactor at two stages: i) after chemical etching, and ii) after subsequent coating with Au; apart from the reference aluminium sample with the standard Ag plating surface, in order to corroborate the surface treatment in real RF devices before possibly ruining all the multipactor samples.

These two stages (i and ii) are equivalent to two well differentiated multipactor samples of the same structure but with different surface material and roughness.

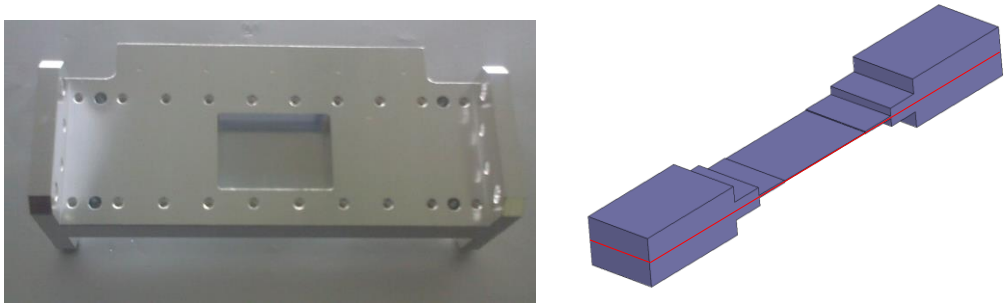

Figure 5*. External appearance and internal space structure of the first multipactor sample. WR75 12 GHz transformer 0.14 mm gap, of Ag-plated aluminium, from Tesat. The wave guide was split in two halves*

Two identical multipactor samples (transformers with 0.14 mm gap, see Fig.1) of Ag-plated aluminium were received from Tesat Spacecom. One was later sent back to ESTEC for testing as a reference sample. The other one was chemically treated (etched) with the optimized etching procedure, and sent to ESTEC in 24 hours. After RF testing a few days later, this same mutipactor sample was returned to Madrid for further treatments, as a consequence of new results on Au coating. It was coated with Au and sent to ESTEC for testing on the next day. The RF testing at ESTEC is concisely described in *Sec.8.2.4*, below.

The gold coating of the multipactor sample with the etched silver surface was undertaken because of its poor multipactor level did not at all correspond to the low SEY measured and because some preliminary experiments showed a lowering of SEY for thick Au coatings on etched Ag surfaces.

More details on the two tested surface treatments: chemical etching and subsequent Au coating, are given in the following.

8.2.2 Chemically-etched silver-plated multipactor sample

The (first) multipactor sample as received is shown in the photo (a) of Fig.2. Other photos in this figure show this sample at different stages after chemical treatment, where it is possible to appreciate some surface "defects". The chemical etching procedure is described above in *Chapter 7*.

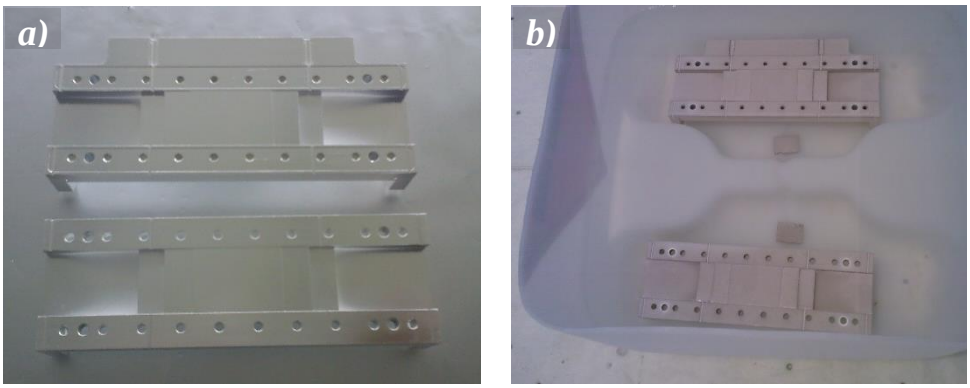

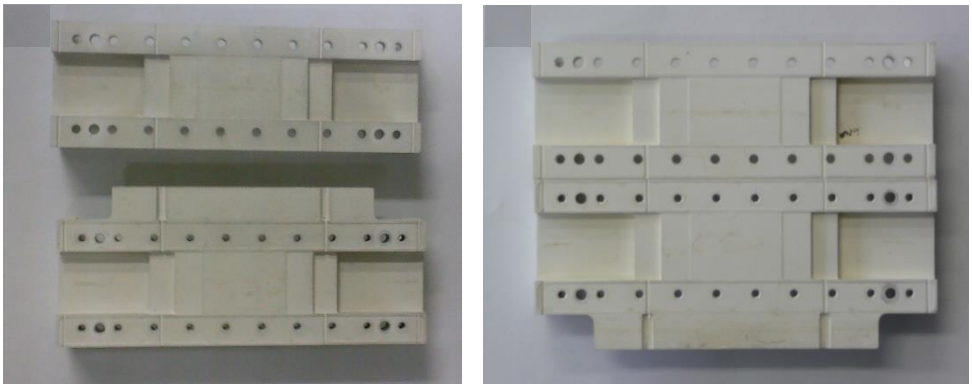

***Figure 2. Photos of the first multipactor sample at various stages of chemical etching procedure**. a) As received from Tesat, b) after chemical treatment, during second rinsing in deionised water, together with witness samples, c) after drying, before sending to ESTEC, and d) as received from ESTEC, where RF testing was performed.*

SEY and SEM analysis

The parameters of the SEY - primary energy curves measured on appropriate witness samples are included in Table 2 below, along with the measured multipactor power level.

In Fig.3, we present SEM images of the witness samples showing characteristic surface roughness.

Both analyses would allow predicting an extremely high multipactor power level in clear contradiction with the results of testing.

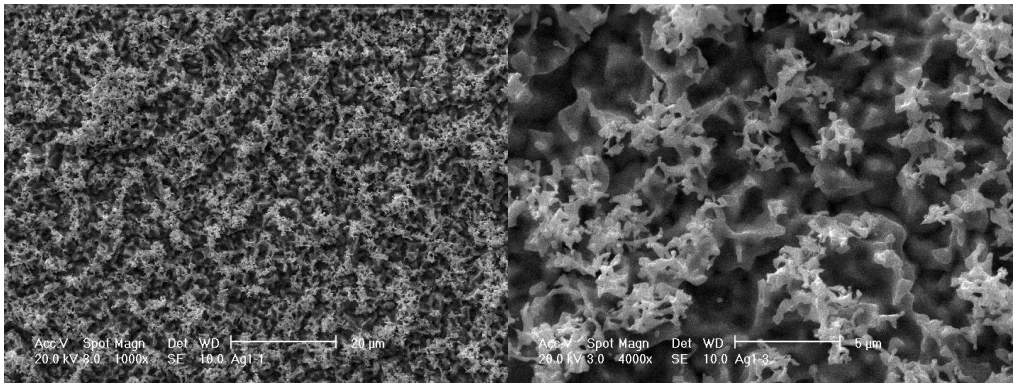

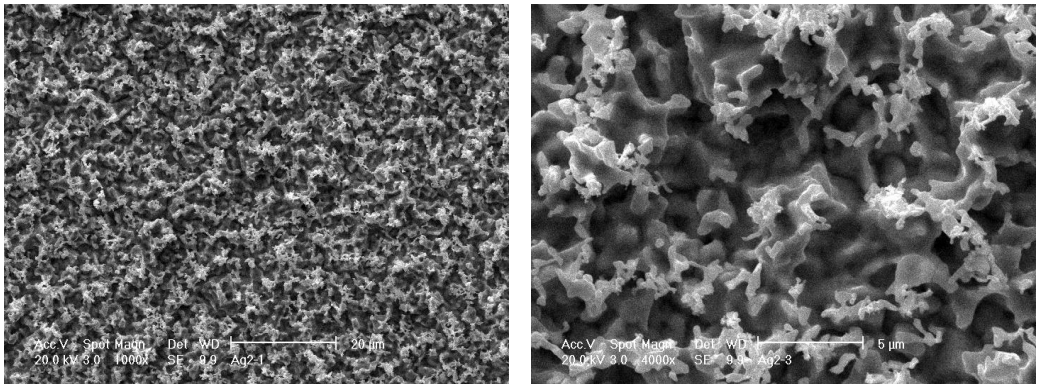

Figure 3. SEM images of the first Ag-plated multipactor sample after chemical treatment*. Witness sample 1, top, and 2, bottom, showing the same surface morphology.*

8.2.3 Au-coated chemically-etched Ag-plated multipactor sample

Preliminary trials

During the preliminary research on potential materials and techniques, it had been observed that coating etched silver with a thin layer of gold produced a light increase of SEY for all energies which discouraged any further investigation on this line. However, while the magnetron sputtering system was being attuned for coating rough dark anodized aluminium, several experiments showed that a thick layer of gold on etched silver could produce a decrease of SEY for low energies.

In Fig.6 and Table 1, we present those results for the samples corresponding to the 3rd trial in the optimization of the etching procedure. The effect of Au coating, a decrease of SEY for low energies, was different for the brick and the corresponding witness and seemed to be more related to the type of surface roughness than to the SEY of the substrate. The SEY curves of the coated rough surfaces should be compared to the SEY of the same coating on a flat smooth substrate such as a highly-polished single-crystal Si wafer. The decrease respect to this SEY curve should be explained by the resulting surface roughness of the Au coating, since no influence at all is expected from the underlying material.

The aim in coating the etched silver surfaces with gold was not only to improve SEY properties but also to modify the surface material, seeking a possible surface material effect, a better stability in air, for example.

Au coating of the multipactor sample

The RF magnetron sputtering system used for coating with Au was described in a previous chapter. Fig.4 depicts a scheme of the experimental arrangement used for coating the two multipactor sample halves. The sputtering conditions were: Ar residual pressure of 6×10^{-2} mb, RF power of 100 W, substrate temperature of 50 - 60 ºC due to the plasma (heating lamps off), and deposition rate of 65 – 85 nm/min. The angle of incidence of the sputtering beam (≈25º) and the rotating sample stage allowed a more uniform coating of differently oriented surfaces and edges. Photos in Fig.5 show the multipactor sample and several witness samples in the sample stage out of the sputtering system.

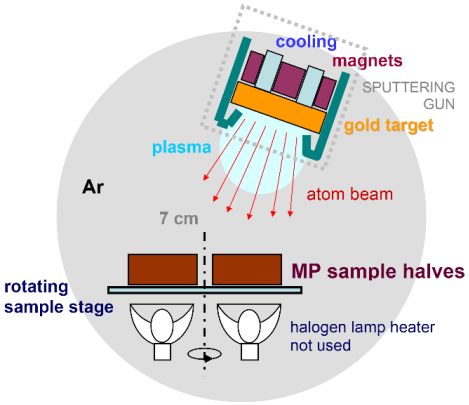

Figure 4. *Gold coating of the multipactor sample by RF magnetron sputtering. Experimental arrangement.*

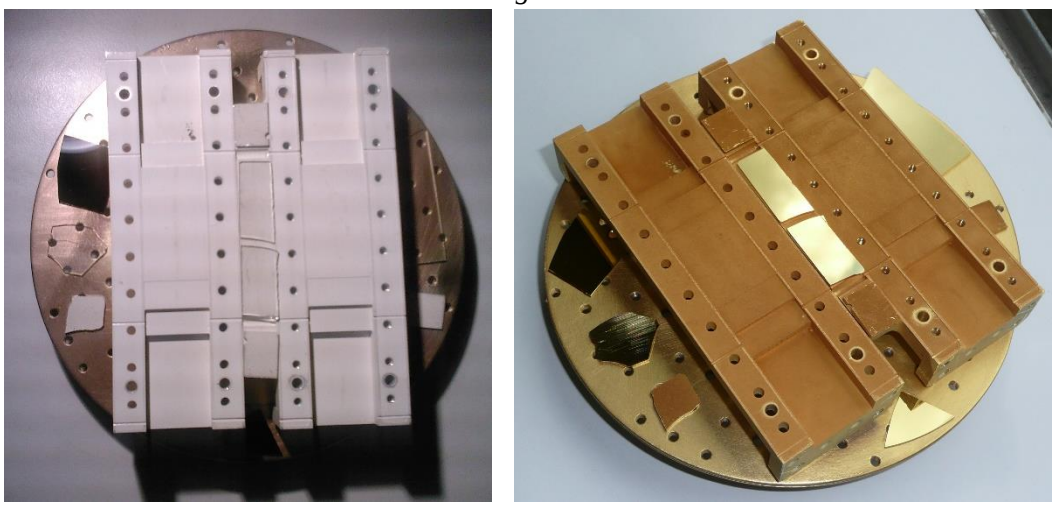

Figure 5. Photos of the first multipactor sample in the sample stage of the sputtering system*, RF magnetron, just before and after deposition of a Au layer of 2 μm thickness. The left photo corresponds to the chemically-etched silver plating. The length of the multipactor sample is 113 mm. Several witness samples are also shown. The differences in reflecting the light allow to identify the rough surfaces.*

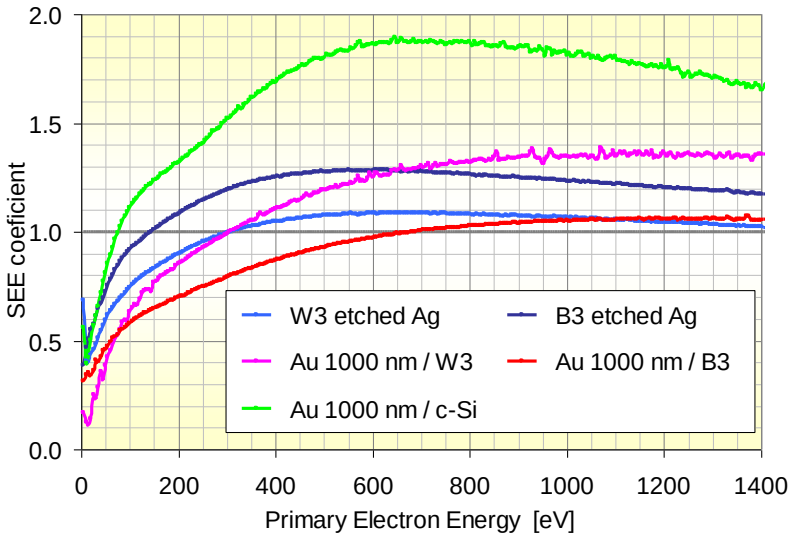

Figure 6. SEY of Au-coated chemically etched Ag plating, preliminary trials. *Effect of coating with 1 - 1.5 μm Au two chemically-etched Ag plated samples: brick #3 and corresponding witness. The SEY of a highly-polished single-crystal Si wafer coated simultaneously is shown for comparison.*

Table 1. Effect of Au coating on SEY of chemically-etched silver, preliminary trials. *SEY parameters of data in Fig.6, Au coating of 1 - 1.5 μm.*

Sample	E_1 / **eV**	σ_m	E_m / **eV**	σ_{2000}	***FoM***
W3 (witness)	307	1.09	670	0.96	16.8
B3 (“brick”)	144	1.28	620	1.10	10.6
Au-coated W3	307	1.36	1115	1.27	15.0
Au-coated B3	683	1.06	1370	1.03	25.3
Au-coated polished Si	77	1.88	668	1.26	6.4

SEY and SEM analysis

In Fig.7, we present the SEY curves of the first multipactor sample (measured on corresponding witness samples) before and after coating with a 2.0 – 2.5 μm Au layer. The corresponding SEY parameters are presented in Table 2. The effect of Au coating on

the SEY was similar to that found for 1.0 – 1.5 μm coatings in preliminary trials and described above.

The resulting surface morphology after Au coating is shown in the SEM images of Fig.8. They should be compared to those in Fig.3. Since, there seems to be no reasons based on SEY properties for such a difference on multipactor power level between the etched silver and the gold coated surfaces as shown in Table 2, an explanation should be sought based on other surface properties. Surface morphology observed by SEM suggests another explanation based on the different shape of the profile of the surface roughness. A profile with sharp points could produce field emission effect under the strong RF field. This field is not present during SEY measurements. However, the sharpness of the profile does not seem to be sufficient for producing field emission. Rather, the presence of fine powder, some precipitate left by the chemical etching procedure, could be the reason. The procedure was completed with final thorough rinsing and sonication with alcohol and deionised water for the following wave guides with excellent results.

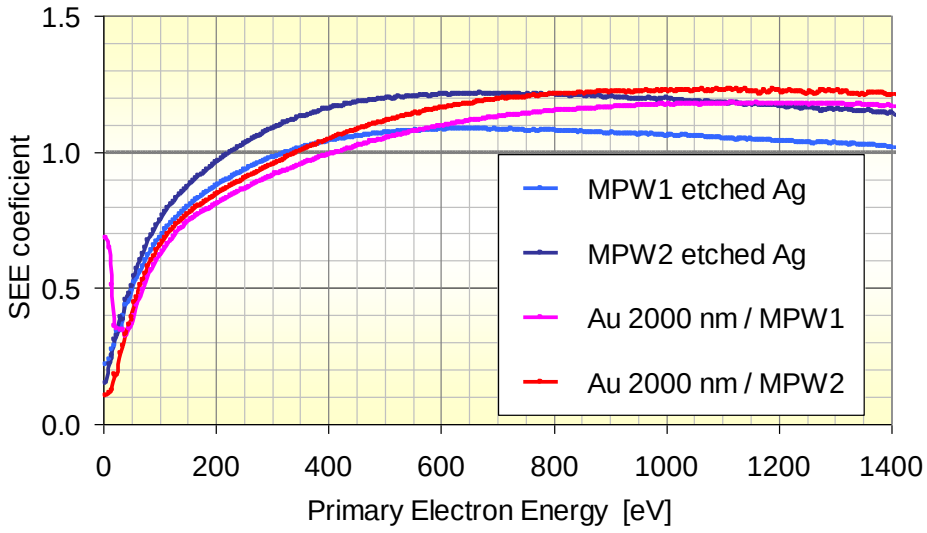

Figure 7. SEY of the first multipactor sample after chemical treatment and after Au coating. *SEY of the multipactor sample (of Ag-plated aluminium) as measured on witness samples, after the two surface treatment stages: chemical etching and Au coating (2-2.5 μm)*

***Table 2. SEY and multipactor level of the first multipactor sample at three stages**. As prepared by Tesat, chemical etching, and Au coating (2-2.5 μm). Multipactor power level (MPL) measured at ESTEC.*

Witness Sample	E_1 / eV	σ_m	E_m / eV	σ_{2000}	*FoM*	*MPL* / W
Ag plating (Tesat)	30*	2.2*	270*	1.4*	3.7*	700
MPW1 (etched Ag)	329	1.09	633	0.95	17.4	1100
MPW2 (etched Ag)	227	1.21	710	1.06	13.7	1100
Au-coated MPW1	417	1.18	1133	1.11	18.8	> 5300
Au-coated MPW2	347	1.23	1043	1.08	16.8	> 5300
* Typical values, ±10%						

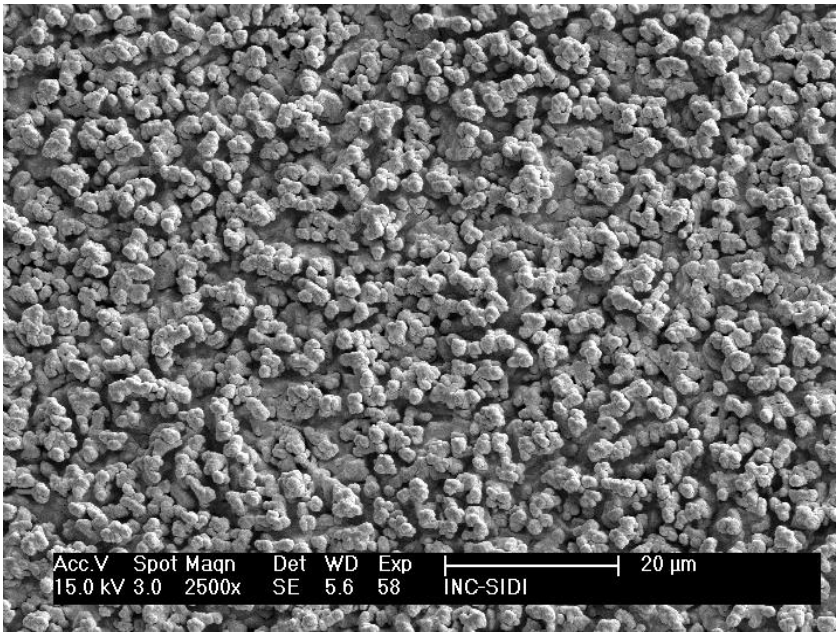

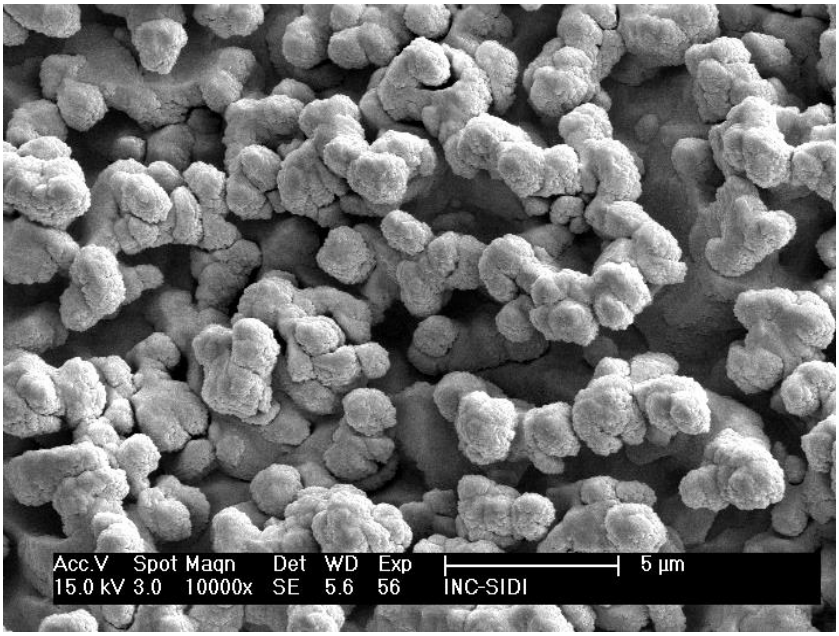

Figure 8. SEM images of the first Au-coated chemically-etched multipactor sample. *Surface morphology of sample 1 of Fig.7 after coating with 2.0 - 2.5 µm of Au by RF magnetron sputtering.*

8.2.4 RF Performance and Multipactor Tests

Introduction

As described above in *Sec.8.2.1,* a multipactor sample at three stages: a) Ag plated, b) after chemical etching, and c) after Au coating, was tested for multipactor power level and RF performance at ESTEC.

The following is a summary of the ESTEC report.

The sample at stage (b), chemically etched, showed some stains, peeling off, and powder. Therefore, it was thoroughly cleaned with isopropyl alcohol in an ultrasonic bath.

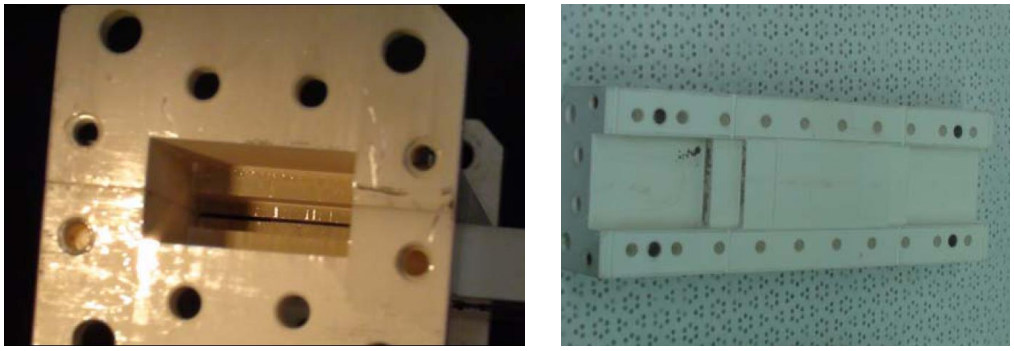

Figure 9. *Photos of the first multipactor sample after chemical etching. Left, before rinsing with isopropyl alcohol l, and right after cleaning.*

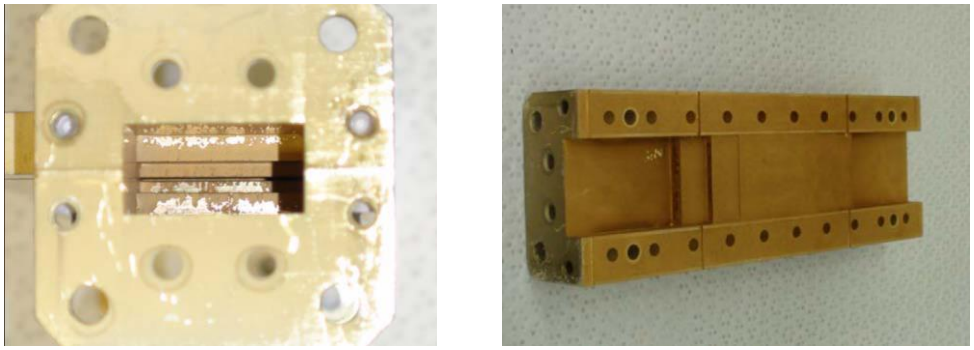

Figure 10. *Photos of the first multipactor sample after gold* coating

Instrumental and Experimental

An HP 83650A Syntetized Sweeper feeding a TMD TWTA Pulse 9 kW (10.5 – 12.5 GHz) was used. The TWTA was pulsed (20 μs pulse length, 1 kHz PFF) with an HP 8116A Pulse Generator. The input, output and reflected power were measured with Agilent E4417A power meters. Several multipaction detection methods were used: "nulling system", "3rd harmonic" and an electrometer. The measurement of the 3rd harmonic was done using a LNA (24-42 GHz). The nulling system and the 3rd harmonic responses were displayed on two spectrum analyzers. The output of the electrometer was displayed and data recorded in a laptop.

Tests were conducted in three different configurations: two with electron seeding and one without seeding. The two ways of seeding electrons inside the multipactor samples were

by a radioactive source (^{90}Sr) and by photoemission (UV light). The radioactive source had an activity of 1 mCu (37 MBq) and the UV light came from an Hg lamp.

The multipactor threshold was tested for each sample in three different electron seeding configurations: with UV light, with the ^{90}Sr radioactive source and without any electron seeding.

The frequency of the RF was 11.8 GHz.

Results of the Tests

Table 3 shows the results of RF performance and multipactor test performed at ESTEC on the multipactor sample. After cleaning with alcohol, the chemically etched sample was tested again but multipactor power level decreased 0.3 dB.

It should be noticed that for the Au-coated sample, no multipactor discharge was detected up to power limit of the testing instruments. The multipactor level increased more than 8 dB. This is really the achievement of an important goal: practical suppression of multipacting is possible by surface roughness in the micron scale.

The S parameter values measured in the RF performance test are presented in Figs.11-12.

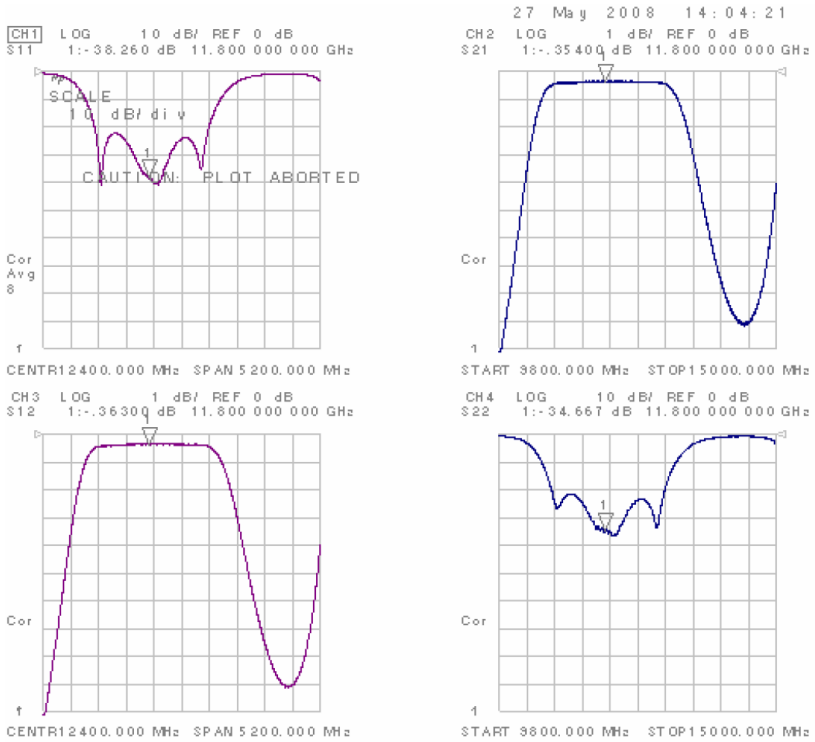

Figure. 11 *The S parameters for the first multipactor sample after chemical etching.*

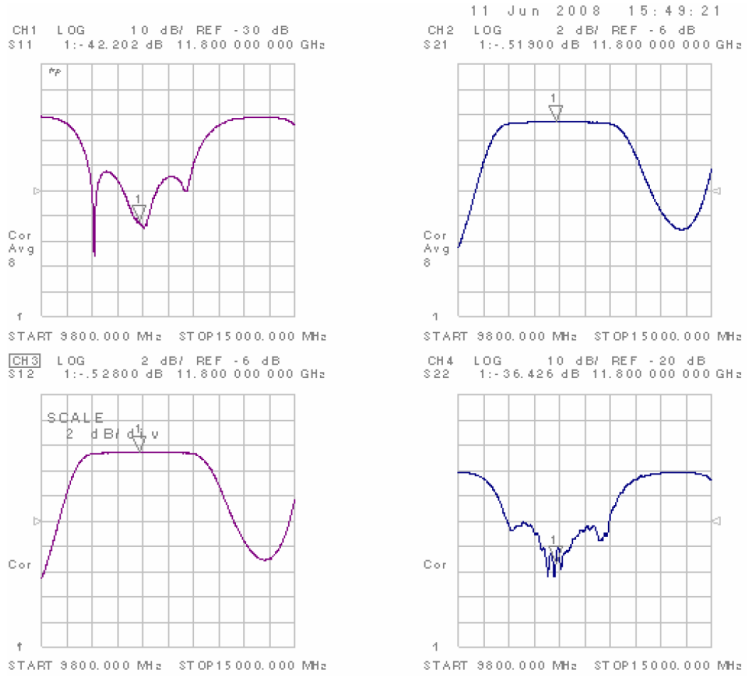

Figure 12. *The S parameters for the first multipactor sample after gold*

Table 3. Results of multipactor threshold and RF performance tests at ESTEC.

First Multipactor Sample	Multipactor Power Level [W]			RF Performance
Sample treatment	^{90}Sr	UV light	No *e*-seeding	Insertion Loss [dB]
a) Ag plated	700	800	1300	0.15
b) chemically etched	1100	1500	1800	0.36
c) Au coated	> 5300*	> 5300*	> 5300*	0.52
* maximum RF power level delivered by the TWTA				

Deterioration of first multipactor sample

However, the completely treated first multipactor sample, i.e., with a Au-coated chemically-etched Ag surface, was tested again in about ½ month with a very poor result for Multipactor power level. The surface had been modified, as confirmed by SEY tests, see below.

This could be attributed to the underlying etched Ag surface with rests a solid fine powder reminder or segregation left by the acid attack. This was later solved with the refined procedure, see Sec.8.3.1 below.

8.2.5 Deterioration of the SEY for the first Multipactor sample

As described above, an abrupt change in Multipactor power level indicted a sudden modification in SEY properties of the surface. This was checked at UAM/CSIC, and results are presented in Fig.13.

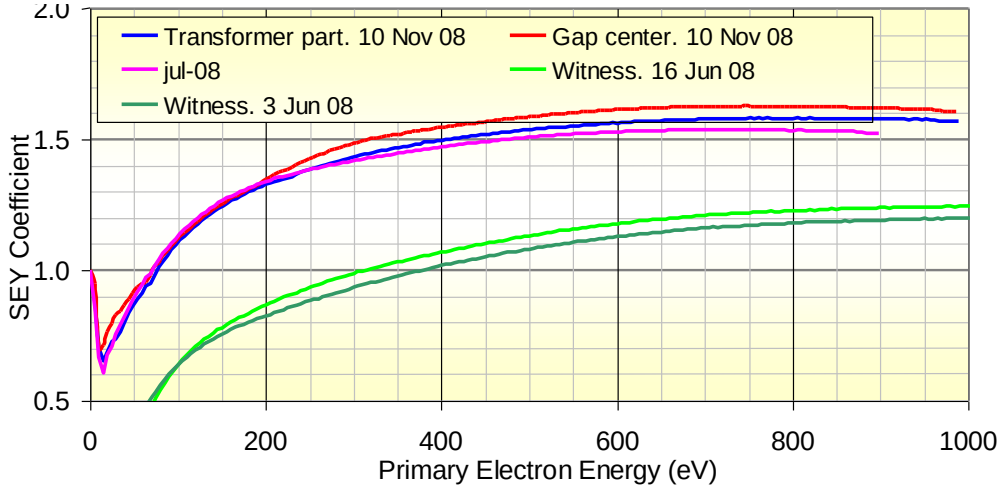

Figure 13. SEY of first multipactor sample (MP1) at different dates.
Surface treatment completed on 03.06.2008. Multipactor tests during June 2008. SEY of 3 and 16 June, on witness samples (no Multipactor test). Others on the waveguide, Multipactor sample, after Multipactor tests.

A possible explanation is that below the Au coating, the underlying etched Ag surface was very week under manipulation because of the remaining rests of the powder segregated during the acid attack. This was solved with the refined procedure, see *Sec.8.3.1* below.

8.3 Multipactor Samples 2nd – 5th by chemical etching

8.3.1 Refined surface treatment procedure

With the experience of the first multipactor sample (MP1), the preparation procedure was improved:

Samples as received should be cleaned in acetone, methanol, and deionized water, 10 min each at room temperature, and finally drying with nitrogen.

Chemical etching should end with the following steps (for eliminating powder precipitate):

- Rinsing for washing out rests of solution. Immerse and rinse twice in deionised water for 20 min at room temperature.
- Sonication (ultrasound) sequentially in methanol and deionized water at room temperature during 10 min each for taking away precipitate powder at room temperature.
- Rinse in deionized water at room temperature.
- Dry with nitrogen at room temperature.

In third step (sonication), small clouds of brown powder can be observed to arise from the Ag etched surface.

Table 4. Multipactor test samples from Tesat, treated in UAM and sent to ESTEC

Multipactor Test Samples, Ku-Band, 12 GHz, Base material: Aluminium. 10 μm Ni plating.			
Sample	Type	Gap / mm	Ag plating / μm
MP1	Trafo short gap version	0.14	20
MP2	Trafo long gap version	0.14	40
MP3	Trafo	0.10	40
MP4	Corrugated low pass	0.34	40
MP5	Ridged low pass	0.70	40

Another improvement was to increase to 40 μm the thickness of the initial Ag plating of the multipactor samples, as a consequence of the observation of poor acid attack or peeling off in some regions of MP1 (first multipactor sample).

Four more multipactor samples (MP2 – 5) were treated and sent to ESTEC for multipactor and RF performance tests. Table 4 presents some defining parameters of all the multipactor samples.

8.3.2 SEY measurements

Results after the chemical etching

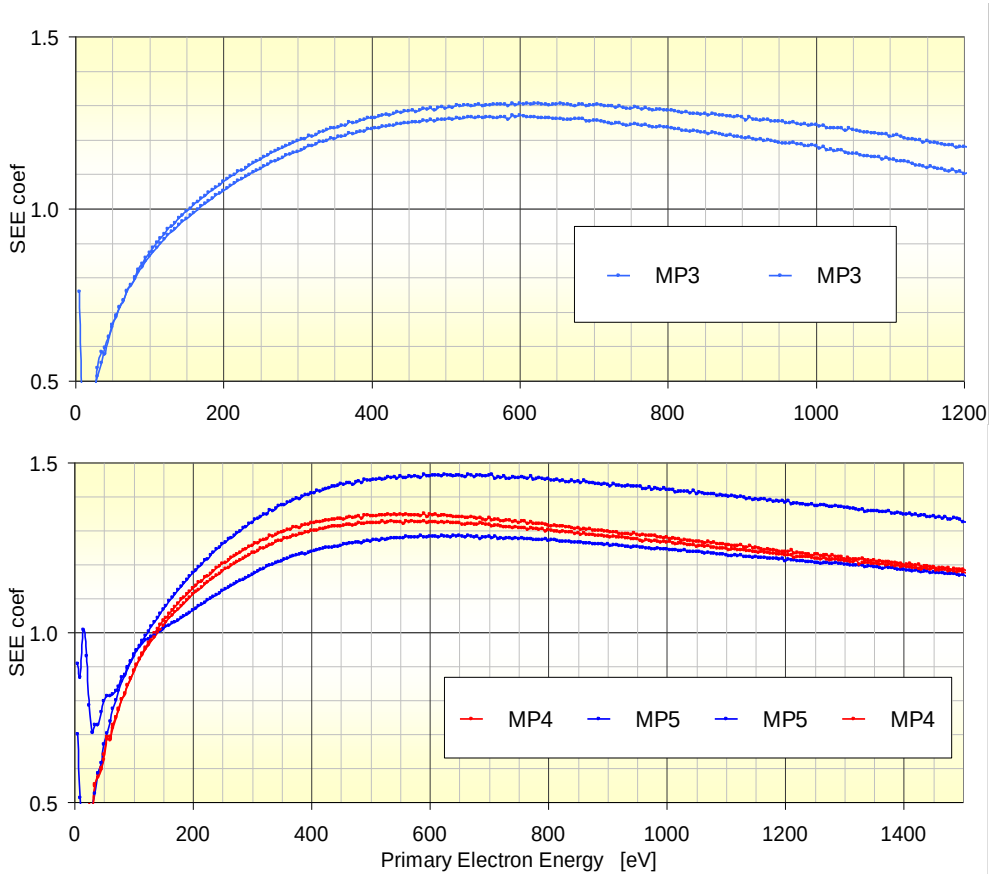

Figure 14. *SEY of witness samples of MP3 – 5 after chemical etching: Ag rough surface.*

Results after the Au coating

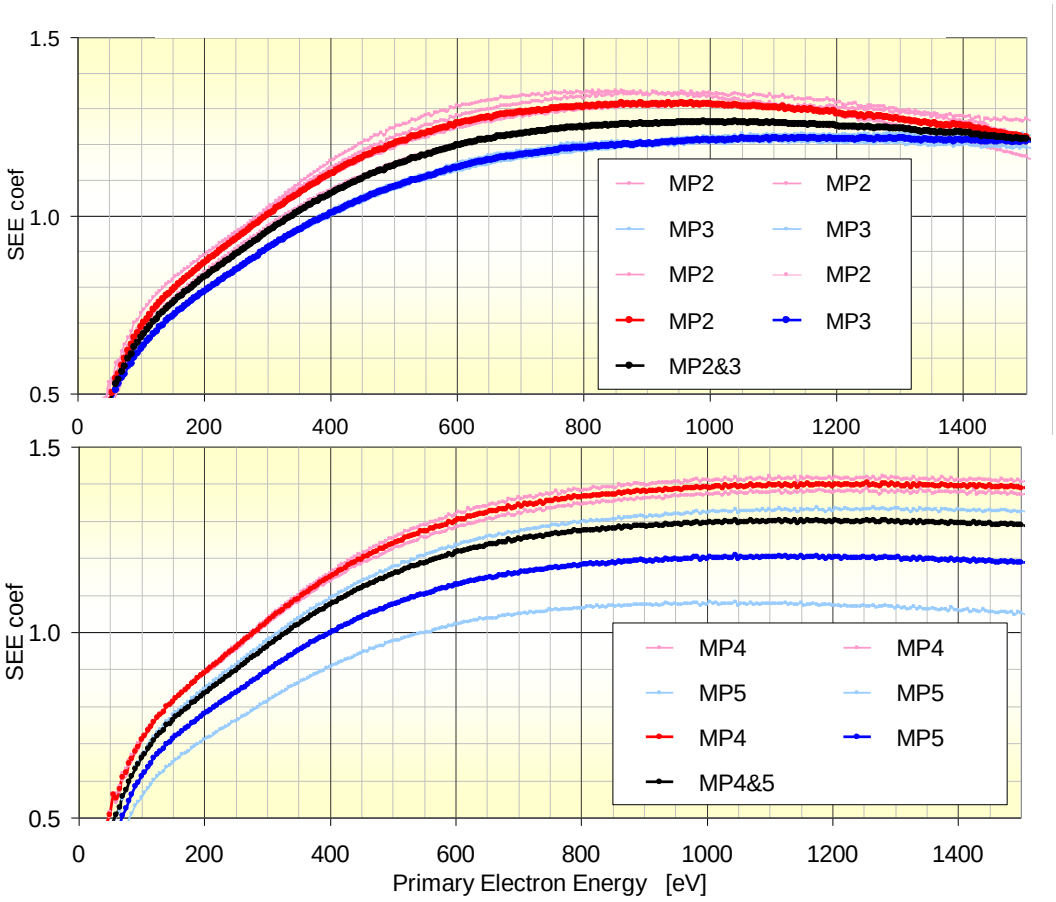

Figure 15. *SEY of witness samples of MP2 – 5 after Au coating: Au rough*

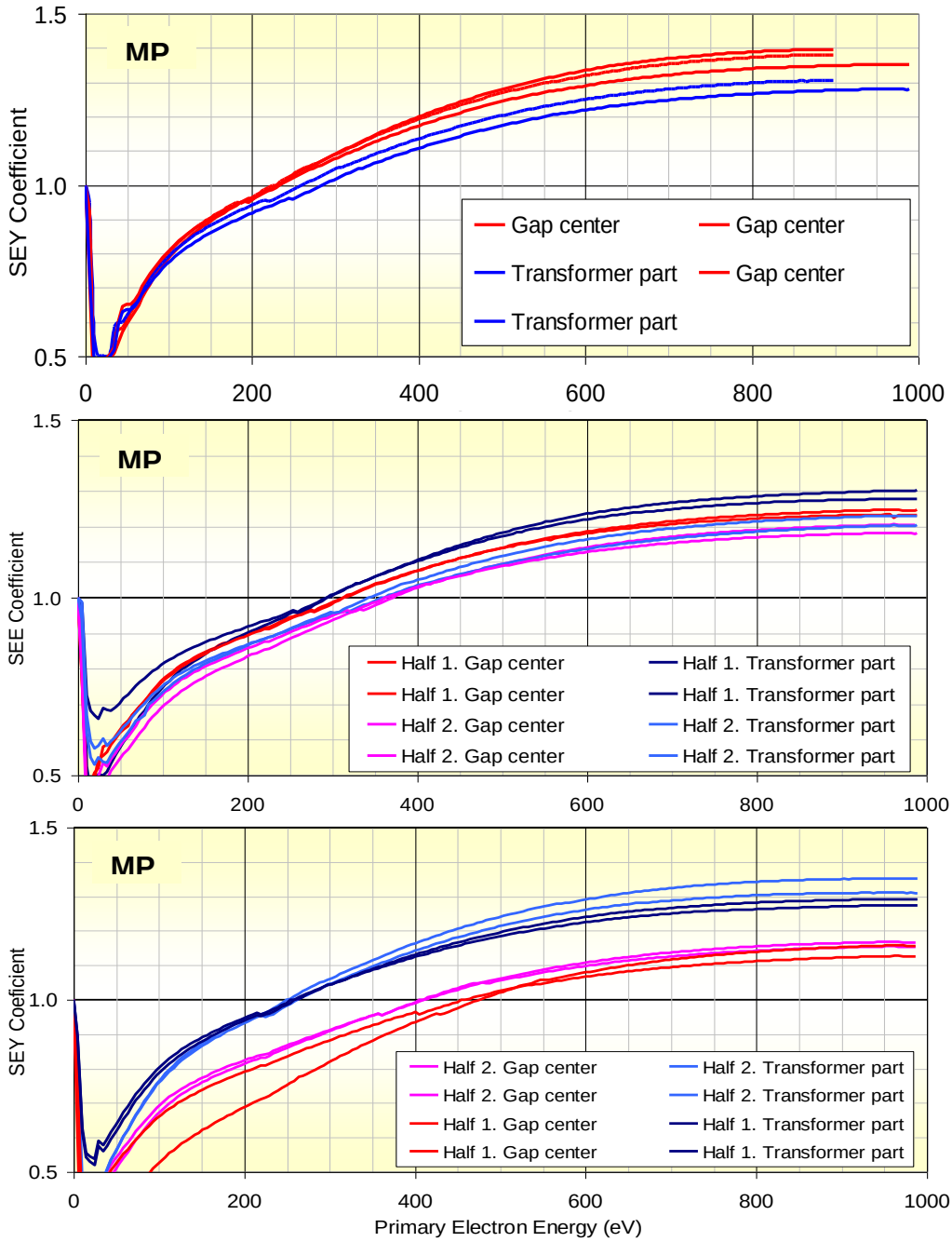

Figure 16. *SEY of Multipactor samples MP3 – 5 after Au coating: Au rough surface. Measurements were performed on the wave guide.*

Effect of Surface Treatment

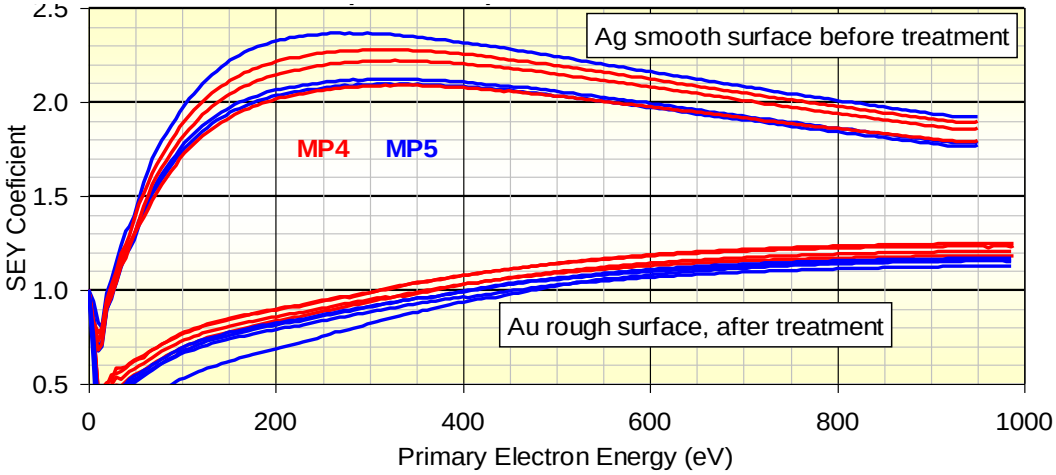

Figure 17. *Effect of surface treatment on SEY of Multipactor samples MP4 and MP5.*

Summary of SEY Tests on Multipactor Samples

Table 5. *Dates of SEY tests on Multipactor samples before RF testing at Tesat*

MP Sample	Prep. date	SEY sample	SEY Date	E_1 /eV	σ_m	E_m /eV	MP test	days
MP1	03.06.08	witness	06.06.08	380	1.21	1090		3
		witness	16.06.08	315	1.25	1100		13
		waveguide	10.07.08	70	1.54	750	after test	34
		waveguide	10.11.08	75	1.58	750	after test	157
MP2	07.09.08	witness	11.09.08	300	1.32	1050		4
MP3	07.09.08	witness	11.09.08	395	1.22	1205		4
		waveguide	04.11.08	240	1.33	900	after test	58
MP4	20.11.08	witness	26.11.08	280	1.40	1270		6
		waveguide	04.12.08	345	1.22	950		14
MP5	21.11.08	witness	26.11.08	400	1.21	1135		5
		waveguide	05.12.08	440	1.16	950		14

8.3.3 SEM analysis

Surface morphology after the chemical etching

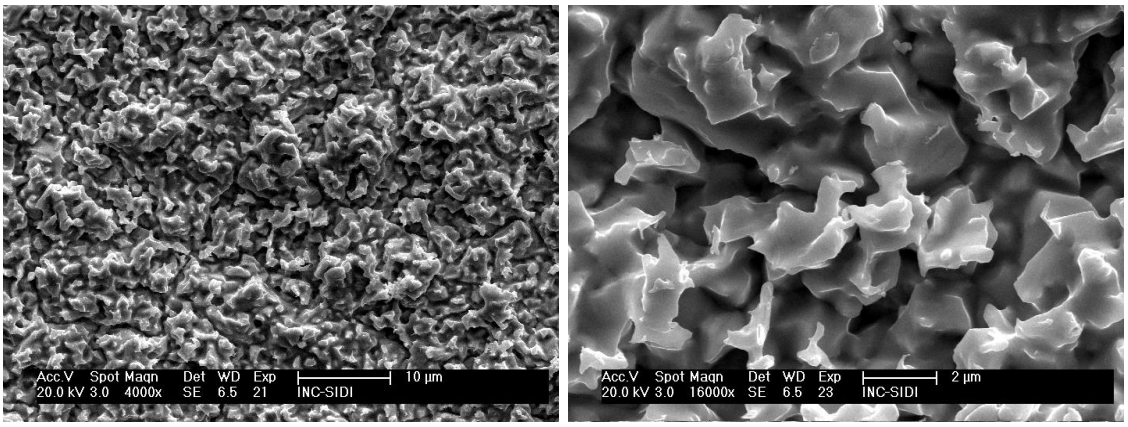

Figure 18. *SEM of witness sample of MP4 after chemical etching: Ag rough surface.*

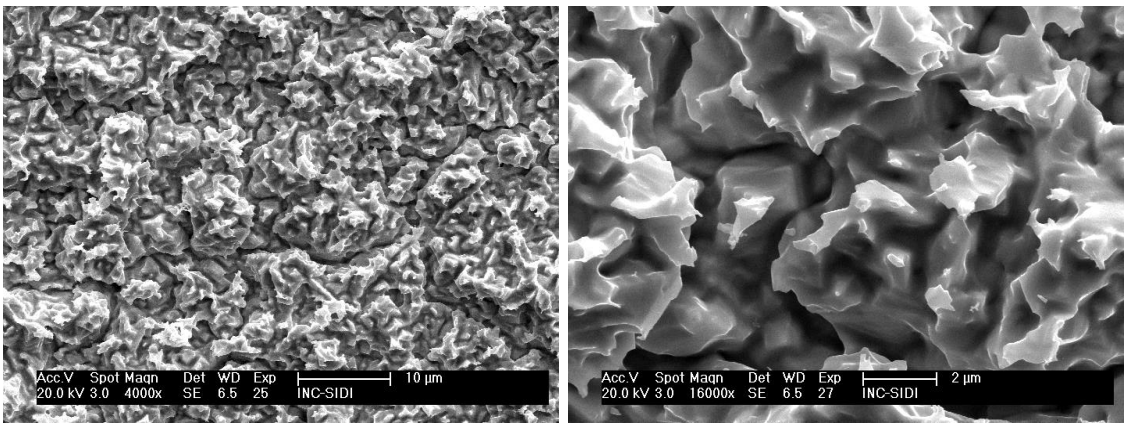

Figure 19. *SEM of witness sample of MP5 after chemical etching: Ag rough surface.*

Surface morphology after the Au coating

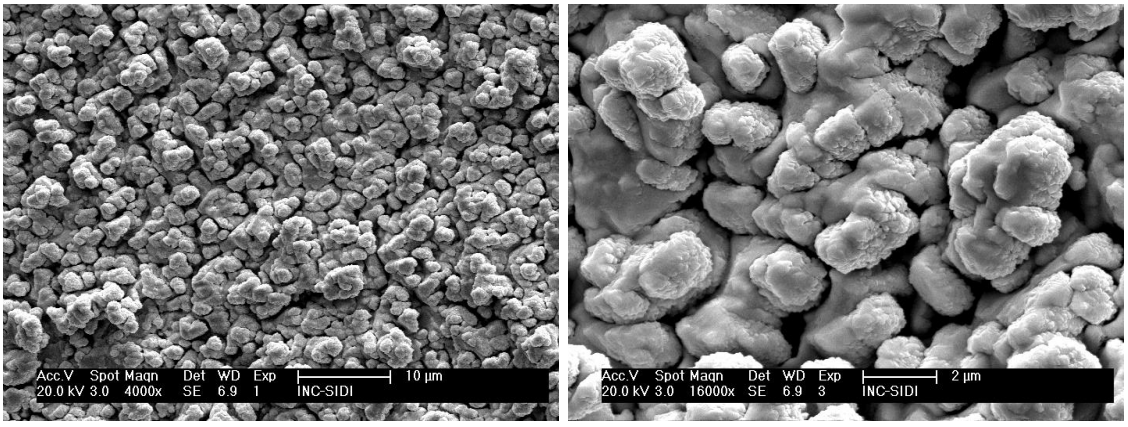

Figure 20. *SEM of witness sample of MP2 after Au coating: Au rough surface.*

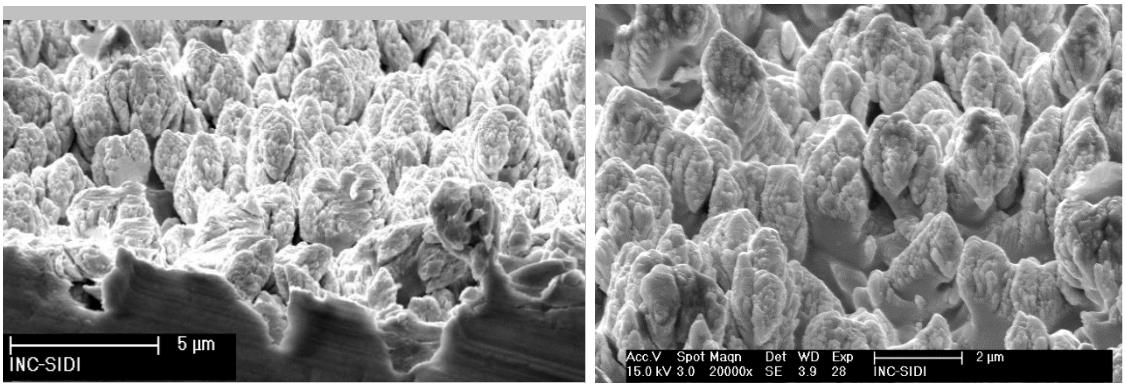

Figure 21. *SEM of witness sample of MP2 after Au coating. Oblique view, > 45º*

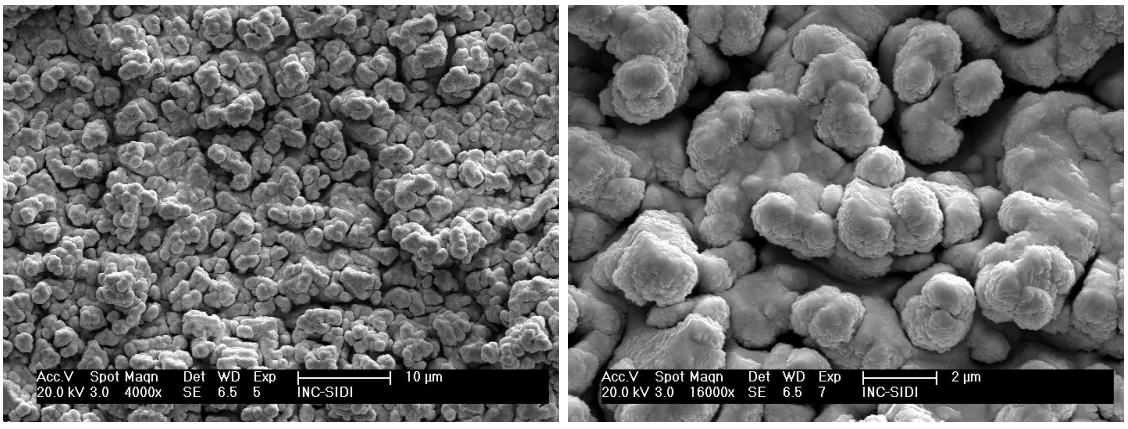

Figure 22. *SEM of witness small sample of MP3 after Au coating: Au rough surface.*

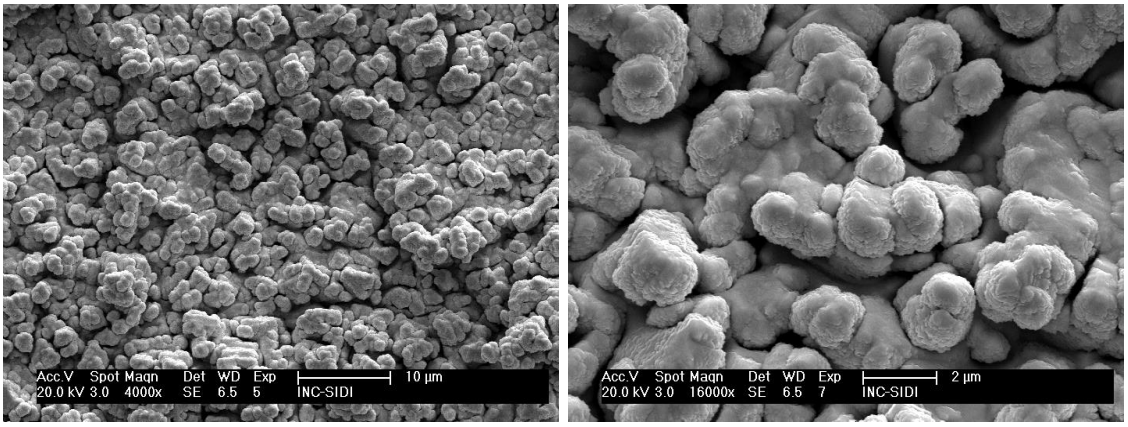

Figure 23. *SEM of witness sample of MP4 after Au coating: Au rough surface.*

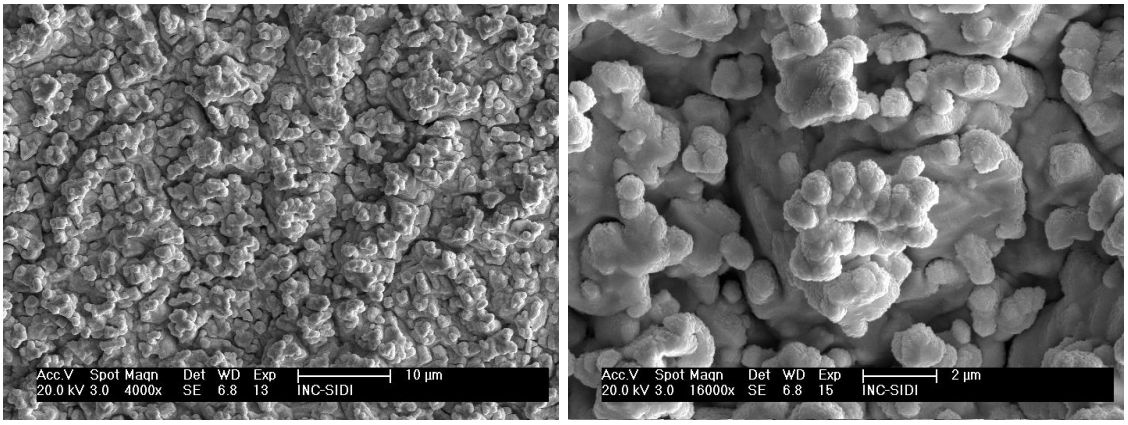

Figure 24. *SEM of witness sample of MP5 after Au coating: Au rough surface.*

8.3.4 Visual inspection

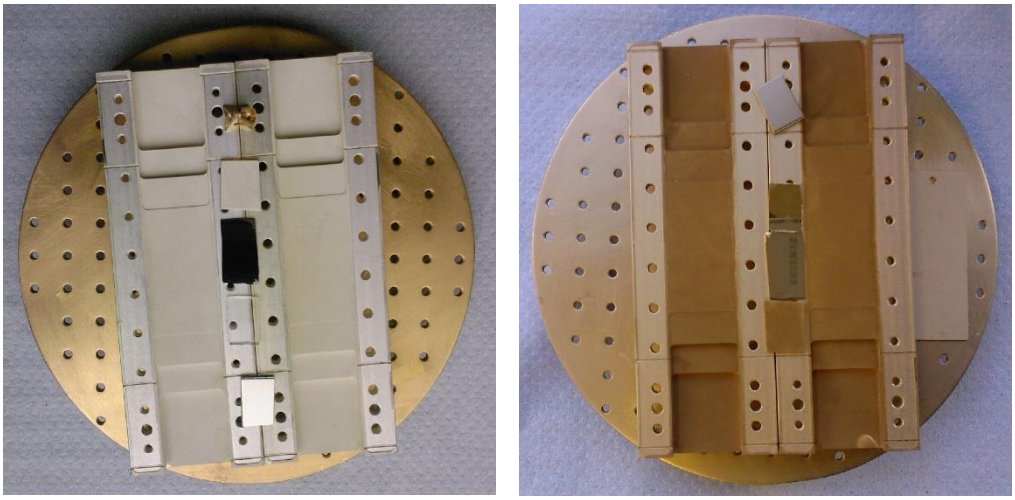

Figure 25. *Photos of MP3 in the sample stage of the sputtering system, RF magnetron, just before and after deposition of a Au layer of 2 µm thickness. The left photo corresponds to the chemically-etched silver plating.*

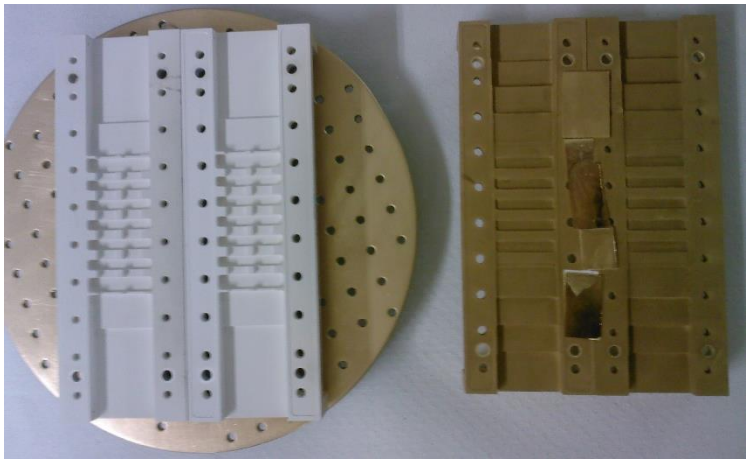

Figure 26. *Photo of MP4 and MP5. The sample on the left is MP5 after chemical etching. MP4 with complete treatment is on the right.*

Figure 27. *Photo of MP4 - left and MP5 - right with completed surface treatment.*

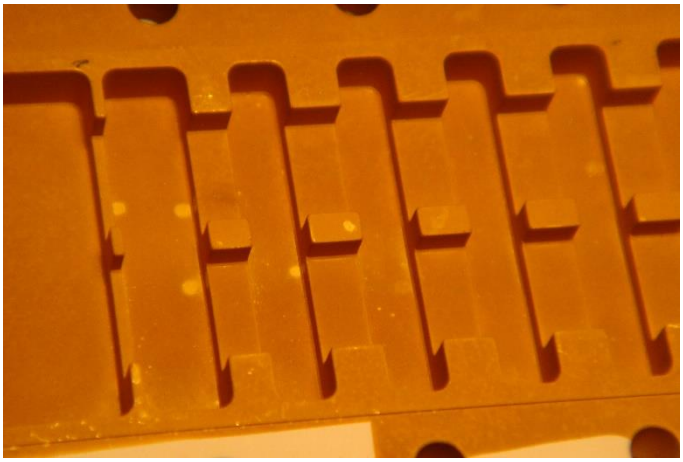

Figure 28. *Detailed photo of MP5 with completed surface treatment in the central critical region*

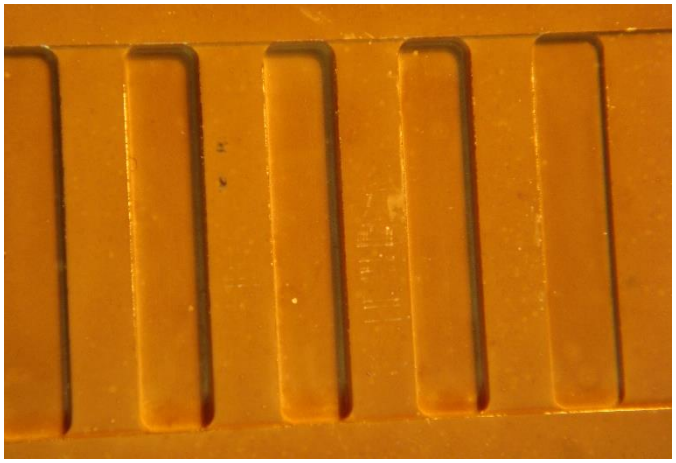

Figure 29. *Detailed photo of MP4 with completed surface treatment in the central critical region*

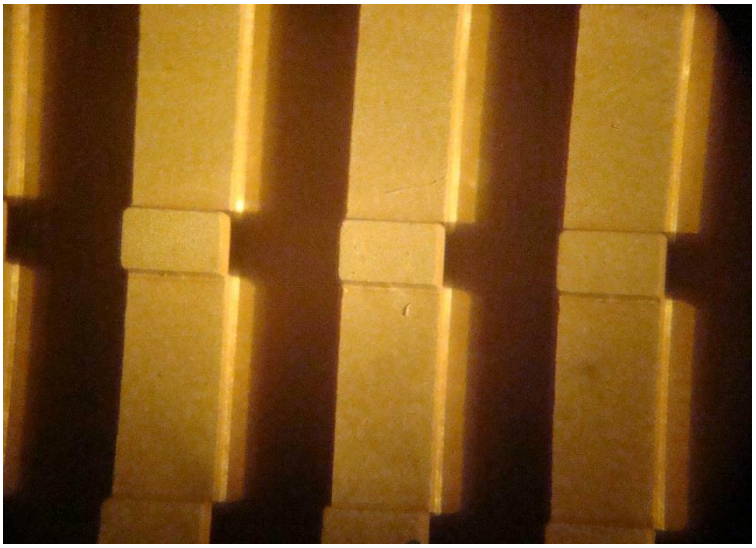

Figure 30. *Photo of MP5 with completed surface treatment. Detail of the coating homogeneity.*

8.4 Final RF and SEY tests on chemically etched filters

In Table 6, we present a general summary of the research results on the rough gold coating of multipactor test samples. The SEE properties of the coatings at different stages are reported. For each sample, it begins with the rough silver surface obtained by chemical etchings and continues with the gold coating by magnetron sputtering. These initial SEY tests were performed on small witness samples which followed the same preparation

procedure as the multipactor test samples. Then, some measurements show the evolution of the SEY with time and exposure to the air and finally the properties after multipactor tests. These tests were performed on the actual multipactor sample wave guides. Several measurements were done in the central region, in the critical gap, but others also in the transformer regions. The corresponding SEY curves for the last stage, i.e., after testing in Tesat, are shown in Fig.32. As an example, the detailed evolution of the SEY of sample MP3/2 is presented in Fig.33.

The SEY parameters for critical gap and transformer regions of the untreated versions (with smooth flat silver surfaces) of the multipactor test samples, are presented in Table 8, where they are compared with those of the same type of surface (smooth flat silver surface of probe samples, small plates from Tesat) which have not undergone any RF testing nor any similar experience. The corresponding SEY curves are shown in Fig.31.

The results of the RF tests at Tesat, multipactor thresholds and insertion losses, are presented in Table 7, along with the characteristics of the samples and the properties of the coatings. Both surface treated and untreated versions of the samples are shown. The SEE parameters correspond to the samples after RF testing and to the critical gap region.

Data presented in mentioned Tables 6 - 8 and Figures 31 - 33 above confirm that SEY values more influencing multipactor susceptibility are those for low primary energies, lower than 500 eV. The SEY parameter $FoM = (E_1/\sigma_{max})^{1/2}$ is thus a good figure of merit for the SEE.

Data in Table 6 were used for Fig.34 which shows a relatively good correlation between SEE *FoM* and multipactor threshold, in spite of test samples being of different types and with different gap distances. The correlation is expected to work only for gap voltage threshold vs. *FoM* for a given geometry and $f \times d$ (frequency-gap product) value. Samples MP3 are singular in being most uncorrelated. Samples MP3 have the smallest gap distance. It is possible that the multipactor susceptibility zone for the rough Au coating is above this small $f \times d$ value.

***Table 6. SEY of surface treated multipactor samples at different stages of preparation and testing**. Characteristics of the samples and their history are shown along with SEY*

Sample	Rough surface material	Sample type	Region of SEY test	Air expo. [day]	RF test		SEY test					
					ESTEC	Tesat	E_1 [eV]	σ_{max}	E_m [eV]	σ_{1000}	FoM [eV]$^{1/2}$	ΔFoM* [eV]$^{1/2}$
MP1/2	Ag	witness		1			278	1.15	672	1.13	15.5	
	Au	witness		1			385	1.21	1090		17.8	
		witness		3			380	1.21	1090		17.7	
		witness		13			315	1.25	1100		15.9	
	Au	waveguide	gap	35	yes(2x)**		80	1.54	745	1.52	7.2	
		waveguide	transf..	157	yes(2x)**		76	1.58	791	1.58	6.9	-0.3
		waveguide	gap	157	yes(2x)**		71	1.63	764	1.61	6.6	
		waveguide	transf.	510	yes(2x)**	yes	76	1.46	798	1.45	7.2	
		waveguide	gap	510	yes(2x)**	yes	73	1.51	749	1.49	6.9	-0.3
MP2/2	Au	witness		4			300	1.32	1050		15.1	
	Au	waveguide	transf.	415		yes	131	1.40	852	1.39	9.7	
		waveguide	gap	415		yes	166	1.44	896	1.42	10.7	1.0
MP3/2	Ag	witness		1			160	1.30	615	1.22	11.1	
	Au	witness		4			395	1.22	1205		18.0	
	Au	waveguide	transf.	58	yes		274	1.25	944	1.25	14.8	
		waveguide	gap	58	yes		219	1.43	927	1.40	12.4	-2.4
		waveguide	transf.	400	yes	yes	167	1.39	898	1.38	11.0	
		waveguide	gap	400	yes	yes	219	1.40	910	1.40	12.5	1.5
MP4/2	Ag	witness		1			138	1.34	565	1.27	10.1	
	Au	witness		5			280	1.40	1270		14.1	
	Au	waveguide	transf.	14			320	1.25	990	1.26	16.0	
		waveguide	gap	14			339	1.22	915	1.22	16.7	0.7
		waveguide	transf.	340		yes	195	1.30	903	1.30	12.2	
		waveguide	gap	340		yes	237	1.30	901	1.30	13.5	1.3
MP5/2	Ag	witness		1			133	1.37	635	134	9.9	
	Au	witness		5			400	1.21	1135		18.2	
	Au	waveguide	transf.	14			258	1.31	990	1.31	14.0	
		waveguide	gap	14			439	1.15	990	1.16	19.5	5.5
		waveguide	transf.	340		yes	145	1.43	879	1.43	10.1	
		waveguide	gap	340		yes	269	1.20	893	1.20	15.0	4.9

*) Difference of FoM's between gap - transformer regions of the wave guide

**) MP1/2 was tested at ESTEC twice. One without multipactor for 5.3 kW and the second time with a poor threshold

Table 7. SEY of the multipactor samples, both treated and untreated versions, after testing at Tesat and the results of RF testing. *Characteristics of the samples and their history are shown along with SEY parameters of the central gap region. The SEY curves*

MP Sample from Tesat				Surface treatment	SEY test						RF tests at Tesat (12 GHz)	
Sample	Type	Gap [mm]	Tesat plating Ag / µm over 10 µmNi	surface	E_1 [eV]	σ_{max}	E_m [eV]	σ_{1000}	FoM $[eV]^{1/2}$	air expo [day]	RF test at ESTEC	Multipactor threshold [W]	Insertion losses [dB]
MP1/1	Trafo 0.14mm	0.14		smooth Ag*	17.9	2.02	144	1.23	3.0			496	0.215
MP1/2	short gap version		20	rough Au	72.7	1.51	749	1.49	6.9	510	yes	1172	0.630
MP2/1	Trafo 0.14mm	0.14		smooth Ag*	31.7	1.83	364	1.58	4.2			759	0.281
MP2/2	long gap version		40	rough Au	165.6	1.44	896	1.42	10.7	415		2469	0.786
MP3/1	Trafo 0.10mm	0.10		smooth Ag*	26.8	1.83	344	1.55	3.8			350	0.359
MP3/2			40	rough Au	219.0	1.40	910	1.40	12.5	400	yes	> 6500	1.067
MP4/1	Corrugated	0.34		smooth Ag*	37.1	1.81	386	1.59	4.5			945	0.178
MP4/2	Low Pass 0.34mm		40	rough Au	236.5	1.30	901	1.30	13.5	340		3353	0.422
MP5/1	Ridged	0.70		smooth Ag*	65.1	1.69	513	1.59	6.2			1300	0.065
MP5/2	Low Pass 0.70mm		40	rough Au	269.0	1.20	893	1.20	15.0	340		3960	0.137

*) Untreated surface: silver plating from Tesat

Table 8. SEY of untreated Ag-plated multipactor samples after RF tests at Tesat.
Surface is smooth flat silver. SEY curves are shown in Fig.31.

Sample	Region of SEY test	E_1 [eV]	σ_{max}	E_m [eV]	σ_{1000}	FoM $[eV]^{1/2}$	ΔFoM* $[eV]^{1/2}$
MP1/1	transformer	17.8	2.27	188	1.37	2.8	
	gap	17.9	2.02	144	1.23	3.0	0.2
MP2/1	transformer	19.4	2.22	320	1.83	3.0	
	gap	31.7	1.83	364	1.58	4.2	1.2
MP3/1	transformer						
	gap	26.8	1.83	344	1.55	3.8	
MP4/1	transformer	35.2	1.73	405	1.57	4.5	
	gap	37.1	1.81	386	1.59	4.5	0.0
MP51	transformer	32.2	1.88	349	1.60	4.1	
	gap	65.1	1.69	513	1.59	6.2	2.1
Probe**		25±2	2.2±0.2	320±15	1.8±0.1	3.4±0.3	

*) Difference of FoM 's between gap - transformer regions of the wave guide

**) Average SEY of probe samples (small plates) from Tesat is included for comparison

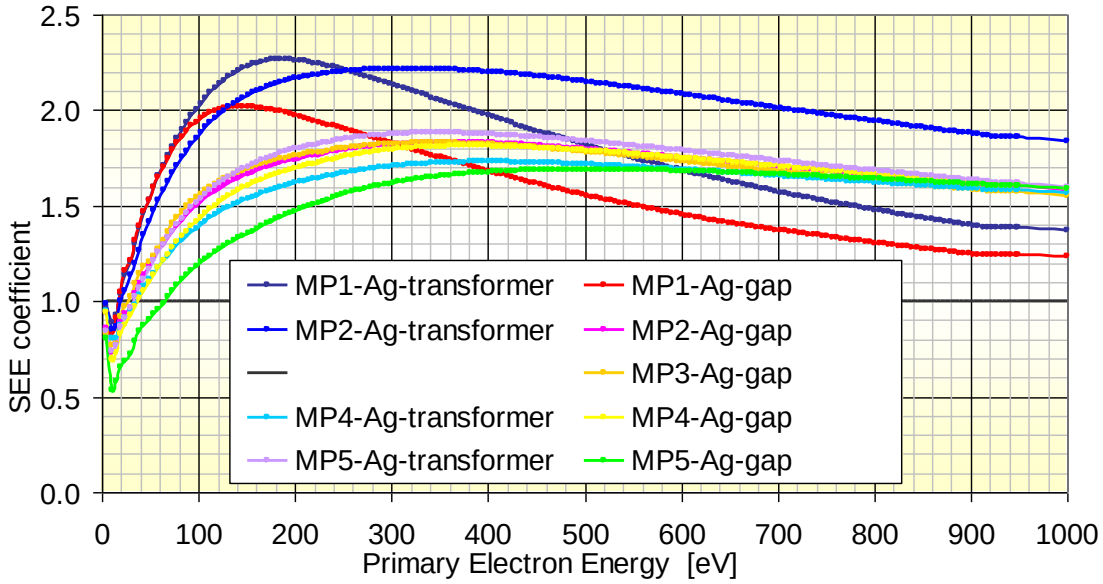

Figure 31. SEY of untreated multipactor samples after RF testing at Tesat. *With smooth flat silver surfaces. Different SEY curves are shown for critical gap and transformer regions of the wave guides. MP1 sample show a different shape of SEY curve.*

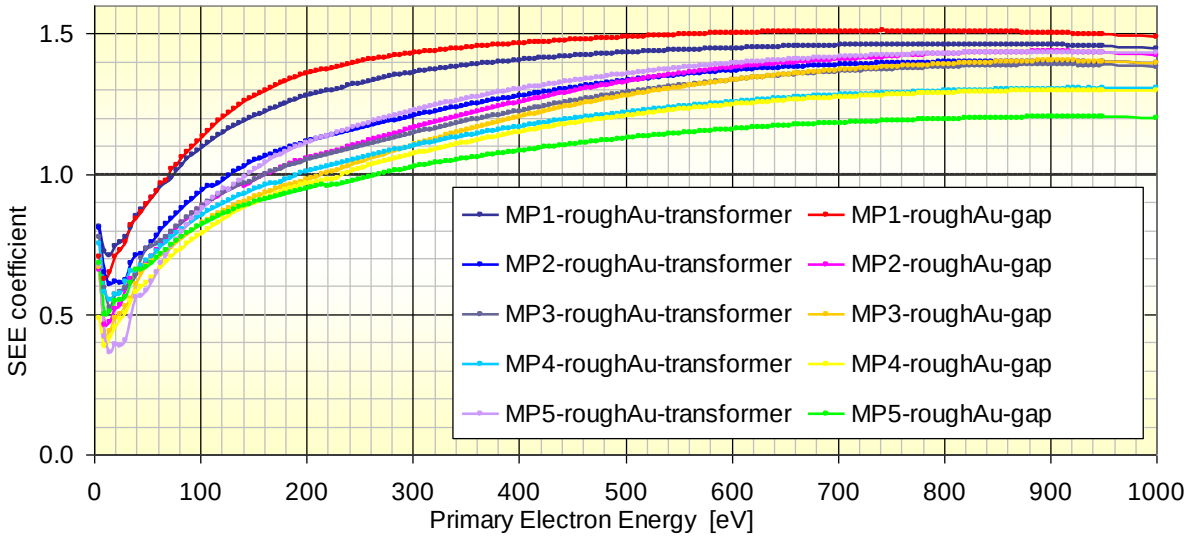

Figure 32. SEY of treated multipactor samples after RF testing at Tesat. *With rough gold surfaces. Different SEY curves are shown for critical gap and transformer regions of the wave guides. MP1 sample shows the highest SEY values.*

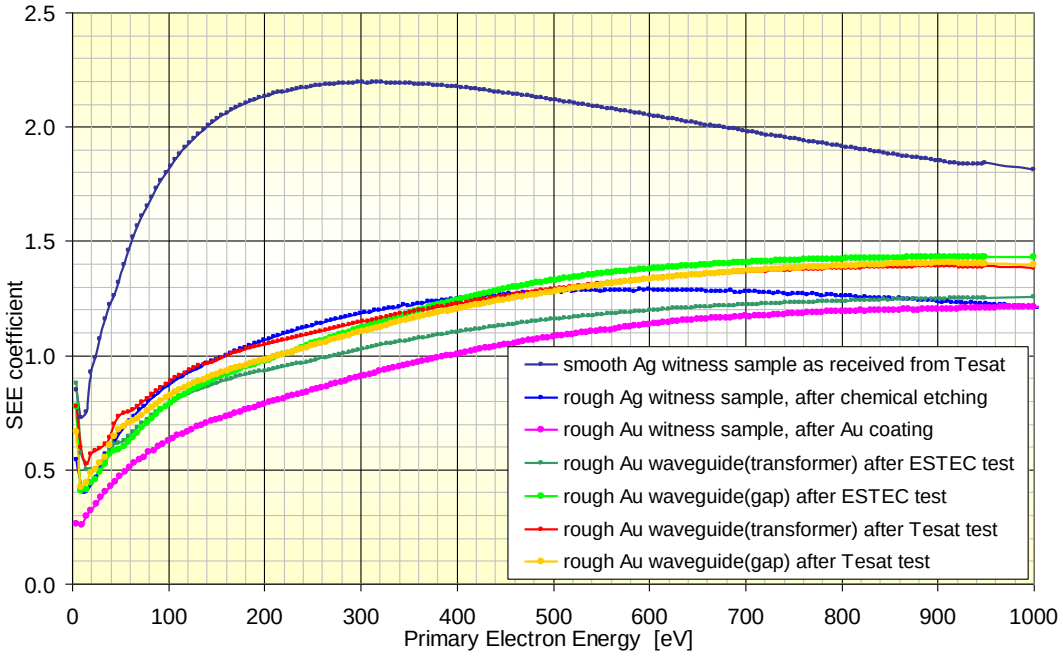

Figure 33. SEY of MP3/2 sample at different stages of preparation and testing. *SEY was measured on a witness sample or on the actual wave guide in both the critical gap and transformer regions. A relatively small increase of SEY during 400 days is observed for the rough gold surface; it seems to be saturated after about 2 months.*

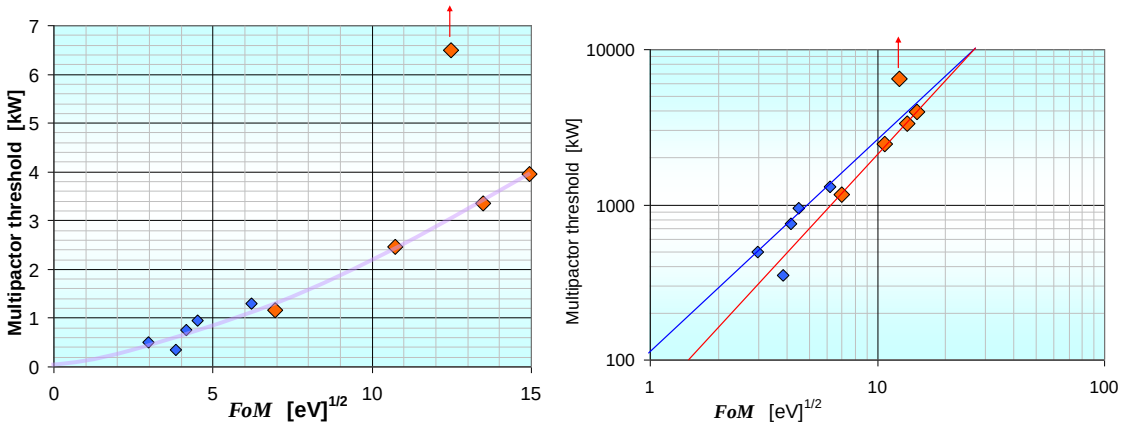

Figure 34. Correlation between the multipactor threshold and the SEY of the multipactor samples. *The SEY properties are represented by the figure of merit* $FoM = (E_1/\sigma_{max})^{1/2}$ *. Large red symbols correspond to the treated samples with rough gold surfaces, and the small blue symbols to the untreated ones with smooth silver surfaces. Both linear and logarithmic plots are used for showing the correlation. The upper red and the lowest blue symbols correspond to the sample MP3.*

Multipactor testing at Tesat has apparently produced some surface "conditioning" of multipactor test samples. It could be indicated by a higher *FoM* of the gap surface

compared to that of the transformer region, see ΔFoM column in Tables 6 and 8. This is apparent for all treated samples except for MP1. This asymmetry is also present in the untreated samples. This surface conditioning could explain why SEE properties of multipactor test samples deteriorate so slowly with time, see Table 6 and Fig.33; this is more evident for MP3. It could also explain the low SEY of untreated multipactor samples (smooth Ag surface) after multipactor testing, see Table 8 and compare with SEY of the "unconditioned" probe samples.

However, the large difference in ΔFoM between the gap and transformer region for sample MP5, both treated and untreated versions, see Tables 6 and 8, is probably indicating also a SEY suppression effect due to surface roughness, in this case macroscopic roughness, for the ridged type wave guide, see Fig.26 – 28, and 30.

The SEY curves of MP1/1 are different from those of the other multipactor test samples in that they show much lower values for high primary energies (> 500 eV). Also MP1/2 was special because of a defective surface treatment procedure, see Sec.8.2.5, but this has no relation to MP1/1 with an untreated Ag surface. The only thing special and common between MP1/1 and MP1/2 is a thinner Ag plating (20 μm compared to 40 μm of the other multipactor test samples); however, 20 μm is too thick to have any influence on SEY.

8.5 Main conclusions for the chemical etching technique

A surface treatment for silver-plated aluminum devices producing a rough gold coating has been developed which has important properties for reduction of multipacting in space RF devices.

It has very low SEY for low energies and thus it is the cause of an important increase of multipactor threshold.

It has been demonstrated that the practical suppression of multipacting is possible with this coating.

The deterioration of the SEY properties with time and air exposure is very slow; those high multipactor threshold values were obtained about one year after coating preparation.

The RF insertion loss values indicate that the surface resistance was higher than that of smooth flat gold but lower than that of Alodine. However, since the size of this surface

roughness causing these RF losses was large, 1 – 5 μm, compared to the RF field skin depth there is still margin for improvement reducing the scale of the surface roughness. That is supported by another conclusion of the work: the suppression effect on SEY due to surface roughness does not depend on the size scale. This size can be decreased to improve surface conductivity.

The rough gold surface was obtained by means of an intermediate rough silver surface. The chemical surface treatment for this rough silver surface is original and developed by our laboratory. This seems to have also interesting applications in other technological fields as microfabrication or SERS (surface-enhanced resonance Raman scattering) for chemical analysis. The amount of work dedicated to this development clearly exceeded that planned in the contract.

This rough silver surface might be coated with other materials alternative to gold, and with different thicknesses. This line also deserves further investigation.

The SEY suppression effect of surface roughness was studied and clearly demonstrated both theoretically (simulations) and experimentally.

This SEY suppression effect does not depend on roughness scale and is experimentally demonstrated in the ample range 100 nm – 1 mm.

Several other rough surfaces and their preparation techniques were investigated which offer important potential for SEY suppression and might deserve testing for multipactor: 100 nm scale rough surface of gold by ion masking-etching, and high-rate deposition of silver or copper by evaporation or sputtering,

An important improvement was obtained in the preparation procedure of the gold-coated Anomag coatings for magnesium alloys devices, already patented in USA.

A lot of work was dedicated to study potential materials and techniques, both in the literature and experimentally. That was a real research work with an innovative approach in a restricted field where results cannot be planned.

8.6 The Multipactor samples treated by masked preferential ion sputtering

Eight harmonic low band pass filters designed and manufactured by Tesat Spacecom were treated with the sputtering technique described in previous sections. Filters 1st to 5th were used for optimization of the surface treatment procedure. The surface roughening technique consisted in low-energy Ar ion etching assisted by Ti mask sputtering deposition on standard Ag plating of the filters. In a first stage, Ti is deposited while preferential ion etching of the Ag substrate. In a second stage, Au is deposited by a magnetron source while low energy Ar ion beam assisted diffusion. Precise equilibrium among different rates involved allowed obtaining the surface roughness of appropriate size and shape.

Filter #1 (the only of kind) was processed with a Ti cone as sputtering target and Au was deposited by magnetron sputtering without Ar ion assistance. The following ones were processed by the magnetron sputtering from a Ti target source, simultaneously with the ion etching of the Ag surface. This operation removed the restriction on the sample size and homogeneity of the coating. Treatment of Filter 4th failed because the magnetron had an electrical leak and did not work correctly. Filters 7th and 8th were treated with the optimized procedure and the treatments showed similar results, thus the coating was considered reproducible. Table 9 reports on crucial conditions of the surface treatment procedure stages 1 and 2:

stage 1: source of Ti atoms and dose of Ar ions assistance, and

stage 2: ion assistance while Au deposition,

along with SEY and low power RF Insertion Loss tests results.

8.6.1 Results on the SEY tests

The SEY-Energy curves of the treated filters are presented in Fig.35 and their main parameters in Table 9. Whereas Fig.36 shows SEY of the as-received Ag-plated surfaces. SEY has been significantly improved from a filter treatment to the next one; mainly due to improvements in stage 2: Au coating. The main improvement in surface roughness of stage 1 has been achieved by the use of the RF magnetron sputtering source instead of the Ti cone. Then, the clustering or growth of a second order coarser roughness was avoided.

It should be noticed that SEY of Fig.35 and Table 9 was measured as an average in an area of about 1 cm^2 and that only about 23 % corresponds to the top of the small pillars in the central zone of the filter and 77 % corresponds to the trenches or grooves formed by the pillars. Surface roughness in these grooves is not optimized and their intrinsic SEY is probably higher; however, there is a suppression effect due to the walls of the grooves and their effective SEY is also low. See Fig.37. The different SEY curves which can be measured on a treated filter are illustrated for Filter 8th in Fig.38.

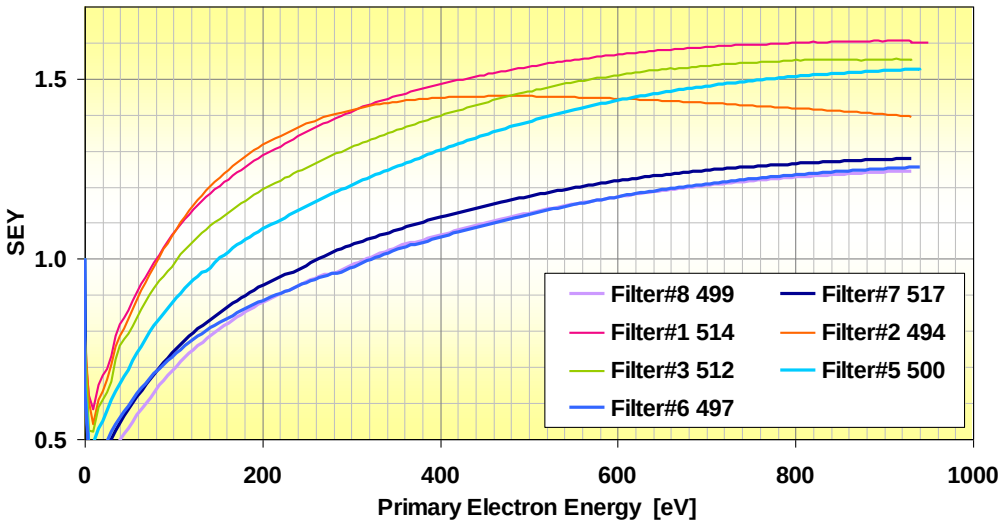

Figure 35. *SEY of filters after complete surface treatment. Average SEY in central zone*

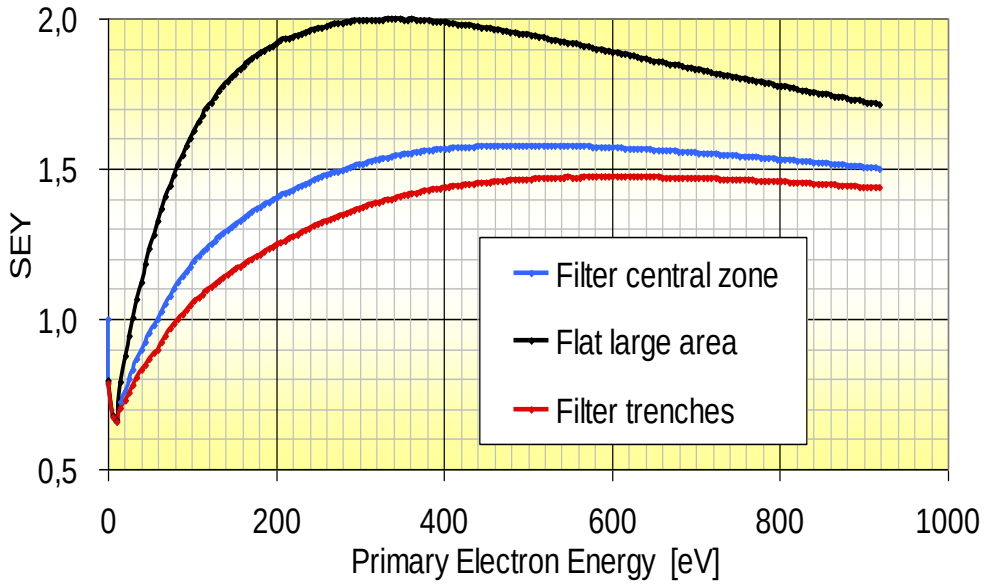

Figure 36. SEY of bare Ag plating Tesat filters before any treatment. *SEY of central zone, as measured in an area of about 1 cm^2 including several pillars. SEY flat large area, as measured on ad hoc probe samples (50×50×1 mm). Effective SEY of filter trenches (grooves between pillars), as computed from 23% (flat) + 77% (groove) = 100%(central), assuming intrinsic SEY is everywhere the same and equal to that of large flat area. Averages of several tests.*

Table 9. Main properties of the sputtering treated filters

Filter #	**495**	514	494	512	500	**497**	**517**	**499**
	reference	1st	2nd	3rd	5th	**6th**	**7th**	**8th**
SEY E_1 */eV*	**25**	81	83	104	151	**325**	**264**	**317**
SEY σ_m	**1.8**	1.60	1.44	1.55	1.52	**1.25**	**1.29**	**1.24**
SEY E_m */eV*	**350**	900	470	880	1000	**1000**	**1000**	**1000**
SEY FoM	**3.7**	7.1	7.6	8.2	10.0	**16.1**	**14.3**	**16.0**
Multipactor [kW]	**2.9**	*not tested*	*not tested*	*not tested*	3.9	**6.3**	**14.0**	**14.8**
RF ***IL***	**0.042 dB ± 5%**	×2.0	×1.15	×1.15	×1.0	**×1.17**	**×1.25**	**×1.19**
Ti deposition*:* *Source*	***no treatment***	*cone*	*mag-netron*	*mag-netron*	*mag-netron*	*mag-netron*	*mag-netron*	*mag-netron*
Assisting ion fluence	--	*low*	*low*	*low*	*low*	*high*	*high*	*high*
Au deposition*:* *Ion assistance*	***no treatment***	*no*	*no*	*no*	*yes*	*yes*	*yes*	*yes*
SEY = average(large spot) value of central corrugated zone								
SEY FoM $= (E_1/\sigma_m)^{1/2}$, *Energy values in eV*								
Maximum available power in the Multipactor test system (VSC ESA) = 15 kW								
Optimization ***trial*** *for improving* ***RF IL*** *Optimization* ***trial*** *for improving* ***SEY***								

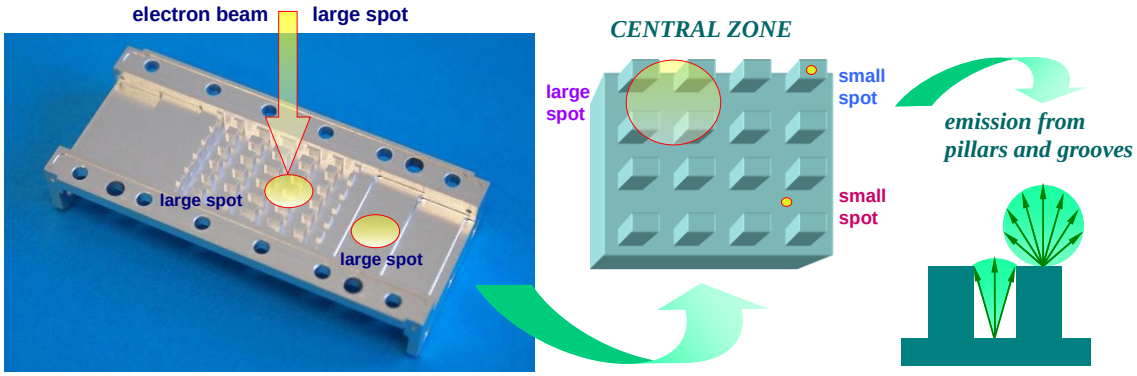

Figure 37. *Schematic diagram of the SEY measurement regions on the filters (multipactor samples).*

The SEY was usually measured with a large spot electron beam (1 cm^2) as in the central corrugated zone of the multipactor sample or in large flat areas as the transformer zone or in large flat witness samples. The central corrugated zone of the filters has 23 % of its area on the top of the pillars and 77 % in the bottom of the grooves among them. The intrinsic SEY of the pillars tops can be measured directly with a small spot electron beam (1 mm^2) but not that of the grooves, then, the effective SEY (affected by the geometry) is measured. That geometry factor can be computed from SEY measurements on a reference Ag plated multipactor sample with the same intrinsic SEY everywhere, Fig.36.

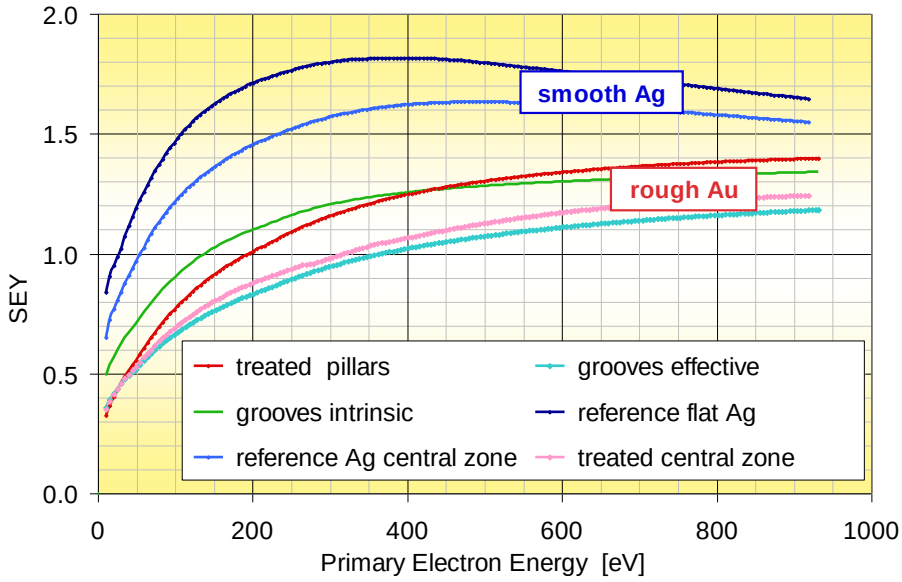

Figure 38. Different SEY curves measured on a treated multipactor sample (Filter 8th). *Reference flat Ag ← large spot measured on a large flat witness sample. Reference Ag central zone ← large spot measured on the central corrugated part of a reference untreated Ag-plated multipactor sample. Treated pillars ← small spot measured on the top of a pillar. Grooves effective ← small spot measured on the bottom of the grooves among the pillars. Grooves intrinsic ← computed for a hypothetical large flat witness sample with the same surface as that of the bottom of the grooves. See Fig.37. Averages of several measurements. SEY of the pillar tops is roughly similar in all of them but different from that of the bottom of the grooves among them, mainly at low primary energies.*

8.6.2 Surface morphology (SEM) analysis

The surface morphology of the treated multipactor samples was analyzed by Scanning Electron Microscopy (SEM) on both witness samples and directly on the filters. Fig.39-40 show SEM photos and computed images of the optimized surface roughness obtained

by the sputtering technique. The surface roughness is homogeneous and smooth, i.e., showing only one size scale. The surface roughness is formed by elongated and meandering protuberances about 30 – 70 nm width and 110 – 300 nm length with a height of 100 – 300 nm. The pore area among them represents about 40 % of the surface. The surface of the protuberances is smooth without any roughness of smaller scale.

The estimated approximated composition of the near surface region, as in images of Fig.40, was obtained from SEM-EDX and XPS analysis.

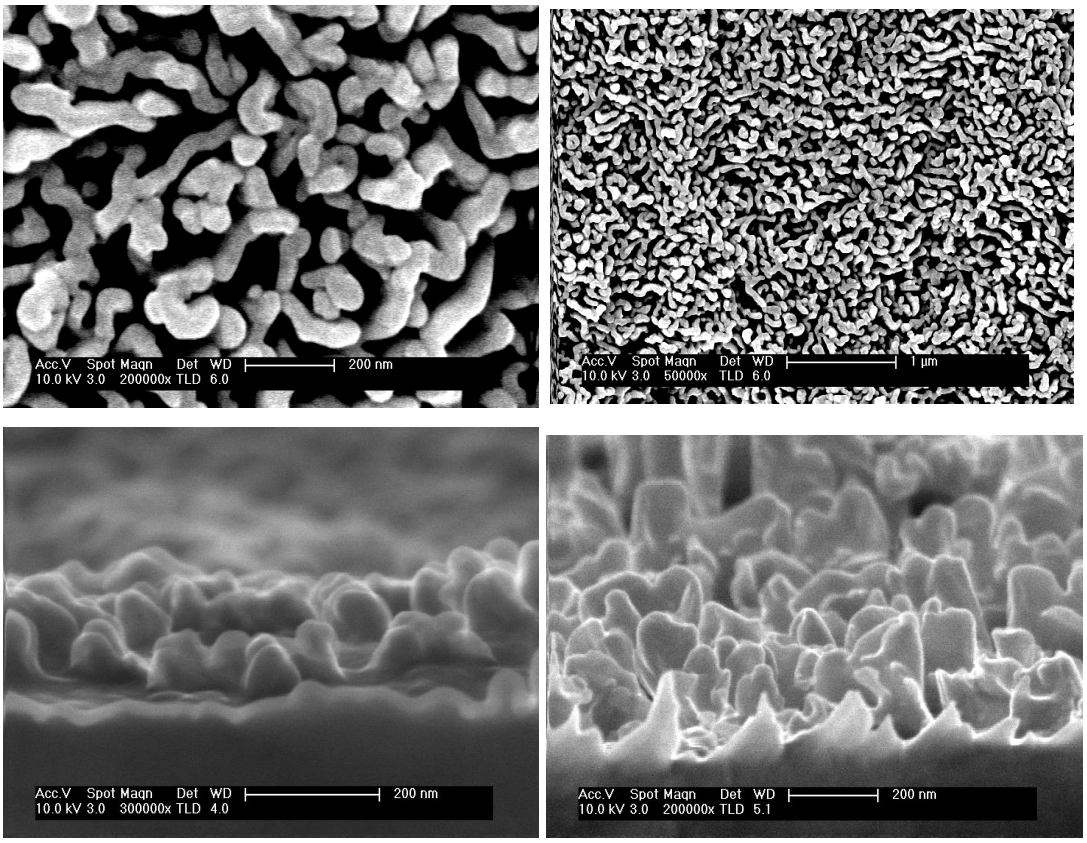

Figure 39. SEM photos of the optimized surface roughness *obtained by the sputtering technique (see text) on witness samples of Filter 8th. For profile photos, the sample was cut by a special technique and its edge was analysed at 90º.*

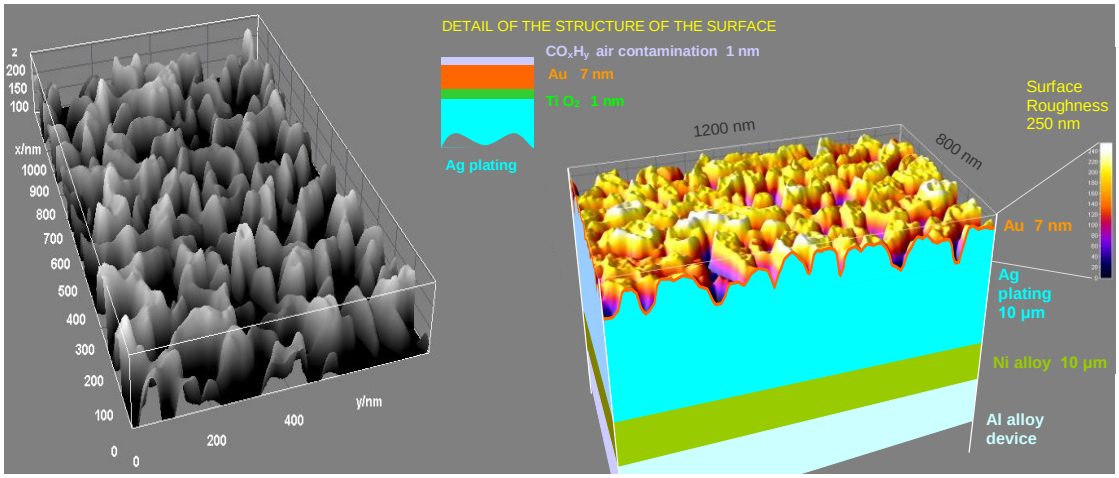

Figure 40. Images of the optimized surface roughness *obtained from SEM photos. See Fig.39. Composition of the near surface region obtained from SEM-EDX and XPS analysis. The Ti (masking material) is fully oxidized and supposedly, mainly on the protuberance tops.*

8.6.3 Low Power RF behaviour: Insertion Loss

The enhancement factor on insertion loss of the waveguide multipactor samples due to the surface coating (surface roughness plus overlayers of Ti oxide and Au) was controlled and practically reduced to the order of the measurement error (less than four times), see Table 9. Low power RF measurements of the S parameters were performed at Tesat. Fig.41 illustrates the insertion loss measurement results for the best filter.

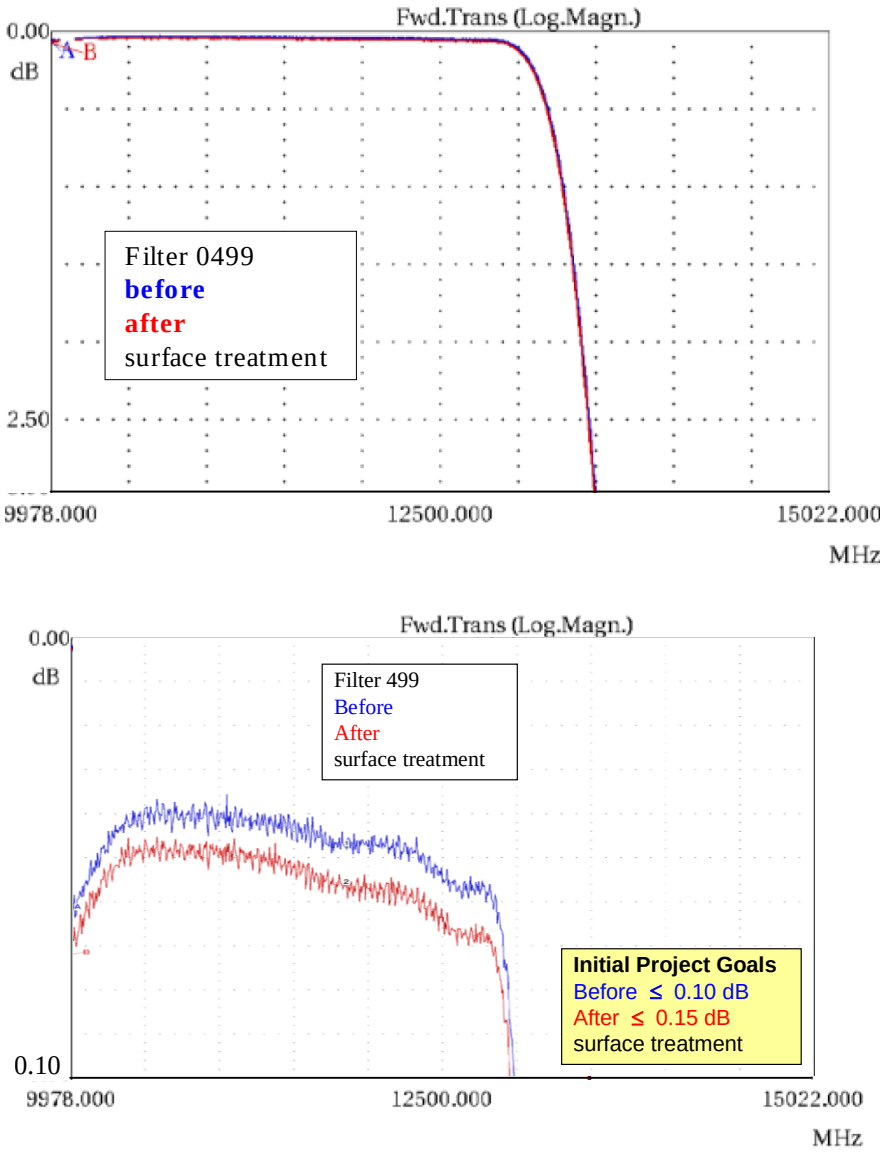

***Figure 41. RF scattering S_{21} parameter of Filter 8th**. Notice that RF performance was excellent, much better than the goal of the project.*

These excellent results were possible because the roughness scale (100 nm) was small compared to the RF skin depth (600 nm in Ag) and also because the thickness of the overlayers of Ti oxide and Au were negligible against the skin depth.

8.6.4 Multipactor Test results

Four RF-multipactor samples (low pass filters) treated by the sputtering technique were sent to the European High Power Laboratory, ESA, VSC, in Valencia, for Multipactor

testing. The samples and the results are summarized in Table 9. For this table, Multipactor power level MPL is defined as the mean value of the power for the 1st and the 2nd discharges.

The first thing that can be observed is that MPL and SEY *FoM* do not correlate well. Since the filters all have the same geometry and frequency, since a correlation between SEY and MPL should be assumed, we should conclude that SEY when testing for MPL was not the same as was measured just after preparation (values are presented in Table 9), i.e., the effect of aging could be the main explanation of the failure of that correlation. This seems to be supported by the time Δt between SEY and Multipactor tests: about 200 day for Filters 5th and 6th, and about 90 day for the 7th and the 8th. The correlation between (FoM /Δt) and MPL is now excellent. This important aging effect could be explained by the extremely thin Au overlayer unable of avoiding reactions of Ag and Ti with oxygen containing molecules of the air.

8.6.5 Main conclusions on the masked sputtering deposition

A surface treatment based on sputtering for Ag-plated aluminum devices producing a rough Au coating has been developed which maintains the multipactor reduction properties of the treatment based on chemical etching described above while maintaining practically the same insertion loss properties (increase < 20 %) than the best possible, that of standard smooth Ag plating.

The dependence of RF surface roughness resistance on size was demonstrated as well as its practical disappearance for sizes very small compared to the RF skin depth. Thus, low surface resistance can be made compatible with surface roughness profiles of high aspect ratios and large SEY suppression effects.

The extremely thin rough Au surface layer was obtained by sputtering deposition with very low energy ion beam assistance over a roughened Ag surface. This rough Ag surface was obtained by low energy ion etching assisted by Ti mask sputtering deposition. The roughness was uniform, only one scale in the range of 100 nm-150nm, of high aspect ratio (estimated 1 – 2), some short range order (one scale, 100 nm), no long range order, and pore area 30 – 50 %.

However, the deterioration of the SEY properties with time and air exposure was only moderately slow; an aging effect was observed for more than 100 days of exposure to the air. A proposal for future research could be to substitute Ti by another masking element more stable in air plus to increase Au overlayer thickness to 20 nm.

Summary and General Conclusions

An ample and thorough investigation on materials and treatments for advanced anti-multipactor coatings for high-power RF devices in space has been performed.

This research was carried out in full and close collaboration with ESA and Tesat Spacecom (Germany).

It has been determined that main crucial requirements for those anti-multipactor coatings,

i) low SEY ($E_1 > 175$ eV, $\sigma_m < 1.3$),

ii) low surface resistance at high frequencies ($< 1.3 \times R_s$ (Ag plating) @ 10 GHz),

iii) slow aging in air (scale of year),

these are somehow contradictory for an homogeneous material alone and can only be accomplished by a multilayer coating with surface roughness of high aspect ratio.

That possibility, i.e., the feasibility of such coatings, is due to the different depth range of the required properties:

- the extremely low surface resistance requires Ag as the conductive layer in a thickness of at least 3 times the skin depth, i.e., > 2 μm,
- SEY of Ag exposed to the air soon deteriorates into $E_1 < 50$ eV, $\sigma_m > 1.8$,
- this SEY can significantly be improved by surface roughness of high aspect ratio without deteriorating surface resistance if the size scale of this roughness is less than skin depth, 600 nm at 10 GHz,
- this SEY can be improved even further by a surface layer of a material with lower SEY like Au or TiN, without deteriorating surface resistance if the thickness of this overlayer is much less than skin depth,
- a simple model for estimating the influence of surface roughness and surface material on the surface resistance at RF was developed and used to guide the experimental research on multilayer antimultipactor coatings with surface roughness,
- the resulting model or concept for an multilayer anti-multipactor coatings on a RF(10 GHz) device of Al alloy is:

i) a ≥ 3 μm Ag layer (electrodeposited) on the Al alloy bulk with an (electrodeposited) intermediate ≥ 3 μm Ni-P alloy layer for improved adherence,

ii) a surface roughness layer of high aspect ratio, uniform one scale (smooth), and high "pore" density (25 – 50 %), scale < 500 nm if on Ag, smaller if other material (iii),

iii) a top surface overlayer of a material of low SEY and high stability in air (Au, TiN, … other? to be investigated) of < 50 nm thickness, either as conformably deposited over the roughness layer or itself being also the roughness layer (ii ≡ iii).

These findings were applied on real space devices (Ku-band WR75 waveguides, gap transformers and low-pass filters) designed, built, and tested by advanced space industry (Tesat Spacecom) in two main research phases, corresponding to two ESA research projects:

- In a first project (ESA AO4025 CCN-02), many potential techniques and materials were investigated in order to achieve practical control of multipactor effect, and several techniques were found to be appropriate for the objective. Roughening of the Ag plating by chemical etching with subsequent Au overlayer was developed and selected for the practical application on real devices which demonstrated suppression of multipacting even for the higher power level available. Insertion loss was only 70 % of that of reference *Alodine* coating. Aging behaviour was excellent: practical control of multipacting was maintained even after one year of exposure to the air. The best typical roughness of Ag plating was chaotic sponge like, as a random distribution of either pores of 3 ±2 μm or protuberances of 1.5 ±1 μm in lateral size and 3 ±2.5 μm in depth or height with a pore area ratio of 40 ±20 %, however, uniform and evenly flat at large scale and in the long range.
- That insertion loss was still 2.8 times that corresponding to the standard coating of Ag plating, thus a second project (ESA ITI B00011822) was carried out in order to decrease surface resistance as far as possible, desirably 1.5 times that of reference Ag plating. It was amazingly achieved, about 1.15 times that of the reference. It was realized by one of the surface structuring techniques investigated in the first project: ion beam etching assisted by sputtering mask deposition, which was specially

developed for treating space industry RF devices. Real practical RF devices of Tesat Spececom were treated in our laboratory by this technique which demonstrated practical control of both multipacting and insertion loss. The best typical roughness was uniform one-scale chaotic distribution of meandering elongated protuberances of (50 ±20)×(200 ±100) nm lateral size and 150 ±100 nm height with in-between pore area ratio of 35 ±10 %, however, uniform and evenly flat at large scale and in the long range.

Several of the investigated surface-roughening techniques demonstrated potential features for practical control of multipacting and insertion loss in high-power RF devices in space, but, however, they could not be applied to real space-industry devices because of lack of resources and time. Chemical etching of Ag plating was selected instead since it appeared simpler. Main ones were:

- sputtering deposition of Cu at high rate and Ar residual pressure, 100 nm roughness, expected to work also for Ag or Au o other convenient materials,
- flash evaporation of Ag at high rate and Ar residual pressure, 100 nm roughness, expected to work also for Au or other convenient materials, and
- chemical etching of a Ag-20%Cu alloy, expected to work also for other suitable alloying elements and compositions.

Also different final surface treatment were tested for the top surface overlayer: a) very low energy ion beam, b) heat treatment in vacuum and in air, and c) very thin Rh coating, apart from thin Au coating selected for application in real RF devices.

Two other surface-roughening techniques appear to have many convenient features for obtaining coatings with strong SEY suppression effect which were not investigated further as they present severe difficulties for applying to the intricate and large geometries of RF devices:

- glancing angle deposition (GLAD) of sculptured thin films (STF) either by thermal evaporation or sputtering, and
- cycles of electrochemical oxidation-reduction (ORC's) finely controlled by voltammetry techniques, used for preparing surfaces for Surface Enhanced Raman Scattering (SERS).

Other techniques for obtaining coatings with SEY suppression by surface roughness of high aspect ratio were not investigated further as those coatings include dielectric material layer into the 3× RF skin depth which can produce abnormally high surface impedance effects:

- chemically etched porous anodic Al oxide electrochemically deposited on the Al-alloy substrate (RF device) with subsequent Au metallization,
- chemically etched porous ceramic Mg oxide (*Anomag*®) prepared by Plasma Electrolytic Oxidation (PEO) on Mg-alloy substrate (RF device) with subsequent Au metallization.

During the technological research summarized above, many other conclusions of scientific and technological interest were arrived at:

- The RF surface resistance enhancement due to surface roughness can be significantly reduced (and practically annulled or hidden into as-received machining-origin roughness) even for high aspect ratios, by reducing roughness size scale well below RF skin depth.
- The SEE suppressing effect of surface roughness of high aspect ratio has been proven from size scale of 10 nm to 10 mm. Thus, it can be made compatible with very low RF surface resistance.
- The SEY suppression effect (SEY smooth ÷ rough) of surface roughness is generally higher for lower primary energies which makes it very efficient in increasing multipactor threshold.
- This higher SEY suppression effect at low primary energies amplifies the benefit (for avoiding multipacting) of using a material of higher E_1 value for the top surface layer, for example, Au against Ag.
- Macroscopic roughness in mm scale such as geometrical structure (grooves, basins or protrusions) of waveguides (transformer and low-pass filters) has also a SEY suppression effect; which should be taken into account when testing SEY directly on the devices.
- There was found a close correlation between Multipactor power threshold and the parameter (E_1/σ_m) even among devices with different structures, i.e., different

((gap voltage)^2 ÷ power) values, which is not expected since the Multipactor relevant magnitude is the gap voltage.

- The effect of Multipactor test (Tesat Spacecom) on devices with standard Ag plating or after chemical etching and Au coating was small: + 15 % on E_1 and – 5 % in SEY.
- The SEY aging in air of Ag plating roughened by HF+HNO_3 chemical etching (procedure developed) is: first, during 20 – 30 days, decrease (5 – 10 %) of SEY for low primary energies, then, increase (10 – 50 %) for all energies until saturation for more than 10 month. Starting from standard Ag plating exposed to the air:

  E_1: 21 $\xrightarrow{\text{chemical etching}}$ 500 $\xrightarrow{\text{1 month}}$ 600 $\xrightarrow{\text{5 month}}$ 100 $\xrightarrow{\text{10 month}}$ 85 eV,

  σ_m: 2.40 $\xrightarrow{\text{chemical etching}}$ 1.05 $\xrightarrow{\text{1 month}}$ 1.05 $\xrightarrow{\text{5 month}}$ 1.40 $\xrightarrow{\text{10 month}}$ 1.60,

  E_m: 325 $\xrightarrow{\text{chemical etching}}$ 750 $\xrightarrow{\text{1 month}}$ 1030 $\xrightarrow{\text{5 month}}$ 550 $\xrightarrow{\text{10 month}}$ 450 eV,

- From the wet chemical etching processes investigated and based on either i) HF+HNO_3, or ii) H_2O_2+NH_4OH+CH_3OH, or iii) KI+I_2, or iv) HCl+HNO_3, or v) H_2SO_4+H_2O_2, only the first one produced the appropriated surface roughness on standard Ag plating.
- The mechanisms of Ag surface roughening by HF+HNO_3 chemical etching was not definitely clarified, however, some suggestion may be made:

  i) The reaction of the HF+HNO_3 aqueous solution with Ag produces $AgNO_3$, AgF, and O_2 and NO gases; and sub-microscopic gas bubbles are formed ($AgNO_3$ is moderately soluble in HNO_3+H_2O, AgF is very soluble in $AgNO_3$+HNO_3 aqueous solution),

  ii) gas bubbles act as etching template by controlling reactant access to the Ag surface and thus are critical for pore formation, if they are not sufficiently stagnant pores are not etched but smooth fast erosion results.

- The main mechanisms involved in the self-organized surface roughness growth on Ag by low energy Ar ion etching assisted by Ti mask (surfactant) sputtering deposition are assumed to be:

i) Ti sputtering deposition on Ag while Ar ion bombarding would mechanically tend to Ti-Ag mixing and formation on an alloy, however, thermodynamically, that alloy is unstable and thermochemical driving forces tend to phase separation by spinodal decomposition,

ii) that spinodal decomposition is triggered once the surface Ti composition reach into the corresponding spinodal composition range,

iii) phase separation by spinodal decomposition and nucleation of Ti phase grains at low temperature is activated Ar ion bombardment induced diffusion,

iv) preferential sputtering of Ag, selective Ti deposition on protuberances, shadowing effect of protuberances, phase separation, and surface diffusion enhanced by Ar ion bombardment lead to the formation, growth, and coalescence of conical protuberances,

v) at advanced stages of the surface roughness growth, protuberances tend to cluster producing an overlapping roughness of larger scale without fading away the initial roughness of smaller scale; and eventually, clusters grow isolated on bald smooth substrate regions. This has been explained in thin-film experimental models of phase separation by resonant capillary wave effects and coarsening of domains. Thus, an energy term associated to the protuberance-substrate boundary should to be identified.

vi) The system of the rotating Ag substrate, the normal incident ion beam, and the oblique mask-surfactant atom beam behaves as *soft matter* and the growth dynamics of the surface roughness shows the corresponding characteristics.

Conclusiones

Las técnicas usuales de micro y nano estructuración de superficies con un gran control detallado de la estructura no son adecuadas para la aplicación considerada por su dificultad, complejidad y costes. La regularidad o simetría no es importante. La rugosidad superficial puede ser caótica pero debe ser homogénea y de una sola escala (suave). De una relación de aspecto grande pero no extremadamente grande. Debe de aplicarse fácilmente a superficies grandes e intricadas. Se han desarrollado técnicas químicas y de haces de iones para esos objetivos tecnológicos.

El concepto de recubrimiento multicapa desarrollado ha sido muy fructífero. Los principales procesos de superficie: i) reactividad química, ii) SEE, iii) efecto de "supresión de SEE" por la rugosidad, y iv) conductividad de RF, son de escalas o penetraciones diferentes, lo que ha permitido satisfacer varios requerimientos tecnológicos aparentemente contradictorios.

Desarrollo de una técnica de grabado químico poroso (micro-estructuración) de gran relación de aspecto para Ag.

Desarrollo de una técnica de auto-estructuración sub-micrométrica para Ag de gran relación de aspecto por grabado con haces de iones asistido por deposición de máscara-surfactante por sputtering.

Aplicación de ambas técnicas en guías de onda transformadores y filtros de banda Ku de características sin precedentes con respecto a su comportamiento de RF a altas potencias: control práctico definitivo de la descarga Multipactor y las pérdidas de inserción.

La caracterización de la SEE de diversos recubrimientos usados en la industria espacial ha permitido probar y perfeccionar varias herramientas de software usadas por la industria espacial para simular la descarga Multipactor en dispositivos de RF.

Comprobación experimental de la influencia de la rugosidad superficial en el efecto de "supresión de la SEE" y del aumento de la resistencia superficial a RF y su dependencia de la forma y el tamaño. Comprobación de la posibilidad práctica de desacoplar ambos efectos.

El interés de ESA y la industria espacial por la importancia tecnológica de los resultados de esta investigación han hecho que se hayan realizado varios proyectos contratados. Y como consecuencia también el apoyo del Plan Nacional de I+D+i.

La investigación en otros laboratorios de prestigio internacional ha sido muy influida y se están abriendo líneas de investigación similares. Esta influencia se observa claramente en los congresos MULCOPIM de ESA del campo tecnológico específico.